AD723347

THE
SHOCK AND VIBRATION
BULLETIN

Part 2
Keynote, Physiological Effects,
Isolation and Damping

DECEMBER 1970

A Publication of
THE SHOCK AND VIBRATION
INFORMATION CENTER
Naval Research Laboratory, Washington, D.C.

D D C

MAY 21 1971

C
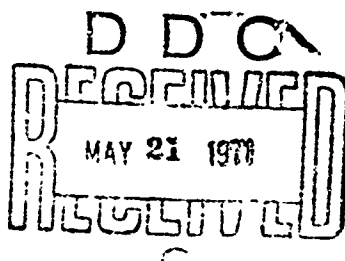
Office of
The Director of Defense
Research and Engineering

SYMPOSIUM MANAGEMENT

THE SHOCK AND VIBRATION INFORMATION CENTER

William W. Mutch. Director
Henry C. Pusey. Coordinator
Rudolph H. Volin. Coordinator
Edward H. Schell. Coordinator
Katherine G. Jahnel. Clerk Typist

Bulletin Production

Graphic Arts Branch. Technical Information Division.
Naval Research Laboratory

THE
SHOCK AND VIBRATION
BULLETIN

DECEMBER 1970

The 41st Symposium on Shock and Vibration was
held at the Air Force Academy, Air Force Academy,
Colorado, on 27-29 October 1970. The U.S. Air Force
was host.

CONTENTS

PAPERS APPEARING IN PART 1
Part 1 - Classified
(Unclassified Titles)

PAPERS APPEARING IN PART 3

Instrumentation

--

vi

Dynamic Stress Analysis

A DISCUSSION ON THE ANALYTICAL DYNAMICS, STRESS,
AND DESIGN INTERFACES
    Irvin P. Vatz, Teledyne Brown Engineering, Huntsville, Alabama

DYNAMIC STRESS ANALYSIS IN A STRATIFIED MEDIUM
    Jackson C.S. Yang, Ames Research Center, NASA, Moffett Field, California

COMPARISON OF STRUCTURAL LOADS: STATIC VERSUS DYNAMIC
    Paul J. Jones and William J. Kacena, III, Martin Marietta Corporation,
    Denver, Colorado

EGGSHELLING AND VIBRATIONS OF A HIGH SPEED SHAFT WITH
NASTRAN ANALYSIS
    Dennis J. Martin and William C. Walton, Jr., NASA Langley Research Center,
    Hampton, Virginia

PARAMETRIC STUDY OF A BEAM WITH A COMPOUND SIDE-BRANCH RESONATOR
AS A DEVICE TO EVALUATE PRELIMINARY DESIGN LOADS
    J. Roger Ravenscraft, Teledyne Brown Engineering, Huntsville, Alabama

RAIL LAUNCHING DYNAMICS OF THE SAM-D SURFACE-TO-AIR MISSILE
    Martin Wohltmann, Leonard A. Van Gulick, H. Carlton Sutphin, Martin Marietta
    Corporation, Orlando, Florida

PAPERS APPEARING IN PART 7

Mathematical Analysis

ROCKET-SLED MODEL STUDY OF PREDICTION TECHNIQUES FOR FLUCTUATING
PRESSURES AND PANEL RESPONSE
    Eric E. Ungar, Bolt Beranek and Newman Inc., Cambridge, Massachusetts

DETERMINATION OF STRUCTURAL PROPERTIES FROM TEST DATA
    A. E. Galef and D. L. Cronin, TRW Systems Group, Redondo Beach, California

VALIDITY OF MATHEMATICAL MODELS OF DYNAMIC RESPONSE OF STRUCTURES
TO TRANSIENT LOADS
    Wilfred E. Baker, Southwest Research Institute, San Antonio, Texas

DYNAMIC RESPONSE OF PLATES WITH CUT-OUTS
    Nicholas L. Basdekas, Office of Naval Research, Arlington, Virginia and
    Michael Chi, Catholic University of America, Washington, D. C.

NATURAL FREQUENCIES AND MODE SHAPES OF PLATES WITH
INTERIOR CUT-OUTS
    Jon Monahan, P. J. Nemergut, USAF Air Force Institute of Technology,
    G.E. Maddux, Air Force Flight Dynamics Laboratory Wright-Patterson AFB, Ohio

FINITE BEAM ELEMENTS FOR DYNAMIC ANALYSIS
    V. H. Neubert, The Pennsylvania State University, State College, Pennsylvania and
    H. Lee, Westinghouse Research Laboratory, Pittsburgh, Pennsylvania

EVALUATION OF MODELS FOR ONE-DIMENSIONAL VIBRATION SYSTEMS
    R. D. Rocke, University of Missouri-Rolla, Rolla, Missouri

KEYNOTE TALK

THE DYNAMIC CENTURY

D. Zonars
Air Force Flight Dynamics Laboratory
Wright-Patterson Air Force Base, Ohio

Webster refers to the word dynamic, derived from the Greek word *dynamikos*, as an adjective characterizing a number of environmental aspects which affect our lives. In physics, it pertains to power or physical forces producing motion. Similarly, it can pertain to change of process as a manifestation of energy. In economics, it has to do with the disturbance of economic equilibrium force, and is independent of whether such change has occurred by the sudden introduction of exceptional conditions or through progressive change in the standards and habits of people. In the fine arts, dynamics involves the effect of motion or progression. In medicine, it pertains to cell changes, physical make-up, the mind and associated thinking. In music, it involves sound variation and contrasts in loudness or power in tones.

The aforementioned disciplines or areas of personal involvement, to mention a few, are indeed undergoing dynamic change. As humans we are deeply immersed in this dynamic environment. The early morning alarm is perhaps the most fundamental of acoustic excitations, for not only does it provide for a kind of awakening, but it also alerts us to an environment that is continually changing. Environmental change is certainly, and for the most part, a manifestation of people attempting to achieve some goal. By necessity, this involves the expenditure of power or energy to achieve such an end.

The nationwide unrest on our campuses is certainly a dynamic situation. The mere mention of youth and campus unrest brings to mind education, learning and the ultimate utilization of such knowledge. Knowledge transforms the unknown into the uncertain. However, fear dwells within the uncertain and, hence, we are driven to identify recognizable

factors and uncover the shroud of uncertainty. The engineer and scientist have always been an inquisitive, searching and progressive type of individual. His goals are to solve problems, generate a technical base for new developments and to create. Creativity is itself very illusive and difficult to develop. Creativity sometimes results from an interdisciplinary approach such as experienced from the intersection of two different technical planes. Such an interdisciplinary approach requires a communication network which is unfailing in providing the proper assumptions, facts and understanding. The germination of such creativity results in continual exchange of information, development of ideas and, finally, the emergence of a "spike" in the dynamic spectrum which exemplifies the created.

The technical stature of this country is a tribute to the scientist and engineer in his loyal and aggressive desire to create a better civilization. We are but 70% of the way through this dynamic century and, already, many advances have taken place which from an equivalent standpoint have taken thousands of years to achieve in the past. Who would have thought in the year 1990 that flight would have occurred in 1903? Isn't it ironic that Wilbur Wright, in conjunction with his brother and after very successful glider flights at Kitty Hawk in 1901, declared his belief that man would not fly within a thousand years. And yet, in a short 66 years, or the equivalent of less than the average man's lifetime, we have landed on the moon. Magnificent achievements such as these can only result from a commitment to achieve a certain goal through the unique resourcefulness contained within man. More specifically, this success must be characterized by man's intellectual resources and his highly geared motivation to succeed. Nearly all of our technology gains and forward

1

steps have been the result of scientific brainpower and the always needed financial support. Having made man knowledgeable and properly outfitted him with material resources, he sets out to accomplish the seemingly impossible. Many times he reverts to increased power and energy techniques. This power expenditure is, by thermodynamic laws, not 100% efficient, and coupled with population increase, it results in a number of talked about phenomena such as air, noise, and water pollution. Looking at the manifestations of energy, one can certainly think of it as a forcing function. Immediately, the scientist and engineer cannot help but relate to response characteristics. As a result, we are experiencing many dynamic phenomena during this century which are of primary importance. Increasing requirements of our military and commerical aviation over the past 20 years has necessitated the development of larger aircraft. Hence, greater and more powerful engines have been required to propel such aircraft to transonic and even supersonic speeds. Consequently, noise pollution is becoming a thorn in the world's side. This problem has been evolving for many years with only a very limited amount of research to complement the technical developments.

Over and above being an annoyance to our senses, intense noise has degraded the structural-material properties of our flight vehicles with numerous and extensive failures. In the area of structural dynamics, we find fracture mechanics looming as a spectrum 'spike" for investigation. This area takes on added complexity when one considers the vibratory and shock aspects imposed upon an arbitrary structure. In another area, the dynamics of airflow systems as experienced in inlet-engine compatibility has reflected adversely upon the flight characteristics of some of our aircraft. In the past, inlet steady-state distortion resulting from both external and internal flow conditions has been one of the primary causes of propulsion instability. However, with the advent of supersonic flight, the unsteady nature of inlet flows has had a profound effect in reducing the engine operational stability margin and consequently causing compressor stalls. The primary source of these inlet flow pulsations or fluctuations has been identified as shock-boundary layer interactions and airflow separations. These fluctuations are generally random in both time and space and are often referred to as "turbulence". "Turbulence" exhibits a large range of amplitude-frequency content. Future couplings between inlet and engines must account for the dynamic or the time dependent characteristics of the ducted flow. Another problem area involves the flight of aircraft and missiles in the transonic flight regime. Today we are at the development threshold of new air superiority fighters, new commercial aircraft which will cruise at slightly above the speed of sound.

Here again, shock boundary layer interactions and flow separation are considered to be the driving potential for excitation of the flight structure. Present day aircraft can experience buffeting in this speed regime while flying in the cruise attitude. Increasing the angle-of-attack normally increases the buffet intensity. With further increases in angle-of-attack, we normally experience flight control instabilities such as wing rock, pitch up or pitch down. The combinations of buffet excitation and loss of stability and control can result in very severe vibration bordering on aircraft destruction. Such conditions require an interdisciplinary treatment of the problem with due consideration for vehicle dynamics, structures, aerodynamics, stability and control, and propulsive influences. One can go on and on enumerating aeronautical phenomena involving a dynamic environment, however, time is of an essence.

Vibration and shock engineers and scientists have always recognized that most phenomena in nature are dynamic, and that a dynamic approach, while difficult and sometimes burdensome, is the best way to unravel the complexity of the environment which affects all vehicles. A recent Air Force program, referred to as Project LAMS (Load Alleviation and Modal Suppression), has brought into focus the possibility of controlling the flight vehicle structure such that it automatically reacts to disturbances or gusts in the environment. This program makes use of accelerometers located at strategic points on the airplane wing to sense gust disturbances which in turn activate a circuit that causes a control surface to immediately deflect in the direction of strongly damping the motion. In a practical sense, this eliminates the dynamic stresses in the structure due to sudden accelerations. The effect of such a system in improving the fatigue life, ride quality, and controlling the flutter modes of the aircraft is immediately apparent. By necessity such a system is composed of sensors, electronic circuits, control surfaces and actuators and must be perfectly reliable. To push the reliability of this overall system to the lofty peak that is required, redundancy is invoked in design. This redundancy is effective only if malfunctions in the redundant arms of the system are uncorrelated, but vibration and shock can affect the whole aircraft and may provide highly correlated excitations that tend to degrade simultaneously all the redundant arms. Other environments that may do this are ionizing radiation and lightning but vibration and noise are perhaps the most pervasive and continuous, and hence, most important to guard against. Thus, the problem of operational reliability becomes as extensive as the degree of design redundancy.

Thirty percent of this dynamic century still remains and it is my personal conviction that we will continue to make technological progress by leaps and bounds even with

2

constrained resources and support. A number
of new challenges face us which will spur
scientists and engineers on to greater heights.
The area of composites as a new structural
material will provide a new dimension for our
future flight vehicles. As much as 50%
vehicle structural weight savings will be
possible and still have a greater fatigue
tolerant article. In addition, the anisotropic
properties will afford new approaches to
increased vehicle performance through aero-
elasticity. Lifting reentry will someday
become a way of life with its attendant cross-
range capability. Boost glide transportation
with partial centrifugal lift could possibly
become a mode of international travel. Hyper-
sonic cruise vehicles could also play an
important role in transportation and at the
same time contribute to a very low sonic boom.
Film cooling techniques of our turbine blades
in advanced propulsion engines will play an
important role in providing added thrust and
increased thermal efficiency. Pre-cooled inlet
airflow systems could become an advanced
propulsive concept which would increase the
mass flow due to increased density and also
afford the opportunity for increased after-
burner operation. Air cushion landing systems
are a strong possibility. While the blowing
characteristics of the on-board compressor
system for this device is used for landing and
take-off requirements, the suction capability
of the same compressor system could be
utilized for laminar flow control of the air-
craft turbulent boundary layer during cruise
flight. In addition, supersonic compre .or
and supersonic turbine developments are
definitely on the horizon. Although many of
these devices may not come to full fruition
during this century, I'm quite certain that
adequate research and development will be
accomplished to enable system development.

Designs for the development of ocean,
ground, continuum flight and space vehicle
of unprecedented size, weight, sophistication
and performance are being conceived for vehicle
development in the remaining portion of this
century. The rapid NASA, Army, Navy, and Air
Force advances made over the past 30 years has
brought into clear focus the need for extensive
component and integral experimental treatment
of the fundamentals involving shock and vibra-
tion. The purpose of this symposium is to
survey a number of the more important aspects
relating to these phenomena and thereby pro-
vide the underlying basic sciences involved.
This research and development must remain a
viable program within our country in order
to maintain our technical superiority in all
fields. As in the past, dynamic problems will
arise and require your diligent and uncompro-
mising attention through existing and new
testing and simulation techniques. The
importance of effective vibration and shock
engineering is thus very apparent. I have a
strong conviction that you ladies and gentlemen
in the future may well control even more than
now, the pacing element in design progress and

3

PHYSIOLOGICAL EFFECTS

TESTING AND MODELING STANDING

MAN'S RESPONSE TO IMPACT

Joseph Gesswein and Paul Corrao, M.D.
Naval Ship Research and Development Center
Washington, D.C.

Volunteers were dropped from heights of two to nine
inches to land stiff-legged onto a rigid force gage.
A linear relationship was found to exist between the
logarithms of the peak force developed and the kinetic
energy at impact. A mathematical model was then devel-
oped to reproduce this relationship and to adhere to
the general shape of subject's force-time response.

INTRODUCTION

Ship shock caused by underwater explosions
results in violent deck motions which lead to a
force buildup in the body of anyone on the decks.
Injury to standing men will occur when the force
exceeds the fracture strength of leg bones. Just
how this force develops in the body in response
to impact seems to have been neglected and yet
knowledge of body response is equally as import-
ant to protection design as is a corresponding
knowledge of input deck motions and the proper-
ties of protective materials. All three units
constitute a system in which each component must
be understood before overall response can be
effectively predicted.

This paper covers the measurement of force
growth when three volunteers were dropped from
various heights to land stiff-legged onto a force
gage. A mathematical model was then developed
which would reflect the force response of the
volunteers and yet be responsive to more general
acceleration typical of ship decks. As a result
of this investigation, injury prediction can now
be made based upon a direct comparison between
force developed in the human body and force re-
quired to cause bone fracture.

TEST METHOD

It was planned initially to have test sub-
jects stand on a force gage mounted to a machine
capable of producing shock-like deck accelera-
tions. The method was abandoned after some
testing, because it required measurement of a
variable input acceleration, which complicated
analysis, and, in addition, catapulted subjects
into the air, an undesired event.

These burdens were avoided by simply drop-

ing subjects from a known height onto a force
gage. By so doing, each subject would experi-
ence the same impact conditions, that is, im-
pact at a given velocity with a rigid surface,
and would develop a force solely as a result of
internal work developed in dissipating the kin-
etic energy acquired during the drop.

Drop Tester

It seemed important to the comparison of
results from different subjects that they all be
dropped in an identical manner. To do this, a
test device was built by which a man could be
dropped from a given height directly onto a
force gage. The device, shown in Figure 1, con-
sisted of two basic parts; a platform to support
the test subject and a guiding arrangement to
assure a controlled drop.

The guide consisted of two concentric pipes
which differed in diameter by about 1/4 inch.
The inner pipe was supported vertically at both
ends while the outer was free to slide on it.
Friction was minimal because of the loose fit.

The platform, which was assembled from
heavy bar stock and welded to the outer pipe,
had a plywood cover to provide a level floor for
a subject to stand upon. The two plywood sect-
ions which supported the subject's heels were
free floating. During a drop, only the weight
of the subject and these two small pieces of
plywood acted on the force gage positioned be-
low the tester; the rest of the tester dropped
an additional half inch before it struck the
floor.

The height positioning and release mecha-
nism consisted of a bar with a moveable flange.
At the start of a test the flange was inserted

under the platform to hold it at a certain distance above the gage. Accurate drop distances were measured after a subject was positioned on the tester. A quick pull on the bar disengaged the flange releasing the tester.
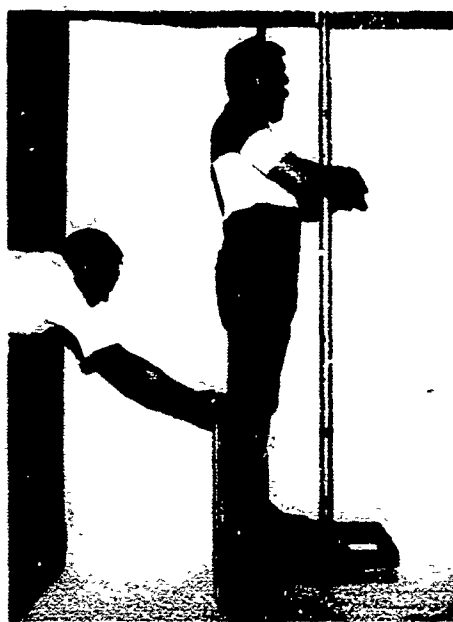
Fig. 1 Drop Tester

Subjects

Three volunteers participated throughout the impact response program. All three were young men in their early twenties. Two men were 69 inches tall, the third 72 inches. Their individual weights were close to those for the 5, 50 and 95th percentile man. Each man was tested while wearing street shoes with hard rubber heels.

Force Gage

The gage which eventually evolved for use in the drop test experiment is shown in Figure 2. It measured force in terms of strain induced in four cylindrical posts, each 1/2 inch in diameter and 4½ inches long. Four foil strain gages were mounted circumferentially on each post. All gages were connected in two opposite arms of a wheatstone bridge circuit to measure total force exerted on the gage.

The four posts were fastened in the center of a 1/2 inch thick steel base plate, geometrically at the corners of a 2 inch by 7 inch rectangle. Initially, two gages were made, one for each foot. The 7 inch post spacing allowed the heel and ball of one foot to bear down on a pair of posts. The top of each post was hollowed slightly to hold a 1/4 inch ball bearing in its center and so to aid in transmitting a pure axial load through each post. A cover plate,

made from 1/4 inch thick aluminum, rested on the ball bearings. During the upward acceleration tests, a subject's foot rested on the cover plate.
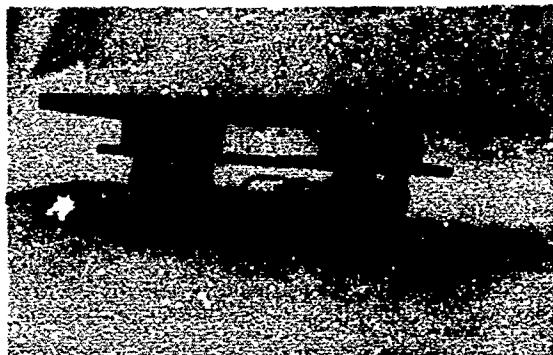
Fig. 2. Force Gage

In the drop tests, however, the gage was modified by adding a pair of 1 inch square bars placed on the cover plate directly over the posts. A top plate of 1/2 inch steel rested on these bars. This arrangement compensated for slightly inaccurate drops and further aided in transmitting axial loading through the posts.

TESTING

The force gage itself was placed on the concrete floor beneath the drop tester and positioned so that each of the subject's heels would strike and load two pair of strain sensitive rods axially. Only the force resulting from impact of the heels was measured. In early testing the force generated by impact of the balls of the feet was also measured, but when this force turned out to be of small magnitude and was later interpreted as a balancing force, the measurement was discontinued. Instead, subjects were instructed to lean back on their heels just before the platform was dropped to reduce the magnitude of this force. In this way the difficulties involved in making double measurements were avoided without compromising accuracy, since muscular force is not multiplied at impact, the time interval being too short to permit body reaction on.

In addition to measuring force, an accelerometer was also strapped to the subject's head to indicate the time of arrival of the decelerating stress wave. Stress propagation velocities could then be calculated using this time interval.

Tests were begun at an initial drop height of 2 inches and increased at 1 inch intervals with the understanding that testing would stop at the subject's request whenever the impact rces caused discomfort or pain. This request was never made. Instead, they unconsciously bent their knees at the higher drops instinctively trying to protect themselves. Eight inch drops were obtained with difficulty, and only one 9 inch drop was successfully completed as it

was obvious that the subjects were bending their knees to cushion the impact, an unexpected limitation of the test method. Short of rigidly locking a subject's knees, an idea with little appeal to the test subjects, drop testing was ended.

Figure 3 shows the force-time curves of one volunteer for a 2, 5 and 8 inch drop. The time scale is applicable to all records with an accuracy of 2 or 3 percent. Each record, however, is labeled with the value of the maximum force since a common signal amplification was not used for each test.
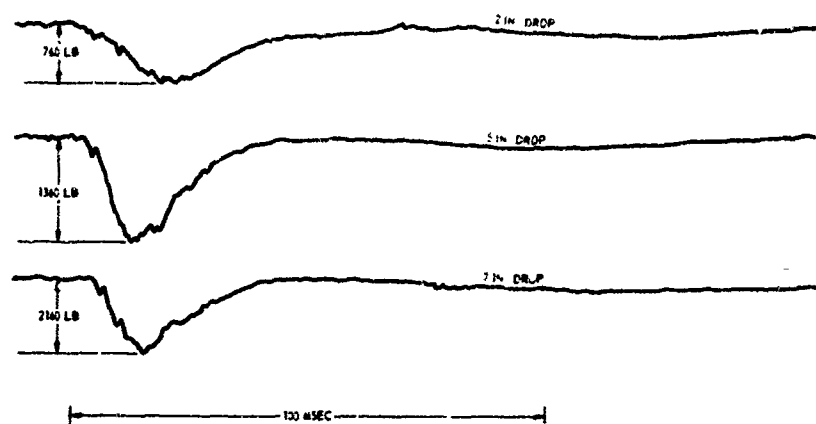
Fig. 3. Force-time Curves for One Volunteer
2, 5 and 7 In h Drops

Figure 4 shows a curve which illustrates the general results obtained in all tests. There occurs first a compression phase in which drop energy results in a force increase to a maximum. The time to peak force decreased from about 13 msec for a 2 inch drop to about 7 msec for a 9 i.ch drop. Then the body recovers from the im-

pact towards its normal weight. This time varied between 30 and 60 msec. It seems significant that in all the tests conducted only twice did the rebound force ever reach zero. Apparently, the body defends against impact largely by energy dissipation rather than by energy storage. This result influenced the design of a lumped parameter model for man.
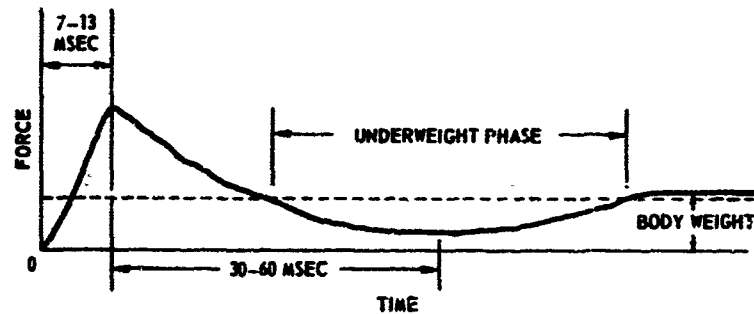
Fig. 4. Typical Features of Force-time Curves
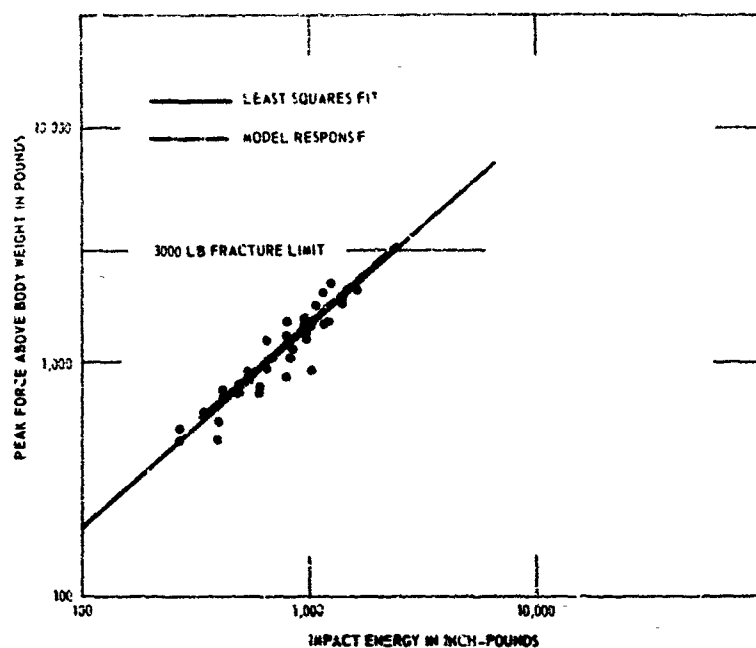
Fig. 5 Peak Force Developed Above Body
Weight Versus Impact Energy

The test result judged most significant to tolerance studies is shown in Figure 5. Here, the two highest values of peak force developed above body weight are plotted against the kinetic energy of each volunteer at impact. The straight line represents the least squares fit to the data which had the highest index of determination (.85) of several curves types tried. Equation 1 is the fitting equation

$$F = 4E^{.85} \qquad (1)$$

where E is impact energy in in-lbs and F is peak force in lbs above body weight.

Fig. 6 Stress Wave Transit Time
Versus Impact Energy

The time interval between foot force and head acceleration against the kinetic energy of impact is plotted in Figure 6. As best as can be determined by curve fitting, the transit time does not seem to be greatly influenced by height of drop. Apparently stress transmission occurs at a rather constant velocity, somewhat less than 1000 ft/sec. This speed is rather low considering that bone transmits sound at a velocity near 10,000 ft/sec and the soft body materials (mostly composed of water) at a speed near 5000 ft/sec. It would seem that the body's response to impact cannot be readily explained by assuming longitudinal stress wave propagation as in an elastic medium. Apparently, joint distortion with its accompanying generation of transverse shear waves slows elastic propagation times considerably.

Figure 7 shows how the time to the peak force varies with the magnitude of the force itself. There is obviously much scatter in this data. In fact, if it were not for the results of the model studies, the trend would be difficult to discern. The solid line represents the best least squares fit to the data; the dashed line represents model response.

8

Fig. 7 Peak Force Versus Time to
Peak Force, One Volunteer

DEVELOPMENT OF MODEL

The test data concerns forces arising from
the impact of stiff-legged man falling onto a
rigid surface. On shipboard, forces will arise
from stationary men being accelerated from up-
ward moving decks. To go from one case to the
other, a model is needed which will be in agree-
ment with the test data and yet be responsive
to deck accelerations.

It seemed that such a model should reflect
two basic human response properties, (1) the
general shape of the force-time curve resulting
from impact should be preserved as far as possi-
ble, and (2) the peak forces developed by the
model over the range of drop test should close-
ly match those developed by the volunteers.
Confidence in predictions could then be taken
in proportion to the agreement between model
and volunteer response.

As a result of these considerations, a
lumped parameter model was eventually evolved
to represent what is basically a complex stress
transmission problem. The model, given as
equation 2, represents a mass supported by a
parallel spring and damper combination. In
this case, however, rather than being constant,
damping is considered to be proportional to
displacement.

$$m(\ddot{x} - \ddot{y}) : cx\dot{x} + kx = 0 \qquad (2)$$

Here, $\ddot{y}$ is the applied acceleration and $\ddot{x}$, $\dot{x}$
and x are the acceleration, velocity and dis-
placement of the spring damper combination.
The spring constant is k, the damping constant
c and the mass m. For the 50th percentile man,
the best agreement of peak forces between man
and model occurred when k had a value of 200
lbs/in and c a value of 65 lb sec/in².

The value of k was somewhat lower than
might be expected, judging from the results of
static compression tests. Hirsch and White (1)
found that the spring constant for a men's legs
was about 1,500 lbs/in. From Ruff's (2) comp-

ression measurements on a human spinal section
from the 10th dorsal through the 5th lumbar
vertebrae, it would appear that this section
has a spring constant of about 3,100 lb/in. An
entire spine of 24 vertebra would accordingly
have a stiffness of about 800 lbs/in. It
follows that the series combinations of legs
and spine would imply a spring constant of about
520 lbs/in. If bending occurs, as it surely
must in the body, the overall spring constant
could be much lower and perhaps not too far
from the value of 200 lbs/in used herein.

Damping was included to take energy from
the system and to skew the force time curve
towards a shape like that observed in drop
tests. The form of the velocity damping term
was conditioned by the shape of the force curve.
In drop tests, force was zero at impact, the
time of maximum velocity, then it increased. It
would not be possible, obviously, to represent
damping as a product of a constant and a velo-
city because then the force would be a maximum
at the time of maximum velocity. To bring about
agreement with test results, damping was made
dependent on both velocity and displacement. In
this way force could not develop without some
displacement occurring, and yet it would be de-
pendent upon velocity as well.

Because of the inclusion of the damping
term, the force produced by the model, both for
impact and for initial accelerations, is strong-
ly dependent upon velocity itself. This result
was somewhat unexpected considering that static
testing indicates that large forces can be de-
veloped in the legs independently of velocity.
Model deflections are only on the order of one
inch at the time that fracture would be indicat-
ed; consequently, the force caused by deflection
alone is not significant in comparison with that
caused by velocity. The model response suggests
that an increased force develops when the body
is compressed rapidly above that developed in
static compression. This pattern follows that
reported by McElhaney and Byers (3) in their
dynamic studies on biologic materials. They
found that an increased stress, as much as two
to one, occurred for the same strain when bone
and muscle tissue were compressed dynamically
rather than statically.

How well does the model response to impact
represent the response of volunteers? The model
response curve shown in Figure 5, while slightly
higher, nevertheless agrees with the least square
square fit to similar values of force produced
by volunteers for the same impact energy. Of
equal importance is the observation that both
curves have about the same slope, a fact which
implies that test data extrapolated to the
fracture limit will not depart seriously from
model predictions. The reasonably good fit in-
dicates that the model's response will be in
agreement with the response of men at least as
far as predicting peak force is concerned.

When calculated and measured values of peak
force are compared for agreement in time of

... as ... ... in ... ... one volun-
... ... Here, the experi-
mental data ... ... influence. The trend toward
a shorter time to reach peak force as the impact
energy increases. ... there is so much
scatter in the representation of the experi-
mental data, that the fitted curve is not well
determined. The establishment of a trend would
require a much larger number of tests to be con-
ducted to obtain a reliable statistical mean
than were run here. Nevertheless, the
model response indicates the same trend with
calculated values of peak force occurring at
about the same time as did the experimental
data.

So far a model was developed with the 50th
percentile man in mind. How well model response
applies to men of other weight must now be con-
sidered.

When weight is varied, model response also
varies with some favorable and some unfavorable
results. Peak force, for example, is greater
for heavy men than for light men, as expected
for the same impact velocity. Accelerations,
however, are contrary to expectations. being
less for large men than for small men. In
addition, for the same impact energy light men,
contrary to test data, develop a greater force
than do heavy men. Obviously, some modifica-
tions are needed to make the response of all
men conform with reason as well as test data.

Consider the matter of acceleration for the
moment. As far as we know stress waves move
through the body with a constant velocity. Thus
when two different size men are dropped to a
deck from a common height. a stress wave should
travel upwards causing portions of their body
equally distant from the deck to be brought to
rest at the same time. Over this interval de-
celeration would be the same in both men. De-
celeration in the taller man, however, would
persist somewhat longer. But since most ser-
vice men differ from a mean height only by about
5 percent, we should expect that a lumped para-
meter model which developed a fairly constant
deceleration could be used to represent. fairly
adequately, what is basically a wave transmiss-
ion phenomenon.

Modifications to equation 1 must not only
tend to bring about a more uniform acceleration
among men but also cause a common force to de-
velop in proportion to their impact energy.

In seeking th modifications, the idea
that spring and damping terms could be represen-
ted as constant for all men was reexamined. This
consideration led to the belief that differen-
ces in size are not likely to occur without
other accompanying changes to the physical pro-
perties of the body: tendons, ligaments, muscles
etc. are all present in greater quantities in
big men than in small men. While damping and
stiffness properties of these components would
be the same on a unit basis, when size increas-
es more material is present, with the result

that stiffness and damping change in proportion
to the quantity of material present.

Now if stiffness and damping are made to
vary directly with mass, the model will then
respond to impact with equal acceleration re-
gardless of mass. However, peak force will then
be proportional to mass. Experimental data in-
dicates that peak force should be proportional
to the 0.85 power of mass for a given impact
velocity. Consequently, it would seem that
stiffness and damping ratios should vary with
some fractional power of mass.

Since volume scaling turned up deficiencies
area scaling, in which stiffness and damping
ratios varied with the 2/3 power of mass, was
tried next. This attempt turned out to be a
happy choice for the peak force developed from
impact of the 5, 50 and 95th percentile man, no
longer varied considerably with mass, but fol-
lowed closely the empirical relationship of equa-
tion 1 reflecting the average test data. In
addition, acceleration differences from the
mean to the outer percentiles was now reduced
to a modest 6 percent. In fact, as a conse-
quence of area scaling, equation 1 causes accel-
erations of different weight men from impact to
be inversely proportional to $w^{1/3}$, that is,
acceleration is directly proportional to the
time it would take a constant velocity stress
wave to traverse their height.

The equation which best represents our
efforts to model man's response to impact is
written as equation 3.

$$m(\ddot{x} - \ddot{y}) + c\left(\frac{m}{m_{165}}\right)^{2/3} \dot{x} + k\left(\frac{m}{m_{165}}\right)^{2/3} x = 0 \quad (3)$$

where the various terms have the meaning pre-
viously assigned. The term m_{165} refers to the
mass of 50th percentile man, whose weight is
taken to be 165 lbs.

SUMMARY

Test results indicate that human response
to impact involves stress transmission through
the body at a velocity near 1000 ft/sec.

A mathematical model was worked out which
developed a force-time response similar to that
recorded during impact testing of volunteers.
Model results show good agreement with human
response in respect to peak force and impact
energy but poorer agreement with respect to
the time at which peak force occurs.

Use of the model will permit injury pre-
dictions for shock excited deck motions by a
direct comparison of force growth in the body
to fracture force.

REFERENCES

1. Hirsch, A.E., and White, L.A., "Mechanical
Stiffness of Man's Lower Limbs," David
Taylor Model Basin Report 1810 (October
1964).

2. Ruff, S., "Brief Acceleration: Less than
One Second," Chapter VI-C, German Aviation
Medicine, World War II, Volume I, Depart-
ment of the Air Force.

3. McElhaney, J.H., and Byars, E.F., "Dynamic
Response of Biological Materials,"
ASME No. 65-WA/HUF-9 (Nov 1965).

DISCUSSION

Mr. Godino (GD/Electric Boat): Would you
please tell me where you get the original constants
you start with for m, c and k?

Mr. Gesswein: c and k were simply adjusted
during the trial and error process of finding an
equation that would model according to the data that
we had. It turned out for the average man that c had
a value of 62 pound-seconds per inch squared, and k
had a value of 200 lbs per inch.

Mr. Hughes (Naval Weapons Evaluation Facility):
Did you try an equation in which the damping term
was raised to a power of x? It would appear that
in progressing from the small man to the 166 pound
man and then to the 203 pound man, your fit was pro-
gressing to one side or the other. I think you would
get a better fit if you raised it to a certain power of
x. Have you tried that?

Mr. Gesswein: We thought of that. We tried
squaring it, and halving it, but these did not work as
well as simple first degree power so we left the
model as it is. The difficulty in changing exponents
is that we do not have really good data to work
with. We only tested three men and I have shown
you the scatter in the data. So any effort at sophis-
ticated modelling I think would be wasted.

Mr. Poete (Naval Undersea R and D Center):
Had a complete physical been given to the test
specimens, in other words, their age factor, any
spinal or leg type injuries, prior to the testing
period?

Mr. Gesswein: Yes, that was Dr. Carrao's
part. All of the subjects were thoroughly examined
at the Naval Medical Research Institute before the
tests and after the tests.

Mr. Stein (Arizona State University): Was
there any correlation in your tests between the
time of day of the drop and the apparent quite large
scatter for the same individual subjected to the
same drop? From one of your slides there is the
apparently considerable scatter in the data for the
same individual being dropped by the same height.
Was there any correlation in the data with time of
day or the relation to meal time? Because it would
seem to me that the soft parts of the body would not
accelerate as a rigid mass with the body, and per-
haps some of the time factors could be explained
that way, like a flabby belly might not come down

at the same time as the heel but at some time later
spreading the pulse out a considerable amount.

Mr. Gesswein: That certainly is a pertinent
point you have raised there. A lot of the scatter
that we observed was due to the volunteers bending
their knees during the drop. (Laughter) I think that
is understandable. We tried to eliminate it as much
as possible by cautioning them to keep their knees
stiff, but there is a lot of scatter in this kind of data
and it may be as you say due to many factors but we
could not investigate them in that kind of detail.

**Mr. Shaffer (Aerospace Medical Research
Laboratory):** How did you determine the 3000 lb
fracture limit?

Mr. Gesswein: I quote a reference in the paper
by Hirsch and White, they had 15,000 lbs per leg and
I looked over the references they had used and I
thought 3000lbs was a nice round number for that
sort of thing. It is not too well established.

Mr. Shaffer: How do you know that this is the
first mode of failure?

Mr. Gesswein: The model is simply designed to
predict when fracture will occur. That is all we de-
signed the model for. Not bruises, contusions and
so forth.

Mr. Clevenson (NASA Langley Research Center):
Would you explain a little bit as to why a heavy man
accelerates differently than a standard man?

Mr. Gesswein: If I left the impression that the
man decelerates differently it was erroneous. I
meant the model itself. You see when you divide by
the mass, then the heavier mass will of course have
the acceleration for the heavier man smaller than
that for the lighter man. I believe that all men,
since they are about the same height, decelerate
equally.

Mr. Smith (Bell Aerospace): Your last slide
seemed to show a partial attempt at least at non-
dimensionalizing your responses, and of course
that is a very good way to reduce scatter of which
you do not seem to have taken advantage. Most
previous information in this area has been, I think,
on frequency response of man and I think this in-
cludes a certain amount in the vertical direction.

11

Have you tried correlating existing data on frequency response with the impact response?

Mr. Gesawein: No I have not. That is probably because I am not aware of the existing data on the frequency response.

Mr. Eaton (Menasco Manufacturing Co.): You mentioned that you had an accelerometer on the top of the man's head and you showed a slide showing the time for the transient response to get up to the top of his head. What was the correlation between the g ratings, or accelerometer readings, and the platform reactions?

Mr. Gesswein: We did not make a measurement of the acceleration on the head. We used the accelerometer to indicate when the shock wave arrived. We did not use the accelerometer for the purpose you mention because we could not fit it to the head very well. We strapped it down but there was still the problem of hair, and we could not keep the man to keep his head vertical, we always seemed to have some horizontal component which would obscure the meaning of the reading.

EQUAL ANNOYANCE CONTOURS FOR THE EFFECT OF SINUSOIDAL
VIBRATION ON MAN

C. Ashley, Ph.D.
Mechanical Engineering Department
University of Birmingham.
England.

Existing experimental techniques have not given satisfactory answers to problems of subjective response to vibration. The author has suggested a new method in which a random vibration spectrum is used as datum and a cross matching procedure with sinusoidal vibration employed to find constant annoyance contours. This method has been applied experimentally to the standing position and shows a minimum sensitivity at 1.7Hz with increased sensitivity towards 0.7 Hz. Maximum sensitivity occurred between 6 and 15Hz. The standard deviations of the results were small compared to previous investigations. The contours agreed with the proposed ISO recommendation on vibration sensitivity of man.

INTRODUCTION

One of the fundamental requirements in assessing the acceptability of a particular environment is knowledge of the effect of vibration on man. The International Standards Organisation (ISO) has been working on this problem for some considerable time and a working group proposal (1)[*] is fairly close to becoming an ISO recommendation. For vertical sinusoidal excitation the proposed standard is given in Fig. 1, and it will be noted that only the frequency range 1-90Hz is included. The most sensitive region in acceleration terms is between 4Hz and 8Hz, which corresponds to the frequency range over which major resonances of the human body occur. Measurements of body strain by Clark, Lange and Coermann (2) show peak levels for the Upper abdomen, chest, lower abdomen and pelvis in this frequency range. Other investigators measuring transmissibility directly have also confirmed the range.

The limits of exposure are given in terms of three limiting criteria which are self explanatory, safe exposure, fatigue decreased performance, and reduced comfort. In this paper we are concerned only with the last criterion.

[*]A list of references is given at the end of the paper
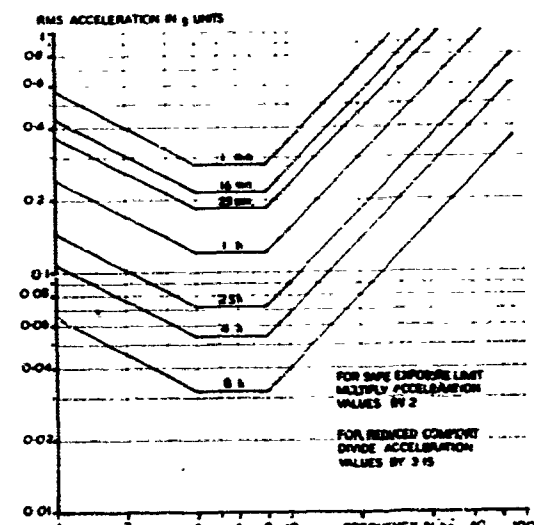
ISO Proposed Recommendations for the effects of vertical vibration on man.

Fig. 1

The straightforward data given by ISO is taken from a background of experimental work which is not at all straightforward. This is demonstrated by the type of data shown in Fig. 2.
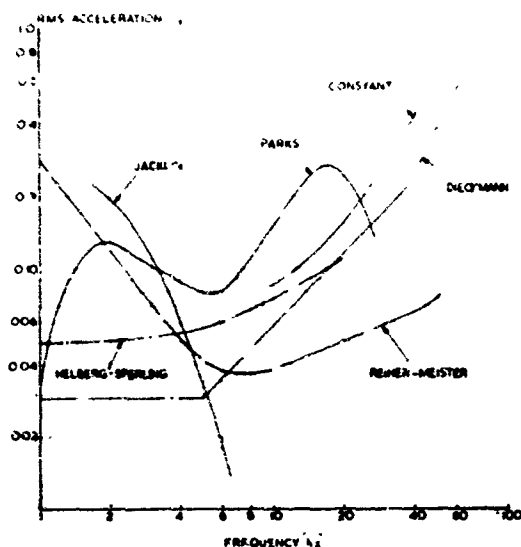
Subjective responses from various laboratory tests for vertical vibration tolerance (after Bryce (3))
Fig. 2,

in which the results of different experimenters are compared. Each one used different criteria, so one can expect differences in overall level but the shapes of the contours also differ in a significant manner, some showing a rise in sensibility of low frequency and others a fall. A wide critical survey of the literature and a comprehensive bibliography has been prepared by Guignard (4) and many further examples may be found.

The reason for this disagreement between investigators is probably due to the experimental methods used. All the subjective work reviewed by Bryce asked the subjects to classify the vibration in semantic terms i.e. acceptable, tolerable, mildly annoying, severe etc. All these terms have different meanings to different people and this makes control of the experiment difficult. During the course of the test the attitude of a single subject to a particular rating can change.

A possible alternative technique used by Woods (5) asked four subjects to classify vibration level in terms of numbers between 1 and 10, but a linear scale did not result from this technique.

For particular types of work such as vehicle ride assessment it is necessary to have satisfactory knowledge of the shape of the contours of equal annoy-

ance, so that one enviroment can be compared with another. The method used and presented in this paper was to accept the ISO proposed levels as correct at one frequency (6Hz), and then to obtain contours by asking subjects to compare the effects of vibration at different frequencies with a standard vibration which was random in nature. This is a similar technique to that used for the equal loudness contours in sound (6).

For this initial work to prove the cross matching technique, vertical vibration in the standing position was chosen as the subject. This choice eliminated problems of seat transfer characteristic which affect experiments conducted in the seated position.

EXPERIMENTAL TECHNIQUE AND RESULTS
CHOICE OF STANDARD

The first decision necessary in a cross matching experiment is selection of the standard. The standard selected was a random vibration excitation with a power spectrum which decreased at 12 db/octave when measured in displacement terms or was substantially flat when measured in velocity terms. The method of generation is detailed in Appendix 1. Choice of such a spectrum was dictated by the experimenters interest in the automobile ride enviroment (7) Study of a wide range of road and runway surfaces by . an Deusen (8) and LaBarre, Andrew & Forbes (9) have shown that on average the power spectrum of amplitude against wavelength shows a slope of two. This infers that bumps are geometrically similar and large bumps are of long wavelength and small bumps of proportionately smaller wavelength. When related to a vehicle travelling at constant speed, a constant mean velocity input spectrum can be inferred, the level being a function of the roughness of the surface and the speed of the vehicle. The vibration standard used corresponds to that which would be experienced on a vehicle with infinite rate springing, and is a useful generalised standard.

It was felt much better to use a random signal as a comparison standard rather than a sinusoidal signal, because at the fixed frequency chosen for the sinusoid, subjects would be excited in differing manner due to physiological differences.

EXPERIMENTAL METHOD

The random signal was related to the ISO proposal for FDP at 6Hz by cross matching for vertical vibration in the standing position. This was achieved by use of two electro-hydraulic vibrators mounted close together, Fig. 3, the subject moving from one to the other until satisfied by the equivalence. The actual printed instructions given to each subject are given in Appendix 2. The type of subjects used were fit males in the age range nineteen to fifty five. The sinusoidal level was fixed at the ISO standard and the random level varied. The acceleration levels were

14

Fig. 3
The subjected being vibrated at large amplitude and low frequency by one vibrator.

Fig. 4
The relationship between the arbitary random vibration and the principal ISO levels at 6Hz. The standard deviation is shown by the bar.

found by calculation from measured displacement of the vibrator.

The average results for 108 tests using 27 subjects are given in Fig. 4 and a satisfactory linear relationship is shown.

The equal annoyance contours for humans excited in the vertical stending position were then found using the average random levels found from the first experiment to correspond to the ISO FDP time limits for one hour, two and one half hours, four hours and eight hours as standards. For this experiment the random levels were kept constant as comparison levels, and the sinusoidal vibration level varied in the a plitude at each fixed frequency. Six subjects only were used for this stage of the investigation. The technique used was to start at 7 Hz and then take equivalence readings at step reduced frequencies down to 0.7 Hz. Then the frequency was increased upwards in steps starting from 7 Hz. By this technique any element of learning, or simple progressive change in amplitude sensitivity would be detected by a step in the contours at 6 Hz to 7 Hz, but no such step was

present. It was also gratifying that the six subjects gave an average at 6 Hz which was remarkably close to the equivalence average of the 27 subjects used in the first part of the experiment. The only major divergence was at the one hour level, but the error was in the direction so giving a better linear relationship than the original experiment. The standard deviations are shown in Fig. 5 and are reasonable though six subjects is much smaller sample than is statistically desirable. When comparison is made, Fig. 6, between the standard deviations occurring with the semantic method as used, for example, by Parks and the cross matching method the reduction in the standard deviation is quite remarkable.

DISCUSSION OF RESULTS

Comparison between the results and the ISO proposals is made in Fig. 7 and shows good agreement except that at higher frequencies more sensitivity is shown. The range of frequency for uniform tolerance to acceleration appears to extend to about 15 Hz. The indicated minimum sensitivity at 1.7 Hz is of great interest in that it is close to the natural

15
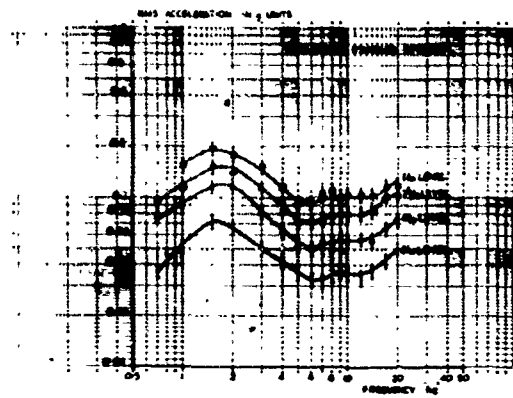
Fig. 5

The annoyance contours for vertical vibration in the standing position
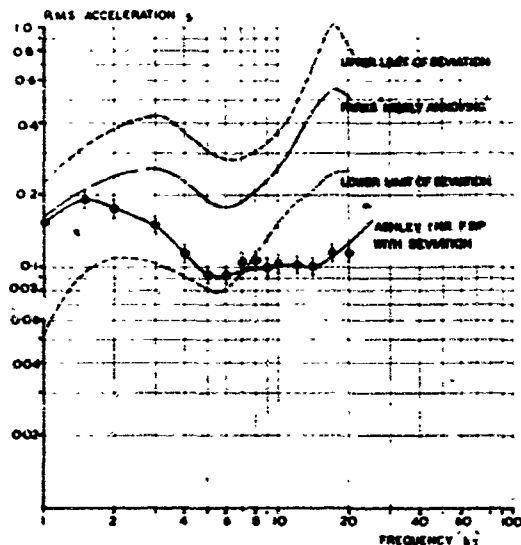
Fig. 6

A comparison between standard deviations found for a semantic based experiment compared with the cross-matching method.

bounce frequency of many road vehicles. The increase in sensitivity at lower frequencies is almost certainly associated with motion sickness, for which 0.3 Hz has been suggested as the frequency of particular sensitivity. The frequency range 5–15Hz includes most of the major resonances of the thorax abdominal system already mentioned.
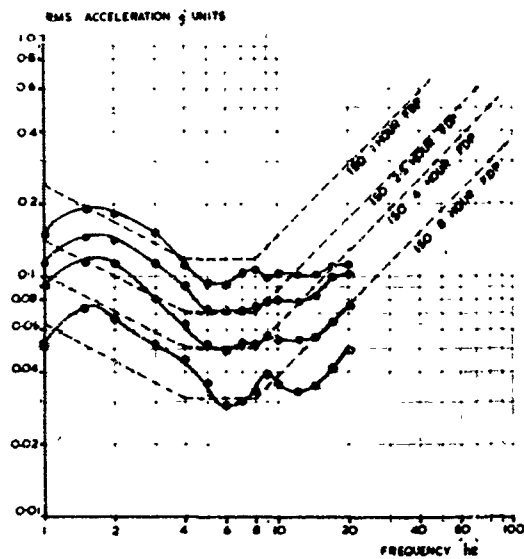
Fig. 7

A comparison between the results of this experiment and the ISO proposals

It is interesting to note that the excitation frequency minimum sensitivity at 1.7 Hz corresponds to a natural walking pace of 102 paces per minute, at which one would expect natural selection to lead to good isolation.

Other recent investigators such as Dupuis (1C) and Louda, Dupuis and Hartung (11) show similar annoyance curves to that given in this paper, though the cross matching technique was not used. A recent experimenter Miwa (12) used the cross matching technique with a sinusoidal at 20 Hz as standard but did not show the increase in sensitivity at very low frequencies. This result may be a function of the high frequency datum concentrating the attention of the subject on the harmonics inevitably present in the low frequency vibration. Another factor was the short exposure time used by Miwa, 6 seconds below 10 Hz and 3 seconds above 10 Hz. It was found in the current experiment periods of up to thirty seconds or more were necessary for the majority of subjects to get a complete feeling for a particular vibration.

THE RESULTS IN RELATION TO PHYSIOLOGICAL FACTORS

The methods used show excellent agreement with the averaged results by Bryce (3) of several previous experiments, Fig. 8, despite the small sample size. The actual shape is closest to that of Goldman who himself considered the results of several investigators. The only other quantitative method for obtaining equal comfort curves is the method of 'absorbed power'
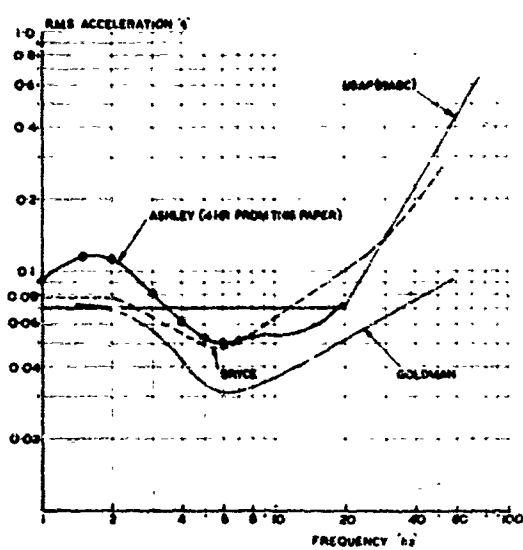
Fig 8
A comparison of the results of this experiment with the
averages of Bryce and Goldman and the USAF (WADC)
criterion

proposed by Pradko and Lee (14). A comparison is
shown in Fig. 9
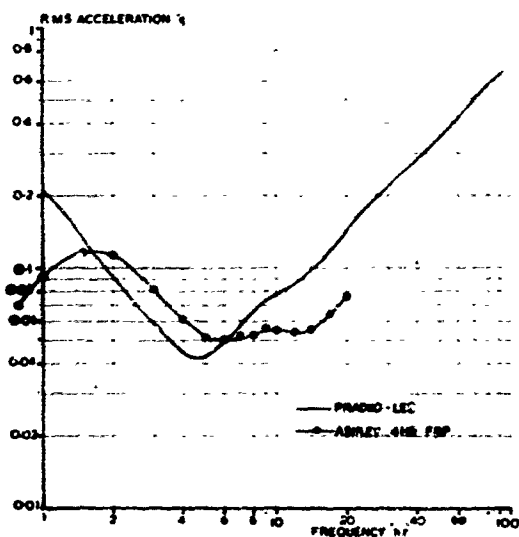
Fig. 9
A comparison between cross matching and normalised
absorbed power for the sitting position.

in which Pradko and Lee's published curved for the
equal comfort boundary in the seated position has been
normalised to the ISO 4 hr 4DP level. This shows
notable divergence at low frequencies. This is to be
expected because at low frequencies the body moves

as a rigid mass with little energy absorbed through
internal damping. The energy absorbed by the
initiation of motion sickness is negligible, though the
end effects can be severe. Despite the fact that people
are known to acclimatise to low frequency motion, the
author feels that the effect of motion sickness should be
included. Thus it may be proposed that comfort is a
function of vascular disturbance at low frequencies and
absorbed power at higher frequencies.

Safe exposure limits may well be based on different
criteria such as acceptable relative motion of the internal
organs of the body. For this case light damping could
lead to low absorbed power, but large amplitudes
particularly if a minor sub-system is envolved such as
the eyeball.

CONCLUSION

The cross-matching technique using a constant
velocity power spectrum as vibration datum is presented
as a valuable new technique which it is hoped other
experimenters will use to clarify the various problems
of comfort. The outstanding problem is the relation-
ship between sinusoidal and random motion, but other
areas could include the effect of differential motion
input at head and seat, two dimensional disturbances
and the effect of mixing noise and vibration. Fatigue
effects are a different problem, and meaningful results
can only be obtained from experiments using sensible
tasks as criteria.

Comparison of the results in this paper with the ISO
proposals shows excellent agreement within the common
frequency range of 1 Hz to 20 Hz. The ISO proposals
are designed to cover safe exposure and fatigue decreased
performance, with comfort as a third consideration and
this work shows that the ISO proposals can be used in
this third application with satisfaction.

REFERENCES

1. ISO Document ISO/TC 108/WG7 (Secretariat 19)
    39, June 1970. 'Guide for the evaluation of
    human exposure to whole body vibration'

2. W. S. Clark, K. O. Lange and R. R. Coermann
    (1962) 'Deformation of the human body due to
    uni directional forced sinusoidal vibration'
    Human Factors, Vol. 4 pp 255-274

17

3. W. D. Bryce (1966). 'A review and assessment of criteria for human comfort derived from subjective responses to vibration' Nat. Gas Turbine Est., Pyestock, England. NGTE Rpt R 286.

4. J. C. and Elsa Guignard (1970) 'Human response to vibration - A critical survey of published work' ISVR Southampton Univ., England ISVR Memorandum No 373.

5. A. G. Woods (1967) 'Human response to low frequency sinusoidal and random vibration' Aircraft Engineering, Vol. 39 pp 6-14.

6. ISO Recommendation 226

7. C. Ashley (1969) 'Simulation of the vehicle ride environment in the laboratory' Transpo 69, Symp. Soc. Enviromental Engineers, London.

8. B. D. Van Deusen (1967) 'Analytical techniques for designing riding quality into automotive vehicles' SAE Congress Detroit, Jan. 1967, Paper 670021.

9. D. L. Parks (1962) 'Defining human reaction to whole body vibration' Human factors, Vol. 4 pp 305 0 314, Pergamon.

10. R. P. LaBarre, k. T. Forbes, and S. Andrew (1970) 'The measurement and analysis of road surface roughness' . Motor Industry Research Association, England. Rpt. 1970/5.

11. H. Dupuis (1969) 'Zur physiologischen beanspruchung des menschen durch mechanische schwingungen.' Fortschr Berichte, VDI-Z Reihem No. 7, VDI - Verlag, Dusseldorf

12. Louda, Dupuis, Hartung (1970) Communication ISO/TC 108/WG 7 (Germany/Dupuis - 5) 41.

13. T. Miwa (1967) 'Evaluation methods for vibration effect. Part 1: Measurements of threshold and equal sensation contours of the whole body for vertical and horizontal vibrations' Ind. Health (Japan), Vol. 5 pp, 182-205

14. C. Ashley and B. Mills (1967) 'The laboratory investigation of vehicle vibration' I. Mech.E. Proc. Vol. 1182 Part 38 Great Britain.

APPENDIX 1 RANDOM WAVEFORM GENERATION

For this type of work in which random vibration is used as a standard, a definable, ergodic source must be used. The device employed was a commercial Solartron 80 1227 random signal generator, which employs 7 binary switches operated at random to form voltages corresponding to any number between 0 and 128 with equal probability. If two successive voltages are averaged, there will be a triangular probability function. If averaged 32 times and the probability distribution becomes virtually gaussian with a crest factor of 9.8. The switching frequency is separately controlled. The spectral density has the form

$$V(f) = V(o) \sin \pi f/fc \Big/ \pi f/fc$$

with zero power at switching frequency, but flat down to zero frequency. The switching frequency used was 32 Hz.

This unit drove a simple filter of form

$$F(jw) = \frac{1}{1 + \mathcal{C}(jw)}$$

where $\mathcal{C}$ = 0.5 sec and the corner frequency was 0.33 Hz. This yields a velocity spectrum which was flat over the range 0-15 Hz. The spectrum is given in Fig. 10.

The actual waveform are shown in Fig. 11 and are substantially identical between driving signal and vibration response, except for a time lag of 10 ms.

APPENDIX 2 INSTRUCTIONS GIVEN TO SUBJECTS

"This is a vibration test to compare the annoyance of random vibration with sinusoidal. Although there is obviously no real equivalent this is a serious attempt to obtain a guide. Please don the ear muffs (to reduce extraneous noise) and then let your weight be carried by each plate in turn. Stand naturally (not rigidly) but do not allow the knees to bend so that vibration is reduced. Imagine that you will have to stand each vibration is reduced. Imagine that you will have to stand each vibration for the specified time. Quickly make up your mind which is more unpleasant and tell the controller. He will then reset one vibration to be more equal. This procedure is to be repeated until both appear of equal annoyance. The test will then be continued for a different setting.

If you feel queasy or unwell at any stage tell the controller and the test will be stopped."

APPENDIX 3 WAVEFORM DISTORTION

In any vibration experiment some degree of waveform distortion is inevitable. The vibrator units used for this experiment were electro-hydraulic units

designed by the author (14) and shown in Fig. 12.
These had minimum distortion as a design objective,
and this was to be achieved through low friction
design of the actuator and low noise design of the
electronic system. The actual distortion at 10 Hz
and ± 0.100 in. is given in Table 1 below

Harmonic	Percentage Content	
	Acceleration	Displacement
1	100	100
2	4	1
3	6.6	0.7
4	2	0.1
5	13	0.5
6	2	0.05
7	13	0.26
8	2	0.03
9	11	0.11
Total Harmonic Disturbance	23%	1.39%

Table I   Harmonic Content of Sinusoidal Response at 10 Hz.
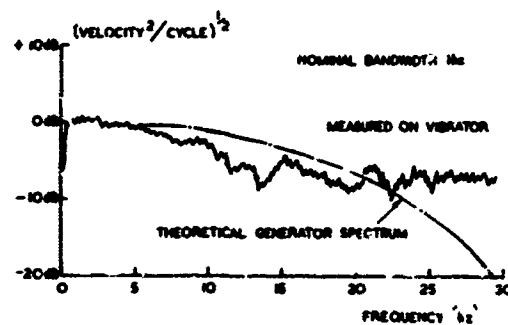
Fig. 10
The Spectra of Input and reproduction

Fig. 12   The 5LB6 Vibrator
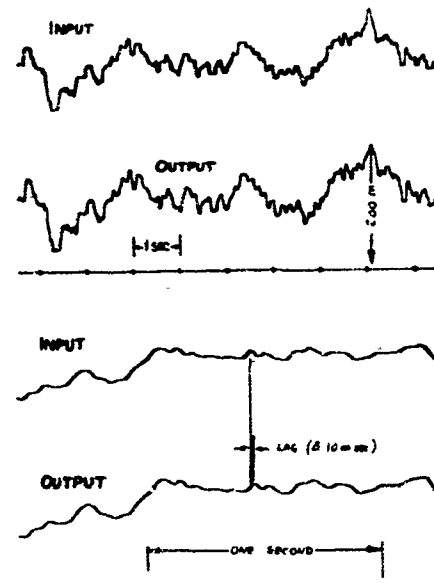
Fig 11
The actual input waveforms and their reproduction

19

DISCUSSION

Mr. Stein (Arizona State University): I was most impressed by your committee averaging procedure between zero and six db per octave. Six db per octave represents a single lumped-parameter energy-storing-element type of response which has a good physical representation to the mathematics. Three db per octave is a committee averaged decision. Is that really a good way to go? Also six would have corresponded with some of your experimental results a little better I believe.

Mr. Ashley: First of all I must stress that the story I told is in fact apocryphal. I was not there at the time that this particular decision was made and I agree with you that it would be very much nicer if the slope had in fact been six db per octave, because it would have meant that the design of filters for using weighting networks would have been very much easier. And again it would have corresponded to the concept of jerk at very low frequency. Apart from that, I think that when you actually study the shape of the curves in relationship to the published form of my paper I think that the agreement with this bastard slope, if you like, is very good.

Mr. Foley (Sandia Laboratories): On your comfort curves and so forth were all of the subjects in your experiments males? Is there a difference with females?

Mr. Ashley: For the work which we did all the subjects were fit males in the age range 18 t 55, in fact, most of them were students around about the age range around about 18 to 22. It would be interesting in fact to do a comparison with females. We have one or two isolated items experimentally and there does not seem to be very much significant difference.

Mr. Parks (Army Tank-Automotive Command): Have any data been collected on the response of children? Most of this work seems to be in the adult category.

Mr. Ashley: It would in fact be interesting to do it for children. One of the difficulties with doing this type of work is the ethics of doing the experimentation in that one has a certain responsibility as far as the likelihood toward physical damage is concerned. I think this is one of the reasons why there has been very little work done in experimentation with children to discover their tolerance to vibration. I personally know of no experimental data whatsoever.

Mr. Parks: Could several of these sinusoidal levels exist at one time at several frequencies? Would that still fall under one of the curves?

Mr. Ashley: This now relates to how one considers the relationship between random and pure sinusoidal environments. You are taking a sort of intermediate stage where one has a mixture of the sinusoidals. An extreme example of the physical situation where this happens is in helicopters where you get sinusoidal vibration as a function of the rotor frequency. In this case the best technique is to use the tolerance curve as I have shown you and to turn it upside down and then to use it as a weighting. If one is six db less sensitive at 10 Hz then one multiplies the sinusoidal component at 10 Hz by a factor of one-half and then sums the effect.

ISOLATION

ISOLATION FROM MECHANICAL SHOCK WITH A MOUNTING

SYSTEM HAVING NONLINEAR DUAL-PHASE DAMPING

J. C. Snowdon
Ordnance Research Laboratory
The Pennsylvania State University
University Park, Pennsylvania

This investigation demonstrates that, when the foundation of a simple mounting system is transiently displaced, the use of a shock mount having nonlinear dual-phase damping can simultaneously reduce or minimize the resulting acceleration and displacement of the mounted item. Normally, such reactions pose conflicting requirements that cannot be satisfied at the same time by a conventional viscously damped linear shock mount. The dashpot of the nonlinear system considered here exerts a dual-phase damping force that is relatively small when the system undergoes abrupt transients, but is significantly larger (1) during the relatively slow decay of motion that follows this abrupt loading, and (2) when the system is subjected to less abrupt transients. The response of the mounted item has been either calculated from closed-form expressions derived for the linear mounting system considered, or obtained by numerical integration of a differential equation of motion that incorporates the dual-phase damping characteristic of the nonlinear mounting system considered. The steplike and pulselike input transients examined are realistic in that they describe how the foundation of each mounting system is displaced through a finite distance in a finite time with finite acceleration and deceleration. The rise times and durations of the transients are chosen to be much larger than, of the same order as, and much shorter than the half-period of natural vibration of the mounting systems.

INTRODUCTION

This paper considers the response of the simple mounting systems of Figs. 1(a) and (b) to a transient time-varying foundation displacement $x_1(t)$; the resultant displacement of the mounted item of mass M is $x_2(t)$, where t is time. A linear spring of stiffness K is common to both systems and the linear dashpot of Fig. 1(a) obeys Newton's law of viscosity; however, the damping force exerted by the dashpot of Fig. 1(b) is a nonlinear function of the relative velocity $(\dot{x}_1 - \dot{x}_2)$.

In general, the contents of the item of equipment M will receive the greatest protection from shock [1] when the acceleration, displacement, and relative displacement of M are small simultaneously. For the simple system of Fig. 1(a), these are conflicting requirements; for example, although the maximum values and decay times of x_2 and $(x_2 - x_1)$ will be reduced if the system is damped heavily, the

maximum acceleration of M will then be increased for all but gradual transients.

The investigation described here was prompted by the belief that the contents of M could be afforded greater protection from damage if the viscous damping force was small when the system experienced abrupt transients, but was considerably larger (1) during the relatively slow decay of motion induced by this abrupt loading, and (2) when the system was subjected to less abrupt transients. Such changes in resistance to motion (viscous damping force decreasing as rate of shear increases) are characteristic of so-called thixotropic substances, which include many polymer solutions [2-9], "non-drip" paints, and even blood [10]. Although thixotropic behavior is well known and many experimental results are documented in the literature, it appears that significant changes in viscous-damping force are obtained only when shear rate changes in value by several orders of

magnitude. Consequently, the pronounced thixo-
tropic characteristic sought after in this in-
vestigation is considered to result from the
nonlinear mechanical action of a dashpot that
contains a linear fluid.

For the linear system of Fig. 1(a), it is
well known that the damping ratio ξ_R -- the
ratio of the coefficient η to the value η_c
that is required to damp the system critically--
is given by the simple relation

$$\xi_R = \frac{\eta}{\eta_c} = \frac{\omega_o}{2K} , \tag{1}$$

where

$$\omega_o = (K/M)^{\frac{1}{2}} \tag{2}$$

is the natural frequency of the system. Equiv-
alently, the nonlinear dashpot of Fig. 1(b) is
considered to have a damping ratio that takes
one of two constant values if the relative
velocity across the dashpot terminals is either
small or large. For intermediate velocities,
there is a linear transition from one level of
the damping ratio to the other. This char-
acteristic is sketched in Fig. 2, where the
damping ratio ξ_R changes in value from δ to
δ/β as the magnitude of the relative velocity

$$|\dot{x}_2 - \dot{x}_1| = |\phi|\omega_o x_{max} \tag{3}$$

increases from $\alpha\omega_o x_{max}$ to $\theta(\alpha\omega_o x_{max})$. Here, α,
β, and θ are arbitrary constants to be speci-
fied, and x_{max} is the maximum value of the in-
put displacement $x_1(t)$. With this notation,
the dual-phase damping characteristic of Fig. 2
can be described in specific terms as follows:

$$\xi_R = \delta \qquad \text{when } |\phi| < \alpha , \tag{4}$$

$$\xi_R = \delta\left[1 + \frac{1}{\beta}\left(\frac{\beta-1}{\theta-1}\right)\left(1 - \frac{|\phi|}{\alpha}\right)\right]$$

$$\text{when } \alpha \le |\phi| \le \theta\alpha , \tag{5}$$

and

$$\xi_R = (\delta/\beta) \text{ when } |\phi| > \theta\alpha . \tag{6}$$

Ways in which the damping characteristic
of Fig. 2 can be generated mechanically are
suggested by the sketches of Fig. 3, where
either (a) additional orifices open in the
dashpot plunger or (b) a return valve operates
once the relative velocity across the dash-
pot--and, therefore, the viscous damping
force--exceeds a certain predetermined level.
The orifice valves of Fig. 3 that adapt to
the changes in damping force could, for example,
be spring-loaded ball bearings or small plates.
The rate of transition of the damping ratio from
a high to a low level, and vice versa, will
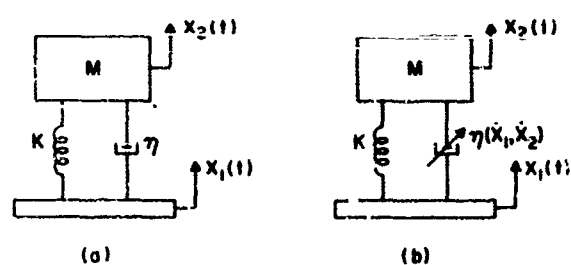
Fig. 1 - (a) Linear shock mount and (b) non-
linear shock mount with dual-phase damping.

RELATIVE VELOCITY/$\omega_o x_{max}$
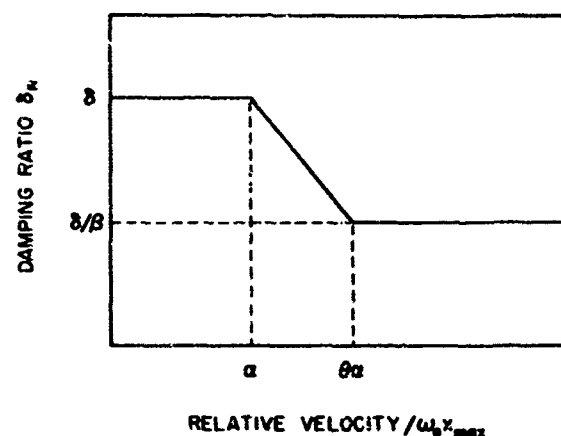
Fig. 2 - Sketch of the dual-phase damping char-
acteristic of the nonlinear mount of Fig. 1(b).
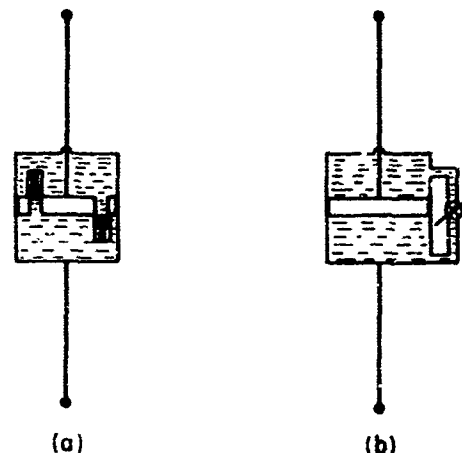
Fig. 3 - Dashpots with nonlinear mechanical
action designed to duplicate the dual-phase
damping characteristic of Fig. 2.

depend on the rate at which the valves open and close. In the calculations to be described here, $\theta = 2$, $\beta = 5$, and $\alpha = 1.0$. For these values, the damping ratio changes in level by a factor of 5 as the relative velocity varies by a factor of 2 above the value $\omega_0 x_{max}$-- a value that is actually the maximum (absolute) velocity attained by M when the mounting system is undamped and is subjected to a discontinuous step displacement $x_1 = x_{max}$.

The three input displacements referred to in this study are defined in the following section. The inputs are chosen to be physically realistic in that they describe the translation of the foundation through a finite distance in a finite time with finite acceleration and deceleration.

STEPLIKE AND PULSELIKE INPUT DISPLACEMENTS

The input transients considered here are (a) a rounded displacement step, (b) a unidirectional displacement pulse, and (c) an oscillatory displacement step. These inputs are defined by the following equations:

$$x_1(t) = 0 \quad \text{when time } t < 0 , \quad (7)$$

$$x_1(t) = x_{max} [1 - e^{-\gamma \omega_0 t}(1 + \gamma \omega_0 t)] \quad (8)$$

$$\text{when } t \geq 0 \text{ (rounded step)} ,$$

$$x_1(t) = x_{max} (e^2/4)(\gamma \omega_0 t)^2 e^{-\gamma \omega_0 t} \quad (9)$$

$$\text{when } t \geq 0 \text{ (rounded pulse)} ,$$

and

$$x_1(t) = x_{max}(0.65684) [1 - e^{-0.25 \gamma \omega_0 t}(\cos \gamma \omega_0 t$$

$$+ 0.25 \sin \gamma \omega_0 t)] \quad (10)$$

$$\text{when } t \geq 0 \text{ (oscillatory step)} .$$

The first two inputs have been considered in previous investigations [1], but they are redefined here for convenience. The input displacements obtained for different values of the parameter γ, and universal curves that describe the velocity and acceleration waveforms associated with these displacements, are plotted in Figs. 4-7.

The parameter γ describes the finite rise times of the steps and the duration of the pulse in terms of the half-period of natural vibration $T/2$ of the mounting system; thus,

$$\gamma = \frac{T}{2\tau} = \frac{\pi}{\omega_0 \tau} . \quad (11)$$

The rise time τ of the rounded displacement step is defined by Eq. 11 as the time required for the displacement to reach 82% of its final value. The duration τ of the displacement pulse is defined as the length of an equivalent rectangular pulse that has the same area $(x_{max} e^2/2 \omega_0)$ as that of the rounded pulse, but which is higher by 17.6% than x_{max}. The rise time τ of the oscillatory displacement step is exactly the time required for the displacement to reach its maximum value x_{max}.

The method of selecting the input displacement defined by Eq. 10 is of interest. An input was sought that would represent the character of an abrupt transient disturbance after it had passed through and had been "filtered" by the foundation structure that supports the mounting system under consideration. Now, when the base of a single-degree-of-freedom (mass-spring-dashpot) system is subjected to a right-angled step displacement $x(t) = x_0$, the resultant displacement x_1 of the system mass is given [1] by the equation

$$x_1 = x_0 \{1 + e^{-\varepsilon_F \omega_F t} [(\varepsilon_F/\Delta_F) \sin \Delta_F \omega_F t$$

$$- \cos \Delta_F \omega_F t]\} , \quad (12)$$

where ω_F is the natural frequency of the system, ε_F is its damping ratio, and

$$\Delta_F = (1 - \varepsilon_F^2)^{\frac{1}{2}} . \quad (13)$$

Although this would seem to be an appropriate input displacement, it is not physically realistic [1] because its first time derivative (velocity) is discontinuous and its second derivative (acceleration) is infinite at the time origin. However, if the sine term in Eq. 12 is reversed in sign, the waveform is not greatly changed, yet $\dot{x}_1$ is then zero and $\ddot{x}_1$ remains finite at the time origin. Further, for all but large values of ε_F, the equation may be simplified as follows:

$$x_1 = x_0 \{1 - e^{-\varepsilon_F \omega_F t} [\varepsilon_F \sin \omega_F t - \cos \omega_F t]\} . \quad (14)$$

It is readily seen that this displacement takes a maximum value

$$x_{max} = x_0 \left[1 - e^{-\varepsilon_F \pi}\right] \quad 15$$

when

$$\omega_F t = \pi , \quad 16$$

which is an equation that directly specifies the step rise time. Consequently, from Eq. 11, it is possible to write that

23
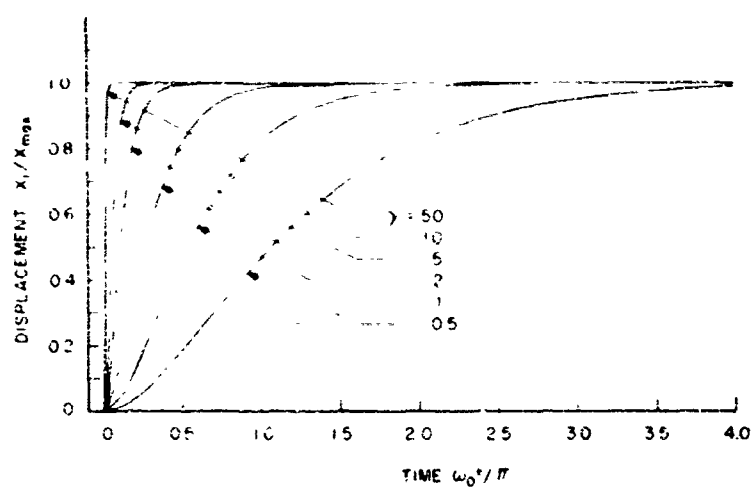
Fig. 4 - The rounded step displacement.
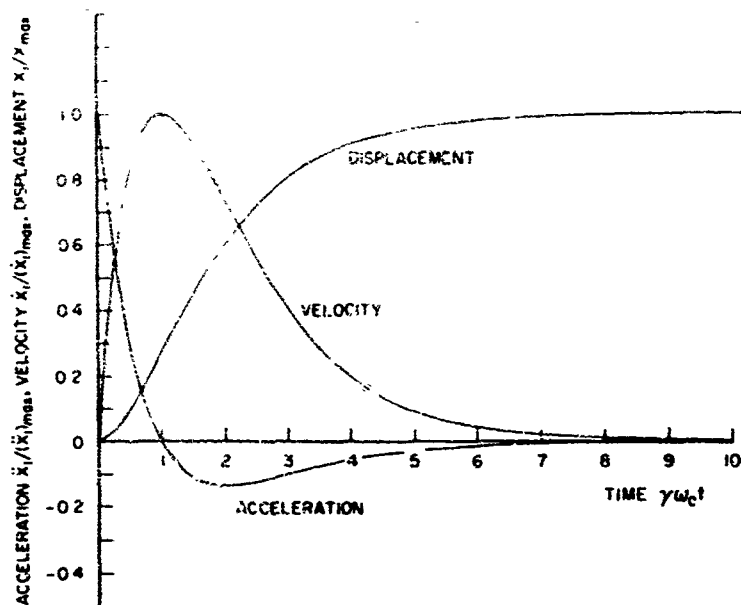
Fig. 5 - Rounded step displacement with its velocity and
acceleration waveforms.

24
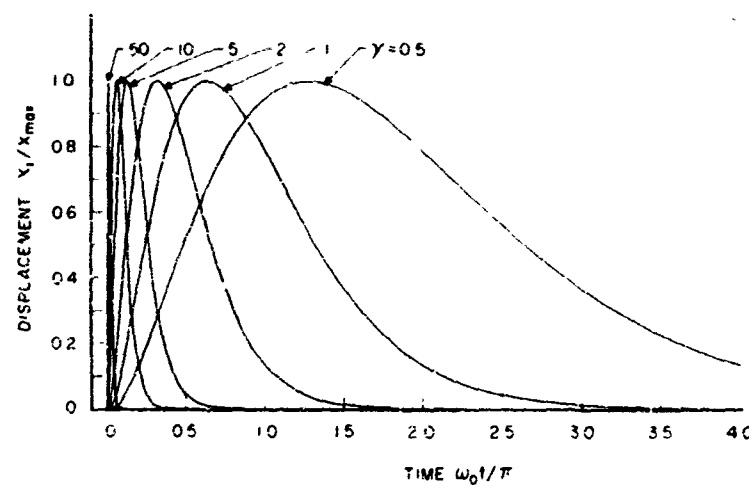
Fig. 6 - The rounded pulse displacement.
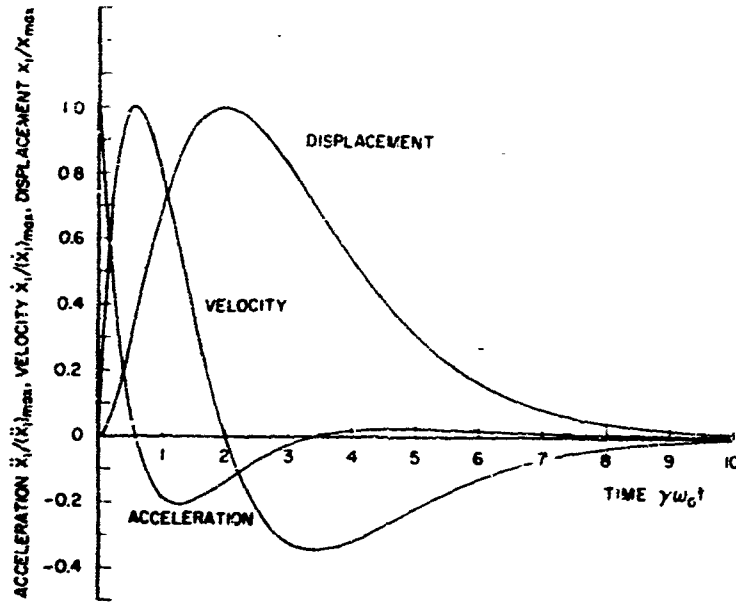
Fig. 7 - Rounded pulse displacement with its velocity and
acceleration waveforms.
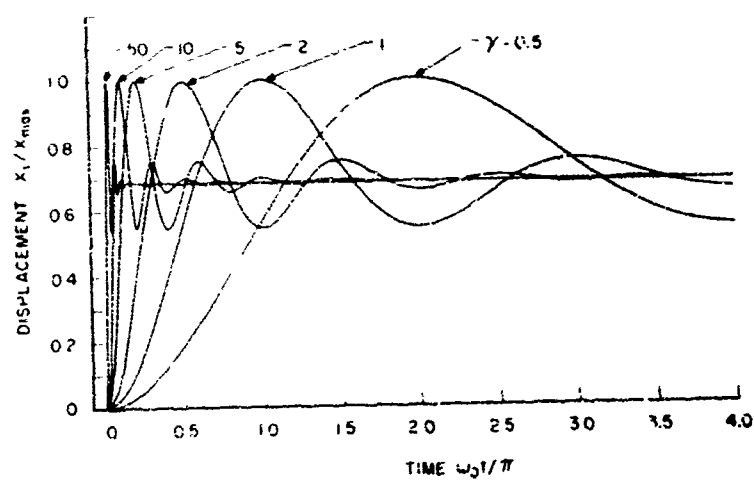
Fig. 8 - The oscillatory displacement step.
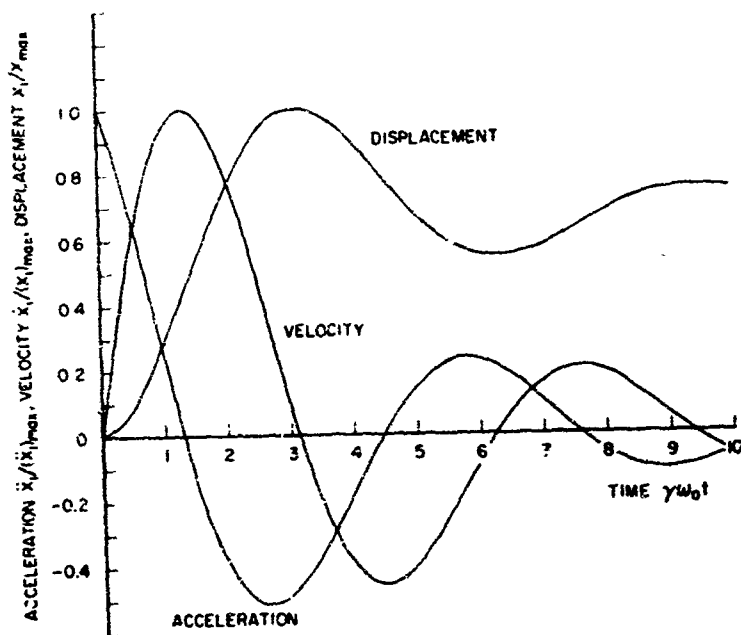
Fig. 9 - Oscillatory displacement step with its velocity and acceleration waveforms.

$$\gamma = \frac{\pi}{\omega_0(\pi/\omega_F)} = \frac{\omega_F}{\omega_0} \qquad (17)$$

and, from Eq. 14, that

$$x_1 = x_{max} \frac{[1-e^{-\delta_F\gamma\omega_0 t}(\delta_F\sin\gamma\omega_0 t+\cos\gamma\omega_0 t)]}{(1+e^{-\delta_F\pi})}. \quad (18)$$

From this equation, by placing $\delta_F = 0.25$, the oscillatory displacement step of Eq. 10 was defined directly.

To conclude, the maximum values attained by the velocity and acceleration waveforms of the input displacements of Eqs. 8-10 are listed here, because these values will be referred to when the effectiveness of different shock mounts in protecting the contents of M from damage is compared. Thus,

$$(\dot{x}_1)_{max} = 0.36788\ \gamma\omega_0 x_{max}$$

$$\text{(rounded step)} ; \quad (19)$$

$$(\ddot{x}_1)_{max} = \gamma^2\omega_0^2 x_{max}$$

$$(\dot{x}_1)_{max} = 0.85188\ \gamma\omega_0 x_{max}$$

$$\text{(rounded pulse)} ; \quad (20)$$

$$(\ddot{x}_1)_{max} = 3.69453\ \gamma^2\omega_0^2 x_{max}$$

and

$$(\dot{x}_1)_{max} = 0.50825\ \gamma\omega_0 x_{max}$$

$$\text{(oscillatory step)}. \quad (21)$$

$$(\ddot{x}_1)_{max} = 0.72977\ \gamma^2\omega_0^2 x_{max}$$

TRANSIENT RESPONSE OF THE LINEAR MOUNTING SYSTEM

The transient response of the mounting system of Fig. 1(a) is described at this point to provide a basis against which the nonlinear results of the following section can be compared. Closed-form expressions for the response $x_2(t)$ of the mounted item M to the three input displacements under consideration can be obtained by the methods of the Laplace transformation [1]. The velocity- and acceleration-time relations for M follow directly by differentiation.

Rounded Step Input

$$\frac{x_2}{x_{max}} = \{1 - e^{-\gamma\omega_0 t}[A(\gamma\omega_0 t) + B] + e^{-\delta_R\omega_0 t}(C\cos\Delta_R\omega_0 t + D\sin\Delta_R\omega_0 t)\} , \qquad (22)$$

$$\frac{\dot{x}_2}{\omega_0 x_{max}} = \{\gamma e^{-\gamma\omega_0 t}[A(\gamma\omega_0 t - 1) + B] + \Theta e^{-\delta_R\omega_0 t}\} , \qquad (23)$$

and

$$\frac{\ddot{x}_2}{\omega_0^2 x_{max}} = \{-\gamma^2 e^{-\gamma\omega_0 t}[A(\gamma\omega_0 t) + (B - 2A)] + \Xi e^{-\delta_R\omega_0 t}\} , \qquad (24)$$

where

$$\Delta_R = (1 - \delta_R^2)^{\frac{1}{2}} , \qquad (25)$$

$$A = (1 - \gamma^2\Gamma) , \qquad (26)$$

$$B = (1 + C) , \qquad (27)$$

$$\Theta = [(D\Delta_R - C\delta_R)\cos\Delta_R\omega_0 t - (D\delta_R + C\Delta_R)\sin\Delta_R\omega_0 t] , \qquad (28)$$

and

$$\Xi = (E\sin\Delta_R\omega_0 t + F\cos\Delta_R\omega_0 t) . \qquad (29)$$

In these equations,

$$C = \gamma^2(1 - \gamma^2)\Gamma^2 , \tag{30}$$

$$D = \gamma^2(-2\delta_R - 2\gamma + \epsilon_R)(\Gamma^2/\Delta_R) , \tag{31}$$

$$E = [2 C \delta_R \Delta_R - D (1 - 2\delta_R^2)] , \tag{32}$$

$$F = -[C(1 - 2\delta_R^2) + 2D \delta_R \Delta_R] , \tag{33}$$

and

$$\Gamma = (\gamma^2 - 2\delta_R\gamma + 1)^{-1} . \tag{34}$$

Rounded Pulse Input

$$\frac{x_2}{x_{max}} = (e^2/4)\{e^{-\gamma\omega_o t}[A(\gamma\omega_o t)^2 + B(\gamma\omega_o t) - C] + e^{-\delta_R\omega_o t}(C \cos\Delta_R\omega_o t + D \sin\Delta_R\omega_o t)\} , \tag{35}$$

$$\frac{\dot{x}_2}{\omega_o x_{max}} = (e^2/4)\{\gamma e^{-\gamma\omega_o t}[-A(\gamma\omega_o t)^2 + (2A - B)(\gamma\omega_o t) + (B + C)] + \Theta e^{-\delta_R\omega_o t}\} , \tag{36}$$

and

$$\frac{\ddot{x}_2}{\omega_o^2 x_{max}} = (e^2/4)\{\gamma^2 e^{-\gamma\omega_o t} [A(\gamma\omega_o t)^2 - (4A - B)(\gamma\omega_o t) + (2A - 2B - C)] + \Xi e^{-\delta_R\omega_o t}\} , \tag{37}$$

where A, Θ, Ξ, E, F, and Γ are defined as before; but now

$$B = 4\gamma^2(1 - \gamma\delta_R) \Gamma^2 , \tag{38}$$

$$C = 2\gamma^2(2\gamma^3\delta_R - 3\gamma^2 + 1) \Gamma^3 , \tag{39}$$

and

$$D = 2\gamma^2[\gamma^3(1 - 2\delta_R^2) + 3\gamma^2\delta_R - 3\gamma + \delta_R](\Gamma^3/\Delta_R) . \tag{40}$$

Oscillatory Step Input

$$\frac{x_2}{x_{max}} = [0.68684 + e^{-0.25\gamma\omega_o t}(A \cos \gamma\omega_o t + B \sin \gamma\omega_o t) - e^{-\delta_R\omega_o t}(C \cos \Delta_R\omega_o t + D \sin \Delta_R\omega_o t)] , \tag{41}$$

$$\frac{\dot{x}_2}{\omega_o x_{max}} = [e^{-0.25 \gamma\omega_o t}(P \cos \gamma\omega_o t - Q \sin \gamma\omega_o t) - \Theta e^{-\delta_R\omega_o t}] , \tag{42}$$

and

$$\frac{\ddot{x}_2}{\omega_c^2 x_{max}} = \{e^{-0.25\ \gamma\omega_o t}[-\gamma(Q + 0.25P)\cos\ \gamma\omega_o t + \gamma(0.25Q - P)\sin\ \gamma\omega_o t] - \Xi\ e^{-\delta_R\omega_o t}\}\ ,\qquad(43)$$

where $\Theta,\ \Xi,\ E,$ and F are defined as before; but now

$$A = 0.34342\ T\ [(1.625\ \gamma^2 - 2) + \delta_R\gamma(2.125\ \gamma^2 - 8.5\ \delta_R\gamma + 2)]\ ,\qquad(44)$$

$$B = 0.34342\ T\ [(1.46875\ \gamma^2 - 0.5) - \delta_R\gamma(3.98438\ \gamma^2 + 2.125\ \delta_R\gamma - 0.5)]\ ,\qquad(45)$$

$$C = 0.72977\ \gamma^2 T\ (1.0625\ \gamma^2 - 1)\ ,\qquad(46)$$

and

$$D = -0.72977\ (\gamma^2 T/\Delta_R)(1.0625\ \gamma^2\delta_R - 0.5\gamma + \delta_R)\ .\qquad(47)$$

In these equations

$$P = \gamma(B - 0.25A)\ ,\qquad(48)$$

$$Q = \gamma(0.25B + A)\ ,\qquad(49)$$

and

$$T = [(1.12891\ \gamma^4 - 1.875\ \gamma^2 + 1) - \gamma\delta_R\ (1.0625\ \gamma^2 - 4.25\ \gamma\delta_R + 1)]^{-1}\ .\qquad(50)$$

Representative calculations of the transient responses that the foregoing equations predict for the linear mounting system are plotted in Figs. 10-13. The first two figures, which were obtained for the rounded step input and values of the damping ratio $\delta_R = 0.05$ and 0.5, show how the oscillatory motion of the mounted item is reduced in amplitude and duration by large mount damping but, for abrupt displacement steps, how this damping introduces a predominant acceleration peak that occurs when the foundation displacement is still small. In fact, when the damping ratio is large and the rise time of the rounded step is short (γ large), this peak acceleration becomes directly proportional to δ_R and γ as follows:

$$(\ddot{x}_2)_{max} \approx 2e^{-1}\gamma\delta_R\omega_o^2 x_{max} = 2.3115\delta_R\omega_o x_{max}/\tau$$

$$\text{(rounded step)}\qquad(51)$$

Although the maximum displacement of the mounted item is smallest when either (a) the damping ratio is large, or (b) γ is not large (the half-period of vibration $T/2$ is comparable with or less than τ), the maximum relative displacement between M and the foundation is of the same order of magnitude as x_{max} once γ is greater than about 10. Even high mount damping does not significantly reduce the maximum relative displacement when γ is large.

Figures 12 and 13 show that M responds to the rounded pulse and oscillatory step input displacements in like manner to that predicted by the curves of Figs. 10 and 11 for the rounded step. Only the displacement curves of Fig. 12 differ basically from those of the accompanying figures. This is because, after the rounded pulse has terminated, M oscillates about its original undisturbed position rather than about a level displaced from it by the final step height of x_{max} or $0.6868\ x_{max}$. In this situation, the displacement of M is smallest when γ is large because the excursion of the foundation has then reached the value x_{max} and returned to zero before M has moved appreciably.

Because Figs. 12 and 13 were calculated for a value of $\delta_R = 0.5$, predominant acceleration peaks are evident in both figures; moreover, the peak accelerations of M, to which
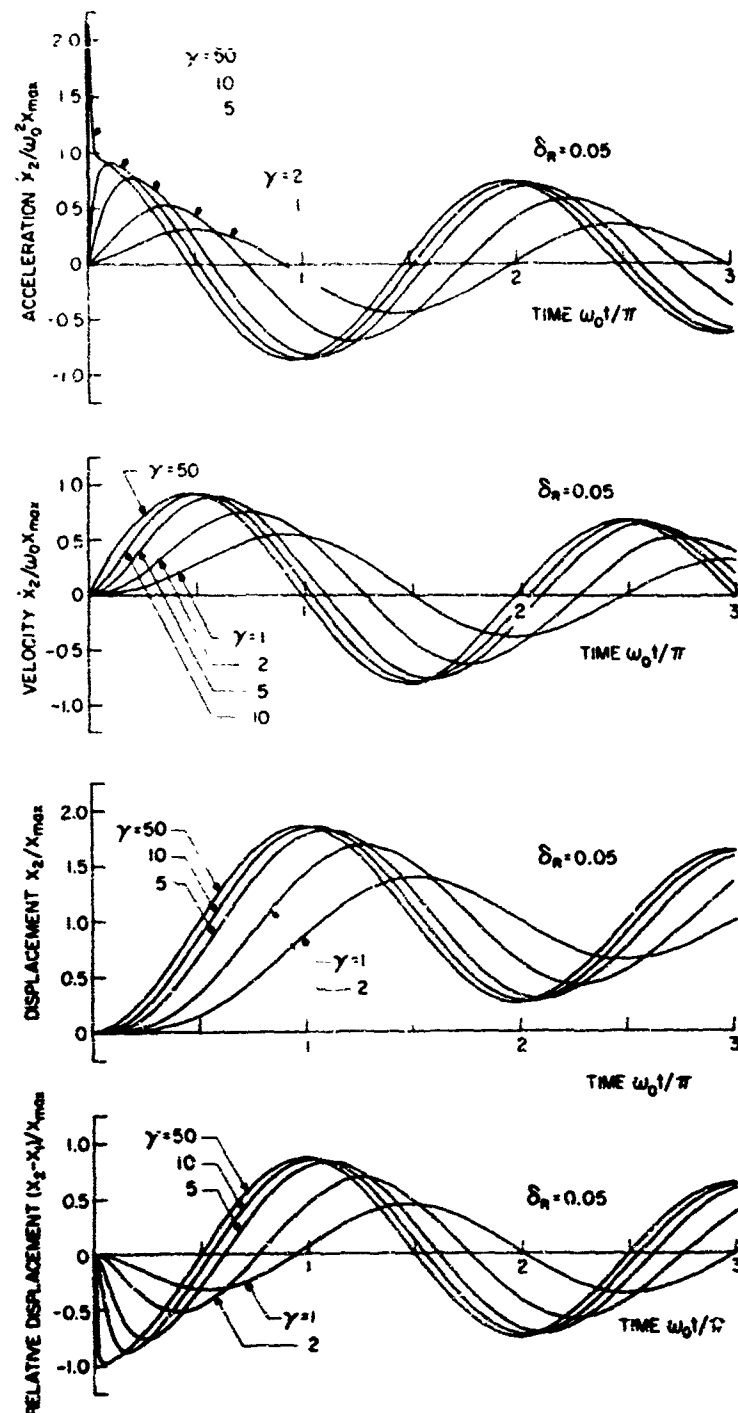
29

Fig. 1⌐ - Acceleration-, velocity-, displacement-, and relative displacement-time relationships for the linear system of Fig. 1(a) subjected to the rounded step displacements of Fig. 4. Damping ratio $\delta_R = 0.05$.

30
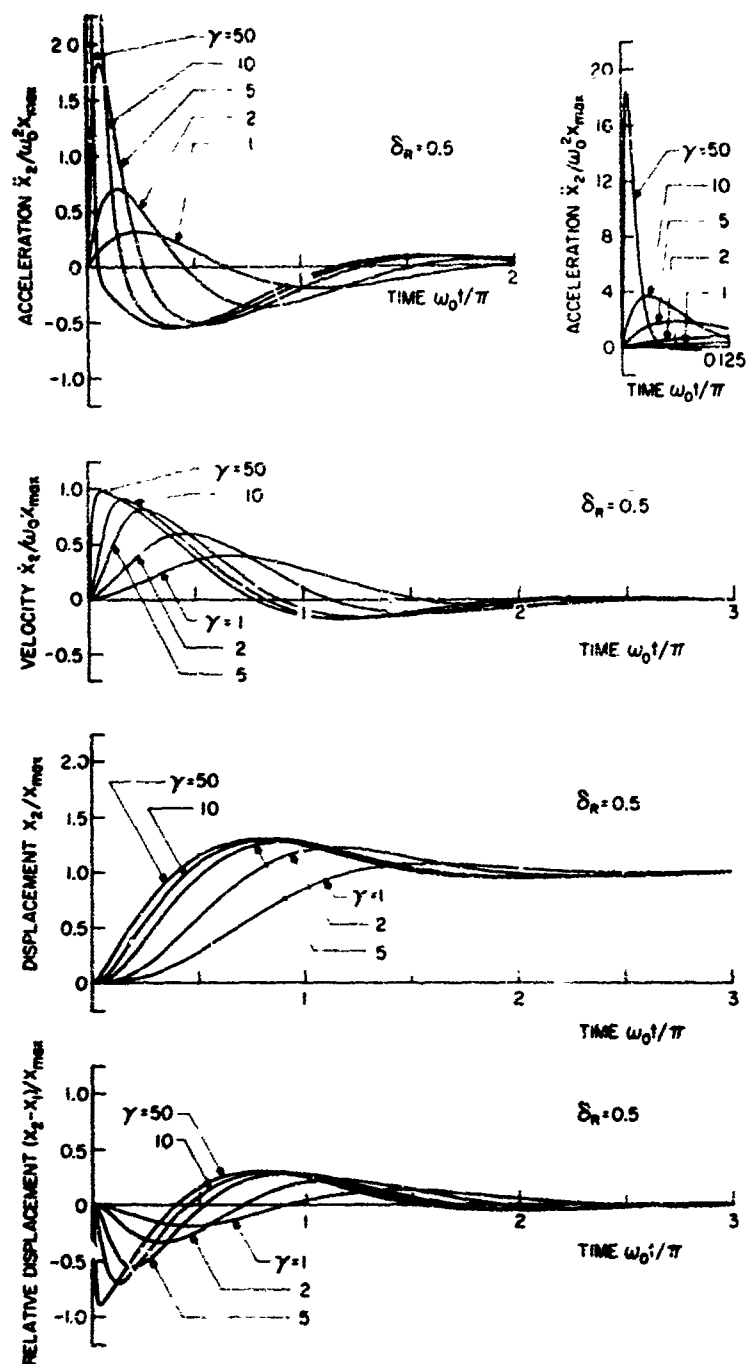
Fig. 11 - Acceleration-. velocity-, displacement-, and relative displacement-time relationships for the linear system of Fig. 1(a) subjected to the rounded step displacement of Fig. 4. Damping ratio $\delta_R = 0.5$.
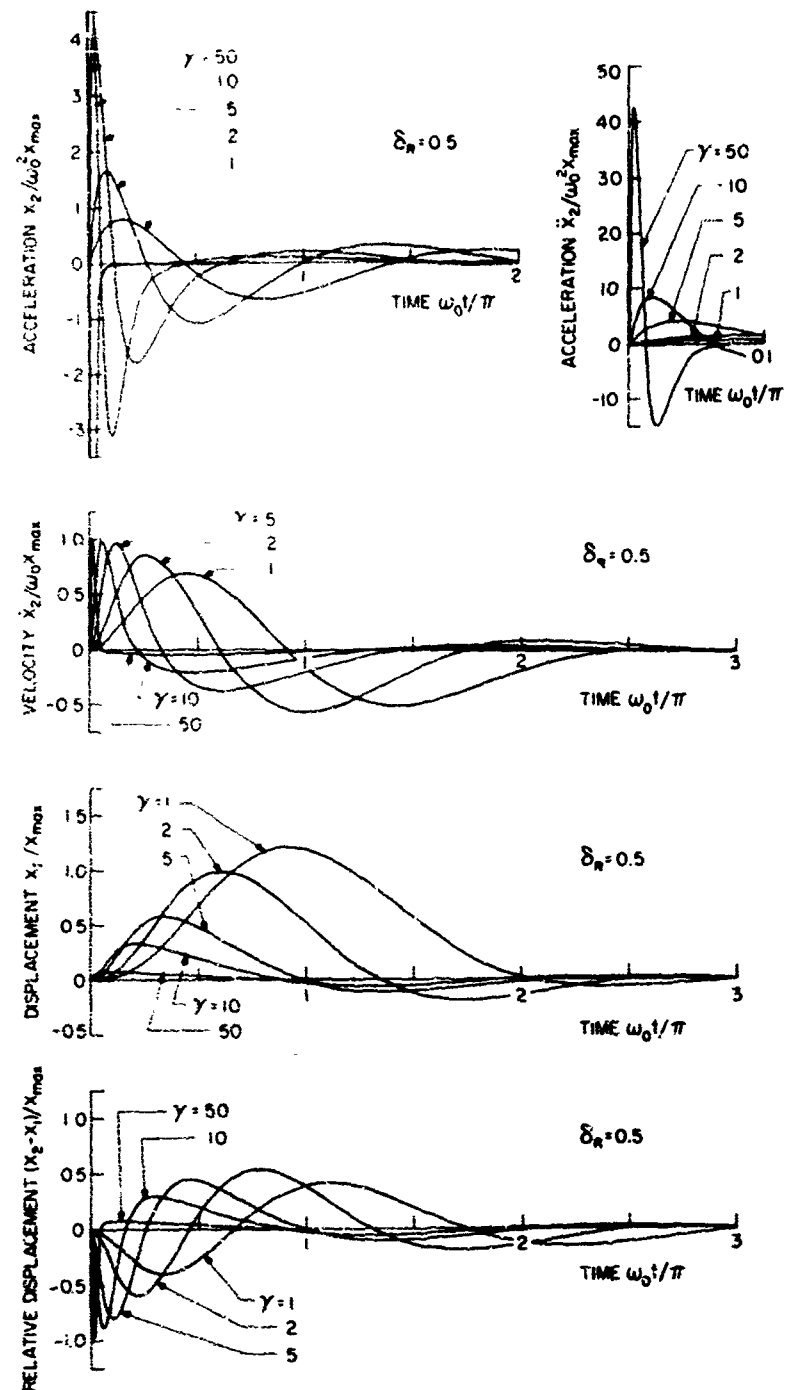
Fig. 12 - Acceleration-, velocity-, displacement-, and relative displacement-time relationships for the linear system of Fig. 1(a) subjected to the rounded pulse displacements of Fig. 6. Damping ratio $\delta_R = 0.5$.

32
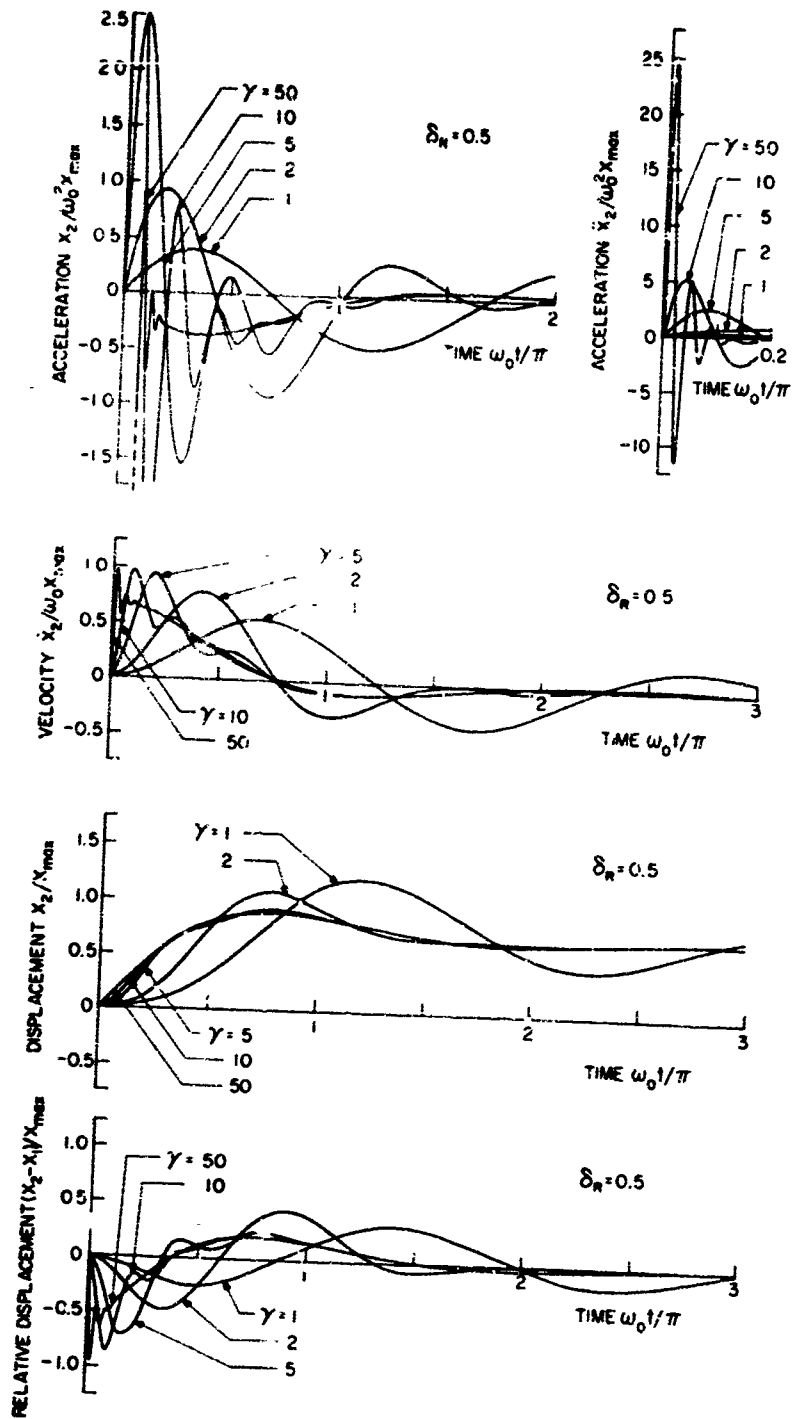
Fig. 13 - Acceleration-, velocity-, displacement-, and relative displacement-time relationships for the linear system of Fig. 1(a) subjected to the oscillatory step displacements of Fig. 8. Damping ratio $\xi_R = 0.5$.

The risk of damage to its contents can frequently be related to parameters directly proportional to ... and to the...

$$\ddot{x}_{2\,max} = ... \qquad \dot{x}_{2\,max} \, \dot{x}_{max} \, t$$

$$r \cdot \Delta x \, , \, \Omega^m \qquad (50)$$

and

$$\ddot{x}_{2\,max} = 1 + \left(\frac{...}{...}\right)^{-1} \dot{x}_{R}\omega_{o}\,x_{max}$$

$$\ddot{x} \, x_{max}$$

oscillatory step . 5^{r}

TRANSIENT RESPONSE OF MOUNTING SYSTEM WITH DUAL-PHASE DAMPING

Representative calculations of the responses of the nonlinear mounting system of Fig. 1(b) to the rounded step and rounded pulse input displacements are plotted in Figs. 14 and 15. The response of the system to the oscillatory step input is not shown because the acceleration waveforms, in particular, are irregular and overlapping and are difficult to plot concisely. Here, and subsequently, the damping ratio is assumed to switch to-and-fro between the values of $\delta_R = \delta = 0.5$ and $\delta_R = r/R = 0.1$ as the magnitude of the relative velocity across the dashpot terminals varies. In fact, the curves of Figs. 14 and 15, and the dashed-line curves of the subsequent figures, have been obtained by numerical integration of the following nonlinear differential equation of motion that embodies the dual-phase damping characteristic of Fig. 2:

$$\ddot{x}_2 = 2\delta_R\omega_o(\dot{x}_1 - \dot{x}_2) + \omega_o^2(x_1 - x_2) . \quad (54)$$

This equation, in which δ_R is defined by Eqs. 4-6, has been integrated numerically by digital computer using the subroutine described in Ref 11.

As compared with the corresponding linear results of Figs. 11 and 12, the greatest effects of system nonlinearity in Figs. 14 and 15 are to reduce the maximum velocity and, particularly, the maximum acceleration of M for all but the smaller values of γ considered. The same comments apply when the linear and nonlinear responses of the mounting systems to the oscillatory step input displacement are compared. The "jerks" in the acceleration waveforms of Figs. 14 and 15 mark the onset or completion of a change in magnitude of the damping ratio.

The maximum values of the displacement x_2 and the relative displacement $(x_1 - x_2)$ of M are not influenced so greatly by system nonlinearity

as are the maximum values of $\dot{x}_2$ and $\ddot{x}_2$. Actually, the nonlinearity reduces the maximum values of x_2 for all but the smaller values of γ considered, although the maximum values of $(x_1 - x_2)$ are increased; in fact, when γ is large, these maximum values reach a level $\approx x_{max}$.

Note that, when the nonlinear system is subjected to the rounded step input, its displacement response exhibits remarkably little overshoot. Also note that the nonlinear damping has only small influence on the period of vibration of the mounting system as compared to the large changes in period observed previously [1] when the effect of nonlinear mount stiffness on system response was determined. Here, the mounting system remains linear until γ is sufficiently large to cause the value of the relative velocity across the dashpot to exceed $\dot{x}_o x_{max}$ (Fig. 2); previously, the influence of nonlinear mount stiffness was apparent for even small values of $\gamma < 1.0$.

COMPARISON OF MOUNT PERFORMANCE

The response of shock mounts to input transients can conveniently be compared by reference to curves such as those of Figs. 16-27, which plot Shock Displacement Ratio, Relative Displacement Ratio, Shock Velocity Ratio, and Shock Acceleration Ratio, as functions of the parameter γ (the ratio of the half-period of the mounting system to the rise time τ of the input step displacements, or the duration τ of the input pulse). The performance of the nonlinear shock mount considered in the foregoing section, for which $0.1 \leq \delta_R \leq 0.5$, is contrasted in these figures with the performance of linear mounts for which $\delta_R = 0.05$, 0.1, and 0.5. The figures represent design curves analogous to the familiar transmissibility-frequency curves that describe the performance of antivibration mountings. The values of γ are such that the rise times and durations of the steplike and pulselike transients are consecutively much larger than, of the same order as, and much shorter than the half-period of natural vibration of the mounting systems.

The shock displacement ratio (SDR) and the shock acceleration ratio (SAR) are simply defined as the ratios of the maximum displacements and accelerations above and below the shock mount. The relative displacement ratio (RDR) is the ratio of the maximum relative displacement across the system to the maximum value x_{max} of the steplike or pulselike displacement of the foundation, the maximum velocities and accelerations of which are specified by Eqs. 19-21. To minimize the risk of damage to the contents of the mounted item, it is desirable that the foregoing ratios should be small simultaneously, although these are conflicting requirements [1] that can only partially be reconciled for the linear mounting system. Notwithstanding, the present use of dual-phase damping makes possible the joint reduction of SDR and SAR, although a simultaneous reduction

34
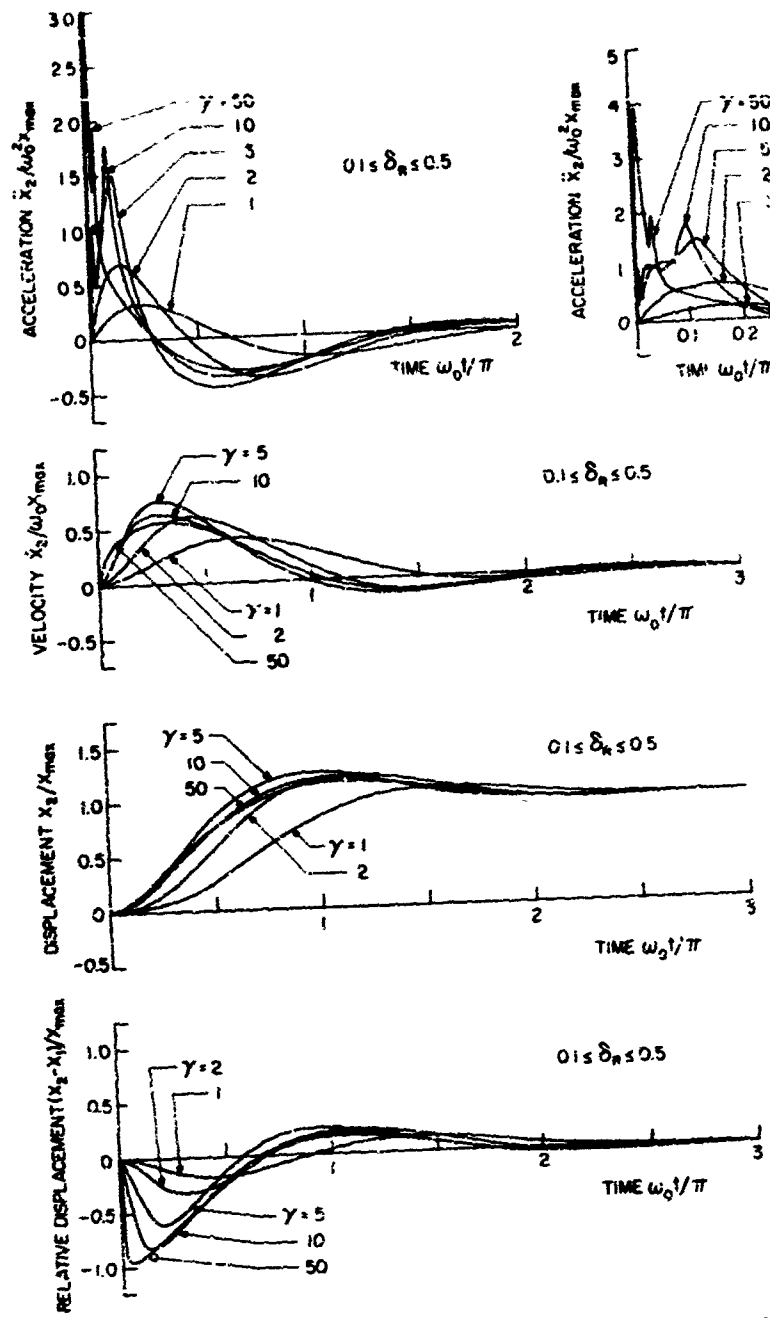
Fig. 14 - Acceleration-, velocity-, displacement-, and relative displacement-time relationships for the nonlinear system of Fig. 1(b) subjected to the rounded step displacements of Fig. 4. Dual-phase damping for which $0.1 \leq \delta_R \leq 0.5$.
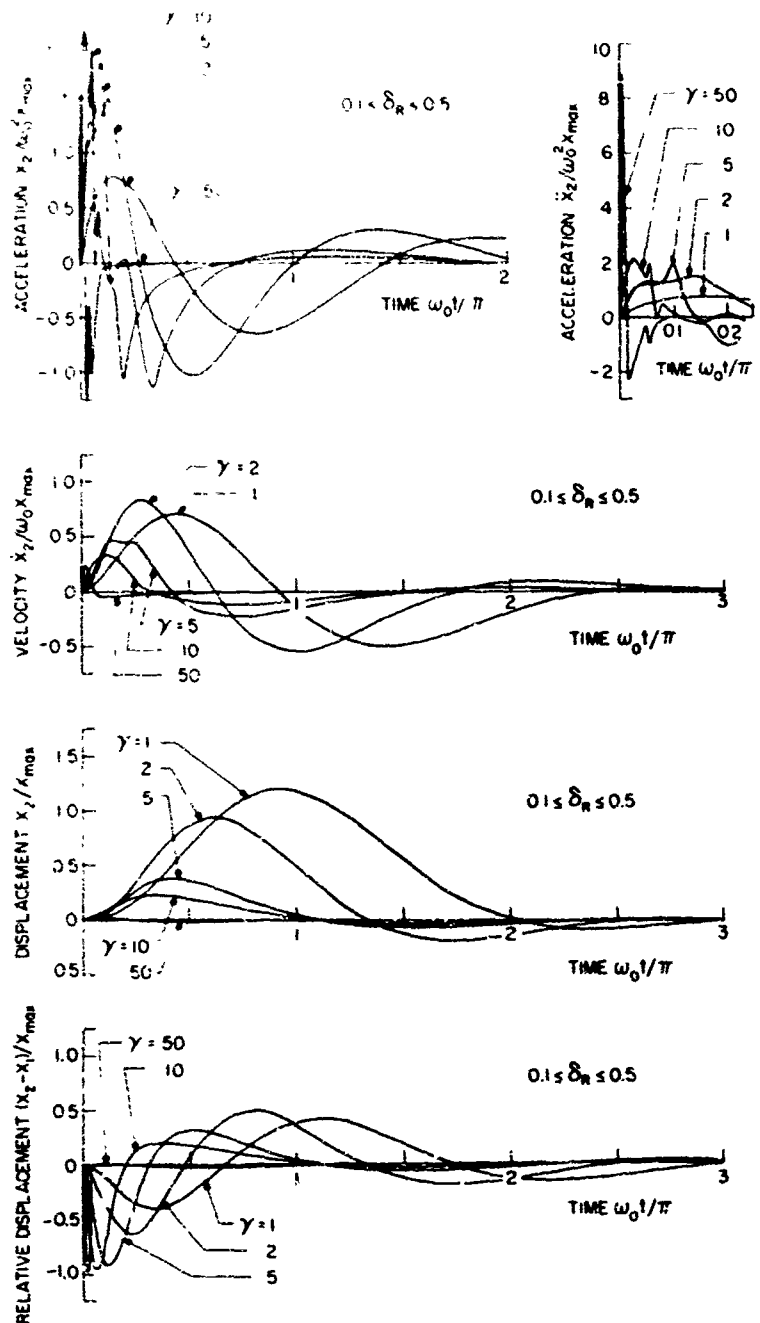
Fig. 15 - Acceleration-, velocity-, displacement-, and relative
displacement-time relationships for the nonlinear system of
Fig. 1(b) subjected to the rounded pulse displacements of Fig. 6.
Dual-phase damping for which $0.1 \leq \delta_R \leq 0.5$.
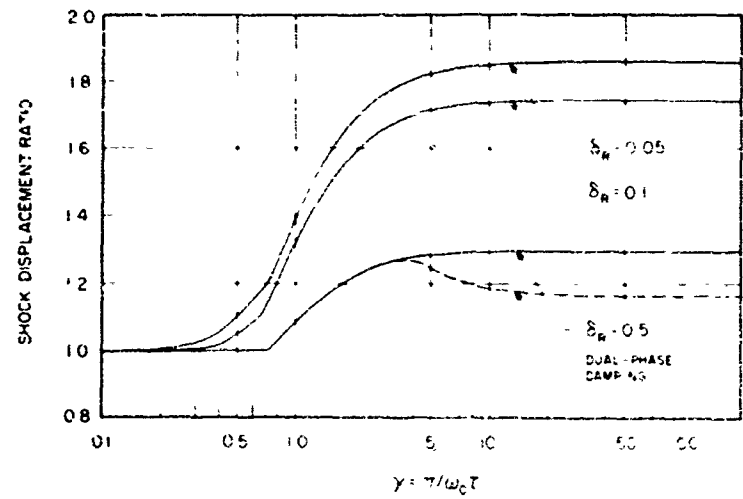
Fig. 16 - Shock displacement ratios of linear mounts for which δ_R = 0.05, 0.1, and 0.5, and of the nonlinear mount with dual-phase damping for which $0.1 \leq \delta_R \leq 0.5$. Mounts subjected to the rounded step displacement of Fig. 5.
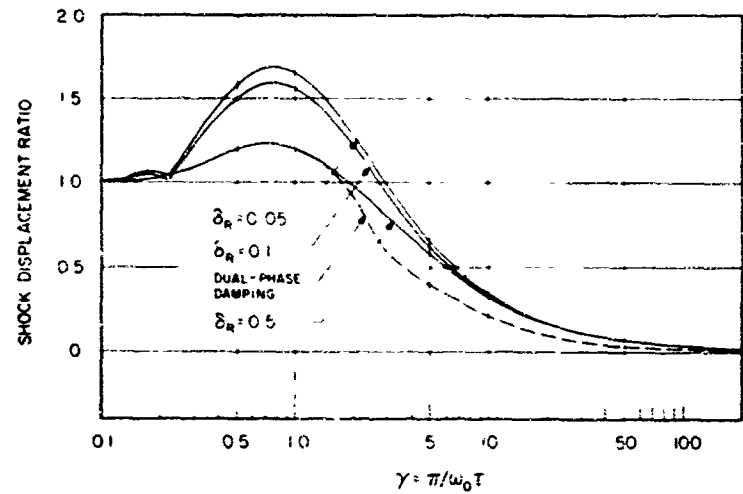
Fig. 17 - Shock displacement ratios of linear mounts for which δ_R = 0.05, 0.1, and 0.5, and of the nonlinear mount with dual-phase damping for which $0.1 \leq \delta_R \leq 0.5$. Mounts subjected to the rounded pulse displacement of Fig. 7.

37
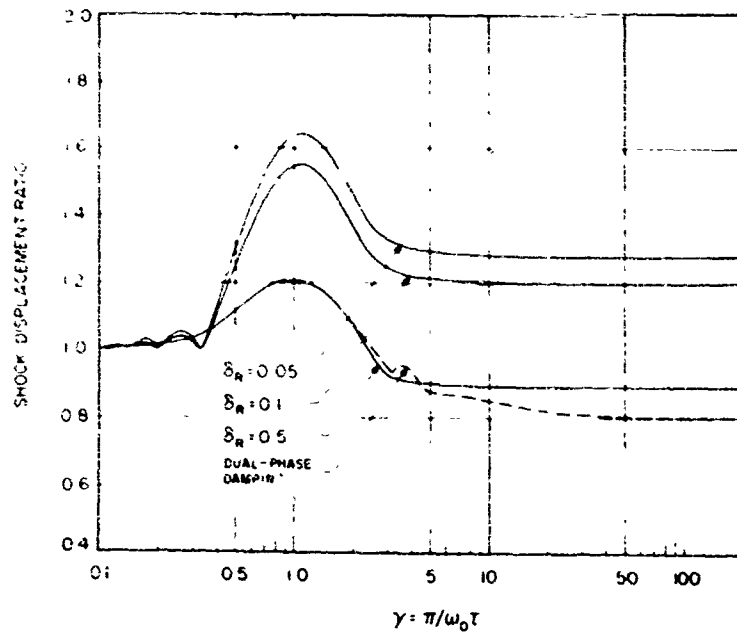
Fig. 16 - Shock displacement ratios of linear mounts for which $\delta_R = 0.05$, 0.1, and 0.5, and of the nonlinear mount with dual-phase damping for which $0.1 \leq \delta_R \leq 0.5$. Mounts subjected to the oscillatory step displacement of Fig. 9.

in RDR is not possible. The shock velocity ratio (SVR), which is referred to here for completeness, is defined as the ratio of the maximum velocities above and below the shock mount. Note that, in Figs. 16-27, the full-line curves that describe the transient response of the linear mounting system of Fig. 1(a) have broader significance than described by the figure captions. For example, the SAR curves can be visualized as SDR curves for input displacements defined by the same equations as those that define the acceleration pulses of Figs. 5, 7, and 9. Alternatively, the SIR curves can be interpreted as SAR curves for input accelerations defined by the same equations as those that govern the input steplike and pulselike displacements of Figs. 5, 7, and 9.

The SDR curves for the rounded step input, the rounded pulse input, and the oscillatory step input, are plotted in Figs. 16-18. In these figures, when γ is small, the SDR curves approach a value of unity. When γ is large, the SDR curves for the input steps attain constant levels that are generally greater than unity; however, the SDR curve for the pulse decreases to a negligible value since the displacement of the foundation has then peaked and returned to zero before the mounted item M has moved appreciably. Figures 16-18 illustrate the fact that only for input transients that are pulselike, or have other shapes with relatively small low-frequency Fourier components, can the displacement of M be reduced by resilient mounting. In each figure, the dashed-line curves clearly indicate how the use

of dual-phase damping provides the lowest values of SDR at all values of γ greater than about 2.5. (For small values of γ, the dashed-line curves coincide with the full-line curves for which $\delta_R = 0.5$.)

For both steplike and pulselike input displacements, the RDR curves of Figs. 19-21 show a like dependence on γ. The greatest difference in level between the curves occurs at intermediate values of γ since, for either small or large values, each RDR curve monotonically approaches the limit of zero or unity. Only in these figures is the performance of the nonlinear mount less satisfactory than that of the linear mount for which $\delta_R = 0.5$. In fact, as the value of γ increases, the RDR of the nonlinear mount changes in level from that of the linear mount for which $\delta_R = 0.5$ to that of the mount for which $\delta_R = 0.1$; however, the actual increase in magnitude is not large since all curves are then approaching the same upper limit of unity (maximum relative displacement = x_{max}).

Comparison of the shock velocity ratios of Figs. 22-24 shows that the velocity of the pulselike input displacement can be isolated more effectively, by both the linear and nonlinear mountings, than can the velocities of the steplike inputs. For the input steps, the shock velocity ratios are influenced only to a small extent by changes in value of δ_R; further, the nonlinear mount provides the lowest values of SVR at essentially all values of γ. For the input pulse, the nonlinear mount
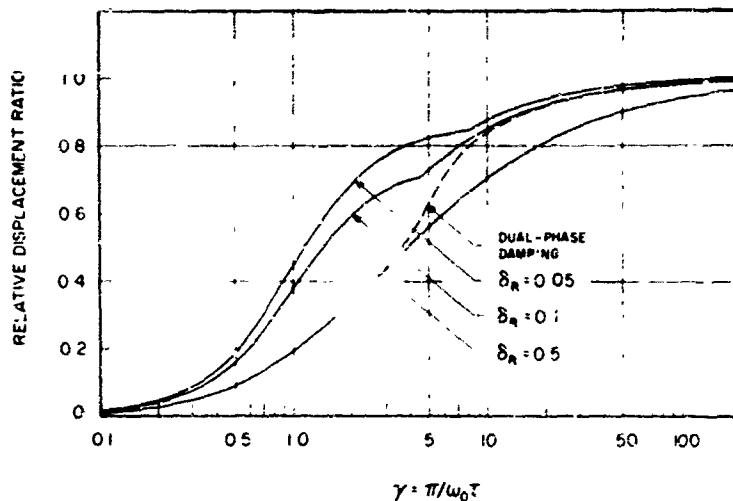
Fig. 19 - Relative displacement ratios of linear mounts for which $\delta_R = 0.05$, 0.1, and 0.5, and of the nonlinear mount with dual-phase damping for which $0.1 \leq \delta_R \leq 0.5$. Mounts subjected to the rounded step displacement of Fig. 5.
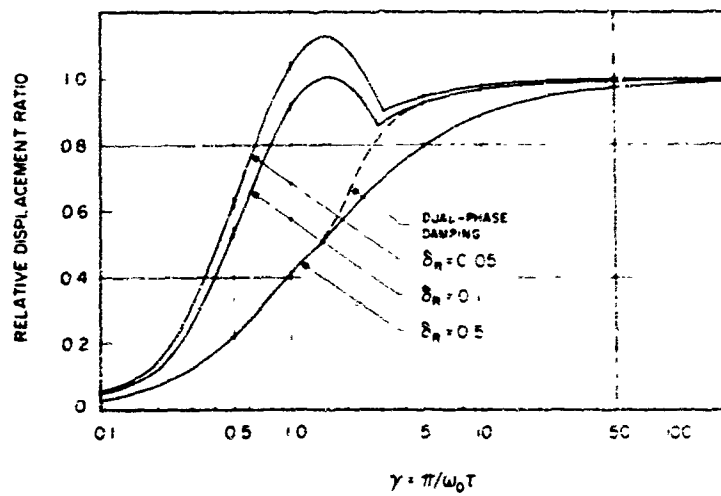
Fig. 20 - Relative displacement ratios of linear mounts for which $\delta_R = 0.05$, 0.1, and 0.5, and of the nonlinear mount with dual-phase damping for which $0.1 \leq \delta_R \leq 0.5$. Mounts subjected to the rounded pulse displacement of Fig. 7.

39
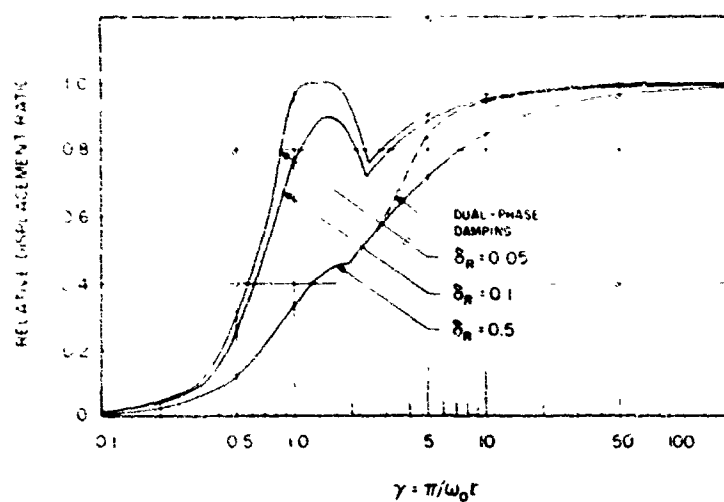
Fig. 21 - Relative displacement ratios of linear mounts for
which δ_R 0.05, 0.1, and 0.5, and of the nonlinear mount with
dual-phase damping for which $0.1 \leq \delta_R \leq 0.5$. Mounts subjected
to the oscillatory pulse displacement of Fig. 9.
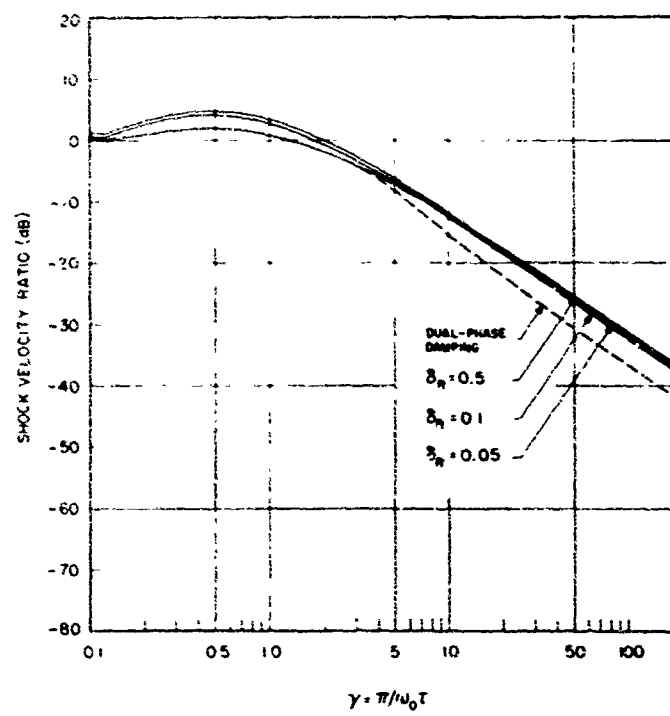
Fig. 22 - Shock velocity ratios of linear mounts for which $\delta_R =$
0.05, 0.1, and 0.5, and of the nonlinear mount with dual-phase
damping for which $0.1 \leq \delta_R \leq 0.5$. Mounts subjected to the
rounded step displacement of Fig. 5.

40
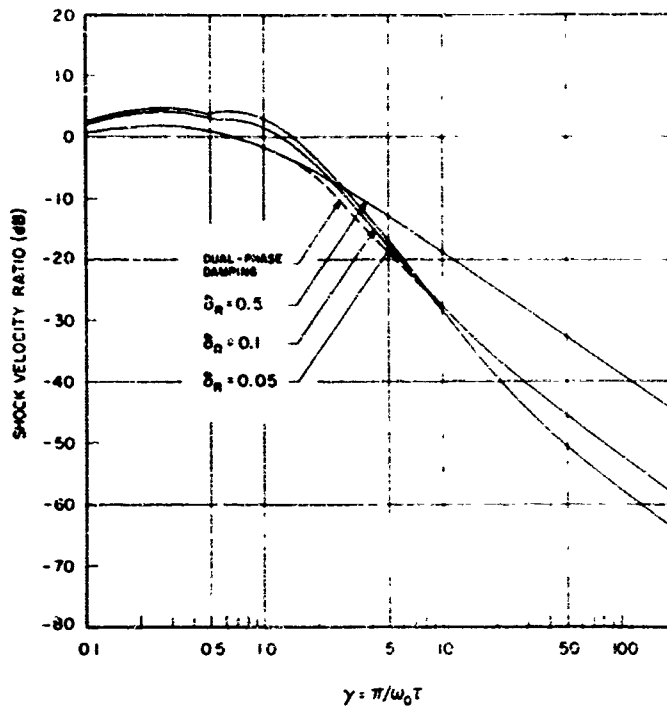
Fig. 23 - Shock velocity ratios of linear mounts for which δ_R = 0.05, 0.1, and 0.5, and of the nonlinear mount with dual-phase damping for which $0.1 \leq \delta_R \leq 0.5$. Mounts subjected to the rounded pulse displacement of Fig. 7.
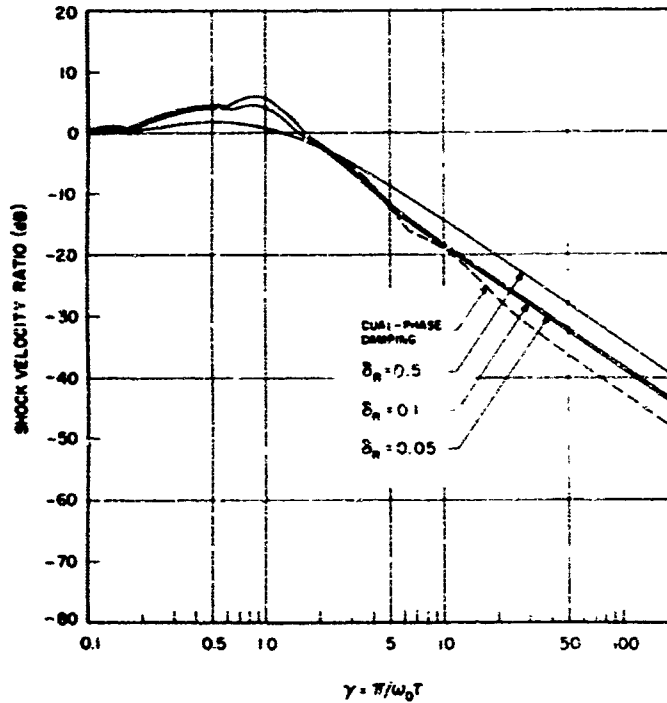
Fig. 24 - Shock velocity ratios of linear mounts for which δ_R = 0.05, 0.1, and 0.5, and of the nonlinear mount with dual-phase damping for which $0.1 \leq \delta_R \leq 0.5$. Mounts subjected to the oscillatory step displacement of Fig. 9.
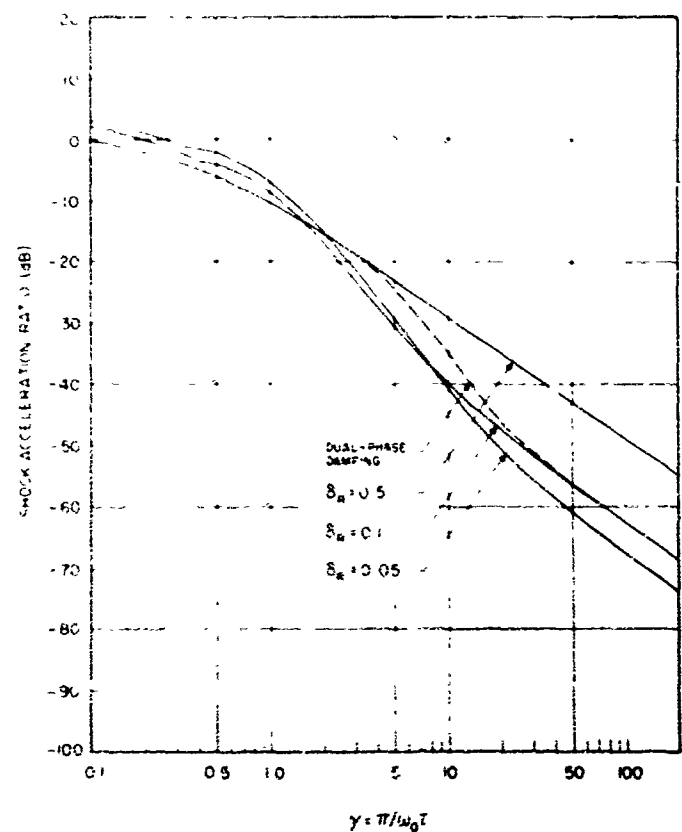
Fig. 25 - Shock acceler.ti n ratios of linear mounts for which
δ_R = 0.05, 0.1, and 0.5, and of the nonlinear mount with dual-
phase damping for which $0.1 \leq \delta_R \leq 0.5$. Mounts subjected to the
rounded step displacement of Fig. 5.
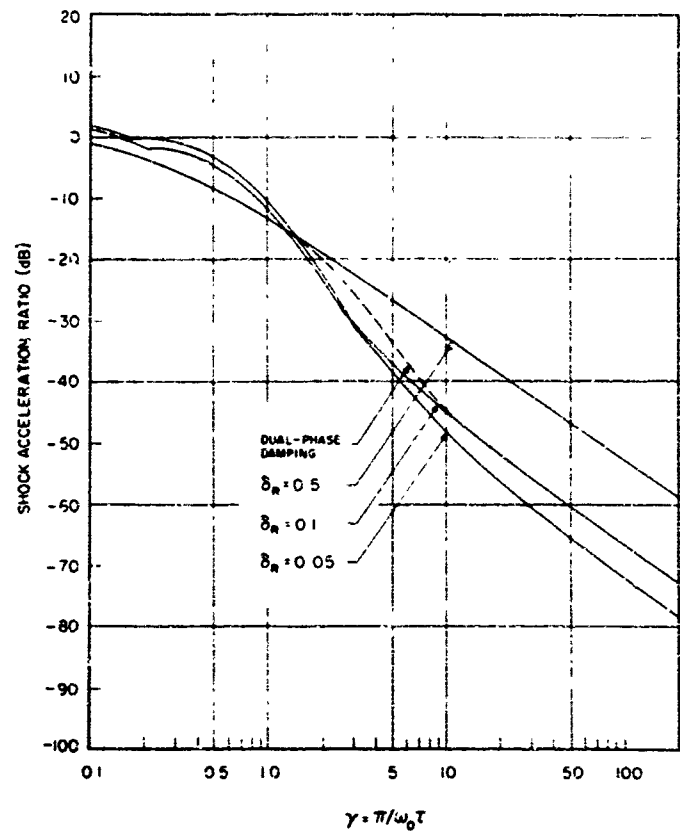
Fig. 26 - Shock acceleration ratios of linear mounts for which
$\delta_R = 0.05$, 0.1, and 0.5, and of the nonlinear mount with dual-
phase damping for which $0.1 \leq \delta_R \leq 0.5$. Mounts subjected to
the rounded pulse displacement of Fig. 7.
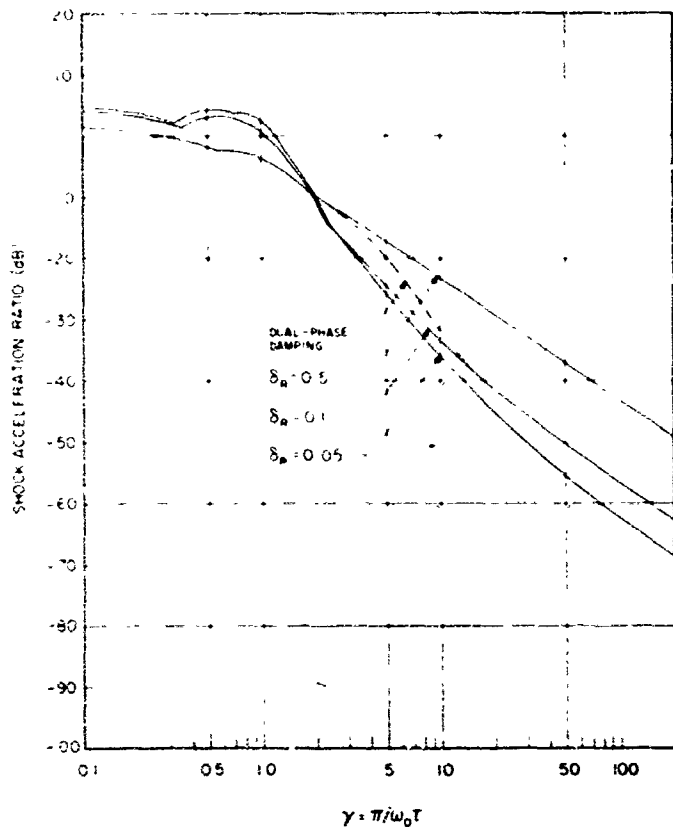
Fig. 27 - Shock acceleration ratios of linear mounts for which
$\zeta_R = 0.05$, 0.1, and 0.5, and of the nonlinear mount with dual-
phase damping for which $0.1 \leq \zeta_R \leq 0.5$. Mounts subjected to the
oscillatory step displacement of Fig. 9.

provides the lowest SAR when γ is 8 and the next to lowest SAR when γ 8. In fact, for large values of γ, the SAR of the nonlinear mount falls approximately 10 and 15.5 dB below the lowest SAR curves of Figs. 22 and 24. All SAR curves decrease at the rate of 6 dB/octave when γ is large.

Shock acceleration ratios for the step-like and pulselike input transients are plotted in Figs. 25-27, which show that the levels of the SAR curves are alike and of the order unity when γ is small. However, the levels of the SAR curves are very effectively reduced by both the linear and nonlinear mounts when γ is large,

and each curve then falls off at the rate of 6 dB/octave; thus, the maximum accelerations of M are proportional to γ (Eqs. 51-53), whereas the maximum accelerations of the foundation are proportional to γ^2 (Eqs. 19-21). Because the accelerations of M are also proportional to ζ_R when γ is large (Eqs. 51-53), the SAR curves for the three values of ζ_R considered here take the same relative levels in each of Figs. 25-27. These figures show that the nonlinear mount with dual-phase damping effectively provides both the lowest SAR when γ is small (SAR curve is coincident with that of the linear mount for which $\zeta_R = 0.5$) and a very low SAR when γ is

44

large (SAR curve is coincident with that of the linear mount for which $\xi_R = 0.1$ and, therefore, is 14 dB below the SAR curve for which $\xi_R = 0.5$).

SUMMARY

The advantages of shock mounting lie primarily in the reduction of the acceleration of the mounted item M that results. Resilient mounting must introduce relative displacement between M and its foundation--and, commonly, the absolute displacement of M is increased as well. The curves of Figs. 16-27 demonstrate how a nonlinear shock mount with dual-phase damping can be extremely effective in simultaneously reducing or minimizing the displacement and acceleration of M, and its velocity, for all but small values of γ, a parameter that is proportional to the reciprocal of the rise time or duration of the input transient. Although the nonlinear mount is clearly more effective than any of the linear shock mounts considered, its performance remains similar to theirs (and to all other shock mounts) in that (1) its SAR and SVR are of the order unity when γ is small, and (2) its RDR approaches the value unity when γ is large.

ACKNOWLEDGMENTS

REFERENCES

1. J. C. Snowdon, Vibration and Shock in Damped Mechanical Systems (John Wiley and Sons, Inc., New York, 1968).

2. F. J. Padden and T. W. DeWitt, "Some Rheological Properties of Concentrated Polyisobutylene Solutions," J. Appl. Phys. 25, No. 9, 1086-1091 (1954).

3. T. W. DeWitt, H. Markovitz, F. J. Padden, Jr., and L. J. Zapas, "Concentration Dependence of the Rheological Behavior of the Polyisobutylene - Decalin System," J. Colloid Sci. 10, 174-188 (April 1955).

4. T. G. Fox, S. Gratch, and S. Loshaek, "Viscosity Relationships for Polymers in Bulk and in Concentrated Solution," contribution to Rheology, Theory and Applications, Vol. 1, F. R. Eirich, ed. (Academic Press, Inc., New York, 1956), Chap. 12.

5. J. D. Ferry, Viscoelastic Properties of Polymers (John Wiley and Sons, Inc., New York, 1961).

6. F. Bueche, Physical Properties of Polymers (Interscience Publishers, Inc., New York, 1962).

7. R. S. Porter, M. J. R. Cantow, J. F. Johnson, "The Entanglement Region and Non-Newtonian Flow," Proc. Fourth Int. Congr. Rheol., Pt. 2, E. H. Lee, ed. (Interscience Publishers, Inc., New York, 1965) pp. 479-489.

8. J. D. Huppler, E. Ashare, and L. A. Holmes, "Rheological Properties of Three Solutions. Part I. Non-Newtonian Viscosity, Normal Stresses, and Complex Viscosity," Trans. Am. Soc. Rheol. 11, No. 2, 159-179 (1967).

9. S. Middleman, The Flow of High Polymers (Interscience Publishers, Inc., New York, 1968).

10. S. Chien, et. al., "Effects of Hematocrit and Plasma Proteins on Human Blood Rheology at Low Shear Rates," J. Appl. Physiol. 21, No. 1, 81-87 (1966).

11. P. A. Kelly and L. Flenker, Differential Equation Solver Subroutine Using Milne and Adams Predictors, The Pennsylvania State University, Computation Center Subroutine DPDEQN, November 1968.

INTERACTIVE OPTIMAL DESIGN OF SHOCK ISOLATION SYSTEMS

W. D. Pilkey
University of Virginia
Charlottesville, Virginia

A computational scheme is described whereby an optimal shock isolation system can be interactively designed. Primary design criteria and constraints are assumed to be physical variables, e.g., rattlespace requirements and peak acceleration of a fragile package, while other factors, e.g., cost, are acceptable as secondary criteria. No restrictions regarding linearity or passivity are placed on the isolator. Character-ist s of the theoretically optimal design are automatically generated and displayed for a prescribed shock environment. The designer then conversationally selects isolation elements and parameters which lead to a system that behaves similarly to the theoretical optimum. The computer program, which can be implemented on remote desk-top terminals, then permits the user to study the sensitivity of his design to changes in design parameters and shock environment.

INTRODUCTION

Optimal design of shock isolation systems has been the subject of many papers [1]. In addition to the trial and error procedures, including automated computational search techniques, to determine near-optimal isolator configurations and parameters, a design approach involving the theoretically optimal isolator has been proposed. With this method various properties of the optimal isolation system are computed without regard to specific isolator configurations. Design configurations and accompanying parameters can then be selected so that the response will approach these theoretically optimal characteristics.

It is usually desirable to introduce numerous considerations, often wholly different from the primary design criteria, into a rational design. However, automated design frequently precludes the consideration of all but those criteria that can be expressed in functional form. The designer is effectively excluded from the design loop. In contrast, the optimal design procedure proposed here permits the designer to introduce any number of secondary design criteria. This is an interactive computational scheme wherein the designer remains on-line with the computer as the design proceeds.

Primary design criteria are assumed to be physical variables such as peak accelerations and rattlespace requirements. Once the designer provides these design criteria and the time history of the shock disturbance, the characteristics of the theoretically optimal design are automatically computed as the solution to a mathematical programming optimization problem. Up to this point no restrictions with respect to the isolator configuration, including linearity or passivity, are imposed. The designer then selects a trial isolator configuration with a set of parameters. The program computes the response of the proposed design and compares graphically the resulting design criteria with the theoretically optimal criteria. A graphical comparison is also made of the time histories for the trial isolator responses with the theoretically optimal time responses. These two comparisons provide the designer with a quantitative and qualitative, respectively, measure of the optimality of his design. The designer may then interact with the design process to choose better design parameters or other isolator configurations. He may also impose other design criteria, e.g., cost, availability, reliability, maintainability, and intangible factors rived from past design experiences, by introducing appropriate considerations into his selection of parameters and configurations. Furthermore, the procedure set forth here permits the designer to automatically examine the sensitivity of his design to changes in parameter values and to environments other than the one for which the design was based.

INTERACTIVE OPTIMAL DESIGN

The problem is to select suitable shock isolators for a mechanical system (Fig. 1). The multitude of considerations which must be
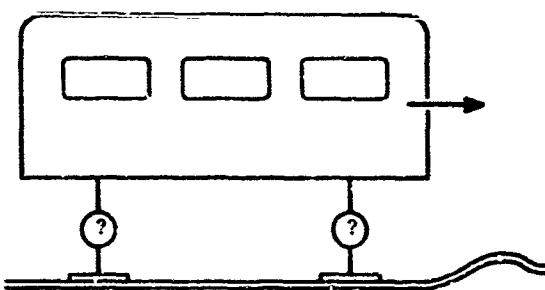
Fig. 1 - Multiple Isolator System

factored into an acceptable design appear
overwhelming at the outset. We suppose that
the most important design criteria are phys-
ical responses. For example, the designer
may wish to choose isolators such that the
peak acceleration experienced by passengers
in a vehicle is minimized while the displace-
ment of the passenger relative to the vehicle
or surroundings is bounded. On the basis of
these types of response criteria, it is possi-
ble [1] to compute characteristics of the theo-
retically optimal isolators for complex, mul-
tiple isolator systems. The interactive
scheme proposed here takes advantage of
these characteristics in designing shock
isolators and permits other design criteria to
be introduced. We choose to discuss the ap-
proach by considering the design of a single
isolator system. Although the single isolator
is selected for illustrative purposes because
of its simplicity, the importance of this model
is underscored by an indication [1] that it is
possible to design a multiple isolator system
one isolator at a time.

The interactive scheme is diagrammed in
Fig. 2. To consider the approach in detail,
we begin with the single isolator system of
Fig. 3. Suppose the primary design objective
is to choose, for a specified shock disturbance,
an isolator that minimizes the peak acceler-
ation of the mass while bounding the relative
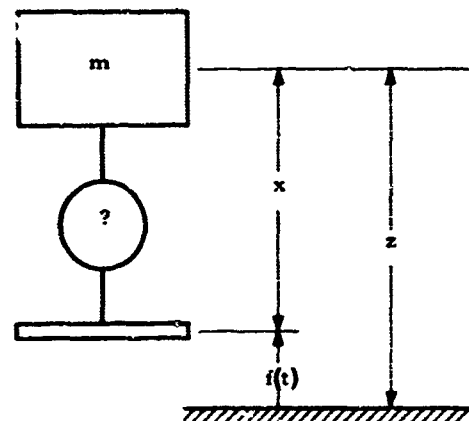
Fig. 3 - Single Isolator

displacement. Thus, for a given $f(t)$ the iso-
lator is to be chosen so that

$$\max_{t} |\ddot{z}|$$

is minimized and

$$\max_{t} |x| \leq X,$$

where X is the prescribed bound on displace-
ment.

A computer program is then used to com-
pute, on the basis of this problem statement,
the characteristics shown in Fig. 4 and Fig. 5
for the theoretically optimal isolator. The
curve in Fig. 4 provides the limiting perform-
ance index for a range of constraint values.
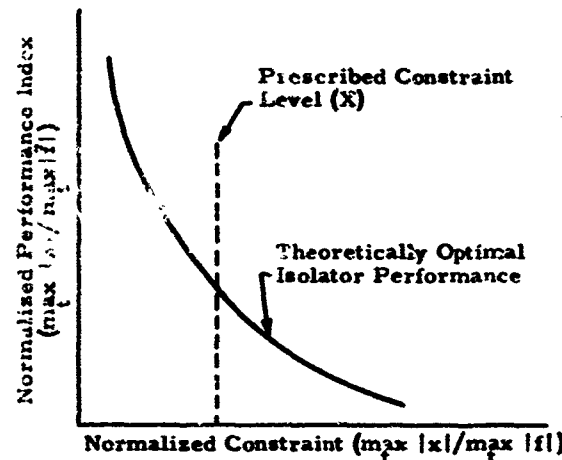
Fig. 4 - Theoretically Optimal Performance
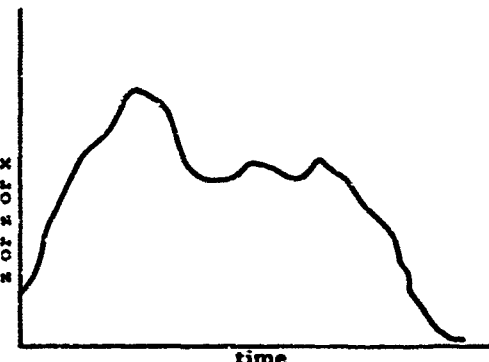
Fig. 5 - Theoretically Optimal Time Response

For a given constraint value X, it is not pos-
sible for an isolator to be designed for the
disturbance $f(t)$ that would exhibit a peak accel-
eration less than the value indicated by the
intersection of constraint X with the theoreti-
cally optimal isolator performance curve. Fig.
5 shows a time response history for a theoret-
ically optimal isolator at a designated
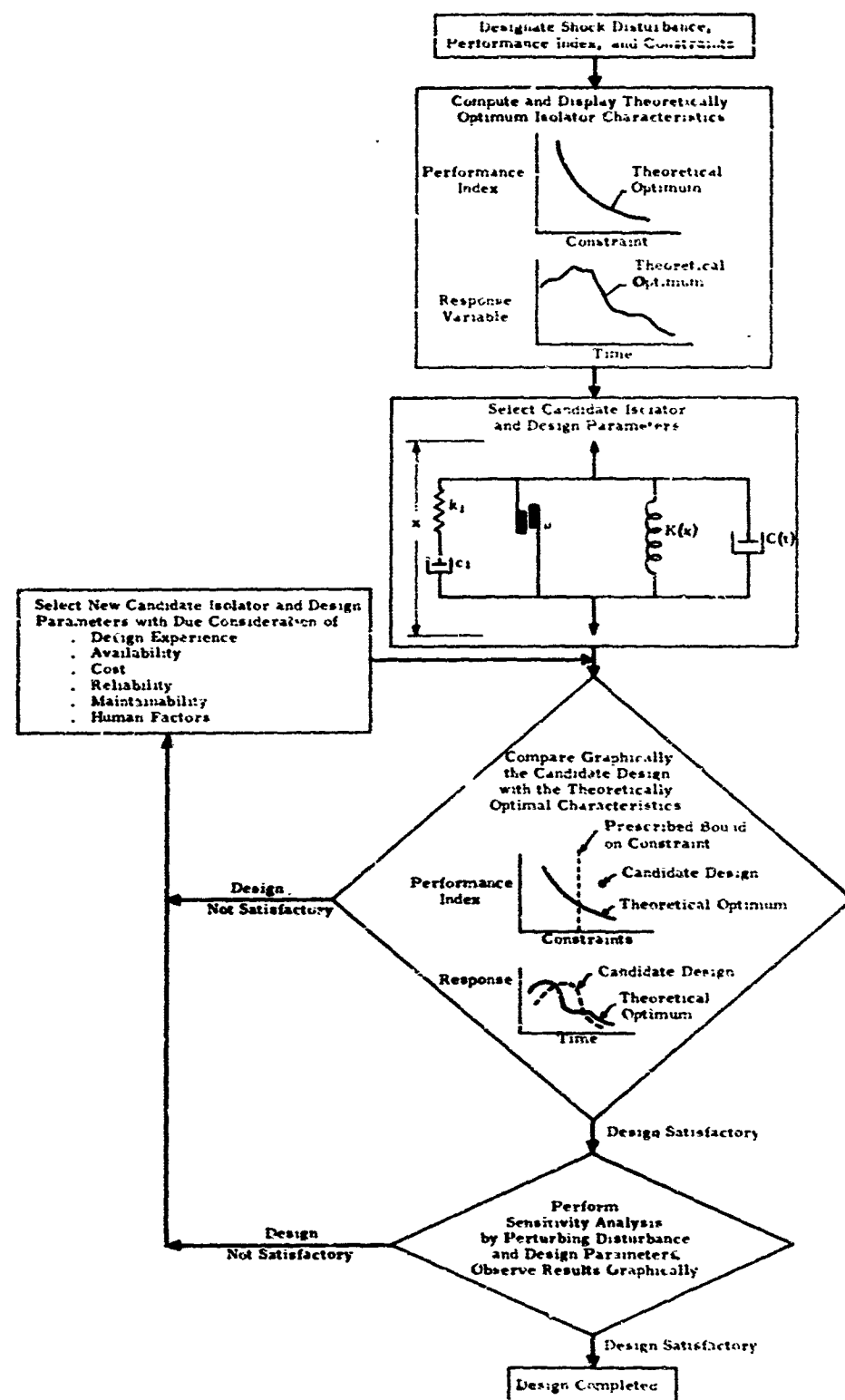
Fig. 2 - Optimal Design of Shock Isolation Systems

constraint level X.

The designer next chooses a candidate
isolator configuration with candidate values of
design parameters. The selection could be
passive, active, linear or nonlinear. Thus, in
Fig. 6 a linear spring dashpot combination is
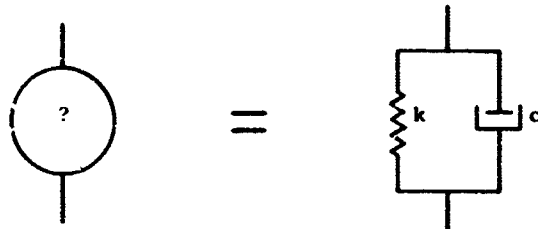
Fig. 6 - Candidate Isolator Configuration and
Design Parameters

chosen with particular values of k and c. The
peak acceleration, peak relative displacement,
and responses in time are computed for this
isolator by integrating the equations of motion
of the system and are superimposed on the
displayed theoretically optimal characteristics
of Fig. 4 and Fig. 5. The designer then sees
curves of his own choosing similar to those of
Fig. 7. The performance curve provides a
quantitative indication of the desirability of
his candidate design while the response curves
give a qualitative measure.

The designer can then recycle the design
by selecting new parameters and, if necessary,
a new configuration to obtain an improved
isolator. In so doing he can introduce any
number of secondary criteria into his selection
of candidate hardware. Such criteria include
availability, cost, maintainability, reliability,
and even human factors. The successive can-
didate designs are automatically plotted on the
theoretically optimal isolator displays. Typi-
cal performance points are shown in Fig. 8.
The trends observed graphically of successive
trial designs assist the user in selecting the
candidate design for each cycle. Naturally the
theoretically optimal characteristics are
stored and need not be recomputed for each
iteration in the design.

After an acceptable, near-optimal iso-
lator design is chosen, the designer may wish
to perform a sensitivity analysis. This is
accomplished automatically by programming
the design scheme to compute performances
for variations in design parameters and input
disturbances. The results of such perturba-
tions are then superimposed on the already
available performance information (e.g., as
in Fig. 9) and displayed. If the sensitivity
characteristics of the candidate design are
satisfactory, the design is considered com-
pleted. If not, the iterative design mode is
reentered and new candidate designs
considered.
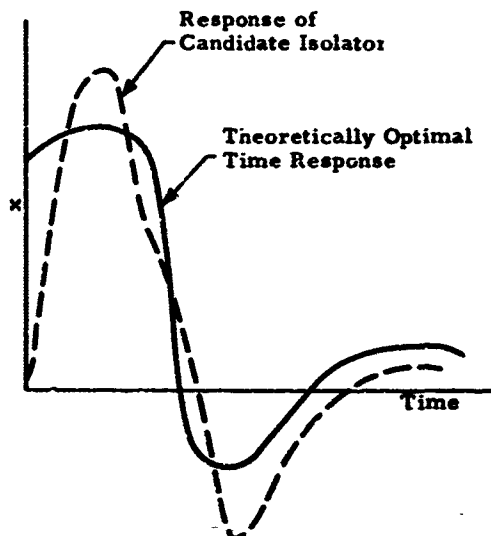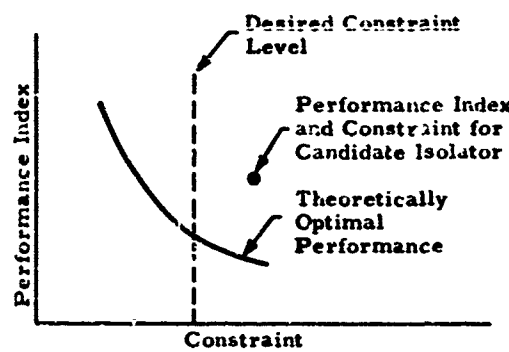
Fig. 7 - The Initial Trial Design
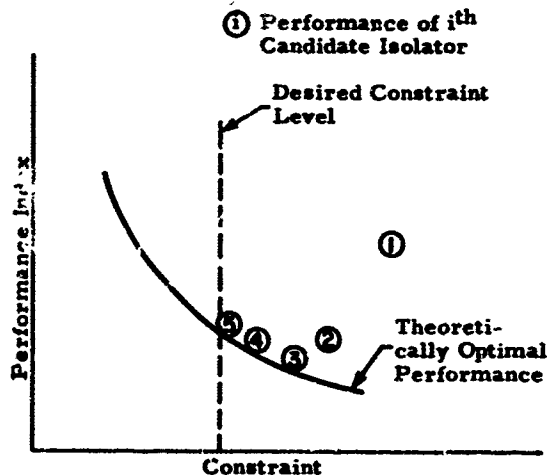
Fig. 8 - Successive Trial Designs

50
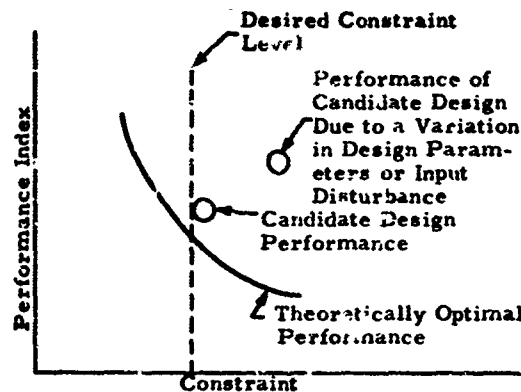
Fig. 9 - Sensitivity Analysis

TECHNICAL DISCUSSION

The technology for characterizing theoretically optimum shock isolation systems is well documented in Ref. 1. Those portions of a mechanical system that are to be designed, e. g., the isolators, are represented by time varying forces. The optimization problem of finding these forces for which system constraints are satisfied and the performance index minimized is one of mathematical programming. Performance index-constraint tradeoff curves are found by solving the mathematical programming problem for a range of constraint values.

In general the optimization problem falls into the category of nonlinear programming, which is difficult to treat, even computationally, for large systems. Some systems of limited degrees-of-freedom can be handled with dynamic programming. However, if those portions of the system that are not being designed are linear and the overall system kinematics is linear, the problem is one of linear programming for which effective, large-scale, efficient computer programs are available. No restrictions with regard to linearity are placed on the isolators.

A problem-oriented computer program for determining the theoretically optimum performance for multi-degree-of-freedom dynamic systems under arbitrary transient disturbances is now being prepared for NASA/ Langley by the University of Virginia. This program will provide both the theoretically optimum response time trajectories and the performance index-constraint tradeoff diagrams employed in the interactive design scheme.

The theoretically optimum isolator can be achieved with simple graphical techniques [1] for single-degree-of-freedom isolators.

IMPLEMENTATION

The optimum design scheme is ideally suited for implementation on an on-line computer graphics capability. It can also be fully implemented on standard time-sharing computers with remote portable terminals. This was accomplished for single isolator systems. The theoretically optimum isolator characteristics for design criteria chosen by the designer are automatically generated using the graphical method. These characteristics are then stored and retrieved as needed during the comparisons with candidate isolator designs and the sensitivity responses. Numerical integration of the equations of motion for a design concept permits the determination of the responses of a generic isolator configuration with arbitrary disturbances. The user can compare the performance of candidate designs with the theoretically optimum performance-constraint tradeoff diagram or with the theoretically optimum time responses or with both. The complete design scheme is controlled using a problem-oriented language.

Various near-optimal isolators were designed with the program. From the standpoint of primary design criteria, the results, as expected, were comparable to the non-interactive procedures described in Ref. 1. However, with the interactive approach, numerous secondary criteria can be easily factored into the design.

SUMMARY

A versatile computational scheme for the interactive optimal design of shock isolation systems has been outlined. Near-optimal designs are selected such that isolator response characteristics approach those of the theoretically optimal design. The designer is permitted to introduce his experience into the design as well as multiple design criteria and constraints. A port design sensitivity analysis option is also provided the user.

REFERENCE

1. E. Sevin and W. Pilkey, Optimal Shock and Vibration Isolation, Shock and Vibration Information Center, Washington, D. C., 1970.

DESIGN OF HIGH-PERFORMANCE
SHOCK ISOLATION SYSTEMS

Ronald L. Eshleman
IIT Research Institute
Chicago, Illinois

Shock isolation of fragile systems from high frequency effects generated by high loading rates and/or random multifrequency input displacement signatures requires the use of new design techniques and procedures. A fundamental physical understanding of the shock isolator's dynamic behavior provides the basis for these design techniques. These design procedures and techniques were developed and utilized in a recent study for the Space and Missile Systems Organization (SAMSO) to evaluate classes of mechanical shock isolators with respect to their function in a specified shock environment. This paper describes these techniques and procedures as they apply to the design of high-performance shock isolation systems. The specification of shock environments is discussed in general terms, and the environment is specified by a pulse. Isolation system performance criteria are prescribed in terms of equipment fragility levels and rattlespace. Isolator concepts with long stroke capability useful in shock applications are described. The procedures in modeling isolators and shock-isolation systems for analysis and experimentation utilize distributed parameter descriptions. Analytical and experimental techniques for use on the selected models are described. The experimental and analytical results of this paper show conclusively that single degree-of-freedom models cannot adequately simulate isolator behavior. The isolator must be modeled as a multidegree-of-freedom system having distributed mass, damping and elasticity.

INTRODUCTION

Shock isolation of fragile systems from high frequency effects generated by high loading rates and/or random multifrequency input displacement signatures requires special design techniques and procedures. A fundamental physical understanding of the shock isolator's dynamic behavior provides the basis for these techniques. The subject design procedure utilizes a judicious combination of analyses and experiments to develop and/or select the isolator and the system.

The design philosophy of this paper was developed from a recent study [1] for SAMSO. Classes of mechanical shock isolators were evaluated with respect to their performance in a specified environment. This study verified analytically and experimentally that single degree-of-freedom models cannot be used to simulate an isolator's dynamic behavior. The isolator must be modeled as a multidegree-of-freedom system having distributed mass, damping and elasticity. The mathematical models of pertinent shock isolators, used for experiment and analysis, are included in Appendix A. An example design of an in-silo shock isolation system is given in Appendix B.

The subject design procedure is composed of the following related steps.

- Environment and performance specification.
- Conceptual design.
- Isolator and system modeling.
- Dynamic response analysis.

- System parameter optimization.

- Experimental characterization and verification.

The initial step in any design procedure is the specification of the system environme and the statement of the system performance requirements. The system environment is specified in the form of a displacement-time pulse; the performance requirements are given in terms of rattlespace and equipment fragility levels. The conceptual design of the system configuration and of the shock isolators provides the basis for the shock isolation system development. The conceptual design stage of this process is largely an innovative process, and, therefore, its success depends on the ingenuity of the engineer. The isolator and system are modeled for mathematical and/or experimental analysis. In addition, this model is utilized for a system parameter optimization. Mathematical models of the system simulate the configuration kinematics, global response, and the mass, elastic and damping properties of its isolators (local response).

Experimental models are designed to characterize the isolator's behavior (if it is not known) and to verify system performance. The dynamic response analysis simulates the action of the shock isolation system under its prescribed environmental conditions. The quality and detail of the simulation will be dependent on the analytical technique employed. The modeling and analysis tasks are related intimately to determine the resulting simulation. System parameter optimization yields the best system under the constraints imposed. These constraints may include rattlespace, isolator type, isolated item size, etc. Experiments described herein are on scaled versions of the system. They are utilized to determine the physical characteristics of the isolator including its force-motion description. The final step in this procedure is the scale model experimental verification of the system's performance. The ensuing sections of the paper describe these procedures and techniques in detail.

ENVIRONMENT AND PERFORMANCE SPECIFICATION

A shock environment is characterized as a disturbance -- displacement, velocity, acceleration or force -- whose duration is short relative to the characteristic period of the system. Equipment, personnel and systems are subjected to many types of shock environments, which are categorized for transportation, manufacturing and military applications. Characterization [2] of these environments is available in the form of shock spectra (response of the system is a measure of its environment) acceleration-frequency envelopes, and force and motion-time curves. Up to this time designers have found it most convenient to use the shock spectrum approach [3] which is simple and logical; however, much detail is lost due to its linear, modal foundations.

The analytical and experimental techniques described in this paper utilize force or motion-time curves. Specification of the pulse shape in this manner has an advantage in that the response permits simple verification of compliance with specifications. The example problem of Appendix B has a typical displacement-time characterization (Fig. 1) of free field motion generated
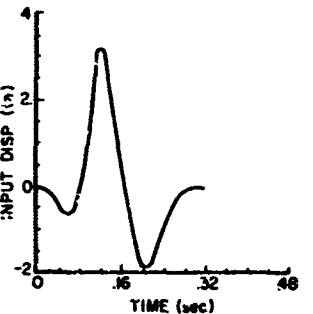
Fig. 1 - Typical environmental shock pulse

by a weapon detonation. Morrow [4] argues the greater value of force controlled shock tests on the basis that a better environmental simulation is obtained for the degree of complexity of the test. Of course, such a method is dependent on the available data on the environmental pulse and on the impedance of the containing structure. One distinct disadvantage of this method is that only small tolerances on the pulse shapes are allowed because the system response is very sensitive to pulse shape variations. In the past, therefore, investigators have not been eager to use this method because of the uncertainty of the pulse rise times, decays and magnitudes. It must be noted, however, that increasingly sophisticated instrumentation and better simulation tests have made this method credible. In addition, sensitivity analysis techniques allow calculation of the sensitivity of the system response to environmental pulse variations.

54

Every isolator or its system has a
measure of performance and/or strength
of either long or short-term duration.
This measure commonly is called its
fragility level. Fragility is used as
a quantitative index of the function and
strength of equipment subjected to shock
and vibration environments. The quanti-
tative index for fragility is expressed
in terms of a system's acceleration re-
sponse and is referred to in terms of g,
gravitational acceleration. The fragil-
ity level is stated in either a plot of
acceleration response as a function of
time, an allowable response pulse, or a
plot of maximum acceleration as a func-
tion of frequency. A simple comparison
of response envelopes to a stated per-
formance specification then shows the d
degree of systems conformity to design
specifications.

It is possible to use a performance
specification on the global motion of
the shock isolation system while having
constraints on the system rattlespace,
isolator performance, and any number of
equipment responses. A satisfactory en-
vironment provided to personnel and
equipment by the shock isolation system
is its principal function.

CONCEPTUAL DESIGN

The development of more sophisticated
electrical, optical and mechanical equip-
ment sensitive to high frequency effects
and the subjugation of such equipment to
more severe shock environments have
dictated a need for high performance
shock isolation systems. Stringent de-
mands for shock mitigation, therefore,
are placed on shock isolation systems
that support equipment in missile launch
facilities, artillery weapons and trans-
portation devices.

In order to develop shock isolation
systems that meet these demands, system
and isolator concepts that provide maxi-
mum development possibilities must be
obtained. Cognizance of the fundamental
characteristics of shock isolation sys-
tems is essential to successful concep-
tual design. The function of any com-
ponent or system is constrained by its
conceptual design because optimization
techniques use the concept as a base.
(A variation of this theme is described
later in this paper). Since there is no
methodical way to synthesize concepts,
ingenuity and experience are necessary.

Experience has shown that selection
of a shock isolation system configura-
tion concept and a shock isolator con-
cept should have kinematic emphasis be-
cause the basis of shock isolation is
controlled constant force motion.

More often than not, rattlespace re-
stricts the degree of isolation of a
system. Kinetic considerations are im-
portant and can be handled within the
original kinematic constraints of the
concept. The pendulum shock suspension
concept shown in Fig. 2 is an effective
system configuration because it allows
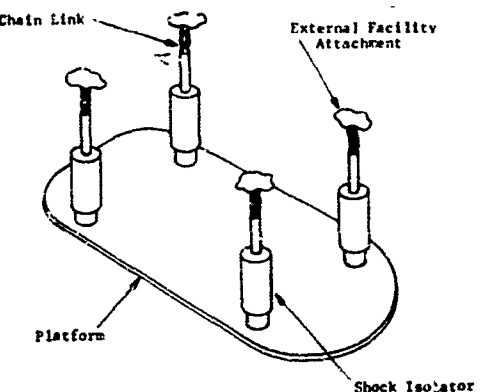
Fig. 2 - Schematic of pendulum type shock
isolation system configuration

isolation in all directions. The pen-
dulus motion of the equipment mounting
platform provides isolation in the hori-
zontal plane, and the shock isolators
provide isolation in the vertical direc-
tion. This concept has many develop-
mental possibilities; damping and an-
gular flexibility could be imposed at
the isolators, at the external attach-
ment points and at the platform isola-
tor attachment point. A second system
configuration, shown in Fig. 3 (devel-
oped in Appendix B), suggests the use
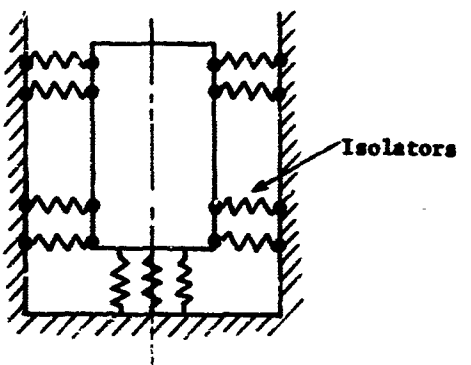
Fig. 3 - Isolator support system

of mechanical isolators for isolation
and support. This system also has de-
velopmental possibilities but is re-
stricted by successful isolator design.
The kinematic description (Appendix B)
of the spring-equipment system is essen-
tial in large equipment motions. In

55

most cases the large motions of the shock isolation system cause kinematic nonlinearities and, if possible, the problem must be alleviated in the conceptual design. Otherwise, these nonlinearities cause difficulties in system analysis, experimentation and optimization.

The conceptual design of new shock isolators (based on definite system requirement) has been rare up to this point, because the requirements generally are not understood. During development of an isolator concept, four factors must be considered: function, reliability, maintainance and cost. Functional considerations should have top priority. A high-performance shock isolator has the following properties: a long stroke capacity, a facility to attenuate high-frequency environmental disturbances and a composition that controls the generation of internal waves. The last requirement implies that the elastic and mass properties of the shock isolator are proportioned with damping to control wave propagation and/or generation; therefore, local damping within the isolator is important. Most commercially available isolators, which are used for vibration isolation, are short stroke inflexible devices. There is a need for development of long stroke isolators. In order to achieve this goal, a balance between stroke and flexibility must be attained; this avoids bottoming of coils. Care must be exercized to size isolators so that induced loading rates do not exceed the isolator's particle velocity; if this does occur, a jump discontinuity similar to a shock wave will result. Some of the springs that show feasibility for development into high-performance shock isolators are discussed below with respect to their working mechanisms and their characteristics.

Helical Coil Spring (Fig. 4)

Fig. 4 - Helical coil spring

This is a good long stroke isolator with minimal local damping. Its working mechanism is the torsion of the coil wire. In order to use successfully the helical coil spring as a high-performance shock isolator, its conceptual design must be reworked to include local damping other than material hysteresis.

Stranded Wire Spring (Fig. 5)
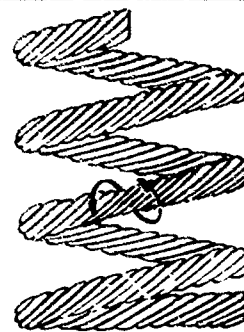
Fig. 5 - Stranded wire spring

The stranded wire spring is an adaptation of the helical coil spring and : a high-performance shock isolator. The helix of the spring must be opposite i direction to the helix of the strands, so that the strands bind together when the spring is compressed; this causes coulomb friction forces between wire strands and yields good local damping Its force-motion characteristics, however, have not been determined accurately.

Ring Spring (Fig. 6)
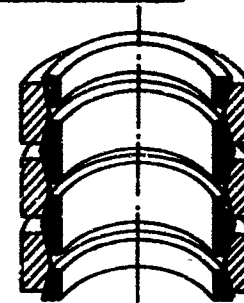
Fig. 6 - Ring spring

The ring spring, which depends on circumferential tension and compression of the rings for its working mechanism, has excellent local damping properties due to the friction between rings. The friction force is a function of displacement, but the ring spring has small displacement capabilities. This problem can be alleviated by stacking or splitting rings.

Belleville Spring (Fig. 7)
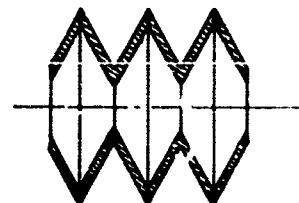
Fig. 7 - Belleville spring

The washers that compose the Belleville spring are stressed radially and circumferentially to resist motion. Many washers must be stacked to obtain large motions. A nonlinear spring, the Belleville spring can be designed so that a hard to soft spring constant desirable for shock isolation is obtained. Local damping can be introduced by parallel elements or contained fluids.

Liquid Spring (Fig. 8)
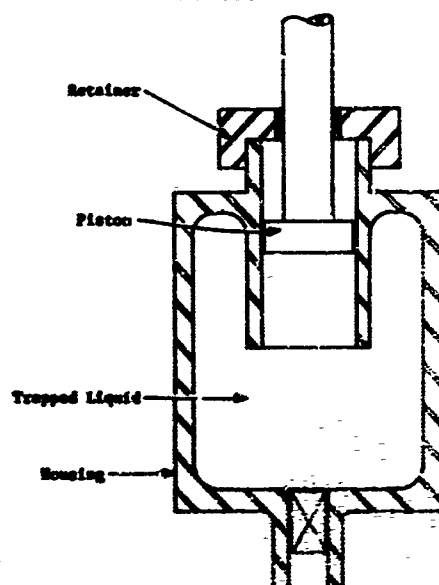
Fig. 8 - Liquid spring

This is probably one of the most desirable shock isolators since it works on compressibility of the fluid. In addition, its stroke is proportional to the volume of constrained fluid, its local damping is inherent and its wave propagation velocities are high. The isolator stroke can be long by designing it with a large, flexibly structured, fluid reservoir. This adds to the flexibility of the device.

Pneumatic Spring (Fig. 9)
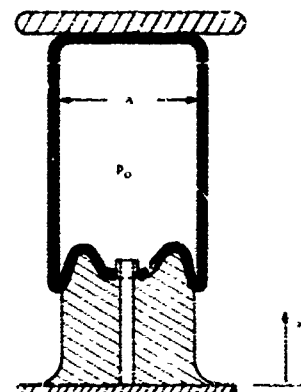
Fig. 9 · Pneumatic spring

The pneumatic spring has characteristics and a working mechanism similar to those of the liquid spring except for the lighter medium. It is an excellent high-performance shock isolator as commercially constructed, and its flexibility can be adjusted by variation of air pressure.

Elastomers (Fig. 10)
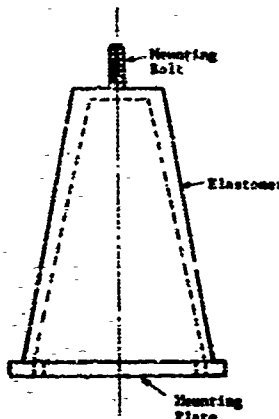
Fig. 10 - Solid elastomer

Elastomeric elements work on the basis of materials in compression or shear. They have tremendous possibilities for development into high-performance shock isolators because both materials and geometry can be synthesized. The synthesis of a material to give optimum local damping is feasible, and the generation of a long stroke capability through geometrical design is possible.

57

MODELING

Modeling of dynamic systems often receives too little attention in design and analysis. Specific fundamental research in this area has been rare; however, data and procedures on modeling are scattered throughout many texts and papers. Models are used to simulate a process or function of a machine numerically and experimentally and to verify the function of conceptual designs. In this paper, experimental models are utilized to determine the response or natural frequencies of a system and to determine the force-motion characteristics of isolation elements. Experimental models may range from full to subscale sizes. Analytical simulation models provide full-scale numerical simulation of a shock isolation system's natural frequencies and its response to environmental disturbances. Models for the previously described shock isolation elements are included in Appendix A.

Digital simulation of shock isolation systems is feasible provided the conceptual design of the system is modeled so that it properly simulates mass elasticity and damping. In the simulation process, modeling error and numerical error are important. Since good numerical techniques cannot overcome a bad model, modeling error must be controlled closely.

In modeling the elasticity of shock isolation systems, the relative flexibility of each component must be derived. Often this means expressing the flexibility of a component in terms of an equivalent length of beam, plate or other structural element. A force motion curve of a component is used to obtain basic data. Through comparison of component flexibilities, those of higher order magnitude can be modeled as rigid links, while those of very low order magnitude provide means of uncoupling portions of the models. During the process of modeling flexibility, mass distribution must be recognized. In mass modeling, component masses are compared with the total system mass. In modeling mass and elasticity, the information expected from a simulation must be known. Natural frequencies and mode shapes of linear systems are influenced by the relative distribution of mass and elasticity.

Damping modeling is difficult because the modeling method depends upon the way in which a particular damping force is related to motion. The following categories and their mathematical description have been offered by Reed [5].

- Viscous $\quad C_1 \frac{\partial x}{\partial t}$

- Velocity $\quad C_2 (\frac{\partial x}{\partial t})^2 \ (\text{sgn} \frac{\partial x}{\partial t})$

- Material-displacement $\quad C_3 |x| \ (\text{sgn} \frac{\partial x}{\partial t})$

- Material-viscoelastic $\quad C_4 |x| \ (\frac{\partial x}{\partial t})$

- Coulomb $\quad C_5$

where:

x is relative displacement, $\frac{\partial x}{\partial t}$ is relative velocity, and C_1 are constants.

Viscous and velocity damping forces are common in isolators; both are proportional to the relative velocity of the isolator structure. Viscous damping is common in fluid films and joints. High-rate phenomena typical of this application are described by velocity damping, which is proportional to the relative velocity of its internal structure to a power.

Linear elastic materials exhibit displacement damping properties such that the damping force is proportional to the stress history of the material. Displacement damping, in which the force is proportional to a coulomb friction coefficient and the displacement can result from such isolators as a ring spring, has been valuable in attenuating high-frequency surge waves. Nonlinear rubber-like materials exhibit viscoelastic behavior, in this case, the damping force is proportional to the deformation and its time derivative. This damping mechanism is found in elastomers, elastomer coatings, adhesives and viscoelastic structures. Coulomb friction energy dissipation, the final damping mechanism considered, usually occurs in conjunction with the other damping mechanisms.

If modal response techniques are utilized, damping data must be described as a function of system mode shapes. All damping mechanisms then must be described in the form of equivalent viscous damping. When a propagation analysis is performed, a more exact physical description (in terms of mathematical functions previously described) can be used. This latter method has distinct advantages because it yields more fundamental information and is not constrained to

linear analysis; therefore, it is recommended over modal methods. The design of high-performance shock isolation systems requires that isolator models with simulated distributed mass, damping and elasticity be used. High frequency effects are simulated and local response is obtained. The local behavior of the isolator determines its value to the system.

For system global response, simple lumped-parameter system models are adequate. Past experience with isolators and isolation systems has shown that a combination continuous-element, lumped-mass system provides the best prediction of the response of complicated dynamic systems. The system is modeled into stations, as shown in Fig. 11, in which the station is composed of a continuous
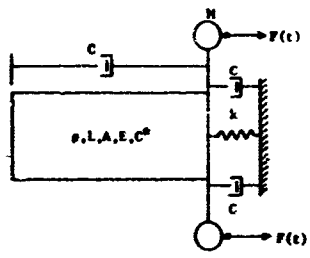
c = density
L = length
A = area
E = modulus of elasticity
C* = distributed damping
C = relative lumped, parallel damping
c = damping to ground
k = flexibility to ground
M = lumped mass
F(t) = environmental disturbance

Fig. 11 - Model station

element and lumped mass. External springs, dissipative elements and forcing functions are permitted at each mass station, along with relative lumped damping and continuous material damping. As many stations of this type as are needed, or wanted, to describe the isolation system properly are selected. This procedure for handling complex multidegree-of-freedom systems has been utilized by IITRI to good advantage in ship shafting systems[6]. The full utilization of these techniques, including modeling of distributed mass in awkward situations, is described.

Environmental disturbance modeling is dependent on the selected analytical technique. For modal analysis, the environmental disturbance is characterized by a Fourier series, and each harmonic term is utilized as an input function. The resulting response is obtained by summing the term-by-term response. For a propagation analysis, the input disturbance is divided into finite time increments, which are sized to the numerical

integration steps. The size of the time steps depends on proper description of the input disturbance, as well as stability of the numerical integration routine.

Experimental simulation of shock isolation system response usually requires scaled system models. The example problem of Appendix B shows the process of obtaining a scaled experimental model. The shock isolation system's isolators are designed from kinematic considerations. The dynamic characteristics of the shock isolator are retained as analytically derived scaling relationships (given in Appendix A). These relationships are obtained by making the systems equations of motion nondimensional [7]. The resulting nondimensional parameters are scaling relationships that retain important system parameters, even though small-scale models are used; for example, for a helical spring, the following relationships hold between the model, M and the prototype, P.

$$\pi_1 = \left(\frac{8ND^3 m_s \Omega^2}{Gd^4}\right)_M = \left(\frac{8ND^3 m_s \Omega^2}{Gd^4}\right)_P$$

$$\pi_2 = \left(\frac{M}{m_s}\right)_M = \left(\frac{M}{m_s}\right)_P$$

where

N = number of springs in coil

D = coil diameter

d = wire diameter

G = shear modulus

m_s = spring mass

Ω = natural frequency

M = isolated mass

For best results, the scaled model should not be distorted by having different system natural frequencies. Note that these two parameters ensure only scaled mass and elastic properties; for response scaling, damping and environmental parameters also must be considered. The example problem of Appendix B was experimentally modeled to use full-scale environmental input disturbances. A word of caution is in order, however, because it is not always possible to design scaled experimental models, i.e., sections may become too small to fabricate, the scaling of damping, (and thus response) parameters may not be compatible with other system requirements and the scale model size may not be compatible with available shock test machines or fixtures.

To analyze the response of shock isolators and shock-isolation systems at high loading rates, the fundamental force-motion characteristics of the isolator often must be determined experimentally. This involves determining stiffness and damping parameters as a function of rate, frequency and space. The discussion of damping showed how these forces may vary. It is important that experimental models to determine basic physical characteristics are designed so that individual forces can be separated according to their working mechanism: For example, in a liquid spring, the fluid damping force should be found independent of the fluid stiffness, or some method of analyzing the data to achieve this goal must be achieved. Data of this type are needed if analysis that predicts system dynamic response is to be obtained.

In conclusion, the design of experimental models depends on the distributed properties of the isolator, the kinematic properties of the shock isolation system, the input environmental disturbance and the available test machine or fixture.

ANALYSIS

The successful prediction of shock-isolation system and component response depends on the analytical technique used. After the problem has been modeled, and both the physical properties of the system and the input loading determined, an analytical technique must be chosen, depending on several aspects of the problem.

- linearity
- form of damping information
- mathematical form of loading
- detail of response

Insight into this problem has been gained from a SAMSO study and the resulting point of view was formed.

First, good shock isolators are long-stroke elements in which constant force is sought. This fact more or less implies nonlinearity of isolator damping and stiffness properties. The important fact is that linear analytical methods are seriously hampered by this restriction, which quickly rules out the use of modal response analytical techniques (since they are tied to the linear combination of weighted modal functions to derive the system's response). A propagation method of solution from initial value definition and system constraints provides a good response prediction because it is implicitly a transient analysis used to analyze a transient phenomenon; i.e., shock. In this case, finite-difference

or finite-element models of the system are utilized to perform the analysis, depending on the size of the model. Of course, solution stability must be considered in the selection of a finite-difference model. In highly nonlinear systems, this is a problem and may be more difficult than the solution of the problem. In linear systems, a simple relationship exists between the space and time step size, depending on the wave constant of the isolator. The second important consideration relates to the detail of the response -- a sufficiently small time and space interval must be used to predict high-frequency response effects. Finite-difference analysis works well if the system analytical model can be simplified to include a detailed description of the isolator and a gross description of the shock isolation system (Appendix B). Note that there is no way to analyze a high-performance shock isolation system with a single degree-of-freedom model because the high frequency response is not simulated.

In cases where the shock isolation system's global characteristics cannot be modeled as an isolator and rigid mass, a finite-element technique should be used. Care must be exercized in modeling because very stiff isolators may require a large number of finite elements to simulate local motion and may, therefore, exceed the storage capability of the digital computer. For linear systems, the first mode corresponds to the global response of the shock isolation system; the second and higher vibration modes correspond to the local response. The propagation methods of analysis reflect this result. The finite-difference [8] and finite-element [9] techniques ha have been well documented in the literature. Previous experience has shown that there is little utility in exact analytical methods or linear analysis in designing high-performance shock isolation systems because of the nonlinear transient nature of the shock phenomenon.

Over the past several years, IITRI has been engaged in extensive studies involving the optimum design of shock-isolation systems. Available optimization techniques[10], [11] are based on linear, nonlinear and dynamic programming, which optimize a system of interconnected mechanical elements subjected to a time-dependent input disturbance. During the course of these investigations, a technology has been developed that is capable of synthesizing shock-isolation elements, so that some measure of system performance (peak response acceleration of some critical component) is optimized subject to

60

prescribed response constraints on the ensuing motion (rattlespace constraints across the terminals of the isolator attachment points).

The scalar quantity Q is defined as the performance index, a number that measures the level of system performance (the peak mass acceleration). Optimization of the system then refers to the process of minimizing Q.

The capability of carrying out performance optimization from two different points of view is available: (1) by determining the force-time characteristics of the perfect isolation device, which results in a system with the best (lowest) possible Q, say Q^*; (2) by determining the isolator parameters (spring rates, damping coefficients) of a selected candidate isolator that leads to a system, which performs in near optimum fashion. The results of the first optimization problem provide the "optimum performance limit", which is the lowest possible performance index Q^* theoretically possible among all possible isolator devices for the system being considered. The results of the second optimization problem provide the near optimum performance Q_c^* of the candidate isolator for the same system considered in (1). The term "near-optimum" is used because the candidate's performance can never be better than the optimum value of the perfect isolator (i.e., $Q^* \leq Q_c^*$). The difference $\Delta Q = Q_c^* - Q^*$ provides the margin of improvement of the candidate isolation device compared to that of the perfect isolator. It must be emphasized that Q^* is used only as a guide for gauging the margin of improvement available; however, there may not be a passive device for which $\Delta Q = Q$.

In designing a high-performance shock isolation system, we must optimize concepts investigated during the study with respect to their own design parameters so that the near-optimum performance Q_c^* is obtained for each isolator. Further, the values of Q_c^* should be such that the comparison of each candidate to the optimum performance limit of the perfect isolator can be obtained. Such a comparison provides a means for judging the relative merits of the candidates to each other and to the best candidate from a theoretical point of view.

EXPERIMENTATION

The success of any design technique depends on the quality of the available data. In the design of high-performance shock isolation systems subject to high loading rates, the basic physical behavior of fluids and solids that form the isolator must be characterized at high rates if meaningful results are to be obtained. Characterization of the fundamental behavior of shock isolators is performed by high-strain-rate testing in order to obtain isolator damping and stiffness properties desirable in predicting the dynamic behavior of a system.

The second important function of experimentation is verification and experimental evaluation of the shock isolation system model and/or prototype global and local response. In performing a study of this type, external disturbance is simulated in a test machine or specially designed fixture. The experimental procedure for testing and/or evaluating high-performance shock isolation systems involves the following tasks.

- specifications
- procedures
- equipment selection
- instrumentation and calibration
- specimen design
- data reduction and analysis

The environmental shock disturbance is specified in terms of a force or motion-time curve (Fig. 1). If a scaled experiment is conducted, the scaled version of the shock pulse is specified. The rattlespace and mounting constraints are specified in conjunction with the test machine selection, as are the rates of loading and other parameters that affect the test machine. Finally, the expected local response is noted so that appropriate instrumentation can be selected.

Test procedures depend on the nature of the experiment. For force-motion characterization of isolators, a series of experiments is set up to obtain necessary design data. Damping and flexibility characteristics should be separated when possible. Usually several parameters are held constant to determine these characteristics or a series of different models are used to obtain a family of experimental results. The procedures used on verification tests are simple. The model or prototype is subjected to a known shock input disturbance, and the local and global response of the shock isolation system are observed and recorded.

The selection of a shock test machine depends on the test objective and the environment that is to be simulated.

61

The damage potential of a shock pulse simulated by a shock test machine is dependent on the nature of the equipment subjected to shock, as well as on the shape and intensity of the shock pulse. A comparative measure of the damage potential of shock pulses simulated by a shock testing machine can be obtained by comparing the response of the testing machine to that of a test standard. Shock spectra of the shock testing machine can be examined. Shock pulses applied to the test machine must be reproducible, and calibration of the shock test machine for a given test must be possible.

The electrohydraulic closed loop system shown in Fig. 12 provides a controlled environmental : ~ck pulse for the prescribed isolatu. The shock isolation

Fig. 12 - MTS closed loop system

system structure and the isolated item structure can be simulated within the machine to provide a complete experimental simulation. The input pulse is described digitally as a velocity-time curve. This type of machine is recommended for test because isolator local response can be observed. The machine also yields an experimental simulation of the total shock isolation system model and has the ability to monitor the dynamic behavior of the isolator, the structure of the isolated item or the structure of the shock isolation system.

For the experimental characterization of shock isolation elements, a high-rate open loop machine can be used to determine the desired force-motion characteristics. The closed loop type machine is needed to provide an experimental simulation if local effects are to be observed, because local effects depend on the shape of the input pulse. The semicontrolled machine that simulates the damage potential of an environment is useful only to check the global response of the isolated item.

Experimental instrumentation equipment is well developed and consists of three stages. At the first level, primary measurement is carried out by a transducer that converts mechanical motion into electrical signals. Transducers consist of strain gages and capacitance pickups which measure displacement, coils in a magnetic field which measure velocity and piezoelectric transducers which measure acceleration. At the second stage the signal from the transducer is prepared by secondary or modifying instruments for the third stage, display of the signal on a cathode ray oscilloscope paper, a recorder or magnetic tape. Modifying instruments attenuate, integrate, modify and condition the signal.

When possible, an actual isolator in its system environment should be tested. If the test is a destructive one, a replica of the actual device should be tested. If the available test machine is too small to allow a full-scale test, then a subscale model of the type previously mentioned of the prototype should be tested. Although it need not have the same appearance as the prototype, a scale model must behave in a manner similar to that of the prototype.

In scaling for shock response, the dynamic characteristics of the prototype must be preserved. Two types of scaling are possible, i.e., the use of either dimensional analysis or nondimensional mathematical system formulation. Dimensional analysis allows selection of pertinent system variables and, through algebraic procedures and fundamental units (time, mass, length, temperature), nondimensional scaling relationships can be determined. In the second scaling technique the dynamic behavior of a shock isolation system is described by differential equations of motion which are converted to a form that is independent of time, size, mass and temperature (nondimensional) by using defined nondimensional variables. The equations of motion are arranged algebraically so that the nondimensional scaling parameters can be selected from them. These

62

techniques are documented by Murphy [12] and Harris and Crede [7].

Test data may be produced in various forms, depending on the display or recording instrument used. The oscilloscope provides a visual display, and data can be recorded immediately and rejected (with a camera). Oscilloscopes are best for cases that involve scanning a large number of test parameters. Data can be recorded directly on a strip recorder or on magnetic tape. Regardless of the method used, shock response data usually must be reduced and analyzed, either by sight, mechanical means or electronic filtering.

The objectives sought in data reduction are the removal of all nonessential information, the retention of essential data and the abstraction of the history of some parameter (usually acceleration) in a concise and useful form. The characteristics of the function that best describes the data should be determined, and the reduced data should be manipulated so that it can be correlated with other significant parameters. The form of the reduced data can be displayed either in a frequency domain figure or the response domain figure.

Data reduction in the frequency domain is one of many sophisticated methods for harmonic analysis of data waveforms. Harmonic analysis is carried out by frequency separation, mechanically, by computer, or electronically; such data reduction in the frequency domain yields a shock spectrum. Data reduction in the response domain is confined to identification of response peak magnitudes and response wave shapes for given environmental shocks. Specific effects resulting from an input pulse can be found by varying the system's properties systematically. In linear systems, response domain data can be converted to frequency domain data, and vice versa with some loss in detail of the response domain data.

SUMMARY

The significant points reflecting the subject philosophy, procedures and techniques concerned with designing high-performance shock isolation systems are summarized.

- Environmental shock disturbances are expressed as motion or force-time curves.

- Design specifications are expressed in terms of system rattlespace and equipment fragility levels. Fragility

levels are given as acceleration response-time curves or peak acceleration response-frequency curves.

- Conceptual innovation of shock isolation systems requires ingenuity and a fundamental knowledge of dynamic systems.

- Shock isolation system concept innovation should have kinematic emphasis. Isolators must possess a long stroke capability, a facility to attenuate high-frequency environmental disturbances and a composition that controls the generation of internal stress waves.

- While simple models suffice for kinematic considerations, flexible, massless spring models are inadequate to kinetically model high-performance shock isolators.

- Propagation methods that begin with initial conditions and use finite-differences or finite-elements are recommended to analytically simulate response.

- Scaled experimental models are acceptable; however, they should be dynamically scaled, using system equations of motion.

- Isolator force-motion characteristics should be obtained experimentally.

- Shock isolation system designs should be verified experimentally under simulated conditions and environments.

REFERENCES

1. Eshleman, R. L. and Kutscha, D.,
"Shock Isolation Elements Testing
for High Input Loadings", Vol. III,
Mechanical Shock Isolation Ele-
ments, SAMSO, TR 69-1118, June,
1969.

2. Ostrem, F. E. and Rumerman, M. L.,
"Transportation and Handling Shock
and Vibration Environmental Cri-
teria", Gen. Am. Res. Div., Con-
tract NAS 8-11451, 1965.

3. Eubanks, R. A. and Juskie, B. R.,
"Shock Hardening of Equipment",
Shock. Vib. Assoc, Environ. Bull.
No. 32, Part III, Dec. 1963,
pp 23-47.

4. Morrow, Charles T., "Force-Control-
led or Free Suspension Shock Tests",
J. Environ. Sci., 13(2): pp 22-24,
Mar.-Apr. 1970.

5. Reed, R. R., "Analysis of Struc-
tural Response with Different Forms
of Damping", NASA TN D-3861, 1967.

6. Eshleman, R. L., "Procedure for
Calculating the Natural Frequen-
cies of Shafting Systems", IITRI
Report K6086, Naval Ship Systems
Command, AD 811 785.

7. Harris, Cyril H. and Crede, Charles,
"Shock and Vibration Handbook",
Vol. 2, Data Analysis, Testing and
Method of Control, p 27-1, McGraw
Hill Book Co. Inc., 1961.

8. Crandall, Stephen H., "Engineering
Analysis", McGraw Hill Book Co.,
New York, N. Y., 1956.

9. Zienkiewicz, O. C. and Cheung, Y.K.,
"The Finite Element Method in
Structural and Continuum Mech-
anics", McGraw Hill Book Co.,
New York, N. Y., 1967.

10. Liber, T. and Sevin, E., "Optimal
Shock Isolation Synthesis", Shock
Vib. Bull. No. 35, Part V, 1966.

11. Sevin, E.; Pilkey, W.; and
Kalinowski, A., "Optimum Perfor-
mance Bounds and Synthesis of Dy-
namic Systems, Computational
Approaches in Applied Mechanics",
ASME, 1969.

12. Murphy, G., "Similitude in En-
gineering", The Ronald Press,
New York, N. Y., 1950.

13. Eshleman, R. L. and Rao, P. N.,
"The Response of Mechanical Shock
Isolation Elements to High-Rate
Input Loading", Shock Vib. Bull.
No. 40, Part 5, Dec. 1969.

NOMENCLATURE

A = cross sectional area

A_i = cross sectional area of inner ring

A_o = cross sectional area of outer ring

a = Belleville spring geometric constant

b = Belleville spring geometric constant

C = Belleville spring geometric constant

d = spring wire diameter

D = spring coil diameter

E = modulus of elasticity

E_1 = storage modulus

E_2 = loss modulus

G = spring shear modulus

h = Belleville spring free height

I_B = second area moment of Belleville spring

k = gas constant

ℓ = spring length

m_s = spring mass

M = lumped mass

N = number of spring coils

n = number of spring strands, number of rings

P_o = pressure

r_m = mean radius of ring spring

s = local space coordinate

t = Belleville spring thickness

u = local displacement

x = lumped mass displacement

y = environmental displacement

α = angle of taper of conical surfaces

γ = gas constant

Δ = fluid bulk modulus

μ = friction coefficient, fluid viscosity

ν = Poisson's ratio

ζ = fluid viscosity

ρ = fluid density

Ω = system natural frequency

$$\frac{Gd^4}{8ND^3}\frac{\partial^2 u}{\partial s^2} = \frac{m_s}{\ell}\frac{\partial^2 u}{\partial t^2}$$

EQUATION OF MOTION

$$u(o,t) = y(t)$$

$$\frac{-Gd^4}{8ND^3}\frac{\partial u(\ell,t)}{\partial s} = M\frac{\partial^2 u(\ell,t)}{\partial t^2}$$

BOUNDARY CONDITIONS

$$\tau_1 = \frac{8ND^3 m_s \Omega^2}{G d^4}$$

$$\tau_2 = \frac{M}{m_s}$$

DYNAMIC SCALING PARAMETERS
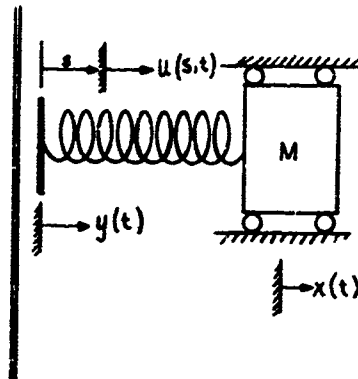
Fig. A.1 - Isolation system with helical spring

$$\frac{K^* n G d^4}{8NC^3}\frac{\partial^2 u}{\partial s^2} = \frac{m_s}{\ell}\frac{\partial^2 u}{\partial t^2}$$

EQUATION OF MOTION

$$u(o,t) = y(t)$$

$$\frac{-K^* n G d^4}{8ND^3}\frac{\partial u(\ell,t)}{\partial s} = M\frac{\partial^2 u(\ell,t)}{\partial t^2}$$

BOUNDARY CONDITIONS

$$\tau_1 = \frac{8ND^3 m_s \Omega^2}{G d^4}$$

$$\tau_2 = \frac{M}{m_s}$$

DYNAMIC SCALING PARAMETERS

*K = 1.05 for three-strand spring
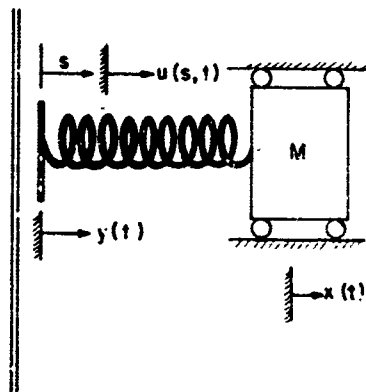
Fig. A.2 - Isolation system with stranded wire spring
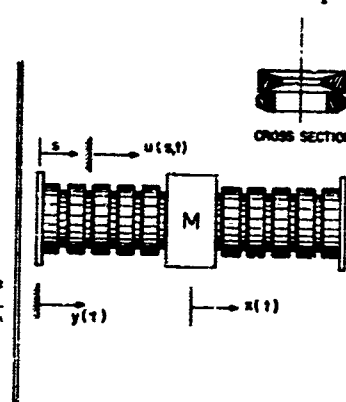
Fig. A.3 - Isolation system with ring spring

$$\frac{kh^4}{(1-\nu^2)ca^2}\left\{\frac{c^3}{h^3}+\frac{c}{h}\left(1+\frac{3u}{\partial c}-\frac{3}{4}\left(\frac{\partial u}{\partial c+}\right)^2\right)\right\}\frac{\partial^2 u}{\partial s^2}=$$

$$\frac{m\gamma}{c}\frac{\partial^2 u}{\partial t^2}+\frac{I_B}{(a-b)^2}\frac{\partial^3 u}{\partial s\partial t^2}$$

EQUATION OF MOTION

$$\frac{kh^4}{(1-\nu^2)ca^2}\frac{\partial u(s,t)}{\partial s}\left[\frac{c^3}{h^3}+\frac{c}{h}\left(1-\frac{3}{4}\frac{\partial u(s,t)}{\partial s}\right)+\frac{3}{4}\frac{\partial u(s,t)}{\partial s}\right]=$$

$$M\frac{\partial^2 u(s,t)}{\partial t^2}$$

BOUNDARY CONDITION

$$\pi_1=\frac{m_B^2 h^2 ca^2(1-\nu^2)}{kh^3}\qquad \pi_3=\frac{M}{m_B h}$$

$$\pi_2=\frac{I_B}{m m_B(a-b)^2}\qquad \pi_4=\frac{c}{h}$$

DYNAMIC SCALING PARAMETERS
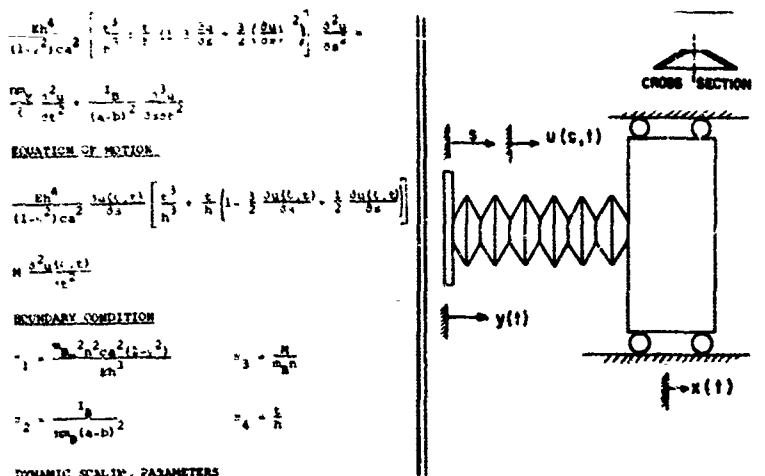
Fig. A.4 - Isolation system with Belleville spring

$$+\frac{\partial^2 u}{\partial t^2}=c\frac{\partial^2 u}{\partial s^2}+\frac{4}{3}\mu\frac{\partial^3 u}{\partial s^2\partial t}$$

EQUATION OF MOTION

$$u(o,t)=y(t)$$

$$A\cdot\frac{\partial u}{\partial s}=M\frac{\partial^2 u(s,t)}{\partial t^2}$$

BOUNDARY CONDITIONS

$$\pi_1=\frac{A l_o^2}{c}$$

$$\pi_2=\frac{M}{m_l}$$

$$\pi_3=\frac{\mu A}{c}$$

DYNAMIC SCALING PARAMETERS
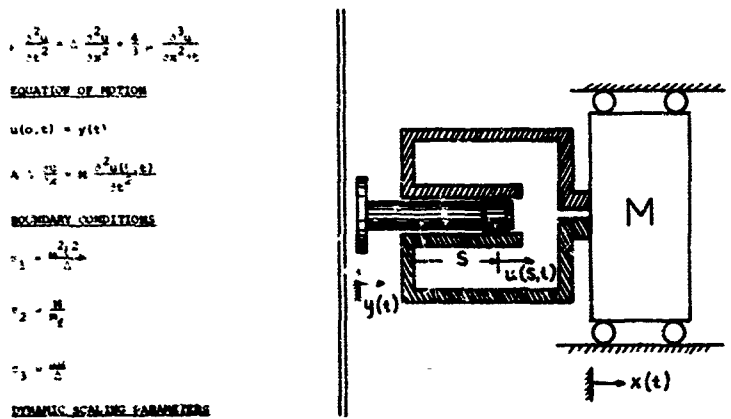
Fig. A.5 - Isolation system with liquid spring

$$\frac{\partial^2 u}{\partial t^2}=kr_f^2\frac{\partial^2 u}{\partial s^2}+\left(\frac{4}{3}\mu+\xi\right)\frac{\partial^3 u}{\partial s^2\partial t}$$

EQUATION OF MOTION

$$u(o,t)=y(t)$$

$$Akr_f^2\frac{\partial u}{\partial s}=M\frac{\partial^2 u(s,t)}{\partial t^2}$$

BOUNDARY CONDITIONS

$$\pi_1=\frac{\mu l_f^2}{kr_f^2-A}$$

$$\pi_2=\frac{M}{c_o}$$

$$\pi_3=\frac{\frac{4}{3}\mu+\xi}{kr_f^2}$$

DYNAMIC SCALING PARAMETERS
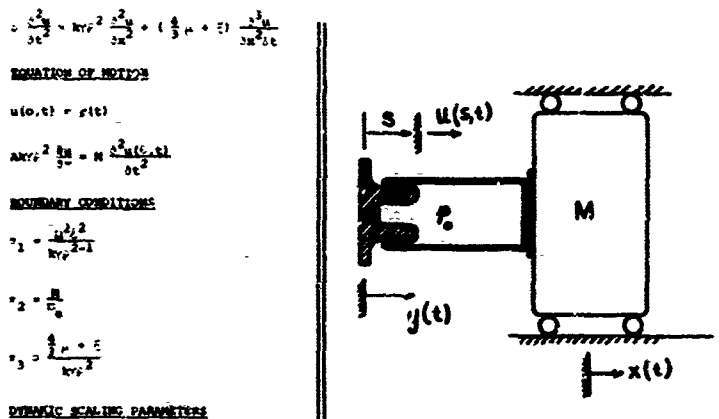
Fig. A.6 - Isolation system with pneumatic spring

66
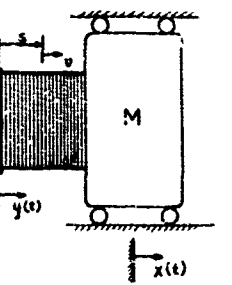
Fig. A.7 - Isolation system with solid elastomer

SYSTEM DESIGN PROCEDURE: A SAMPLE PROBLEM

The following design tasks were completed to evolve test elements, local response predicting and a shock isolation system.

- Full-scale prototype design
- Scaling relationship development
- Subscale test model design
- Local analysis
- Model testing

A full-scale prototype was conceptually designed for a shock isolator element (helical spring) to provide a basis for scaling test elements. This design was evolved through the use of typical facility data, shock isolator characteristics and the ISOLATOR computer program (a single degree-of-freedom model that accepts nonlinear, damped isolation devices). Dynamic scaling relationships were evolved for the helical spring from the mathematical models of the pertinent shock isolation system. The scaling relationships, the prototype designs, the test machine characteristics and the element stroke-to-length capability were considered in the design of the subscale test model. A method for local analysis of the tested helical spring within the MTS test facility was evolved. Natural frequency calculation and response analysis were conducted on the test element.

PROTOTYPE ELEMENT DESIGN

The schematic design of a representative full-scale element which could be used in a typical missile shock isolation system is achieved. This example problem is not concerned with detail designs of isolators, joints, attachments, subassembly couplings and all the details required in the construction of an actual system. It must be emphasized that prototype elements are evolved to provide a realistic basis for model design. The schematic gross design is obtained through the use of a typical shock pulse, gross missile -- silo geometry and missile fragility levels.

- Physical Constraints

The missile and silo diameters are specified. The available rattlespace in either direction is obtained.

- Material Constraints

The shock isolation element is designed such that the stresses induced during stroking of the element do not exceed the elastic limit of the material. All the elements must exhibit total recovery to insure that the system is viable for succeeding shock pulses.

- Design Criterion and Constraint

The element motion is constrained to meet facility rattlespace requirements. The design criterion is the fragility level of equipment specified in gravities of acceleration. This means that the element must have a spring and damping rate such that the applied pulse will cause a missile response motion of less than the specified acceleration.

The problems associated with kinematic nonlinearities were analyzed. These arise from the large deformation of the helical spring and the fact that the motions are not always axial with it.

The indeterminate input motion direction and influence of large displacements are significant problems to spring selection. The first problem is illustrated in Fig. B.1 where the input motion (Fig. 1) can have any arbitrary

(a) Effect of Phase Angle Between Input Motion and Isolator

(b) Effect of Large Deflection
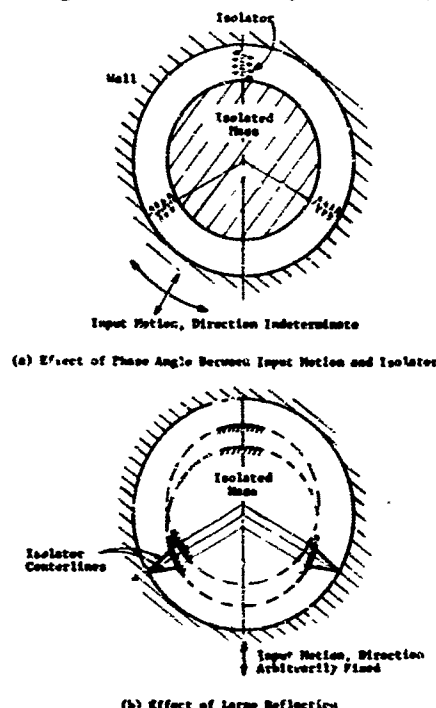
Fig. B.1 - Combined effects which cause system stiffness variation

direction with respect to a given isolator. Since mechanical isolators cannot completely "fill-up" the rattlespace, some variation of effective stiffness is naturally expected for different directions of input. Initially, the number of springs per array or layer was set at three because

- The least practicable number of isolators are desirable,

- Closer analogy is thereby retained between the full-scale and model isolators

- Calculation of effective spring stiffness is simplified

- Such an arrangement gives the least excursion of effective spring stiffness for small displacements.

It was found that small displacements cannot be assumed; therefore, large displacements became the second problem, as shown in Fig. B.1(b). Actually, the two effects are not separate but act together to cause variation of effective spring stiffness. Note that Fig. B.1(b) implies that both ends of the springs will need a pivot arrangement. The large displacement effect produces stiffness variations as a function of displacement as well as input pulse phase angle. The severity of the situation is illustrated in Fig. B.2 for a symmetrical array of three spring isolators; this figure takes into account the previously mentioned combined effects which cause system stiffness variation. The significance of the two curves in Fig. B.2 is that they represent effective stiffness at the two extremes of input displacement (points 1 and 2 of the pulse respectively).

For design, the situation can be significantly improved from that of Fig. B.2, which shows the equivalent stiffness of a three spring array. Actually, many such spring arrays or layers will comprise the full isolation system where adjacent layers of isolators (or additional ones) will smooth out effective stiffness variation. The improvement resulting from this type of procedure is given in Fig. B.3 where both amplitude and period of effective stiffness variation are seen to decrease as the total number of springs is increased. A very slight nonlinearity of stiffness with displacement still exists, as is evidenced by the two sets of curves k_1 and k_2; this variation is caused by the somewhat unequal relative motion extremes of the missile silo system about its neutral position.

The stiffness nonlinearity which remains due to the presence of input pulse phase angles is tolerable even for the relatively small total number of springs shown in Fig. B.3. As more springs are introduced, the amplitude and period of the effective stiffness "ripple" decrease.

Figures B.2 and B.3 give a constant limiting value of effective system stiffness or the effective number of springs for isolators radially arranged.

$$k_{ave} = \frac{1.89}{\text{per 3 total springs}} \quad \text{(Fig. B.2)}$$

$$k_{ave} = \frac{3.84}{\text{per 6 total springs}} =$$

$$\frac{1.92}{\text{per 3 total springs}} \quad \text{(Fig. B.3)}$$

$$k_{ave} = \frac{7.68}{\text{per 12 total springs}} =$$

$$\frac{1.92}{\text{per 3 total springs}} \quad \text{(Fig. B.3)}$$

The effective number of springs per symmetrical spring array is approximately two.

The prototype shock isolation element is analytically designed using a single degree-of-freedom model. In more complex systems, multidegree-of-freedom models are used. The effective allowable spring rate k^* is obtained by determining what spring will yield a global response less than the allowable rattlespace and fragility levels for the specified input pulse. Material damping was used to obtain the maximum acceleration response results of Fig. B.4. The actual spring rate of the prototype element is equal to $3k^*/2mn$ where m is the number of layers in the silo and n is the number of springs in each layer. Figure B.5 shows the design chart used to select the spring sizes.

SCALING RELATIONSHIP DEVELOPMENT AND SUBSCALE TEST MODEL DESIGN

The development of scaling relationships by using nondimensionalized equations of motion for the shock isolation system was explained in the experimentation section of this paper. The resulting scaling parameters for typical shock isolators is given in Appendix A. For the helical spring in this design example, the following relationships were
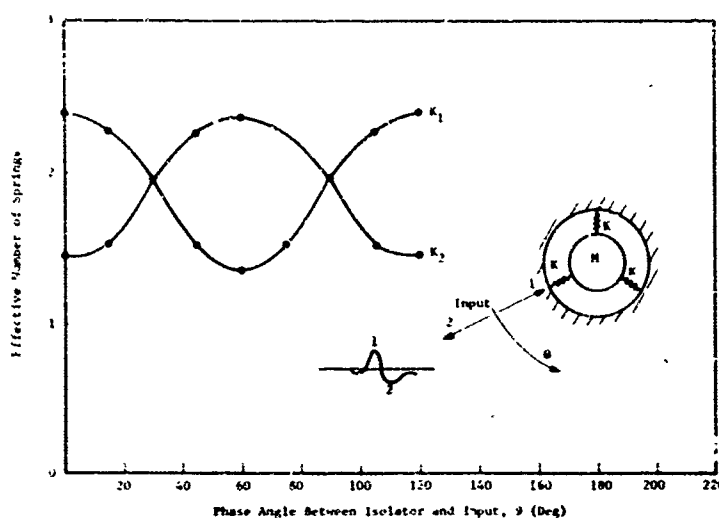
**Fig. B.2 - Effective number of springs, variation resulting
from input phase angle and large displacements
for an array of three springs**
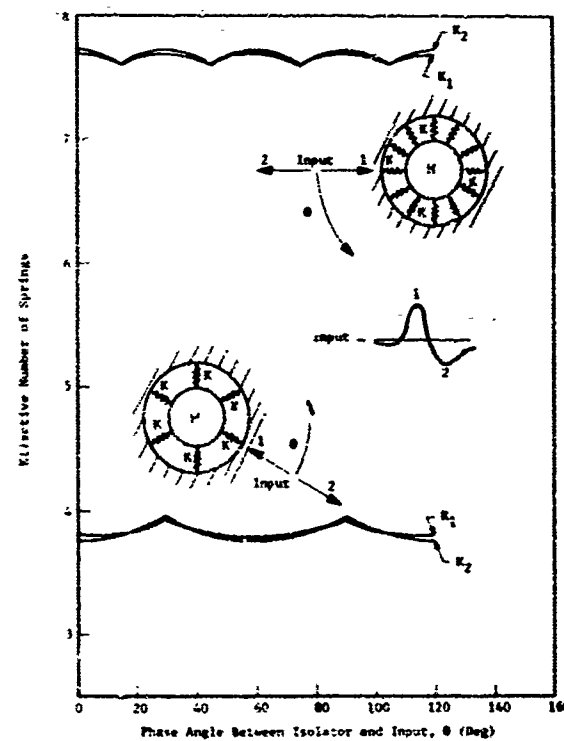
**Fig. B.3 - Effective number of springs, variation
resulting from large displacements and
input phase angle for two spring arrays**

70
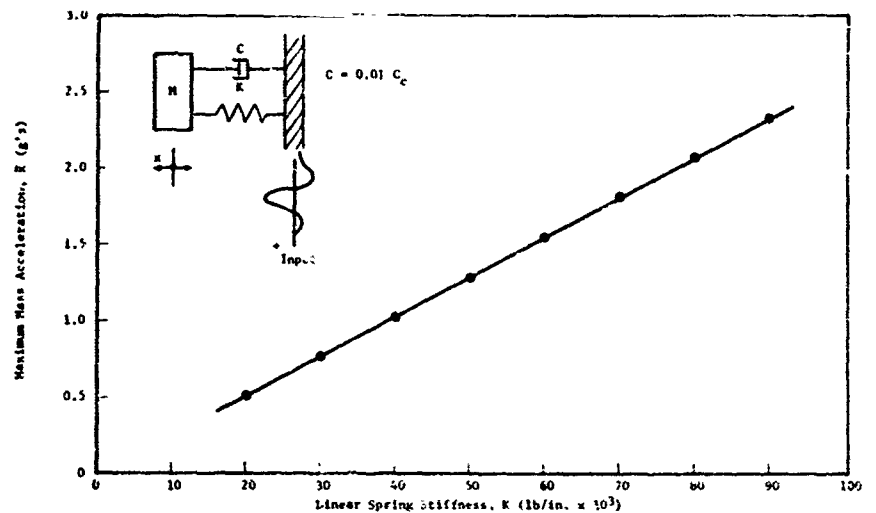
Fig. B.4 - Maximum mass acceleration as a function
of isolator system stiffness

Fig. B.5 - Full-scale helical coil spring analysis

71
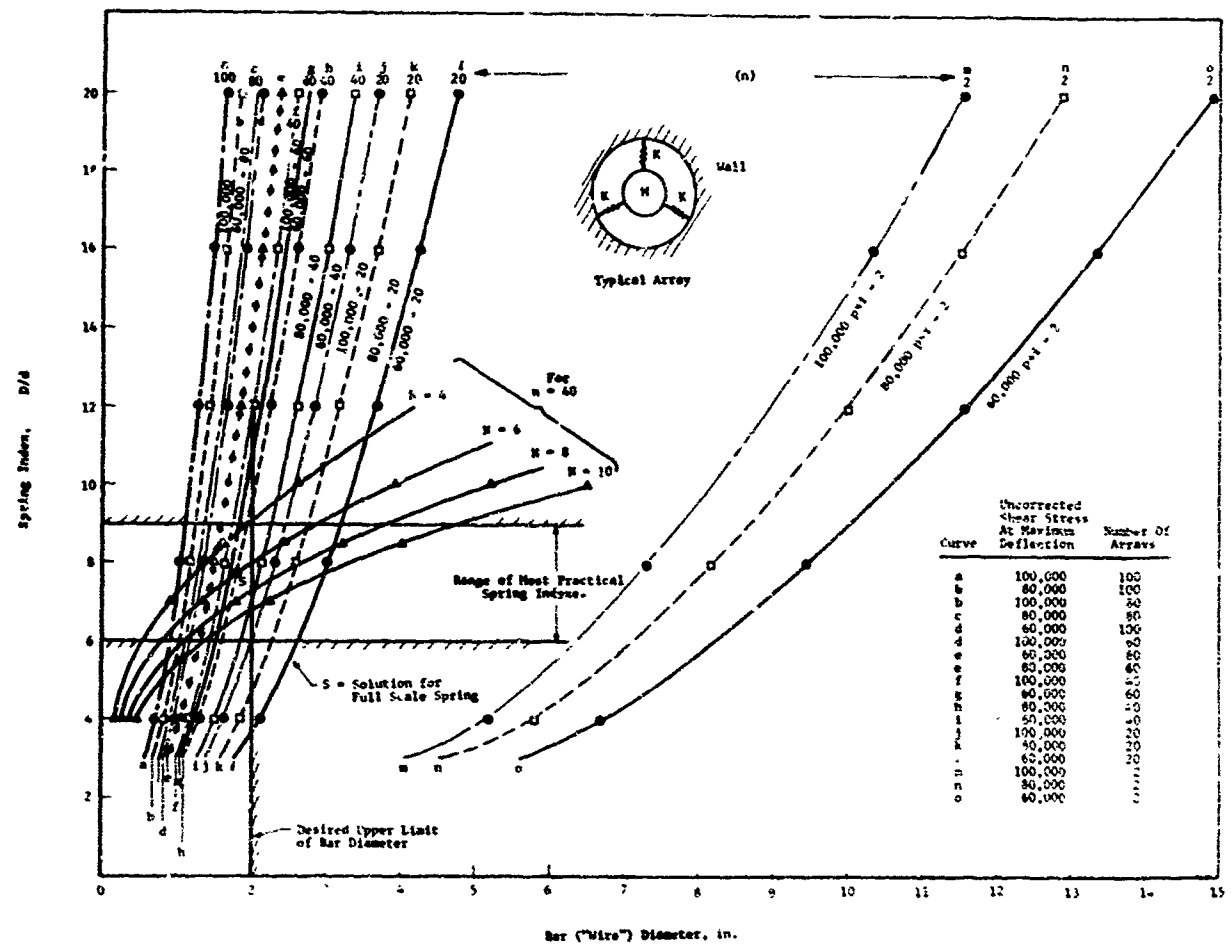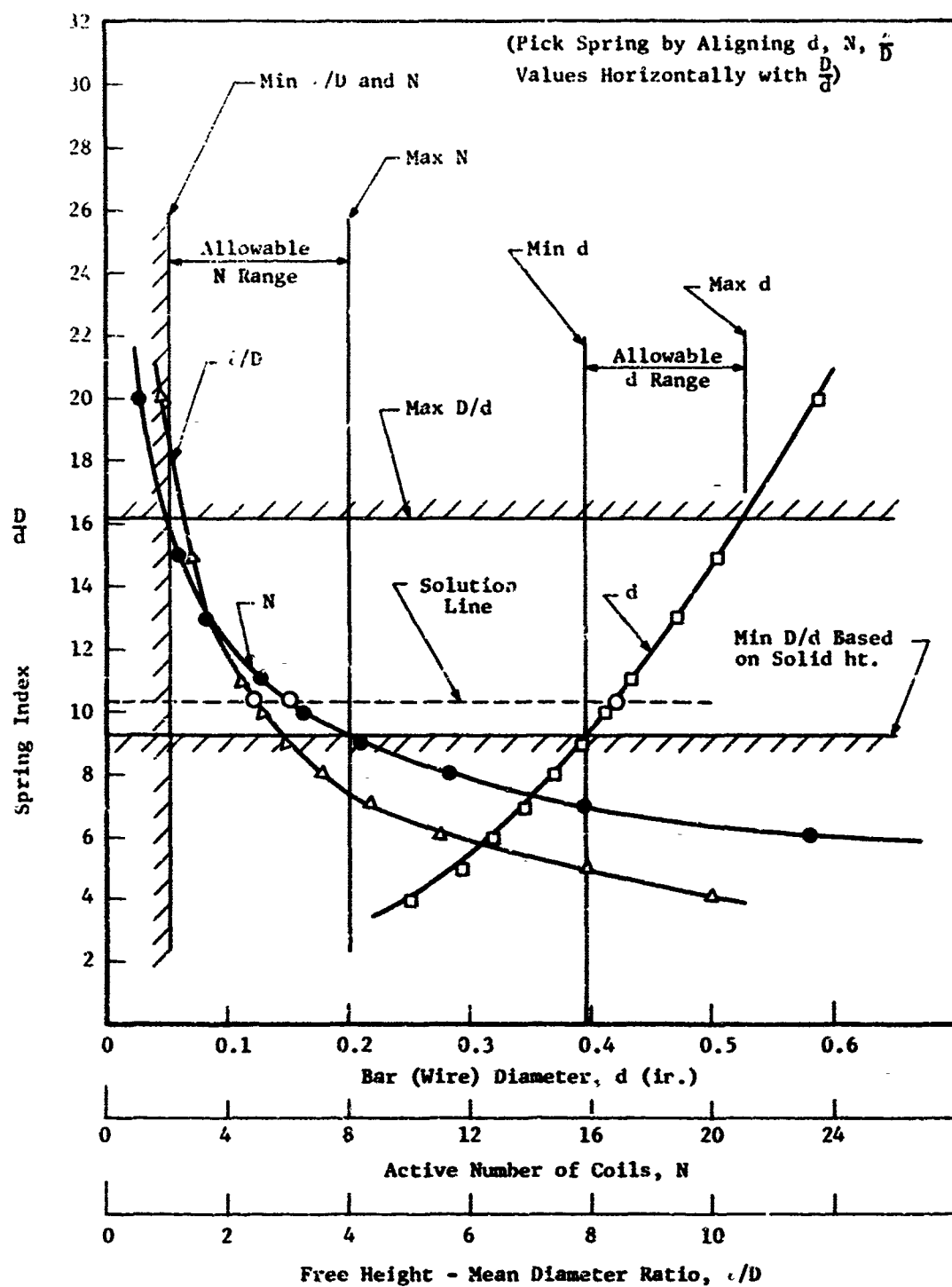
Fig. B.6 - Helical coil spring design chart

utilized because they characterize the important isolator dynamic properties.

$$\left(\frac{M}{m_s}\right)_{prototype} = \left(\frac{M}{m_s}\right)_{model} \quad \text{--- mass}$$

where

M is the isolated mass (missile)

$$m_s = \frac{\pi^2 D d^2 \rho N}{4}\left[1 + \frac{4\ell^2}{N^2 D^2}\right] \quad \text{spring mass}$$

$$\left(\frac{8ND^3 m_s \Omega^2}{Gd^4}\right)_p = \left(\frac{8ND^3 m_s \Omega^2}{Gd^4}\right)_M \quad \text{---frequency}$$

$$\left[\frac{d\ell}{ND^2}\left(\frac{\frac{4D}{d}-1}{4\frac{D}{d}-4} + \frac{0.615d}{D}\right)\right]_M =$$

$$\left[\frac{d\ell}{ND^2}\left(\frac{\frac{4D}{d}-1}{4\frac{D}{d}-4} + \frac{0.615d}{D}\right)\right]_p \quad \begin{array}{l}\text{---spring}\\ \text{stress and}\\ \text{local damp-}\\ \text{ing}\end{array}$$

Figure B.6 shows the design chart for the model helical coil spring of Table B.1, which was designed to be used in an existing test facility. A single degree-of-freedom model global analysis was run on this spring to find that it has response characteristics similar to those of the prototype.

LOCAL ANALYSIS AND MODEL TESTING

The local analysis and model testing of a shock isolation system are difficult subjects. These topics were covered in detail for the subject helical coil spring in Ref. [13]. The global response to the input pulse (Fig. 1) obtained by analysis of a single degree-of-freedom system is shown in Fig. B.7 and its comparison to the model experiment is shown in Fig. B.8. The local analytical response using a continuous parameter model of the isolator using a finite-difference technique is shown in Fig. B.9 and its comparison to experiment is shown in Fig. B.10. These experiments were made on the MTS machine shown in Fig. 12. The results of these analyses show (1) that the continuous parameter model is needed to simulate high frequency effects, and (2) that the helical coil spring needs additional damping to qualify as a high performance isolator with low local response.

Table B.1

Model Helical Spring Data

$\frac{D}{d} = 10.3$

$d = 0.420$ in.

$N = 6$

$K' = 6$

$S_s = 94,200$ psi

$C = 1.14$

$S_s' = CS_s = 107,300$ psi

$OD = 4.74$ in.

$\ell = 10.5$

$\frac{\ell}{D} = 2.45$

$SH = 2.52$ in.

Total Weight $= 4.24$ lb

Clearance when most compressed $= 0.180$ in./coil
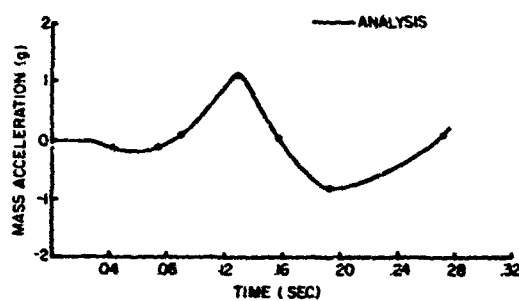
Fig. B.7 - Analytical response of a helical spring-
mass system subject to high-rate input
loading (lumped parameter spring model)
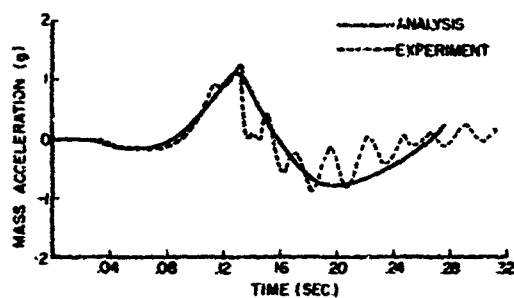
Fig. B.8 - Comparison of analytical and experimental
response results for a helical spring-mass
system subject to high-rate input loading
(lumped parameter analytical model).
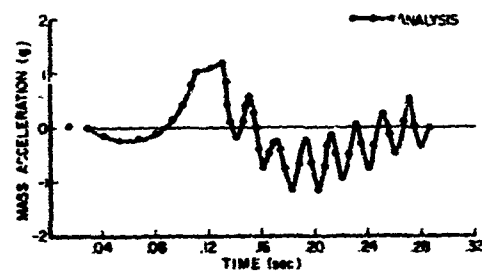
Fig. B.9 - Analytical response of a helical spring-
mass system subject to high-rate input
loading (continuous parameter spring model)
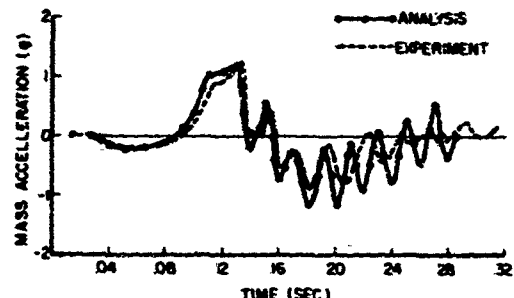
Fig. B.10 - Comparison of analytical and experimental
response results for a helical spring-mass
system subject to high-rate input loading
(continuous parameter analytical model)

74

Mr. Grant (The Boeing Company): You talked about high frequencies in the systems and the capability to analyze them. I presume that what you are saying is that you can analyze accurately at least the first surge mode of the spring, is that correct?

Mr. Eshleman: Yes.

Mr. Grant: Would you care to predict the accuracy of your analysis for the higher surge modes since if that spring is accelerated fast enough the other surge modes will also participate?

Mr. Eshleman: One thing that I did not mention that is important is that there is a balance between the flexibility of the spring and the wave propagation problem, because if you load the spring at too high a rate there is a discontinuity like a shock wave, and you do not want that at all. This analysis technique has the advantage that one obtains all of the frequency components. This is not a modal analysis. Here you see basically two modes in the response, the first mode and the second mode. You do not see much of the higher modes. Perhaps my model was not sensitive enough to pick up any of the higher modes or maybe they were not induced from that rather simple step function or pulse shape. But this type of analysis has the capability to take into account all of the modes, even though it is not a modal analysis.

Mr. Grant: The next question is about the mass scaling. Obviously it has an influence on the second mode of the system. You only applied your scaling relationship to the fundamental kinematical problem rather than to the higher modes of the system. Is that correct?

Mr. Eshleman: The mass scaling, in this simple example, only referred to the isolator itself. In a more complex system one should describe the whole system mathematically in terms of a lumped parameter system, and there you would again take into account the other masses in the system. It turned out that this one was so simple that the isolator was the only important mass except for the isolated mass.

Mr. Grant: Then you would depart there from wave theory as you have used it?

Mr. Eshleman: Yes.

Mr. Eckblad (The Boeing Company): In your presentation you stated that at high frequencies the finite difference method did not work so well and that you applied the finite element technique which seemed to work better for your high frequency analysis. Would you elaborate on that?

Mr. Eshleman: I did not mean that it did not work well. It is impractical because it takes too much computer space. A simple problem like this took up the storage of a 7094 computer. I do not know how many bits it was but it is impractical from a point of view of computer storage.

Mr. Eckblad: How did you get around this with the finite element technique?

Mr. Eshleman: I did not actually work this problem with the finite element technique but it seems to me if one were to use the finite element technique one would be able to do a better job of modelling for analysis than is possible with the finite difference technique.

Mr. Eckblad: What happens when you analyze a complex structure, when you get away from the simple rod where you feed into plates and have to transfer to other complex structures? Does this method also work conveniently for that?

Mr. Eshleman: Yes.

Mr. Forkois, NRL: What happens when you have two spring systems such as a soft spring and a stiff spring in series? There are many isolation systems which act as vibration isolators and also act as shock isolators.

Mr. Eshleman: I do not think that problem would be very difficult to handle. I think you could model it fairly easily. I really do not think that would be a problem because it is small enough. The problem is the size of the computer.

75

ELASTIC WAVE PROPAGATION IN A HELICAL COIL WITH VARYING CURVATURE
AND ITS APPLICATION AS AN IMPACT LOAD DISPERSER

Nam P. Suh
Department of Mechanical Engineering
Massachusetts Institute of Technology
Cambridge, Massachusetts 02139

Elastic stress pulse propagation in a helical coil with varying radius of curvature is experimentally investigated by loading the coil tangentially as a means of effectively dispersing impact loads to lower their amplitudes. It is shown that the stress pulse decomposes into many components, with the high frequency components propagating faster than the low frequency components. The pulse disperses faster when the helical coil is loaded at the smaller end than when it is loaded at the larger end. The coil with the smallest radius of curvature acts as an acoustic filter in that the amplitudes of the waves passing through this coil do not change afterwards. The experimental results are discussed qualitatively in terms of a theoretical analysis of dispersion characteristics. The radius of the cross-section influences the phase and group velocities in the range considered in this paper.

INTRODUCTION

In a previous paper[1*] the writer discussed the applicability of helical coils as impact load dispersers by considering the elastic stress pulse propagation in a tangentially loaded helical coil of constant curvature. In this paper the effect of varying curvature is investigated. This paper is based on the results obtained in a continuing effort to find effective means of dispersing impact loads so that high amplitude impact loads can be degenerated into low amplitude waves.

Helical coils are usually loaded along the axis of the helix by compressing the coil. In this case, the generated distortional wave propagates almost without any dispersion. On the other hand, if the helical coil is loaded tangentially, the stress pulse continually disperses because of the continuous reflection of the pulse at the lateral surface of the coil. This effect is quite significant in solids since an incident dilational or distortional wave may generate both types of waves upon reflection, except when the incident angle of the distortion wave exceeds a certain critical limit. Therefore, a helical coil, especially one with a varying radius of curvature, may be useful as an impact load disperser.

Vibration and wave propagation in curved rods were investigated at the turn of this century[2-4] for inextensible rods. Philipson[5] extended the work by including the extension of the locus of centroids. Recently, stress pulse dispersion in curved rods was also investigated by Britton and Langley[6] for constant curvature and by Wittrick[7] for helices.

The use of tangentially loaded helical coils as shock dispersers and acoustic filters has not been considered before. The experimental results presented in this paper are new. The exact theoretical analysis of the experiment is difficult. The theoretical analysis presented in this paper is for the case of propagation of an infinite train of sinusoidal waves in an infinite helix of a constant radius. Although the theoretical treatment is not for the varying curvature case, the theoretical results are presented here since some of the experimental results can be explained qualitatively by the theoretical results. The theoretical results presented in this paper differ from the previous results[1] in that the previous analysis neglected the effect of torsion.

---

*Numbers refer to references at end of paper

LIST OF SYMBOLS

A_1, A_2, etc.	Parameters defined in text
A	Cross sectional area
a	Projected radius at any θ
a_0	The largest projected radius of of curvature at $\theta = 0$
B	Rotation function defined in text
C	Torsional rigidity
c	Elevation constant $= h/2\pi$
C_g	Group velocity
C_p	Phase velocity
C_0	Bar velocity $= (E/\rho)^{1/2}$
C_s	Shear wave velocity $= (G/\rho)^{1/2}$
D_1, D_2, etc.	Parameter defined in text
E	Young's modulus
F_x, F_y	Force acting on the cross-section of the coil along x_0 and y_0, respectively
f	Constant related to the rate of curvature change
F_1, F_2, etc.	Parameter defined in text.
G	Shear modulus
H_1, H_2, etc.	Parameter defined in text
h	Pitch
I_x, I_y, I_z	Moments of inertia of mass per unit length about x_0, y_0, and z_0, respectively
i, j, k	Unit vectors along X, Y, Z, respectively
J_x, J_y	Moments of inertia of the cross-sectional area about x_0 and y_0, respectively
k	Wave number
m	Mass per unit length of the coil
p	Angular frequency
R	Radius of principal curvature
r	Radius vector in the (X,Y,Z) coordinate system
S_0	Length measured along the length of the unstrained coil
t	Time
U,V,W,	Displacement function defined in text
u,v,w	Displacements along the x_0, y_0, and z_0 directions respectively
X,Y,Z	Axes of a fixed coordinate system
x_0, y_0, z_0	Axes of a moving coordinate system
β	Rotation of the cross-section about z_0
γ	Radius of gyration about x_0 and y_0
γ_z	Radius of gyration about z_0
θ	Angle measured counterclockwise from the X-axis to the position vector projected on the X-Y plane
θ_0	Characteristic angle
λ	Wavelength
ν	Poisson's ratio
σ	Radius of torsion
τ_0	Torsion

I. EXPERIMENTS

a) Experimental Arrangements

Figure 1 shows the helical coil with varying radius of curvature, which was made from a commercially pure aluminum rod of 1/2 inch diameter. The internal diameter of the coil was 8 inches at the larger end and 2 inches at the smaller end. The coil had about 7 1/2 turns and the pitch was about 1 inch. The coils had straight ends, at one of which a hammer was dropped from a known height to generate the stress pulse. The length of the straight portion of the coil was made much larger than the length of the hammer in order to make certain that the wave reflection from the curved section of the coil would not interfere with the generation of the wave at the impact end. Plastic deformation of the coil at the impact end was prevented by placing a 1.5 inch long spacer made of a hard aluminum alloy with the same mechanical impedance as a commercially pure aluminum. The ends of the coil and the spacer were carefully lapped for complete transmission of the stress pulse across the interface. The other end of the spacer was slightly rounded to insure axial loading. The coil was supported at the opposite end from the impact end and in order to make certain that the waves reflected at the supports would not interfere with the measurements.

One of the hammers was a 4 1/2 inches long cylindrical rod made of the same aluminum alloy as the spacer. The other hammer was a 1/2 inch diameter steel ball. The pulses generated by the cylindrical hammer were long enough so that there was no dispersion in the straight section. The cylindrical hammer mounted on two nylon sliders slid down a guide from a predetermined height for impact with the coil. The steel ball was dropped through a copper tube. The hammers were dropped from 3 feet.

The stress pulses were monitored by strain gages (BLH, FAP 12-12) mounted along a coil; the locations are shown in Fig. 1 with the distances from the first set of strain gages, measured along the inner, outer, and centroidal radii of the coil. At each position, a set of two strain gages, designated by A, were mounted along the axial direction of the bar 180° apart and connected in series to measure the axial elongation. Another set of strain gages, designated by B, were mounted circumferentially 180° apart from each other to measure the circumferential expansion of the bar. The outputs from the bridge circuits were amplified by amplifiers and measured by an oscilloscope, Tektronix 555. The beams were triggered when the hammer came into contact with the coil.

b) Experimental Results

Figures 2 and 3 illustrate the experimental results obtained using the ball. These results are tabulated in Table 1. Figure 2 and Figure 3 are the results obtained by loading the smaller end and the larger end of the helical coil, respectively. Comparison of these two figures shows that the stress pulse loaded at the

GAUGE STATION	DISTANCE FROM FIRST STRAIN GAUGE (in inches)		
	inner	outer	centroid
2	6 26	6 63	6 44
3	11 61	14 51	13 06
4	20 66	28 57	24 87
5	45 06	59 13	52 09
6	81 49	102 63	92 06
7	104 66	128 81	116 73
8 A	128 94	154 74	140 34
8	128 96	155 36	142 16

Fig. 1 Experimental Arrangement and Gage Locations

smaller end disperses faster than that loaded at the larger end, after the pulses propagate an equivalent distance. It should be noted that the upper beams were amplified 10.5 times, whereas the lower beams were amplified 16.7 times. Because of the curvature, the measurements by the "A" gages did not completely cancel the bending effects. However, the previous work[1] showed that the effects were rather small. Similar results are obtained using the cylindrical hammer, as shown in Table 1.

The wave that arrives at each station first has the lowest amplitude and the highest frequency in all the cases, and as shown in Table 1, propagates with velocities close to the bar velocity $C_0 = \sqrt{E/\rho}$. The bar velocity is used to mean the limiting group velocity in a straight circular bar when the wavelength approaches infinity. The succeeding waves have lower frequency and finally reach steady state oscillations. These results are in accordance with the theoretical predictions made in the following section.

The experimental results will be discussed in more detail based on the numerical values shown in Table 1. The group velocities are shown in the fifth column. These values were obtained by dividing the distance the stress pulses traveled, measured along the centroids, by the time taken to arrive at each station. These group velocities are close to the bar velocity within the experimental approximation, which for this aluminum is 1.98×10^5 inches/sec. The group velocities decrease as the distance covered by the pulses increase which may be due to the inability of the present technique to measure very low amplitudes associated with high frequency waves. These group velocities are slower than

79

those measured in a constant radius helix[1] due to severe degeneration of the stress pulse in the present case because of the smaller radius of curvature.

The sixth column shows the pulse lengths. It should be noted that the amplitudes of the waves propagating from the smaller end to the larger end of the helical coil are much lower than those propagating in the opposite direction.

The eighth column lists the half periods of the oscillatory portion of the waves. The half periods of the upper traces may be compared with the natural frequency of rings with the same radius as the coil. At the larger end of the coil where the radius is approximately 4.25 inches, the half period is 66.8 micro-seconds which compares very favorably with the experimental results. At the smaller end the comparison is not as favorable. This could be because of the large ratio of the radius of the cross-sectional area to the radius of principal curvature and the long straight section at the smaller end of the coil.

II. THEORETICAL ANALYSIS

The analysis given here is similar to that presented in Ref. [1], except that the effect of torsion is included. The theoretical results are included to provide qualitative interpretation of the experimental results. The phase velocity, the group velocity and the natural frequency are determined for a helical coil with constant radius of curvature. From the present analysis it was found that as soon as the effect of torsion is included, there is no longer the wave component which propagated with the distortional wave velocity at large wavelengths.

a) Geometric Relations

A right-handed helix with varying radius of curvature is loaded tangentially as shown in Fig. 1. The rectangular coordinate (X,Y,Z) is fixed in space so that the Z-axis is along the axis of the helix and the $X - Y$ plane cuts the coil at the larger end of the helix. The distance from the origin to the point of intersection between the $X - Y$ plane and the coil at the larger end of the coil is given by a_0. The pitch of the coil is constant. The radius of curvature varies linearly with Z.

The position vector from the origin of the coordinate system to any point on the helix is given by

$$r = a_0(1-f\theta)\cos\theta\hat{i} + a_0(1-f\theta)\sin\theta\hat{j} + c\theta\hat{k} \quad (1)$$

At any time the wave with the longest wavelength occupies a segment of the coil subtended by a characteristic angle θ_0 given by

$$\theta_0 = \lambda/a \quad (2)$$

In Eq. (1), if the value of $f\theta_0$ is much smaller than unity, then the rate of curvature change may be neglected without much loss in the inter-

pretation of the experimental results. In the following analysis, for simplicity, the principal radius of curvature R and the torsion τ_0 will be approximated by

$$R = \frac{a^2 + c^2}{a}; \quad \tau_0 = \frac{1}{\sigma} = \frac{c}{a^2 + c^2} \quad (3)$$

b) Equations of Motion

The equations of motion may be derived in a similar manner as done previously[1,5]. The basic assumptions are that plane sections parallel to the principal normal direction before deformation remain plain after deformation, the cross section of the coil is uniform, the displacements and the rotations of the plane cross section are represented by those of the centroid, strains are small, and that there is no shear deformation. The equations of motion may be written with respect to a moving coordinate system (x_0, y_0, z_0) at any arbitrary point of the unstrained coil. The coordinate system is defined so that z_0 is tangent to the coil, x_0 is parallel to the principal normal vector, and the y_0-axis is oriented so as to complete the right handed coordinate system.

The equations of motion are

$$\frac{\partial F_x}{\partial s_0} - \frac{F_y}{\sigma} + \frac{EA}{R}\left(\frac{\partial w}{\partial s_0} - \frac{u}{R}\right) = m\frac{\partial^2 u}{\partial t^2} \quad (4a)$$

$$EA\left[\frac{\partial^2 w}{\partial s_0^2} - \frac{1}{R}\frac{\partial u}{\partial s_0}\right] - \frac{1}{R}F_x = m\frac{\partial^2 w}{\partial t^2} \quad (4b)$$

$$\frac{\partial F_y}{\partial s_0} + \frac{1}{\sigma}F_x = m\frac{\partial^2 v}{\partial t^2} \quad (4c)$$

$$EJ_y\left[\frac{\partial^3 u}{\partial s_0^3} + \left(\frac{1}{R^2} - \frac{1}{\sigma^2}\right)\frac{\partial u}{\partial s_0} - \frac{2}{\sigma}\frac{\partial^2 v}{\partial s_0^2}\right] + \frac{EJ_x}{\sigma}\left[\frac{R}{R}\right.$$

$$-\frac{\partial^2 v}{\partial s_0^2} - \frac{2}{\sigma}\frac{\partial u}{\partial s_0} + \frac{v}{\sigma^2} - \frac{w}{R\sigma}\right] + F_x = I_y\frac{\partial^2}{\partial t^2}$$

$$\left[\frac{\partial u}{\partial s_0} - \frac{v}{\sigma} + \frac{w}{R}\right] \quad (4d)$$

$$EJ_x\left[\frac{1}{R}\frac{\partial\beta}{\partial s_0} - \frac{\partial^3 v}{\partial s_0^3} - \frac{2}{\sigma}\frac{\partial^2 u}{\partial s_0^2} + \frac{1}{\sigma^2}\frac{\partial v}{\partial s_0} - \frac{1}{R\sigma}\frac{\partial w}{\partial s_0}\right]$$

$$-\frac{EJ_y}{\sigma}\left[\frac{\partial^2 u}{\partial s_0^2} + \left(\frac{1}{R^2} - \frac{1}{\sigma^2}\right)u - \frac{2}{\sigma}\frac{\partial v}{\partial s_0}\right] + \frac{C}{R}\left[\frac{\partial\beta}{\partial s_0}\right.$$

$$+ \frac{1}{R}\frac{\partial v}{\partial s_0} - \frac{1}{\sigma}\frac{\partial w}{\partial \theta_0} + \frac{2u}{R\sigma}\right] - F_y = I_x\frac{\partial^2}{\partial t^2}\left[\frac{\partial v}{\partial s_0} - \frac{u}{\sigma}\right] \quad (4e)$$

80

$$C\left[\frac{\partial^2 \beta}{\partial \theta_o^2} + \frac{1}{R}\frac{\partial^2 v}{\partial \theta_o^2} - \frac{1}{\sigma}\frac{\partial^2 w}{\partial \theta_o^2} + \frac{2}{R}\frac{\partial u}{\partial s_o}\right] - \frac{RJ_x}{R}$$

$$\left[\frac{\beta}{R} - \frac{\partial^2 v}{\partial \theta_o^2} - \frac{2}{\sigma}\frac{\partial u}{\partial s_o} + \frac{v}{\sigma^2} - \frac{w}{R\sigma}\right] = I_z \frac{\partial^2 \beta}{\partial t^2} \qquad (4f)$$

Eqs. (4d) and (4e) may be solved for F_x and F_y and substituted into the rest of the equations (4a, b, c, f) to obtain four equations in terms of the four unknowns, u, v, w and β. If $\sigma \gg R$, the above equations may be separated into two groups, one involving only u and w components and the other including only v and β components.

c) Frequency Equations

If we assume an infinite train of sinusoidal waves is propagating in the coil, the displacements and β may be expressed as

$$u = U(x_o, y_o)\exp[i(k\, z_o - p\, t)]$$
$$v = V(x_o, y_o)\exp[i(k\, z_o - p\, t)]$$
$$w = W(x_o, y_o)\exp[i(k\, z_o - p\, t)]$$
$$\beta = B(x_o, y_o)\exp[i(k\, z_o - p\, t)] ; \text{ where } (5)$$
$$p = 2\pi \bar{f} ; \quad k = 2\pi/\lambda; \quad \bar{f} = \text{frequency}$$
$$z_o = s_o ; \quad i = \sqrt{-1}$$

Substituting Eqs. (5) into Eqs. (4), which are obtained after eliminating F_x and F_y, the following four equations are obtained:

$$iA_1 U + D_1 W + F_1 V + H_1 B = 0$$
$$iA_2 U + D_2 W + F_2 V = 0$$
$$iA_3 U + D_3 W + F_3 V + H_3 B = 0$$
$$iA_4 U + D_4 W + F_4 V + H_4 B = 0 \qquad (6)$$

where

$$A_1 = -\left[-\left(\frac{p}{C_o}\right)^2 + k^2 + \frac{6}{\sigma^2} - \frac{1}{R^2}\right]k^2 + \left(\frac{1}{\gamma^2} + \frac{1}{\sigma^2}\right)$$
$$\left(\frac{p}{C_o}\right)^2 - \frac{1}{R^2\gamma^2}\left(1 + \frac{\gamma_s^2}{\sigma^2(1+\nu)}\right) + \frac{1}{\sigma^2}\left(\frac{1}{R^2} - \frac{1}{\sigma^2}\right)$$

$$D_1 = \frac{k}{R}\left\{\left(\frac{p}{C_o}\right)^2 - \frac{1}{\sigma^2}\left[2 + \frac{1}{2(1+\nu)}\left(\frac{\gamma_s}{\gamma}\right)^2\right] - \frac{1}{\gamma^2}\right\}$$

$$F_1 = \frac{k}{\sigma}\left[-2\left(\frac{p}{C_o}\right)^2 + 4k^2 + \frac{6}{\sigma^2} + \frac{1}{2(1+\nu)}\frac{1}{R^2}\left(\frac{\gamma_s}{\gamma}\right)^2\right]$$

$$H_1 = \frac{k}{\sigma R}\left[2 + \frac{1}{2(1+\nu)}\left(\frac{\gamma_s}{\gamma}\right)^2\right]$$

$$A_2 = \frac{k}{R}\left[-1 + \gamma^2\left(\frac{p}{C_o}\right)^2 - \gamma^2 k^2 + \left(\frac{\gamma}{R}\right)^2 - 3\left(\frac{\gamma}{\sigma}\right)^2\right]$$

$$D_2 = \left[-k^2 + \left(\frac{p}{C_o}\right)^2\left(1 + \frac{\gamma^2}{R^2}\right) - \frac{\gamma^2}{\sigma^2 R^2}\right]$$

$$F_2 = \frac{\gamma^2}{R\sigma}\left[-\left(\frac{p}{C_o}\right)^2 + 3k^2 + \frac{1}{\sigma^2}\right]$$

$$A_3 = \frac{k\gamma^2}{\sigma}\left\{4k^2 - 2\left(\frac{p}{C_o}\right)^2 + \frac{4}{\sigma^2} + \frac{1}{R^2}\left[\frac{1}{1+\nu}\left(\frac{\gamma_s}{\gamma}\right)^2 - 2\right]\right\}$$

$$D_3 = \frac{\gamma^2}{R\sigma}\left\{\left[1 + \frac{1}{2(1+\nu)}\left(\frac{\gamma_s}{\gamma}\right)^2\right]k^2 - \left(\frac{p}{C_o}\right)^2 + \frac{1}{\sigma^2}\right\}$$

$$F_3 = \gamma^2\left\{-k^4 - \left[\frac{c}{\sigma^2} + \frac{1}{2(1+\nu)R^2}\left(\frac{\gamma_s}{\gamma}\right)^2\right]k^2 + \left(\frac{1}{\sigma^2} + \frac{1}{\gamma^2}\right)\left(\frac{p}{C_o}\right)^2 + k^2\left(\frac{p}{C_o}\right)^2 - \frac{1}{\sigma^4}\right\}$$

$$H_3 = \frac{\gamma^2}{R}\left\{\left[1 + \frac{1}{2(1+\nu)}\left(\frac{\gamma_s}{\gamma}\right)^2\right]k^2 + \frac{1}{\sigma^2}\right\}$$

$$A_4 = \frac{2k}{R\sigma}\left[1 + 2(1 + \nu)\left(\frac{\gamma}{\gamma_z}\right)^2\right]$$

$$D_4 = \frac{1}{\sigma}\left[k^2 + \frac{2(1+\nu)}{R^2}\left(\frac{\gamma}{\gamma_z}\right)^2\right]$$

$$F_4 = \frac{1}{R}\left\{-\left[1 + 2(1+\nu)\left(\frac{\gamma}{\gamma_z}\right)^2\right]k^2 - \frac{2(1+\nu)}{\sigma^2}\left(\frac{\gamma}{\gamma_z}\right)^2\right\}$$

$$H_4 = -k^2 + \left(\frac{p}{C_o}\right)^2\left(\frac{C_o^2}{C_s^2}\right) - \frac{2(1+\nu)}{R^2}\left(\frac{\gamma}{\gamma_z}\right)^2 \qquad (7)$$

In Eqs. (7) the radii of gyration γ and γ_z and the wave velocities C_o and C_s are obtained from the following definitions:

$$C_o^2 = EA/r; \quad \gamma^2 = I_y/m = J_y/A = J_x/A$$
$$C_s^2 = GA/m; \quad \gamma_z^2 = 2(1+\nu)\left(\frac{C}{EA}\right)$$

Eqs. (17) are satisfied if

$$\begin{vmatrix} A_1 & D_1 & F_1 & H_1 \\ A_2 & D_2 & F_2 & 0 \\ A_3 & D_3 & F_3 & H_3 \\ A_4 & D_4 & F_4 & H_4 \end{vmatrix} = 0 \qquad (8)$$

The above equation is the frequency equation. The phase velocity C_p and the group velocity C_g are

$$C_p = \frac{p}{k} ; \quad C_g = \frac{dp}{dk} \qquad (9)$$

The frequency equation is first solved for p and C_p. The group velocity is obtained numerically from the values of p at given values of k. The phase velocity is the rate at which a point of constant phase travels along the boundary and the velocity with which energy is transmitted is given by the group velocity.

Eq. (8) has four positive real roots except at very large wavelengths. The phase and group velocities are plotted in Figs. 4

81

through 9. As shown in Fig. 4 for fixed values of curvature and torsion, two of the phase velocities approach infinity as the wave number k decreases for various values of radius of gyration while the other approach zero. One of the latter two curves starts increasing again as the value of k is decreased further, while the other assumes complex values with very small imaginary parts. This result is due to the manner of computation; if the frequency equation is solved for the wave number for real values of frequency, the wave number would assume complex value.** Therefore, there are only three real values for C_p when k is smaller than approximately $1/R$. The phase velocity approaches infinity when the wavefront is almost parallel to the boundary. Three of the values approach the bar velocity C_o as $k \to \infty$, while one of the values approach C_s as $k \to \infty$. Similar results were obtained when the effect of σ is neglected. Comparing the results with those of the previous work[1], it is seen that the curves marked "1" and "2" are associated with the $u - w$ mode of propagation and the ones marked "3" and "4" are associated with the $\beta - v$ mode of propagation. These results differ from those of the previous work[1] in that when σ is neglected, the "3" curve does not approach infinity as $k \to 0$.

It should be noted that the "1" mode is not affected appreciably by the change in the radius of gyration, indicating that it is closely associated with the extensional deformation of the centroid of the cross-section. The "2" mode is nearly independent of the principal radius of curvature, as shown in Fig. 6, and is associated with the radial flexural deformation of the coil. The phase and group velocities for flexural modes, given by "2" in Figs. 6 and 7, closely resemble the approximate theory of Rayleigh[9] for flexural wave propagation in a straight rod.

The influence of the radius of torsion on phase velocity C_p of "1" is small when it is varied from 2 to 60 inches as shown in Fig. 5, except when k is small. Its effect of "2" is appreciable at large wavelengths, since it is associated with the flexural mode of deformation. The "3" curve behaves about the same as "2". The "4" mode is also influenced by torsion at very small values of k.

As shown in Fig. 6, the curvature has negligible effect on C_o except when k is small. Fig. 7 shows that the group velocity C_g faster with decrease in wavelength as the radius of curvature increases in the limit as $R \to \infty$, the present analysis should yield $C_g = C_o$. The present result differs from the previous work[1] in that the group velocity for the "3" mode approaches 0 as $k \to 0$ in the present case, whereas previously it approached the shear wave velocity. Both the "2" and "3" modes exceed the bar velocity C_o and then approach it

** Similar results have been obtained for vibration of plates and were shown to be associated with edge vibrations.

asymptotically which is similar to the approximate theory of Rayleigh for a straight rod. The "4" mode also exceeds the shear wave velocity and approaches it asymptotically as the wavelength is decreased.

Fig. 8 shows that the group velocity of the "1" mode is not influenced much by the change in torsion. However, when σ is small, i.e. $\sigma = 2$ inches, the "2" mode undergoes a saddle-point-like transition which is quite different from when $\sigma = 60$ inches. The "3" and "4" modes depart from each other when the wave number is larger than 10 inches^{-1}. Fig. 9 shows the variation of the group velocity as a function of the radius of gyration. All the modes are influenced by the radius of gyration, except the "1" mode.

In short, the analytical results show that the waves with short wavelengths propagate faster than the longer wavelength waves and as the radius of curvature decreases, the group velocity decreases for a given wavelength, especially the "1" mode. The torsion is not as important as the other parameters, at least in the range of parameters considered in this paper. The diameter of the cross-section of the coil has significant influence.

III. DISCUSSION OF THE EXPERIMENTAL RESULTS BASED ON THE THEORETICAL RESULTS

The experimental results can be discussed qualitatively in terms of theoretical findings. Both the experimental work and the theoretical results show that dispersion of waves exists in a tangentially loaded helical coil. The rate of dispersion is greater when the radius of the coil is small, as predicted by the theoretical results. The experimental results also show that the stress pulse disperses faster when the coil is loaded at the smaller end. The dispersion occurs because the initial pulse is composed of many waves of various frequencies which propagate with different velocities, high frequency waves propagating faster than the low frequency waves. The length and amplitude of the first pulse that arrives at a given station in the coil become shorter and smaller with the distance of propagation, since it represents the superposition of several short wavelength components.

The comparison of the experimental results obtained by loading the larger end with those obtained by loading at the smaller end indicated that the amplitudes of the pulse in the former case decrease gradually, whereas in the latter case the amplitudes decrease suddenly after passing through the coil with the smallest radius of curvature and remain about the same afterwards. This indicates that the first coil in the latter case acts as a filter. The difference between these two cases is brought about by the difference in the radii of curvature rather than by the rate of curvature change, since the rate of curvature change in one case is negative, while in the other case it is positive. Therefore, the approximation made in the analysis

82

regarding the rate of curvature change is reasonable for the experimental conditions employed in this paper.

IV. CONCLUSION

Because of its dispersion characteristics, a tangentially loaded helical coil may be used as a shock load disperser and/or an acoustic filter. The curvature and the rate of curvature change of the helical coil can be chosen for a given application to control the rate of dispersion and the frequency of filtration.

ACKNOWLEDGEMENT

The author wishes to thank Messrs. R.S. Lee and T.F. Lin for their assistance in the preparation of this paper.

REFERENCES

1. N. P. Suh, "Helical Coil as Impact Load Dispersers," to appear in *Journal of Engineering for Industry*, *Transactions of American Society of Mechanical Engineers* (1969)

2. A.E.H. Love, "The Propagation of Waves of Elastic Displacement Along a Helical Coil," *Cambridge Philosophical Society Transactions*, 18, 364-374 (1900)

3. H. Lamb, "On the Flexure and the Vibration of a Curved Bar," *London Mathematical Society Proc.*, 19, 365-376 (1888)

4. K. H. Michell, "On the Stability of a Bent and Twisted Wire," *Messenger of Mathematics*, 19, 181-184 (1890)

5. L. L. Philipson, "On the Role of Extension in the Flexural Vibrations of Rings," *Journal of Applied Mechanics*, 23, 364-366 (1956)

6. W.G.B. Britton and G. O. Langley, "Stress Pulse Propagation in Curved Mechanical Waveguides," *Journal of Sound and Vibration*, 7, 417-430 (1968)

7. W. H. Wittrick, "An Elastic Wave Propagation in Helical Springs," *International Journal of Mechanical Sciences*, 8, 25 (1966)

8. A.E.H. Love, *Mathematical Theory of Elasticity*, Chapter XVIII, Dover, New York (1944)

9. R. M. Davies, "A Critical Study of the Hopkinson Pressure Bar," *Philosophical Transactions*, 240A, 375-457 (1948)

TABLE 1

TABULATION OF EXPERIMENTAL RESULTS

No.	Hammer C-Cyl B-Ball	A*	B**	C***	D****	Upper Trace 1st	Lower Trace 1st	2nd	3rd	4th	Half Period (micro-sec.) Upper	Lower	Lower Trace Arrival Time
1	B	1A	2A	2.05	51.5	1	0.855	0.629	0.629	0.562	46.5	46.5	31.4
2	B	1A	2B	--	45.7	1	0.70	0.925	0.542	0.765	46.5	45.7	25.7
3	B	1A	4A	2.07	45.7	1	0.048	0.097	0.09	0.125	46.5	21.5	128.6
4	B	1A	4B	1.86	42.9	1		0.044	0.061	0.061	46.5	--	143.0
5	B	1A	5A	1.86	42.9	1	0.032	0.043	0.096	0.096	45.7	22.2	280.0
6	B	1A	5B	1.86	42.9	1	0.023	0.031	0.093	0.093	45.7	--	280.0
7	B	1A	6A	1.82	42.9	1	0.038	0.048	0.058	0.077	45.7	24.2	507.0
8	B	1A	6B	1.83	42.9	1	0.027	0.065	0.102	0.111	45.7	--	503.0
9	C	1A	2A	2.05	88.7	1	0.785	0.237	0.475	0.144	45.7	45.0	31.4
10	C	1A	2B	2.25	88.7	1	0.795	0.415	0.134	0.486	45.7	45.7	28.6
12	C	1A	3B	1.99	--	1	0.036	0.107	0.142	---	45.7	--	65.7
13	C	1A	4A	2.58	94.2	1	0.024	0.036	0.048	0.041	45.7	--	103.0
14	C	1A	4B	2.08	88.7	1	0.024	0.036	0.024	0.036	45.7	--	128.0
15	C	1A	5A	1.88	91.5	1	0.023	0.023	0.041	0.046	45.7	17.7	277.2
16	C	1A	5B	1.88	91.5	1	0.028	0.028	0.044	0.055	45.7	--	277.2
17	C	1A	6A	1.85	91.5	1	0.033	0.033	0.033	0.039	45.7	--	497.2
18	C	1A	6B	1.85	91.5	1	0.011	0.026	0.037	0.053	45.7	--	497.2
20	B	8A	4A	1.88	37.1	1	0.052	0.052	0.155	0.135	72.9	27.9	606
21	B	8A	4B	1.86	37.1	1	0.017	0.044	0.061	0.044	72.9	--	612
22	B	8A	5A	1.99	37.1	1	0.068	0.144	0.221	0.306	72.9	41.5	443
23	B	8A	5B	1.98	37.1	1	0.051	0.153	0.255	0.306	72.9	--	446
24	B	8A	6A	2.06	37.1	1	0.13	0.402	0.507	0.314	72.9	59.2	234
25	B	8B	6B	1.95	37.1	1	0.013	0.404	0.665	0.450	72.9	--	248
26	B	8A	7A	2.12	37.1	1	0.343	0.496	0.332	0.334	72.9	65.6	111
27	B	8A	7B	2.12	37.1	1	0.081	0.234	0.072	0.099	72.9	--	111
28	B	8A	8B	--	37.1	1	---	---	---	---	72.9	--	-
29	C	8A	4A	1.94	88.5	1	0.023	0.07	0.081	0.128	71.4	17.1	585
30	C	8A	4B	1.87	88.5	1	0.023	0.034	0.045	0.045	71.4	15.7	608
31	C	8A	5A	1.97	88.5	1	0.65	0.119	0.152	0.129	71.4	(41.5)	448
32	C	8A	5B	1.95	88.5	1	0.055	0.121	0.165	0.132	71.4	--	452
33	C	8A	6A	2.12	88.5	1	0.129	0.036	0.219	0.248	71.4	(58.5)	228
34	C	8A	6B	2.00	88.5	1	0.017	0.281	0.309	0.365	71.4	--	242
35	C	8A	7A	--	88.5	1	0.331	0.348	0.324	0.292	71.4	67.0	-
36	C	8A	7B	--	88.5	1	---	---	---	---	71.4	--	-
37	C	8A	8B	--	88.5	1	---	0.313	---	---	71.4	--	-

*   Upper Trace Strain Gage
**   Lower Trace Strain Gage
***   Group Velocity[+] (10^{-5} in/sec) ([+]Based on the distance measured along the centroids)
****   Initial Pulse Length (u sec)

84

SWEEP SPEED $10^{-4}\ \frac{\text{sec}}{\text{cm}}$

SENSITIVITY :

UPPER BEAM $5 \times 10.5\ \frac{\text{mv}}{\text{cm}}$

LOWER BEAM $5 \times 16.7\ \frac{\text{mv}}{\text{cm}}$
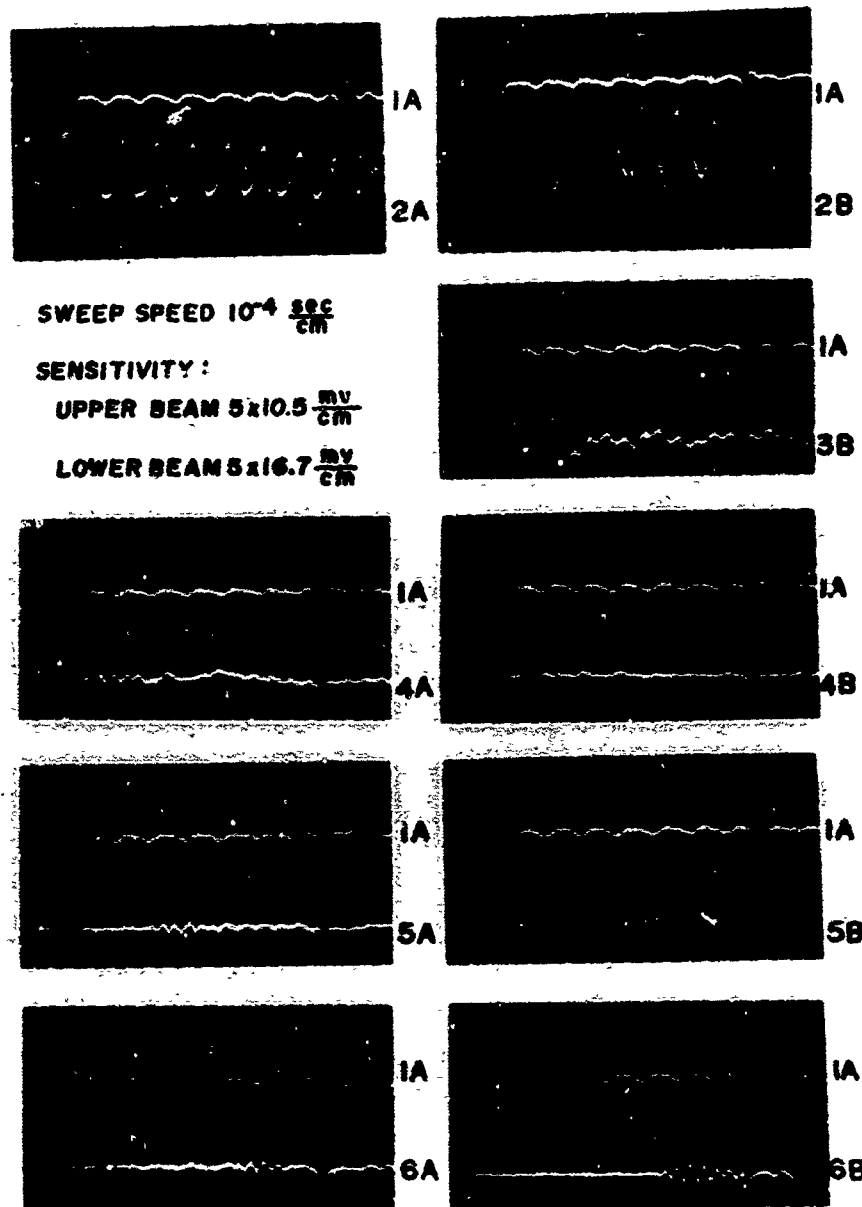
Figure 2 Experimental Results

Impact at the Smaller End of the Coil

(Ball) — Sweep Speed 10^{-4} sec/cm;

Sensitivity: upper beam 52.5 mv/cm, lower beam 83.5 mv/cm.

SWEEP SPEED 10^{-4} $\frac{sec}{cm}$
SENSITIVITY:
  UPPER BEAM $5 \times 10.5 \frac{mv}{cm}$

  LOWER BEAM $5 \times 16.7 \frac{mv}{cm}$
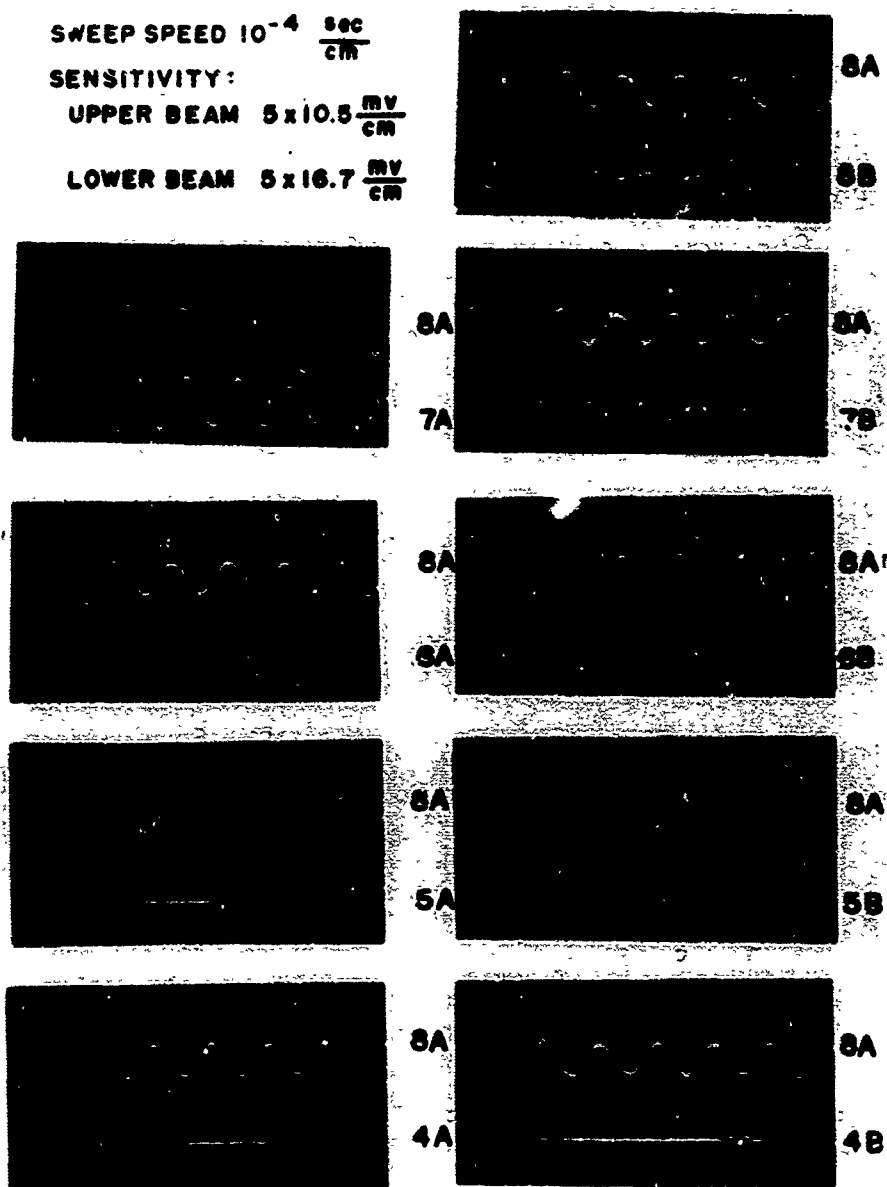
Figure 3 Experimental Results
Impact at the Larger End of the Coil
(Ball) -- Sweep Speed 10^{-4} sec/cm;
Sensitivity: upper beam 52.5 mv/cm, lower beam 83.5 mv/cm
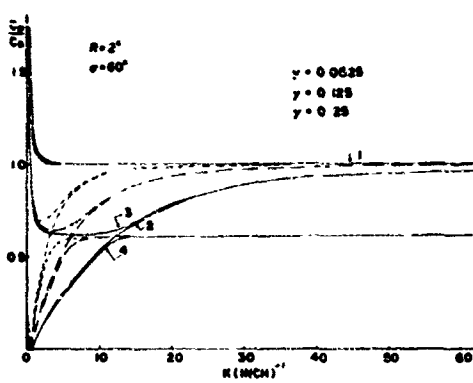
Figure 4 Phase Velocity vs. Wave Number for
Various Values of γ -- "1" and "2"
are Associated with the u - v mode; "3" and "4"
are Associated with the β - v mode.
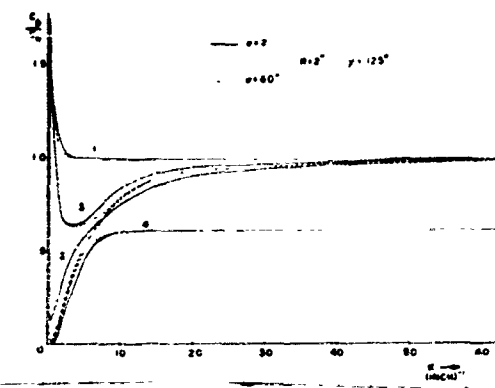
Figure 5 Phase Velocity vs. Wave Number for
σ = 2 and σ = 60. "1" and "2" are
Associated with the u - v mode; "3" and "4" are
Associated with the β - v mode.
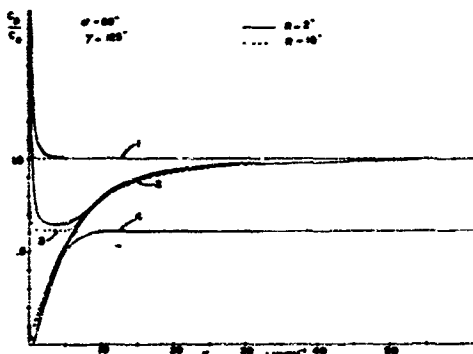
Figure 6 Phase Velocity vs. Wave Number for
R = 2 and R = 60. "1" and "2" are
Associated with the u - v mode; "3" and "4"
are Associated with the β - v mode.
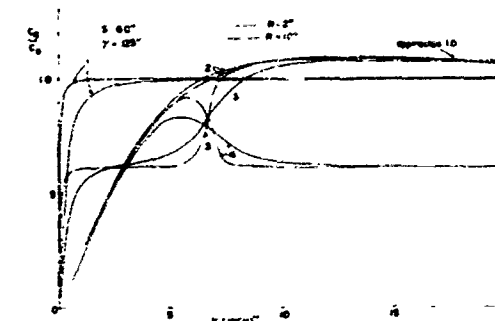
Figure 7 Group Velocity vs. Wave Number for
Various R. "1" and "2" are Associated with
the u - v mode; "3" and "4" are Associated
with the β - v mode.

87
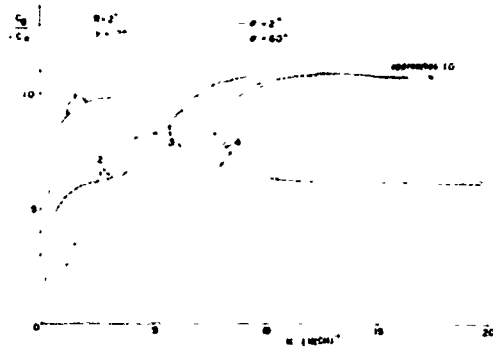
Figure 8 Group Velocity vs. Wave Number for σ = 2 and σ = 60. "1" and "2" are Associated with the u - v mode; "3" and "4" are Associated with β - v mode.
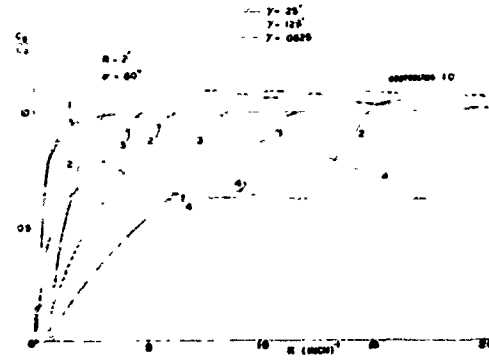
Figure 9 Group Velocity vs. Wave Number for Various Values of γ. "1" and "2" are Associated with the u - v mode; "3" and "4" are Associated with the β - v mode.

DISCUSSION

Mr. Eckblad (The Boeing Company): What is the length of a spring necessary for low frequency isolation down to 2 or 3 Hz?

Mr. Suh: In this case the wavelength was rather short and I really do not know what happens when a real long pulse is applied. Clearly if you have a long pulse then much of that will be near the origin of the curve that was shown and only a very small component will be at the other side, so that all of the waves may end up travelling with a nearly constant velocity. Our main concern here is the transmission of energy and the amplitude, so in that, case we may have to make the coil fairly large. We have not looked into that area yet.

Mr. Cary (B and K Instruments): I had a question as to whether you had done any conjecturing as to whether this may represent a cochlear phenomenon in the human ear? Also, have you experimented with a graduated cross sectional area wire?

Mr. Suh: No, we have not done that. In fact, most of this work was done some time ago. We are contemplating various geometric shapes and cross sectional areas, and we are also contemplating the use of this type of dispersion phenomena and coupling this with absorbtion phenomena by coupling this in elastomers. So we are thinking of doing something along that line but we have not done that yet. We have actually made some experimental devices in which we have hung two quarters together and applied a shock load. At one end of the quarter where the load is applied you can really feel a fair amount of motion by just putting your hand on it. But if you put your hand at the other end you do not feel a thing. I asked a graduate student to work on this and to get some experimental data. He tried to measure the wave transmitted through the top when we have had some complicated shape and every time he did it he did not get any output from the strain gages at the other end, the output of the coil. So I though he made a mistake and I was going to show him how to do it, and I went to the laboratory and did it and the same thing happened. Apparently if you combine this in a very ingenious fashion then you can practically eliminate all of the amplitude, so I think it is very interesting.

88

ANALYSIS OF THE INVERTING TUBE ENERGY ABSORBER

J. M. Alcone
Sandia Laboratories
Livermore, California

An approximate analysis of the plastic deformation encountered when a
thin-walled cylinder is inverted is developed. Interest in this type of
device arises from the energy absorbing requirements for protection
of critical components (or people) during crash conditions. Mechanisms
utilizing this process are characterized by high specific energy absorption
(SEA) and a rectangular force-displacement relation. Generalized design
curves for predicting the inversion geometry and force characteristics
are developed (Figures 3, 4). The analytical results compare well with
experimental data from two independent sources (Figures 3, 4).

INTRODUCTION

The energy absorption requirements of
spacecraft landing structures have created an
interest in plastic deformation processes.
Various plastic deformation processes have
been suggested in the literature; [1, 2, 3] of
these, one of the most interesting is the inver-
sion (turning inside out) of a thin-walled cylin-
der. Mechanisms utilizing this process are
characterized by high specific energy absorp-
tion (SEA) and a rectangular force-displace-
ment relation. This allows them to be used as
rigid structural members which possess pro-
tection against overloading.

DISCUSSION

The inverting-tube configuration con-
sidered here is shown in Figure 1. The tube
is assumed to be in the position shown at time
zero (i.e., we are interested only in the prop-
agation of the inversion). To facilitate the
analysis, the following model process will be
assumed.

The cylinder experiences plastic bending,
tangential extension, radial thinning, and axial
shortening while passing from its original dia-
meter, through a half-toroidal shape, to its
final diameter. The plastic bending is

assumed to occur in two steps. The first bend
through 180° is spread over the half-toroidal
shape. The second (straightening) bend
through 180° is concentrated at the intersec-
tion of the half toroid and the final cylinder.
The tangential extension is assumed to occur
gradually over the half toroid. The radial
thinning and axial shortening strains are as-
sumed to be equal [4] and to satisfy constancy
of volume (see Figure 2).

In addition the following assumptions are
made:

1. The material is a rigid plastic.

2. The stress-strain relation is unaffect-
   ed by triaxial stress and rate of
   straining.

3. The material volume remains constant.

4. The wall curvature effects are negli-
   gible.

5. The neutral axis lies on a semicircle
   of radius $R = Ct_0/2$.

6. The propagation force is constant.

7. There are no friction losses.
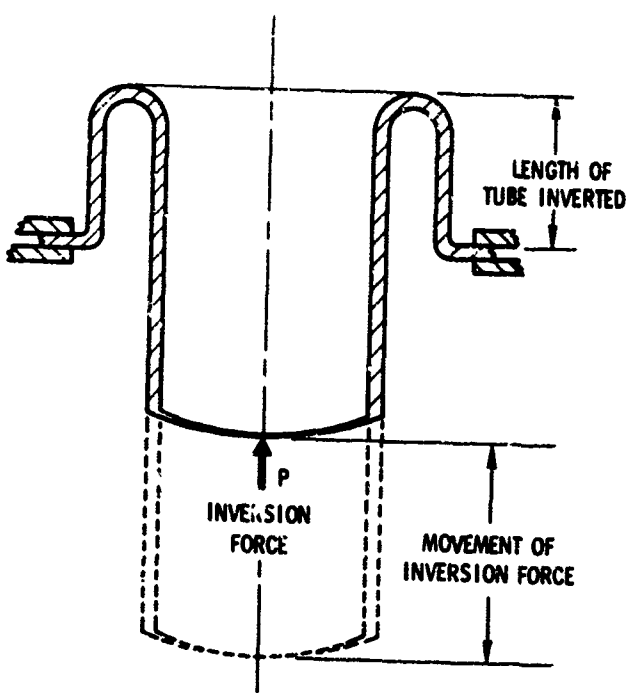
Figure 1. Inverting Tube Configuration
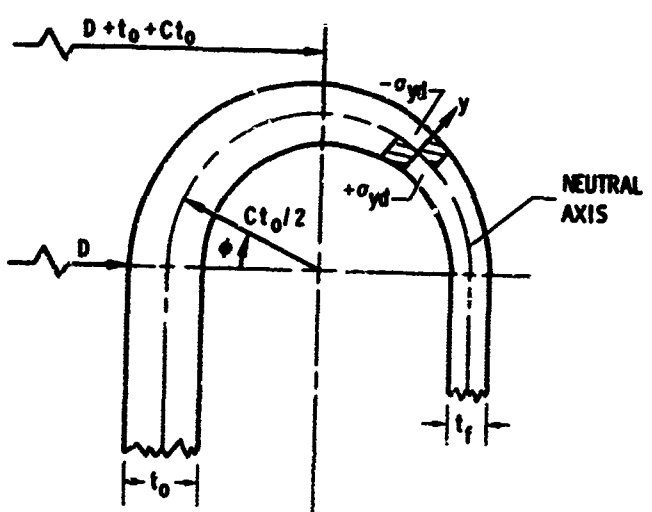
Figure 2. Bend Configuration

90

A discussion of the above assumptions is included in the final section of this report.

Generalized design curves for predicting the inversion geometry and force characteristics have been developed (Figures 3, 4). The analytical results compare well with experimental data from two independent sources (Figures 3, 4). When these curves are used, the tube diameter, wall thickness, and material required to satisfy the needs of any application can be determined.

As can be seen from Figure 3, the analysis developed in this paper is in much better agreement with the experimental data than analyses previously published. [3] Figure 4 is a new presentation of the data which facilitates the determination of the geometric configuration and the material properties which satisfy a specific application.

MATHEMATICAL ANALYSIS

Plastic Deformation Energy/Bend

1. Bending Energy, U_b

We assume the bending energy consists of two terms as shown below.

$$U_b = \int_0^\pi M_1 d\Phi + \int_\pi^{2\pi} M_2 d\Phi \qquad (1)$$

M_1 is the average bending moment acting on the material during the toroidal phase of the inversion. If a stress distribution, as shown in Figure 2, is assumed and the cylinder wall cross-sectional area at $\Phi = \pi/2$ is used, M_1 can be written as shown below.

$$A1_{AV} = \pi(D + t_0 + Ct_0) \frac{t_0}{2} \qquad (2)$$

$$M_1 = \sigma_{yd} A1_A / 2 = \pi(D + t_0 + Ct_0)$$

$$\frac{t_0^2}{4} \sigma_{yd} \qquad (3)$$

In a similar manner, with $A2_{AV}$ as shown below, we can evaluate M_2, the average "straightening" moment.

$$A2_{AV} = \pi(D + t_0 + 2Ct_0) \frac{t_0}{2} \qquad (4)$$

$$M2 = \pi(D + t_0 + 2Ct_0) \frac{t_0^2}{4} \sigma_{y} \qquad (5)$$

Thus

$$U_b = \frac{\sigma_{yd} t_0^2}{4} (2D + 2t_0 + 3Ct_0) \qquad (6)$$

2. Tangential Expansion Energy, U_{TAN}

$$U_{TAN} = \int_{\pi(D+T_0)}^{\pi(D+t_0+2Ct_0)} \sigma_{yd} \pi \frac{Ct_0}{2} t_0 d\ell$$

$$= \pi^2 C^2 t_0^3 \sigma_{yd} \qquad (7)$$

3. Radial Thinning and Axial Shortening Energy, U_{TS}

Assuming that the axial and thinning strains are equal and that the volume of the deformed material remains constant, let

$$\epsilon_t = \epsilon_S = \epsilon \qquad (8)$$

Initial material volume

$$V_i = \frac{\pi Ct_0}{2} t_0 \pi(D + t_0) \qquad (9)$$

Final material volume

$$V_f = \frac{\pi Ct_0}{2} (1 - \epsilon)t_0(1 - \epsilon)\pi(D + t_0 + 2Ct_0) \qquad (10)$$

$$V_f = V_i$$

Therefore

$$\epsilon = 1 - \sqrt{\frac{D + t_0}{(D + t_0 + 2Ct_0)}} \qquad (11)$$

To calculate the energies involved, we assume that the deformations occur at the average of the initial and final tube diameters. Thus, the axial shortening and radial thinning (U_S and U_T)
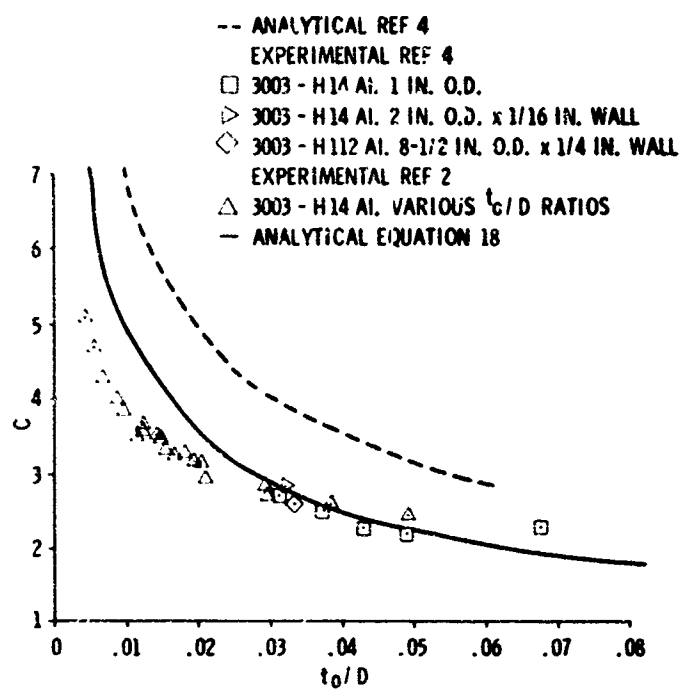
Figure 3. Bend Radius Coefficient versus Thickness-to-Diameter Ratio
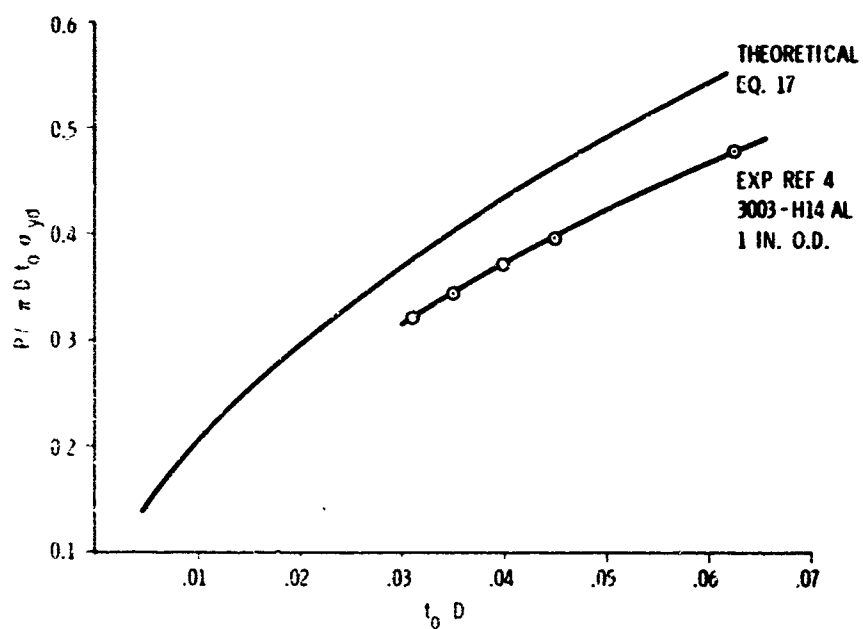
Figure 4. Propagation Force Efficiency Ratio versus Thickness-to-Diameter Ratio

can be written as shown below.

$$U_S = \sigma_{yd} t_0 \pi (D + t_0 + Ct_0) \frac{\pi Ct_0}{2}$$

$$\left[1 - \sqrt{\frac{D + t_0}{(D + t_0 + 2Ct_0)}}\right] \tag{12}$$

$$U_{\cdot} = \sigma_{yd} \frac{\pi Ct_0}{2} \pi (D + t_0 + Ct_0) t_0$$

$$\left[1 - \sqrt{\frac{D + t_0}{(D + t_0 + 2Ct_0)}}\right] \tag{13}$$

and

$$U_{TS} = U_T + U_S = \sigma_{yd} \pi^2 C t_0^2$$

$$(D + t_0 + Ct_0) \left[1 - \sqrt{\frac{D + t_0}{(D + t_0 + 2Ct_0)}}\right] \tag{14}$$

Total plastic deformation energy/bend, U

$$U = U_b + U_{TAN} + U_{TS} \tag{15}$$

Minimization of Propagation Force, P

By equating the work done by the propagation force to the plastic deformation energy, we can solve for P.

$$WORK = P\pi Ct_0 = U \tag{16}$$

Therefore

$$P = \sigma_{yd} t_0 \left[\frac{(2D + 2t_0 + 3Ct_0)\pi}{4C}\right.$$

$$+ \pi Ct_0 + \pi(D + t_0 + Ct_0)$$

$$\left.\left(1 - \sqrt{\frac{D + t_0}{(D + t_0 + 2Ct_0)}}\right)\right] \tag{17}$$

To find C, the inversion radius coefficient, we assume the process wants to occur at a minimum force. Thus, we minimize P with respect to C. Setting $\partial P/\partial C = 0$ yields the equation shown below.

$$0 = 120\left(\frac{t_0}{D}\right)C^7 + 188\left(\frac{t_0}{D}\right)^4\left(1 + \frac{t_0}{D}\right)C^6$$

$$+ \left\{96\left(\frac{t_0}{D}\right)^3\left(1 + \frac{t_0}{D}\right)^2 - 64\left(\frac{t_0}{D}\right)^4\left(1 + \frac{t_0}{D}\right)\right\}C^5$$

$$+ \left\{16\left(\frac{t_0}{D}\right)^2\left(1 + \frac{t_0}{D}\right)^3 - 96\left(\frac{t_0}{D}\right)^3\left(1 + \frac{t_0}{D}\right)^2\right\}C^4$$

$$+ \left\{8\left(\frac{t_0}{D}\right)^3\left(1 + \frac{t_0}{D}\right)^2 - 48\left(\frac{t_0}{D}\right)^2\left(1 + \frac{t_0}{D}\right)^3\right\}C^3$$

$$+ \left\{12\left(\frac{t_0}{D}\right)^2\left(1 + \frac{t_0}{D}\right)^3 - 8\left(\frac{t_0}{D}\right)\left(1 + \frac{t_0}{D}\right)^4\right\}C^2$$

$$+ 6\left(\frac{t_0}{D}\right)\left(1 + \frac{t_0}{D}\right)^4 C + \left(1 + \frac{t_0}{D}\right)^5 \tag{18}$$

The above equation was solved for C for t_0/D values between 0 and 0.1 (range of interest) via numerical techniques. The resulting values of C are plotted in Figure 3. Experimental values of C from References 2 and 3 are also shown in Figure 3 for comparison purposes.

EVALUATION OF ASSUMPTIONS

Average areas and diameters were used to simplify the development of the analysis. This is justifiable in view of their relatively small variation. The assumption that radial thinning and axial strains are equal is based on the experimental observation made in Reference 3. Assumptions 1, 2, and 3 were made on the basis of the fact that most materials used for this application are described by these assumptions (at low strain rates). For small t_0/D ratios, assumption 4 should be valid. Assumptions 1 and 6 are actually equivalent. Assumption 7 implies lubricated dies of the proper dimension. Assumption 5 is not justifiable. It can be easily checked by introducing other terms into the radius expression and observing the resulting minimum propagation force requirements.

REFERENCES

1. R. W. Warner and D. R. Marble,
   "Materials Needs for Energy Absorption
   in Space Vehicle Landings," Proceedings:
   Symposium on Newer Structural Materials
   for Aerospace Vehicles, Chicago, 1964.
   ASTM Special Technical Publication No.
   379, ASTM, Philadelphia, 1965, p. 55.

2. C. K. Kroell, "A Simple, Efficient, One
   Shot Energy Absorber," Shock Vibration
   and Associated Environments, Part III,
   Bulletin 30. Thirtieth Symposium on Shock,
   Vibration and Associated Environments,
   Detroit, October 10-12, 1961. Office of the
   Assistant Secretary of Defense, January
   1962.

3. R. L. Puthoff and K. H. Gumto, Parametric
   Study of a Frangible-Tube Energy Absorp-
   tion System for Protection of a Nuclear
   Aircraft Reactor, NASA-TN-D-5730,
   Lewis Research Center, Cleveland, Ohio,
   March 1970.

4. L. R. Guist and D. P. Marble, Prediction
   of the Inversion Load of a Circular Tube,
   NASA-TN-D-3622, Ames Research Center,
   Moffett Field, California, September 1966.

94

THE EFFECTS OF PAYLOAD PENETRATION AND VARIOUS ANALYTICAL MODELS
ON THE DESIGN OF A SPHERICAL CRUSHABLE CASING
FOR LANDING ENERGY ABSORPTION

by Robert W. Warner and Margaret Covert
NASA Ames Research Center

SUMMARY

The important consequences of penetration by a spherical payload into its crushable casing during landing impact, as established earlier for two analytical models, are verified for five additional models. Three groups of design examples are presented for an impact velocity of 300 feet per second with a choice of zero or "perfect" bonding between the payload and the casing. In two of these three groups of examples, the use of bonding to prevent payload penetration increases the weight of the crushable casing.

INTRODUCTION

For the safe unmanned landing of a data-transmitting or supply payload on a celestial body or elsewhere, the ability of rocket controls to achieve a soft and oriented touchdown will be diminished if a strong and turbulent lateral wind is present, particularly in the neighborhood of a steep landing site. If, therefore, a hard and unoriented impact is the design choice, with possible secondary impacts due to bouncing and rolling, a safe landing requires that the payload be surrounded by a crushable casing. In fact, an unoriented impact suggests the use of a spherical payload and a spherical casing (refs. 1-9), as shown in figure 1, although other shapes are under consideration for various reasons (refs. 2, 3, 8, 10).
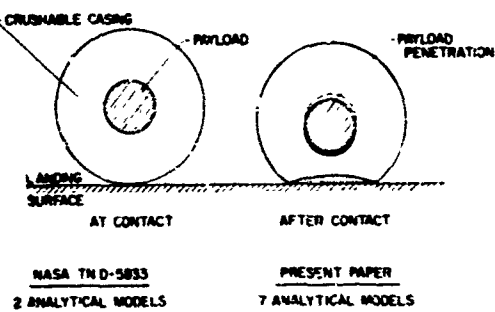
Until a few months ago, previous work on crushable casings (refs. 1-10) neglected the effect of penetration by the payload into its casing. This effect is illustrated in figure 1 by the relative motion between the payload and the casing. Except for analyses with unusually limiting assumptions, previous work (refs. 1-10) also neglected the effect of variations during the impact in the mass being decelerated. This effect results from the accumulation of crushed casing material on the landing surface at rest and, if penetration occurs, on the payload surface at the payload velocity, as illustrated in two locations by the vertical shading in figure 1. Also neglected in past analyses has been the fact that the crushed casing material just discussed builds up during impact and the fact that decelerating stress values, which are available primarily from nearly static crushing tests, must act at the boundary between the built-up material and the uncrushed material rather than at the ground surface or the payload surface. The resulting change in the decelerating force is referred to herein as the "built-up-material" effect.

The fairly probable increase in crushable casing weight when penetration is prevented by bonding the payload to the casing has recently been demonstrated for two analytical models in NASA TN D-5833 (ref. 11). In the present paper, the primary purpose is to determine whether that conclusion continues to apply for seven analytical models, where the five additional models involve simple departures from the original two with regard to variable mass and built-up material.

NOMENCLATURE

g_e	value of g on earth (32.17 ft/sec² herein)
a_{pmax}	maximum value of g loading that occurs during impact stroke
q_{pmax}	maximum absolute displacement of payload after initial contact between crushable material and landing surface

Fig. 1. Illustration of Definitions and Purpose

q_s value of payload displacement at which payload penetration occurs or would occur if unbonded

R   overall radius for spherical system

R_p payload radius for spherical system

SEA   specific energy absorption; energy absorbed per unit weight of the absorber

U_o value of landing vehicle velocity at the instant the crushable material hits the landing surface (300 ft/sec herein)

W_{co} original earth weight of uncrushed crushable material

W_{po} earth weight of payload

ϵ_d fictitious value of compacting strain assumed for design purposes; always less than ϵ_m

ϵ_m compacting strain of crushable material (0.8 herein)

ρ_{cm} uniform density of crushable material

ρ_p payload packaging density: $\dfrac{W_{po}/g_e}{(4/3)\pi R_p^{3}}$

σ_o maximum value of crushing stress of crushable material

DEVELOPMENT OF ANALYTICAL MODELS

All of the analytical models are based on a one-degree-of-freedom analysis prior to payload penetration, with the payload and the crushable casing acting as a unit, and a two-degree-of-freedom analysis when penetration occurs, with relative motion permitted between the payload and the casing. The existence of penetration requires that the material crushing stress is exceeded at the payload surface and is assumed to require that the payload is not even partially bonded to the crushable material. The decelerating forces during penetration are provided by the crushing stresses at the payload surface and the landing surface, or near those surfaces if the built-up-material effect is incorporated in the particular analytical model. These stresses are assumed to be maximum and uniform in the direction radial from the original sphere-center.

It should be noted that acceleration and stress equations are incorporated in the analysis as well as motion equations (where the acceleration equation is simply a motion equation solved for acceleration, with different parameters allowed). The acceleration equation is included because the payload is limited to a specified g-loading and the stress equation because the stress at the payload lower surface must be known to determine the presence or absence of penetration for an unbonded upper surface. These equations are presented in ref. 11, together with a detailed discussion of assumptions.

Some of the assumptions in the development of the analytical models are illustrated in figure 1. No crushed material, for example, is shown trailing outboard of the penetrating payload; nor is any crushed material shown lifted off the landing surface. Such shear deformations are neglected in the analysis. In addition, the symmetrical distribution of crushed material in figure 1 indicates that rolling is not incorporated in the analysis. This is a conservative approach because the symmetrical landing should be the most critical for a spherical system. The landing surface is assumed to be smooth, as shown in figure 1, with projections assumed accounted for by the stroke margin of safety. For the inclusion of gravity effects, the landing surface is assumed to be horizontal; but these effects turn out to be negligible for hard impacts (the local gravity acceleration being taken as 12.3 ft/sec², the value for Mars).

It is also apparent in figure 1 that definite boundaries have been assumed between the crushed material (vertical shading) and the uncrushed material (unshaded). It is, in fact, assumed that each successive layer of material has a jump in velocity as it moves from the uncrushed to the crushed region and that there is only one velocity in each region. In addition, the effects of shear resistance, end fixity, Poisson's ratio, damping, and dynamic buckling are considered adequately incorporated because of their assumed presence in the crushing tests which determine the crushing stress used in the analysis. The density of the uncrushed crushable material is assumed uniform, and perfect rigidity is assumed for the payload and the landing surface. Finally, an exterior cover is assumed for the crushable casing material which is strong enough to prevent material shattering and yet weightless (except for comparison with experiment, in which case the known cover mass is assumed uniformly distributed in the crushable material).

When the equations of motion are used to describe an impact, the sizes of the vertically shaded regions of crushed material in figure 1 are important if stressed areas are to be known for the built-up-material effect. These sizes are determined by the compacting strain of the crushable material, which is the strain at which the stress rises abruptly from a relatively constant value. A second and fictitious compacting strain is also used for an entirely different purpose. This strain is smaller than the actual value and increases the apparent size of the vertically shaded regions in figure 1. For an efficient impact design, these enlarged regions are required to touch each other when the impact energy is fully absorbed, and thus the fictitious design compacting strain provides a margin of safety for the stroke.

At this point, it is useful to distinguish the various analytical models, as illustrated in figure 2. They are labeled "A" through "G" and differ as to whether they account for variable mass and built-up material in the motion equations or in the acceleration and stress equations. The acceleration and stress equations are treated together rather than independently with respect to variable mass and built-up material in order to reduce the number of analytical models.

ANALYTICAL MODEL	VARIABLE MASS		BUILT-UP MATERIAL	
	VARIABLE MASS IN MOTION EQUATIONS	VARIABLE MASS IN ACCELERATION AND STRESS	BUILT-UP MATERIAL IN MOTION EQUATIONS	BUILT-UP MATERIAL IN ACCELERATION AND STRESS
A	NO	NO	NO	NO
B	YES	YES	YES	YES
C	NO	YES	NO	NO
D	NO	NO	NO	YES
E	NO	YES	NO	YES
F	YES	YES	NO	NO
G	NO	NO	YES	YES

Fig. 2. Analytical Models for Landing Impact Energy Absorption

The "A" and "B" models are the models analyzed in ref. 11, with the "B" model having all of the effects of variable mass and built-up material and with the "A" model having none. Since these effects are easier to incorporate in the acceleration and stress equations than in the equations of motion, the "C", "D", and "E" models represent the simplest additions of complexity relative to the "A" model. The "F" and "G" models are included to incorporate the effects of variable mass and built-up material separately and consistently.

It is apparent that "C", "D", "E", "F", and "G" are intermediate models which could be used to investigate counteracting influences. For present purposes, however, they are restricted to checking prior conclusions from the "A" and "B" models on the desirability of preventing penetration by bonding the payload to the casing.

It should be noted that the "A" model is the only one for which the local acceleration due to gravity is assumed to be zero and the resistance to payload penetration to be constant. Fortunately, these limitations have been shown to have essentially no effect on the design results for the examples to be discussed later, and they do permit the use of simple design charts for the "A" model. These design charts are presented and discussed in ref. 11.

For all models except the "A" model, designs are based exclusively on computer programs which solve the one or two ordinary differential equations numerically. If desired, these programs can, of course, be used for the "A" model as well as the

others, and the "A" model results to be presented in this paper are program results.

Three programs have been assembled and are available from the Ames Research Center. Each program can be used for any of the analytical models by a simple selection procedure. The first of these programs checks a given configuration, including payload penetration when it occurs, but does not automatically carry out a design function. The second program iterates successive configurations to determine the outer radius and crushing stress required for a given class of crushable material to achieve a specified deceleration and stroke margin of safety with a given payload. Payload penetration is not included in the second program because the crushing stress required for a specified payload deceleration can be determined in advance for penetration. In addition, with or without penetration, the lightest configurations can sometimes be achieved by specifying the crushing stress in advance. As a result, a third program has been assembled, including penetration when it occurs—a program which iterates successive configurations for a given crushing stress to determine only the crushable material outer radius required to achieve a specified stroke margin of safety.

For the second and third programs, the execute time depends on the quality of the initial design guess as well as the complexity of the model. These usually nonseparable quantities caused a range from 0.40 to 0.85 minutes of execute time (with some sub averaging) for the present applications of the second program, which achieves a specified deceleration as well as a specified stroke margin. The third program, which achieves only a specified stroke margin, required from 0.17 to 0.23 minutes in the absence of payload penetration except for some times up to 1.16 minutes resulting from a search for nonexistent penetration. In the presence of payload penetration, the third program required from 0.47 to 0.66 minutes for the "A" model and from 4.55 to 6.25 minutes for the other models, with the time advantage for the "A" model resulting from its harmless limitation to a constant resistance to penetration. A series of spot checks indicated that the presence or absence of the local acceleration due to gravity has no significant effect on execute time.

It is important to realize that only the "A" and "B" models in figure 2 have been compared with experimental results, with the other models added to check the sensitivity of prior conclusions on payload bonding. These experimental results, which were determined elsewhere (ref. 9 and a private communication*), demonstrate the existence of payload penetration and agree within 10 to 30 percent on deceleration and stroke with corresponding analyses by the "A" and "B" models. There are not enough

---

*Donald R. Cundall, December 1967.

97

data to determine which model is quantitatively better, and this suggests the use of the "A" model, for which simple design charts are available (ref. 11).

DESCRIPTION OF CRUSHABLE MATERIALS

The foregoing discussion of analytical models has already suggested some of the properties of the crushable materials involved. In figure 3, for example, curve ABCDE is a typical stress-strain curve with the compacting strain at point C, where the stress rises abruptly from a relatively constant crushing stress, as stated earlier. This strain ranges from 0.6 for close-packed crushable materials to nearly 1.0 for open crushable structures. In the present analysis, the compacting strain is assumed to be uniform and isotropic throughout the material, regardless of the direction of maximum stress.
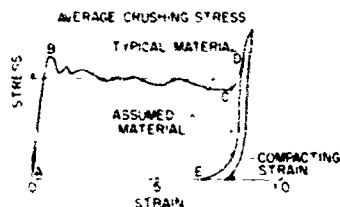
Fig. 3. Stress-Strain Curve for Typical Crushable Material

With regard to the shape of the stress-strain curve, the strain increments in the elastic region between A and B and the rebound region between D and E should be as small as possible in order to minimize bounce-back. Since the area enclosed by the stress-strain curve is the energy absorbed per unit of material volume, the curve should approach a rectangle, which gives the maximum area for a specified maximum crushing stress. This is the reason for limiting the maximum usable strain to that at point D, which has a stress equal to the previous maximum at point B. Actually, for the analytical models, the material is assumed to have a perfectly rectangular stress-strain curve which is bounded by the compacting strain at point C and the average crushing stress, as shown dotted in figure 3.

When the area enclosed by the stress-stain curve, in foot-pounds per cubic foot, is divided by the crushable material density, in pounds per cubic foot, the resulting quantity, in foot-pound, per pound of material, is sometimes called the specific energy absorption. This is a commonly accepted figure of merit for energy absorbing materials, struts, or overall systems—the higher the better. In figure 4, it is plotted against crushing stress as a means of defining the three classes of crushable material considered herein.

The classes of material in figure 4 are labeled light balsa, heavy balsa, and honeycomb-like, with the formulas for the light balsa and honeycomb-like classes based on curve fits available in the literature (ref. 2, p. 259). The modest term "honeycomb-like" is used because its curve fit of the data is rather loose and covers several types of aluminum and fiberglass honeycomb. For the material of intermediate efficiency, heavy balsa, the constant specific energy absorption is verifiable in the literature (ref. 12, p. H-17); but the value of the constant has been lowered to make a later point. This decrease in efficiency can be roughly accomplished physically by covering the spherical outer surface of the crushable casing on the landing vehicle with a heavy layer of weak material.
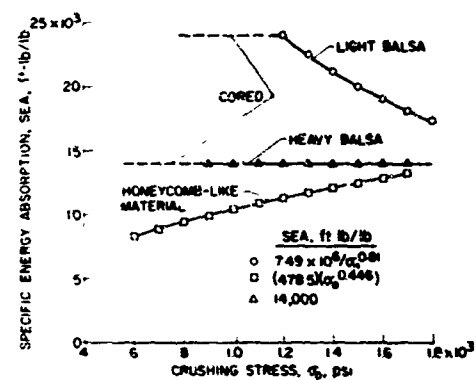
Fig. 4. Energy-Absorption Properties for Three Classes of Crushable Material

The lowest values of crushing stress for the solid curves in figure 4 correspond to the stated limits for the solid materials. For the light balsa and the heavy balsa, however, the curves have been extended with dashed lines down to two-thirds of the lower limits for the solid curves. This assumes that one-third of the material can be removed by coring in the radial direction without introducing significant buckling, end effects, and/or Poisson ratio effects and thereby reducing the specific energy absorption.

It should be noted for future reference that the coring just described produces a knee where the dashed curve for the light balsa in figure 4 meets the decreasing solid curve. It should also be noted that specific energy absorption increases with increasing crushing stress for the honeycomb-like class, in contrast to the light balsa. It should finally be noted that each curve in figure 4 represents a class which contains, in principle, an infinite number of crushable materials, one of each crushing stress.

98

RESULTS AND DISCUSSION

Several design examples have been carried out utilizing the honeycomb-like material just discussed for a payload weight of 100 pounds. The resulting crushable casing weights in pounds are plotted in figure 5[†] against payload radius in feet, with a nonlinear scale attached for payload packaging density in pounds per cubic foot. These casing weights are fairly high because the honeycomb-like material is inefficient. An inefficient material, with the resulting heavy casing, is required to keep the 100 pound payload from feeling g-loadings higher than the arbitrarily assigned limit of 2000 when payload penetration is absent (open symbols in fig. 5).
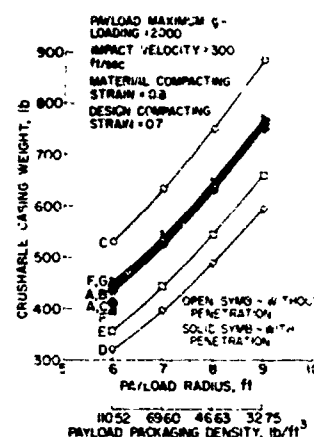
Fig. 5. Crushable Casing Weight for Honeycomb-like Material and a Payload Weight of 100 Pounds.

An important design condition is that all design examples in figure 5, including the penetration examples with solid symbols, are required to have a g-loading of 2000. Preliminary examples have shown that this use of the maximum permissible g-loading results in minimum crushable casing weight for all examples with honeycomb-like material. The impact velocity is 300 feet per second, the material compacting strain is 0.8, and the design compacting strain is 0.7. For these and all subsequent examples, there is a choice between zero and a hypothetical "perfect" bonding between the crushable casing and the top of the payload.

As might be expected, the crushable casing weight increases as the payload radius increases (and as the packaging density decreases) in figure 5.

†Numerical results for these and other examples, including outer radius and other pertinent parameters, are presented in Table I.

without penetration. This trend applies for all the analytical models, "A" through "G", with the "A" and "B" models of reference 11 roughly in the middle of a rather wide band. The band is wide enough to make a designer wish there were enough experimental data to determine the best analytical model in the absence of penetration.

When penetration is present in figure 5, however, the band is small enough to be neglected as shown by the filled symbols. Note that only three models involve payload penetration, and these only at the lowest payload radius considered. The existence of penetration at this radius means, however, that the "A", "C", and "F" models require bonding for universally nonpenetrating designs.

It is important at this point to notice in figure 5 that the nonpenetration designs for the "A", "C", and "F" models have higher crushable casing weights than the corresponding penetration designs (the reason being that penetration permits a higher crushing stress without exceeding the g-loading limit of 2000, which increases the specific energy absorption for the honeycomb-like class of material). Thus the "C" and "F" models bear out what was noted in ref. 11 for the "A" model, namely that penetration should not be prevented by bonding for the honeycomb-like material. This result may be fairly general since most materials have a positive SEA -v_0 slope similar to the honeycomb-like material in figure 4. This is true even for most balsas, with the two balsa curves in figure 4 being exceptions.

In figure 6, several design examples are presented utilizing the light balsa material with a payload weight of 450 pounds. Although the payload weighs 4 1/2 times the weight in the previous examples and has radii almost twice as large for the same impact velocity and compacting strains, the crushable casing weights without penetration are roughly the same or slightly smaller. The reason is that the heavy payload permits the use of the highly efficient light balsa without exceeding the g-loading limit of 2000.

The crushing stress was specified as the lowest available value (800 psi) without penetration and the value at the knee of the specific-energy-absorption curve (1200 psi) with penetration. These stresses define the extremes of the cored-balsa region, for which the specific energy absorption is a constant 24,000 foot-pounds per pound, and yield the lightest possible casings for each example according to preliminary calculations.

In the absence of payload penetration (open symbols in fig. 6), the crushable casing weight increases with increasing payload radius as before. The trend is once again the same for all analytical models, but the band is a little narrower this time.
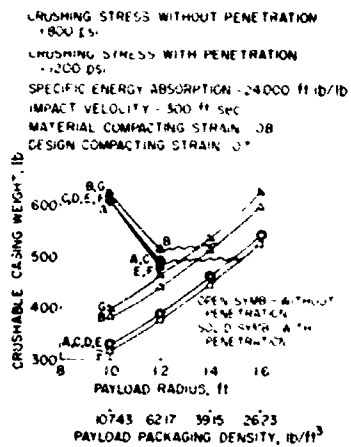
Fig. 6. Crushable Casing Weight for Light Balsa
Material and a Payload Weight of 450
Pounds.

In the presence of payload penetration (solid
symbols in figure 6), the band is small enough to oe
neglected. This time, however, all models penetrate
at the lowest payload radius considered and most
models at the next to lowest; and this time the pene-
tration adds to the crushable casing weight and makes
bonding desirable.

If the payload is not bonded, the wavy lines in
figure 6 indicate ranges for the payload radius which
yield the lowest crushable casing weight. The exis-
tence of such an optimum payload radius for all
models strengthens a similar result for the "A"
and "B" models in ref. 11.

In the examples given so far, the effect of pene-
tration has been evaluated only within a single class
of crushable materials. For the 100 pound payload,
however, penetration permits a change from the
honeycomb-like class of material to the much more
efficient light balsa class without exceeding the g-
loading limit of 2000. As illustrated in figure 7,
this change results in a substantial decrease in
crushable casing weight at payload radii of 0.6 and
0.7 feet. (The unshaded parts of the bars represent
the often substantial weight range resulting from the
variety of analytical models.) This decrease cor-
roborates for all seven models an earlier result
for the "A" and "B" models (ref. 11).

It is to be expected that the weight saving just
discussed will be sharply reduced if the honeycomb-
like material is replaced by a material of inter-
mediate efficiency which is just heavy enough to
bring the g-loading down to 2000 without penetration.
As seen in figure 7, such is indeed the case for the
presently specified heavy balsa material. An even
better material or structure might well have been

found or developed—one which would compete favorably
with the penetrating light balsa design. The penetrating
design will always have the advantage of simplicity,
however, in the sense of requiring no bond between the
payload and the crushable material.
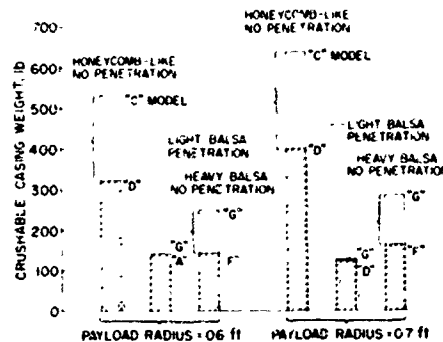
Fig. 7. Effect of Penetration on Crushable Material
Weight for Different Classes of Material
with a 100 Pound Payload at Two Payload
Radii.

CONCLUDING REMARKS

In summary, the important influence of payload
penetration on crushable casing weight and overall
design, recently demonstrated for two analytical
models, has been corroborated for several additional
models utilizing different combinations of assumptions.
This corroboration is based on three groups of design
examples: one group involving a 100 pound payload
and a specified honeycomb-like class of material, a
second group involving a 450 pound payload and a much
more efficient light balsa class, and a third group
involving the 100 pound payload and three classes of
material. In both groups of examples with the 100
pound payload, the payload should not be bonded to
prevent penetration because penetration decreases
the crushable casing weight.

REFERENCES

1. Bresie, Don: Practical Limits for Balsa Impact
   Limiters. NASA TN D-3175, 1966.
2. Research and Advanced Development Division of
   Avco Corporation: Conceptual Design Studies of
   an Advanced Mariner Spacecraft. Volume III
   Lander Design. RAD-TR-64-36, Contract
   950896, Jet Propulsion Lab., Oct. 28, 1964.
3. Carley, W. J.: Mars Entry and Landing Capsule.
   NASA TM 33-236, 1965.
4. Cundall, Donald R.: Balsa-Wood Impact Limiters
   for Hard Landing on the Surface of Mars. AIAA/

AAS Stepping Stones to Mars Meeting, Baltimore, Maryland, March 28-30, 1966, pp. 302-308.

5. Cloutier, G. J.: Landing Impact Energy Absorption Using Anisotropic Crushable Materials. J. Spacecraft Rockets, Vol. 3, No. 12, Dec. 1966, pp. 1755-1761.

6. Berkowitz, Harvey M.; and Rodriguez, David A..: Dynamic Analysis and Development of Response Histories and Tradeoff Study Charts for Spherical Impact Limiters. AIAA/ASME 8th Structures, Structural Dynamics, and Materials Conf., Palm Springs, Calif., March 29-31, 1967, pp. 400-412.

7. Anon.: Mars Lander Entry Studies. Volume II - System Analysis. Grumman Status Rep., Advanced Space Systems Group, March 1966.

8. Anon.: Mars Probe Final Report. Vol. II - Probe/Lander, Entry From the Approach Trajectory, Book 2 - Mission and System Specifications. Contract NAS1-5224, Avco Space Systems Div., May 11, 1966.

9. Anon.: Final Report for Impact Limiter Design, Fabrication, and Testing. Publ. UG-3934, Lunar and Planetary Programs, Space and Re-Entry Systems Div.. Philco-Ford Corp., Jet Propulsion Lab. Contract 951261, Jan. 30, 1967.

10. Knoell, A. C.: Landing Dynamics Program for Axisymmetric Impact Attenuating Vehicles (Land it). Technical Rep. 32-1341, Jet Propulsion Lab., November 15, 1968.

11. Warner, Robert W.: Approximate Analytical Models for Landing Energy Absorption, Including the Effect of Penetration by the Payload into Its Crushable Casing. NASA TN D-5835, 1970.

12. Anon.: Final Report - Systems Study for Lunar Reconnaissance Probe. Space General Corp., El Monte, Calif. Report SGC 410R-2, Part II, February 21, 1964.

101

CASE	MODEL	PARAMETERS DETERMINED BY PROGRAM	R_p ft	ρ_{pe} lb/ft	BONDED?	MATERIAL H=HONEYCOMB LIKE B=LIGHT BALSA	PAYLOAD PENETRATION?	$n_{p\,max}$	σ_0 psi	ρ_{cm} lb/ft³	SEA ft lb/lb	$n_{p\,max}/\sigma_t$	R	W_{co} lb	AVERAGE PROGRAM EXECUTE TIME FOR CLASS, MIN	NO. OF CASES IN CLASS
1A2RS	A	R σ_0	06	110 52	YES	H	NO	1999.9	1073 7	11.499	10,756	1.5191	2.0969	434.92	0.40	9
1B2RS	B	R σ_0	06	110 52	YES	H	NO	2000.0	1395 3	13 297	12,090	NON EX	2.0077	438.75	0.58	9
1C2RS	C	R σ_0	06	110 52	YES	H	NO	2000.9	893 6	10 384	9,910	1.8455	2 3157	630 85	0.76	9
1D2RS	D	R σ_0	06	110 52	YES	H	NO	2000.1	1545 0	14 058	12,652	NON EX	1.7814	320.42	0.85	9
1E2RS	E	R σ_0	06	110 52	YES	H	NO	1999 5	1338 6	12 994	11,868	NON EX	1.5926	357.24	0.82	9
1F2RS	F	R σ_0	06	110 52	YES	H	NO	1999.8	862 9	10 186	9,757	i 9226	2.2041	447.75	0.59	9
1G2RS	G	R σ_0	06	110 52	YES	H	NO	1999 5	1668 2	14.679	13,092	NON EX	1.9569	448.80	0.61	9
2A2R	A	H	06	110 52	NO	H	YES	1999 9	1228 0	12 388	11,420	1.4044	2 0123	411.61	0.66	2
2B2R	B	R	06	110 52	NO	H	NO	1802.9	1228 0	12 388	11,420	NON EX	2.1465	501.99	1.00	2
2C2R	C	R	06	110 52	NO	H	YES	1999 6	1228 0	12 388	11,420	1.5698	2 0083	409 08	5.64	2
2D2P	D	R	06	110 52	NO	H	NO	1694 0	1228 0	12 388	11,420	NON EX	1.9695	384.57	0.43	2
2E2R	E	R	06	110 52	NO	H	NO	1875.0	1228.0	12 388	11,420	NON EX	1.9695	384.57	1.16	2
2F2R	F	R	06	110 52	NO	H	YES	1999 5	1228 0	12 388	11,420	1 5753	1.9881	396.56	5.96	2
2G2R	G	R	06	110 52	NO	H	NO	1515 4	1228.0	12 388	11,420	NON EX	2.3702	679.73	0.56	2
3A2R	A	R	06	110 52	NO	B	YES	1954.3	1200.0	5.758	24,007	3 0281	1.8107	137.99	0.47	8
3B2R	B	R	06	110 52	NO	B	YES	1954.8	1200 0	5 758	24,007	2.8774	1.8213	140.50	4.55	7
3C2R	C	R	06	110 52	NO	B	YES	1957 9	1200 0	5.758	24,007	3.0708	1.8147	138.94	6.25	8
3D2R	D	R	06	110 52	NO	B	YES	1953 9	1200.0	5 758	24,007	2.8118	1.8136	138.67	5.12	6
3E2R	E	H	06	110 52	NO	B	YES	1954 7	1200 0	5 758	24,007	2.9690	1.8141	138.80	5.02	8
3F2R	F	R	06	110 52	NO	B	YES	1961 4	1200 6	5 758	24,007	3.0698	1.8133	138.51	5.82	8
3G2R	G	R	06	110 52	NO	B	YES	1953.9	1200.0	5.758	24,007	2.8232	1.8221	140.70	5.08	6
4A2RS	A	R, σ_0	07	69 60	NO	H	NO	1999 5	1122.7	11 787	10,972	NON EX	2.2297	530.40	0.40	9
4B2RS	B	R, σ_0	07	69 60	NO	H	NO	1999 9	437.3	13.316	12,250	NON EX	2.1313	528.73	0.56	9
4C2RS	C	R σ_0	07	69 60	NO	H	NO	2000.2	941.7	10.094	10,145	NON EX	2 4397	535.11	0.76	9
4D2RS	D	R, σ_0	07	69 60	NO	H	NO	20G0.0	1586.6	14.277	12,603	NON EX	1.9111	386.94	0.85	9
4E2RS	E	R, σ_0	07	69 60	NO	H	NC	2000.0	1373 0	13.178	12,003	NON EX	2.0315	443.82	0.82	9
4F2RS	F	R, σ_0	07	69 60	NO	H	NO	1999 9	306 6	9.975	9,975	0.9843	2.3313	540 08	0.59	9
4G2RS	G	R, σ_0	07	69 60	NO	H	NO	1999.5	1731.7	14.988	13,312	NON EX	2.0761	540.2C	0.61	9
5A2R	A	R	07	69 60	NO	B	YES	2000.3	902 4	4.332	24,000	2.4901	1.9297	123.94	0.47	8
5B2R	B	R	07	69 60	NO	B	YES	2000.0	902 4	4 332	24,000	2.3232	1.9411	126.47	4.55	7
5C2R	C	R	07	69 60	NO	B	YES	2002.1	902.4	4 332	24,000	2 5234	1.9303	124.27	6.25	8
5D2R	D	R	07	69.60	NO	B	YES	2000.0	902 4	4.332	24,000	2.2416	1.9280	123.81	5.12	6
5E2R	E	R	07	69 60	NO	B	YES	2000 0	902.4	4.332	24,000	2.3097	1.9292	123.08	5.02	8
5F2R	F	R	07	69 60	NO	B	YES	2005.2	902.4	4.332	24,000	2.5207	1.9288	123.95	5.82	8
5G2R	G	R	07	69 60	NO	B	YES	2000.0	902.4	4.332	24,000	2.2583	1.9432	126.91	5.08	6
6A2RS	A	R, σ_0	08	46 63	NO	H	NO	2000.0	1182.1	12.129	11,228	NON EX	2.3632	636.03	0.40	9
6B2RS	B	R, σ_0	08	46 63	NO	H	NO	20G0.1	1491.8	13.798	12,455	NON EX	2.2997	637.28	0.58	9
6C2RS	C	R, σ_0	09	46 63	NO	H	NO	1999 9	999.5	11.062	10,418	NON EX	2.5698	762.81	0.76	9
6D2RS	D	R, σ_0	08	46 63	NO	H	NO	1999.9	1645.4	14.587	13,012	NON EX	2.0422	468.47	0.85	9
6E2RS	E	R, σ_0	08	46 63	NO	H	NO	2000.2	1420.3	13.427	12,185	NON EX	2.1691	545.20	0.82	9
6F2RS	F	R, σ_0	08	46 63	NO	H	NO	1999.9	960.6	10.812	10,236	NON EX	2.4547	648.43	0.59	9
6G2RS	G	R, σ_0	08	46 63	NO	H	NO	2000.3	1808 1	15.354	13,574	NON EX	2.1954	647.62	0.61	9
7A2RS	A	R, σ_0	09	32.75	NO	H	NO	2000.5	1251 4	12.518	11,517	NON EX	2.4743	756.06	0.40	9
7B2RS	B	R, σ_0	09	32.75	NO	H	NO	2000 0	1554.3	14.115	12,685	NON EX	2.3876	761.59	0.58	9
7C2RS	C	R, σ_0	09	32 75	NO	H	NO	1999.7	1085.3	11.451	10,719	NON EX	2.5799	865.15	0.76	9
7D2RS	D	R, σ_0	09	32 75	NO	H	NO	1999.8	1716.3	14.912	13,259	NON EX	2.1715	594.01	0.85	9
7E2RS	E	R, σ_0	09	32 75	NO	H	NO	2000.0	1477.2	13.723	12,401	NON EX	2.3047	661.76	0.82	9
7F2RS	F	R σ_0	09	32 75	NO	H	NO	2000.1	1022.7	11.193	10,525	NON EX	2.5740	765 46	0.59	9
7G2PS	G	R, σ_0	09	32 75	NO	H	NO	2000.0	1894.5	15.751	13,856	NON EX	2 3155	771.00	0.61	9

102

TABLE I – NUMERICAL RESULTS FOR U_o = 300 FT/SEC, ϵ_d = 0.7, ϵ_m = 0.8, AND $n_{p\,max} \leq 2000$ (ROUGHLY) – Continued

(b) HEAVY BALSA MATERIAL WITH W_{po} ~ 100 LB
[Symbols are defined in the section on Nomenclature]

CASE	MODEL	PARAMETERS DETERMINED BY PROGRAM	R_p ft	$\rho_{p,\theta}$ lb/ft³	BONDED?	PAYLOAD PENETRATION?	$n_{p\,max}$	σ_o psi	$\rho_{cm,\epsilon}$ lb/ft³	SEA ft lb/lb	$q_{p\,max}/c_s$	R ft	W_{co} lb	AVERAGE PROGRAM EXECUTE TIME FOR CLASS, MIN	NO OF CASES IN CLASS
15A2RS	A	R, σ_o	0.6	110 52	YES	NO	1999 7	534.71	4 400	14,000	4 021?	2 0986	163 35	0 40	9
16B2R	B	R	0.6	110 52	YES	NO	1674 6	553 0	4 550	14,000	3.8622	2 2436	211 16	0 22	11
16C2RS	C	R, σ_o	0.6	110 52	YES	NO	1999.9	398.8†	3.281	14,000	5 1444	2 2449	152 53	0 76	9
16D2R	D	R	0.6	110 52	YES	NO	1534.6	553 0	4 550	14,000	3 7021	2 0845	168 51	0 22	11
16E2R	E	R	0.6	110 52	YES	NO	1965.4	553 0	4 550	14,000	3 7494	2.0845	168 51	0 22	11
16F2RS	F	R, σ_o	0.6	110 52	YES	NO	1999 7	409 7†	3.371	14,000	4 9569	2.1708	141 40	0 59	9
16G2R	G	R	0.6	110 52	YES	O	1522 5	553 0	4 550	14,000	3.8454	2 3624	247 19	0 23	11
18A2RS	A	R, σ_o	0 7	89 60	YES	NO	2000 1	523 3†	4 306	14,000	2 7350	2 2277	193 22	0 40	9
18B2R	B	$\circ$	0 7	89 60	YES	NO	1687 0	553 0	4 550	14,000	2 4748	2 3557	242 63	0 22	11
18C2R2	C	R, σ_o	0 7	89.60	YES	NO	2000 3	387 3†	3.187	14,000	3 6082	2 3747	174 22	0 76	9
18D2R	D	R	0.7	89 60	YES	NO	1548.4	553 0	4 550	14,000	2 3377	2 2029	197 22	0 22	11
18E2R	E	R	0.7	89.60	YES	NO	1580 7	553.0	4 550	14,000	2 4256	2 2029	197 22	0 22	11
18F2RS	F	R, σ_o	0.7	89.60	YES	NO	2000 2	495 8†	3 257	14,000	3 4953	2 3007	161 46	0 59	9
1B32R	G	R	0.7	89.60	YES	NO	1516 4	553 0	4 550	14,000	2 3838	2 4790	283 85	0 23	11

†These σ_o values, which indicate a coring of more than one-third of the material, were required to keep $n_{p\,max} \leq 2000$ (roughly) and resulted in lighter designs than with σ_o = 553 0 psi

113

(c) LIGHT BALSA MATERIAL WITH W_{po} = 450 LB

Symbols are defined in the section on Nomenclature

CASE	MODE	PARAMETER DETERMINED BY PROGRAM	t	p_w lb	BONDED	PAYLOAD PENETRATION	$h_{p\,max}$	p_s	$c_m q_s$ lb ft	SEA ft lb/lb	$q_{p\,max}/q_s$	R ft	W_{co} lb	AVE PROGRAM EXECUTE TIME FOR CLASS MIN	NO OF CASES IN CLASS
5A2R	A	H	1.0	107.43	YES	NO	1772.7	800.0	3840	24 000	3.4786	2.7751	327.67	0.18	13
5B2R	B	H	1.0	107.43	YES	NO	1480.5	800.0	3840	24 000	3.5288	2.9044	377.98	0.22	11
5C2R	C	H	1.0	107.43	YES	NO	1878.4	800.0	3840	24 000	3.5012	2.7754	327.77	0.17	11
5D2R	D	H	1.0	107.43	YES	NO	1358.6	800.0	3840	24 000	3.2902	2.7754	327.77	0.22	11
5E2R	E	H	1.0	107.43	YES	NO	1434.4	300.0	3840	24 000	3.3195	2.7754	327.77	0.22	11
5F2R	F	H	1.0	107.4	YES	NO	1859.9	800.0	3840	24 000	3.4504	2.7468	217.28	0.17	11
5G2R	G	H	1.0	107.43	YES	NO	1409.4	800.0	3840	24 000	3.567C	2.9532	398.19	0.23	11
9A2R	A	H	1.0	107.43	NO	YES	1206.4	1200.0	5758	24 007	2.9350	2.9721	604.15	0.47	8
9B2R	B	H	1.0	107.43	NO	YES	1736.4	1200.0	5758	24 007	2.7839	2.9898	620.49	4.55	7
9C2R	C	H	1.0	107.43	NO	YES	1208.5	1200.0	5758	24 007	2.9774	2.9778	612.74	6.25	8
9D2R	D	H	1.0	107.43	NO	YES	1206.0	1200.0	5758	24 007	2.7155	2.9759	611.52	5.12	6
9E2R	E	H	1.0	107.43	NO	YES	1206.4	1200.0	5758	24 007	2.7726	2.9768	612.11	5.02	8
9F2R	F	H	1.0	107.43	NO	YES	1210.4	1200.0	5758	24 007	2.9744	2.9756	611.37	5.82	8
9G2R	G	H	1.0	107.43	NO	YES	1206.0	1200.0	5758	24 007	2.7264	2.9915	621.62	5.08	6
11A2R	A	H	1.2	62.17	YES	NO	1835.4	800.0	3840	24 000	2.2016	2.9592	389.01	0.18	13
11B2R	B	H	1.2	62.17	YES	NO	1556.2	800.0	3840	24 000	2.1383	3.0757	440.23	0.22	11
11C2R	C	H	1.2	62.17	YES	NO	1843.3	800.0	3840	24 000	2.2376	2.9595	389.13	0.17	11
11D2R	D	H	1.2	62.17	YES	NO	1431.9	800.0	3840	24 000	1.9688	2.9595	389.13	0.22	11
11E2R	E	H	1.2	62.17	YES	NO	1522.8	800.0	3840	24 000	2.0283	2.9595	389.13	0.22	11
11F2R	F	H	1.2	62.17	YES	NO	1926.2	800.0	3840	24 000	2.2066	2.9302	376.88	0.17	11
11G2R	G	H	1.2	62.17	YES	NO	1465.0	800.0	3840	24 000	2.1204	3.1223	461.80	0.23	11
11A2R	A	R	1.2	62.17	NO	YES	1737.2	1200.0	5758	24 007	1.5562	2.8074	492.01	0.47	8
11B2R	B	R	1.2	62.17	NO	YES	1736.8	1200.0	5758	24 007	1.3483	2.8457	514.17	4.55	7
11C2R	C	R	1.2	62.17	NO	YES	1736.6	1200.0	5758	24 007	1.6145	2.8073	491.97	6.25	8
11D2R	D	R	1.2	62.17	NO	NO	1796.4	1200.0	5758	24 007	NON EX	2.7320	450.17	0.43	2
11E2R	E	R	1.2	62.17	NO	YES	1736.8	1200.0	5758	24 007	1.3119	2.7960	485.54	5.02	8
11F2R	F	R	1.2	62.17	NO	YES	1736.8	1200.0	5758	24 007	1.6097	2.8002	487.89	5.82	8
11G2R	G	R	1.2	62.17	NO	NO	1730.0	1200.0	5758	24 007	NON EX	2.8091	528.00	0.55	2
12A2R	A	R	1.4	39.15	YES	NO	1879.1	800.0	3840	24 000	1.4158	3.3534	460.24	0.18	13
12B2R	B	R	1.4	39.15	YES	NO	1627.9	800.0	3840	24 000	1.2994	3.2590	512.64	0.22	11
12C2R	C	R	1.4	39.15	YES	NO	1988.4	800.0	3840	24 000	1.4770	3.1537	460.41	0.17	11
12D2R	D	R	1.4	39.15	YES	NO	1498.8	800.0	3840	24 000	NON EX	3.1537	460.41	0.22	11
12E2R	E	R	1.4	39.15	YES	NO	1605.8	800.0	3840	24 000	1.1294	3.1537	460.41	0.22	11
12F2R	F	R	1.4	39.15	YES	NO	1973.0	800.0	3840	24 000	1.4579	3.1233	445.94	0.17	11
12G2R	G	R	1.4	39.15	YES	NO	1517.4	800.0	3840	24 000	NON EX	3.3076	537.93	0.23	11
13A2R	A	R	1.6	26.23	NO	NO	1907.4	800.0	3840	24 000	NON EX	3.3564	542.32	0.18	13
13B2R	B	R	1.6	26.23	NO	NO	1686.8	800.0	3840	24 000	NON EX	3.4535	596.62	0.22	11
13C2R	C	R	1.6	26.23	NO	NO	2016.3	800.0	3840	24 000	0.9607	3.3568	542.53	0.17	11
13D2R	D	R	1.6	26.23	NO	NO	1557.0	800.0	3840	24 000	NON EX	3.3568	542.53	0.22	11
13E2R	E	R	1.6	26.23	NO	NO	1670.1	800.0	3840	24 000	NON EX	3.3568	542.53	0.22	11
13F2R	F	R	1.6	26.23	NO	NO	2002.4	800.0	3840	24 000	0.9478	3.3252	525.51	0.17	11
13G2R	G	R	1.6	26.23	NO	NO	1563.3	800.0	3840	24 000	NON EX	3.5040	626.10	0.23	11

DAMPING

EFFECT OF FREE LAYER DAMPING

ON RESPONSE OF STIFFENED PLATE STRUCTURES

David I. G. Jones*
Air Force Materials Laboratory
Wright-Patterson AFB, Ohio 45433

Simple formulae are derived using the normal-mode method, representing the effect of uniform free layer treatments on the modal damping and stiffness and the stress levels under uniform random loading of stiffened skin-stringer type structures. The damping and stiffness formulae are simple generalizations of the well known Oberst equations for uniformly covered unstiffened structure and are subject to similar limitations and restrictions. The formulae for random rms stress levels give a simple accounting for multi-modal response and give the maximum nominal stress in the skin regardless of where this maximum occurs, but do assume that the design is adequate, so that the stress levels in the stiffeners do not exceed this level. Experimental verification is offered in some instances.

INTRODUCTION

Stiffened skin-stringer structures are still used in many areas of modern aerospace vehicles wherein they are expected to withstand jet engine and boundary layer noise excitation on fuselage and control surface areas and to have reasonably low acoustic transmissibility and propagation characteristics in embedded-engine duct regions. To achieve these desirable characteristics, careful attention must be paid to design details such as stringer and frame spacing, skin thickness, curvature effects, stringer geometry, ratio of stringer to frame spacing, noise absorbing materials etc. However, the damping of the structure is also a characteristic which often has an important bearing on response amplitudes, stress levels, noise transmissibility, and sound propagation along ducts. For some structures of the skin-stringer category, for which the geometry is such that the modes of vibration occur in distinct and well separated groups in the frequency domain, tuned damping devices might conceivably be used for the purpose of introducing useful amounts of damping; although no successful practical applications are known.

For most skin-stringer structures,

however, the geometry is such that the modes do not fall into distinct groups and may occupy a very wide frequency band, so that tuned dampers would be ineffective. In such cases, layered damping treatments would be more suitable. These include the free layer treatment, the constrained layer treatment, the sandwich skin and the many variations of these. However, analysis of complex skin-stringer structure with such treatments applied is usually difficult.

An examination of the literature pertinent to the effect of free layer treatments on structural response reveals a number of important milestones, such as Oberst's celebrated equations [1] for the effect of uniform free layer treatments on stiffened (or rigidly stiffened) structures, Mead's investigations [2] of the effects of random loading and partial coverage and, more recently, the possibility of applying transfer matrix techniques to the exact solution of response problems of multiple bay stiffened structures with additive damping [3]. Most of these analyses have been rather complicated, however, and no simple formulae for stiffened plates with uniform coverage, comparable with those of Oberst for unstiffened plates, have appeared

---

*Technical Manager for Vibrations and Damping, Strength and Dynamics Branch, Metals and Ceramics Division.

in the literature.

It is the purpose of this paper to derive, by means of the normal mode method, simple formulae representing the effect of uniform free layer treatments on the response and damping of skin-stringer structures and to verify experimentally the accuracy of the results. The formulae are simple generalizations of those of Oberst for unstiffened structures and are subject to similar limitations and restrictions as to conditions of applicability. The analysis may also possibly be extended to take account of the effect of multiple layer constrained damping treatments on response and damping, by making use of the fact that, within limits, such treatments can be treated as equivalent free layer treatments [4].

RESPONSE TO HARMONIC EXCITATION

Analysis

a. Damping of Unstiffened Plates

The equations describing the effect of a stiff free-layer treatment, as illustrated in Figure 1, completely covering an unstiffened (or rigidly stiffened) plate, on the damping and resonant frequency are well established, as for example by Oberst [1]. These equations are:

$$\frac{\eta_s}{\eta_D} = \frac{en}{1+en} \left[\frac{3+6n+4n^2+2en^3+e^2n^4}{1+2en(2+3n+2n^2)+e^2n^4}\right] \quad (1)$$

$$\left(1+\frac{\rho_D h_D}{\rho h}\right)\frac{f_r^2}{f_{nm}^2} = \frac{1+2en(2+3n+2n^2)+e^2n^4}{1+en} \quad (2)$$

where η_s is the loss factor of the structure, η_D the loss factor of the damping material at the resonant frequency f_r of the damped structure. f_{nm} is the undamped natural frequency of the structure in the n,m mode. These formulae are the basis of the Oberst technique for measuring the damping properties of stiff viscoelastic materials [5].

An alternative derivation to that of Oberst is more convenient for present purposes. The Euler-Bernoulli equation for the plate-damping layer combination may be written in the form:

$$D_e \nabla^4 W - (\rho h + \rho_D h_D) \, \omega^2 W = P(x,y) \quad (3)$$

where $D_e = D + D_D \quad (4)$
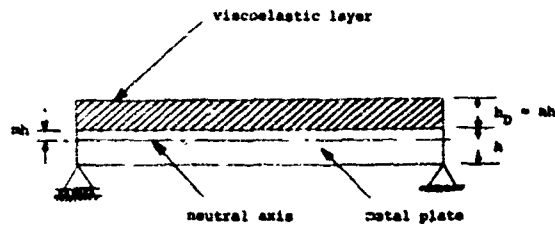
Figure 1. Free layer treatment on unstiffened plate

and D is the flexural rigidity of the plate, and D_D that of the free layer, allowing for the movement of the neutral axis. The distance mh of the neutral axis from the center plane of the metal plate may be determined by recognizing that the net thrust in the x and y directions must be zero in the absence of in-plane forces i.e. $\int \sigma_x dz = \int \sigma_y dz = 0$. From the standard theory of bending of plates, it is therefore readily seen that [6]:

$$m = (1-n^2 e)/2(1+ne) \quad (5)$$

The flexural rigidities D and D_D are, therefore:

$$D = \int_{-(1-m)h}^{mh} [E/(1-\nu^2)]z^2 dz = Eh^3 A/24(1-\nu^2) \quad (6)$$

$$D_D = \int_{mh}^{(m+n)h} [E_D(1+i\eta_D)/(1-\nu^2)] \, z^2 dz =$$

$$E_D h^3 B(1 + i\eta_D)/24(1 - \nu^2) \quad (7)$$

if it is assumed that $\nu_D = \nu$. In these equations A and B are defined by:

$$A = \{(1-n^2 e)^3 + (1+[2n+n^2]e)^3\}(1+ne)^{-3} \quad (8)$$

$$B = \{(2n+1+n^2 e)^3 - (1-n^2 e)^3\} \, (1+ne)^{-3} \quad (9)$$

If η_s is the effective loss factor of the structure, it is then readily seen from an examination of equation (3) that:

$$\eta_s = \text{Im}(D_e)/\text{Re}(D_e) = \eta_D(1+A/Be)^{-1} \quad (10)$$

and the frequency ratio f_r/f_{nm} is given by:

$$(1+\rho_D h_D/\rho h)(f_r/f_{nm})^2 = Re(D_e)/D_O =$$

$$(A + Be)/2 = 1 + (A-2+Be)/2 \qquad (11)$$

if use is made of the undamped and damped plate equations for free motion:

$$D_O \nabla^4 W - \rho h \omega_{nm}^2 W = 0$$

$$Re(D_e) \nabla^4 W - (\rho h + \rho_D h_D) \omega_r^2 W = 0$$

Eq⁻ ns (10) and (11) are apparently sc t different from those of Obeist. Ho :, it is readily verified that the two sets of equations are, in fact, identical.

b. Damping of Stiffened Plate Structure

The analysis of the stiffened plate is necessarily somewhat different from that of the unstiffened plate because of the different equations governing stiff-ener motion. A useful approximate analysis may be developed by considering the effect of an elementary rectangle $\Delta x \Delta y$ of damping layer attached to the surface of the plate, as in Figure 2. It is assumed that the element $\Delta x \Delta y$ is small, so that the curvature of the deformed plate surface is uniform. It is assumed, as in standard plate theory, that plane sections remain plane. The unbalanced moments M_x and M_y at the ends of the element oppose the motion of the plate and give rise to the damping. These moments are, from standard theory:

$$M_x = (D_e - D_O)[(\partial^2 W/\partial x^2) + \nu(\partial^2 W/\partial y^2)] \qquad (12)$$

$$M_y = (D_e - D_O)[(\partial^2 W/\partial y^2) + \nu(\partial^2 W/\partial x^2)] \qquad (13)$$

where $D_e = D + D_D$.
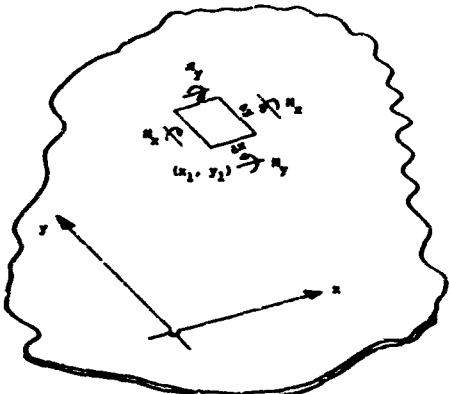
Figure 2. Element of free layer treatment on stiffened plate

These moments, in turn, may be represented as pairs of forces $M_x/\delta x$ and $M_y/\delta y$, a distance $\delta x, \delta y$ apart respectively, as in Figure 3. The damping material element has therefore been replaced by a set of forces acting on the plate and the Equation of Motion may be written:

$$D\nabla^4 W - \rho h \omega^2 W - \rho_D h_D \omega^2 W \, I(x_1,x_2) \, I(y_1,y_2) =$$

$$P(x,y) - (M_x/\delta x)[\delta(x-x_1) - \delta(x-x_1-\delta x) - \delta(x-x_2) + \delta(x-x_2-\delta x)] \, I(y_1,y_2) +$$

$$(M_y/\delta y)[\delta(y-y_1) - \delta(y-y_1-\delta y) - \delta(y-y_2) + \delta(y-y_2-\delta y)] \, I(x_1,x_2) \qquad (14)$$

We now expand W and P as series of normal modes of the undamped structure, i.e. $W = \sum_{nm} W_{nm} \phi_{nm}(x,y)$; $P = \sum_{nm} P_{nm} \phi_{nm}(x,y)$ where the modes ϕ_{nm} satisfy the homogeneous differential equation

$$D_O \nabla^4 \phi_{nm} = \rho h \omega_{nm}^2 \phi_{nm} \qquad (15)$$

and the orthogonality property

$$\iint_S \phi_{nm}(x,y) \phi_{pq}(x,y) \, dx \, dy = 0 \, (m,n \neq p,q)$$
$$\neq 0 \, (m=n, p=q) \qquad (16)$$
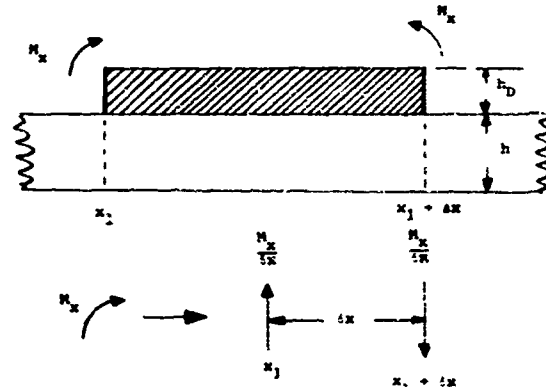
Figure 3. Forces and moments arising from damping layer element

Using these expansions, factoring Equation (14) throughout by ϕ_{pq}, integrating over the surface area S, using the properties of the delta functions, taking the limit as Δx and $\Delta y \to 0$, and integrating over the treatment area D, we therefore have:

$$W_{pq}(\rho h_{pq}^2 - \rho h^2) \iint_S \phi_{pq}^2 \, dxdy \; -$$

$$\rho_D h_D \omega^2 \iint_D \sum_{nm} W_{nm} \phi_{nm} \phi_{pq} \, dxdy \; =$$

$$-(D_e - D_o) \iint_D \sum_{nm} W_{nm} \left[\frac{\partial^2 \phi_{nm}}{\partial x^2} + \frac{\partial^2 \phi_{nm}}{\partial y^2} \right] \frac{\partial^2 \phi_{pq}}{\partial x^2} \; +$$

$$\left[\frac{\partial^2 \phi_{nm}}{\partial y^2} + \frac{\partial^2 \phi_{nm}}{\partial x^2} \right] \frac{\partial^2 \phi_{pq}}{\partial y^2} \right] dxdy \; +$$

$$P_{pq} \iint_S \phi_{pq}^2 \, dxdy \qquad (17)$$

This is a series of coupled equations for the various W_{pq} and cannot be solved exactly in most cases. However, if the treatment covers the structure surface uniformly, the coupling terms are usually small. The criteria necessary for this step to be allowable are:

$$\iint_D (\partial^2 \phi_{nm}/\partial x^2)(\partial^2 \phi_{pq}/\partial x^2) \, dxdy$$

$$\ll \iint_D (\partial^2 \phi_{nm}/\partial x^2)^2 \, dxdy$$

$$\iint_D (\partial^2 \phi_{nm}/\partial y^2)(\partial^2 \phi_{pq}/\partial y^2) \, dxdy$$

$$\ll \iint_D (\partial^2 \phi_{nm}/\partial y^2)^2 \, dxdy$$

$$\iint_D (\partial^2 \phi_{nm}/\partial y^2)(\partial^2 \phi_{pq}/\partial x^2) \, dxdy$$

$$\ll \iint_D \left(\frac{\partial^2 \phi_{nm}}{\partial y^2} \right) \left(\frac{\partial^2 \phi_{nm}}{\partial x^2} \right) \, dxdy$$

Ultimate verification of the validity of neglecting coupling will demand a knowledge of the modes and their derivatives for each specific structure. For the moment it will be assumed that this step is allowable, so that to a reasonable degree of approximation:

$$W_{pq}(\rho \omega_{pq}^2 - \rho h \omega^2) \iint_S \phi_{pq} \, dxdy \; -$$

$$\rho_D h_D \omega^2 W_{pq} \iint_D \phi_{pq}^2 \, dxdy \; =$$

$$-(D_e - D_o) W_{pq} (I_{pq}/L^4) + P_{pq} \iint_S \phi_{pq}^2 dxdy \quad (18)$$

where:

$$I_{pq} = \iint_D [(\partial^2 \phi_{pq}/\partial \alpha^2)^2 + (L/\ell)^4 (\partial^2 \phi_{pq}/\partial \delta^2)^2 +$$

$$2\nu (L/\ell)^2 (\partial^2 \phi_{pq}/\partial \alpha^2)(\partial^2 \phi_{pq}/\partial \delta^2)] dxdy$$
$$(19)$$

Therefore:

$$W_{pq} = \frac{P_{pq} L^4 / D_o}{\varepsilon_{pq}^4 - \varepsilon^4 \left\{ 1 + \frac{\rho_D h_D \alpha_{pq}}{\rho h} \right\} + \frac{(D_e - D_o) 2 \varepsilon_{pq}^4}{D_o \beta_{pq}}} \quad (20)$$

where

$$\alpha_{pq} = \iint_D \phi_{pq}^2 \, dxdy / \iint_S \phi_{pq}^2 \, dxdy \quad (21)$$

and

$$\beta_{pq} = 2\varepsilon_{pq}^4 \iint_S \phi_{pq}^2 \, dxdy / I_{pq} \quad (22)$$

Now $(D_e - D_o)/D_o = \Lambda/2 - 1 + B\varepsilon/2 + i\eta_D B\varepsilon/2$ so that, if η_s is the effective loss factor in the pqth mode:

$$\eta_s = \eta_D [1 + (\Lambda - 2 + \beta_{pq})/B\varepsilon]^{-1} \quad (23)$$

and the frequency ratio is given by:

$$(1 + \rho_D h_D \alpha_{pq}/\rho h)(\xi_r/\xi_{pq})^4 = 1 + (\Lambda - 2 + B\varepsilon)/\beta_{pq}$$
$$(24)$$

It is seen that equations (23) and (24) are more general representations of the Oberst equations and reduce to those equations for unstiffened plates, in which case $\beta_{pq} = 2$ and $\alpha_{pq} = 1$. Essentially, α_{pq} is a parameter measuring the inertial effect of the treatment, and is equal to unity for full coverage of stiffened and unstiffened plates, and β_{pq} is a measure of the effect of the stiffeners. The generalized Oberst equations are applicable under much the same conditions as the original Oberst equations, i.e. the structure must be fully and uniformly covered with the treatment. If the structure is only partially covered, neither the Oberst nor the generalized Oberst equations are applicable, and coupling must be allowed for through equations (17) or some other means. Nevertheless, the equations are extremely useful since they give simple algebraic expressions for the damping and resonant frequencies of any uniformly covered structure for which α_{pq} and β_{pq} are known or can be estimated.

The functions A and B are defined in equations (8) and (9) if the treatment is applied directly to the skin surface of the structure. Graphs of useful combinations of these functions, namely A-2+Be, A/Be and Be, versus e and n are illustrated in Figures 4 to 6. The other variables on which the modal damping depends are β_{pq} and α_{pq}. α_{pq} is about unity for uniform coverage, but β_{pq} can vary widely. For example, $\beta_{pq} = 2$ for a very lightly stiffened structure, or a very heavily stiffened structure in which the stiffeners do not move to all intents and purposes. For typical skin stringer structure β_{pq} can vary from 3 to 10 or more. For integrally stiffened structures, illustrated in Figure 7, β_{pq} can vary from 10 to 30 or more, so that very little damping can be achieved unless, as is possible in some cases, the treatment is applied across the tops of the stiffeners, as suggested by Cicci and Clarkson [7]. In this case, the β_{pq} remain the same, but the functions A and B are changed to take account of the new neutral axis location, leading to greatly increased damping. Further damping may also accrue if the strips of viscoelastic material resonate and act as tuned damping devices [7]. However, this latter source of damping is of very uncertain value in view of the variation of the properties of most viscoelastic materials with temperature, leading to highly variable resonant frequencies for the strips of damping material. If, in the system illustrated in Figure 7c, the stiffeners are assumed to rotate without bending as the plate deforms, the free layer treatment may be treated as if merely separated by a distance $H = Mh$ from the skin surface and the distance mh of the new neutral axis, obtained as before, becomes:

$$m = \frac{1 - ne(2M + n)}{2(1 + ne)} \qquad (25)$$

and, upon determining D and D_D as in equations (6) and (7), it turns out that:

$$A = \frac{\{1 - ne(2M + n)\}^3 + \{1 + ne(2 + 2M + n)\}^3}{(1 + ne)^3} \qquad (26)$$

$$B = \frac{\{2n + 1 + 2M + n^2 e\}^3 - \{1 + 2M - n^2 e\}^3}{(1 + ne)^3} \qquad (27)$$

all of which expressions reduce to equations (5), (6) and (7) respectively for $M = 0$. For large values of M, of the order of 10 or more as is quite typical, the values of A and B are far greater than for $M = 0$. As an example, let $n = 1$, $n_D = 0.5$, $e = 0.1$, and $\beta_{rm} = 20$. Then for $M = 0$, Be = 2.2, and

A-2+Be $\doteq$ 2.4, whence B $\doteq$ 22, A $\doteq$ 2.2, and $n_s \doteq 0.031$. On the other hand, when $M = 10$, A $\doteq$ 26.2 and B $\doteq$ 2350, where $n_s \doteq 0.42$. This represents an increase in n_s by a factor of over ten. Even greater relative gains can be achieved if β_{rm} is greater than the value assumed in the above example, as may readily be verified.
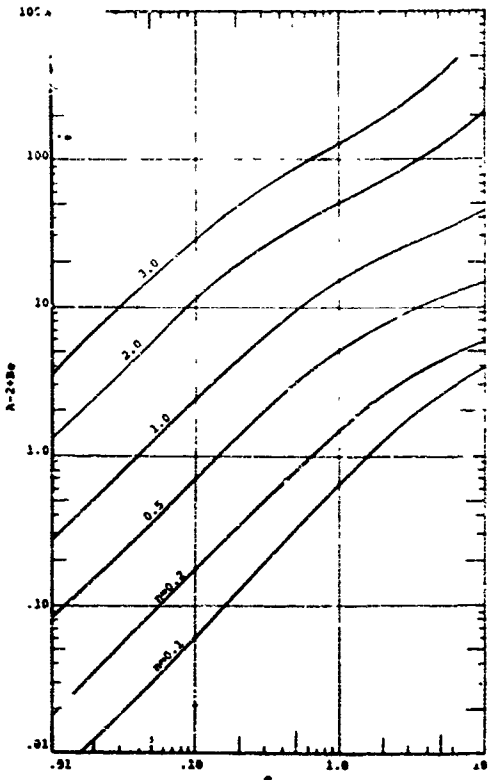
Figure 4.   Graphs of A-2+Be versus e and n

Experimental Investigations

a. Tests on Cantilever Beams

In order to verify the analysis, it was first necessary to measure the properties of the material to be used for the free layer treatment. The material selected was LD-400, attached to the structure surface by means of a very thin layer of self adhesive tape (Scotch brand #410, 3M Co.). The cantilever beam tests were carried out on an aluminum beam 0.05 inches thick and 7 inches long. The free layer thickness was equal to the beam thickness in each case. The beams were clamped at the root in the fixture of the Bruel and Kjaer complex modulus apparatus as shown in Figure 8, in the customary manner [5]. The response characteristics

109
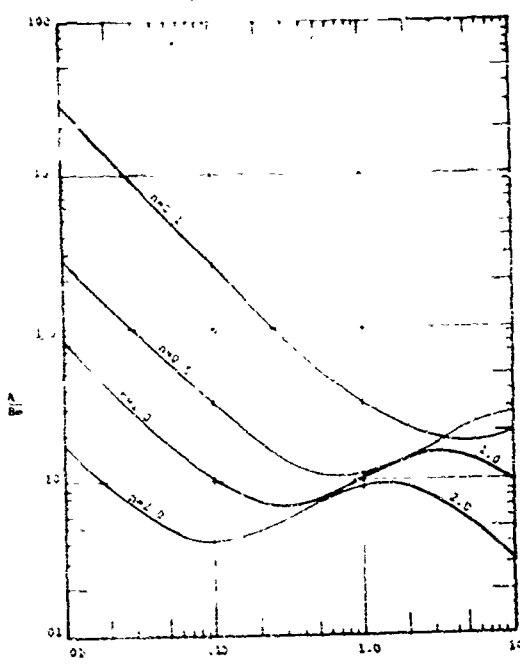
Figure 5.   Graphs of A/Be
versus e and n
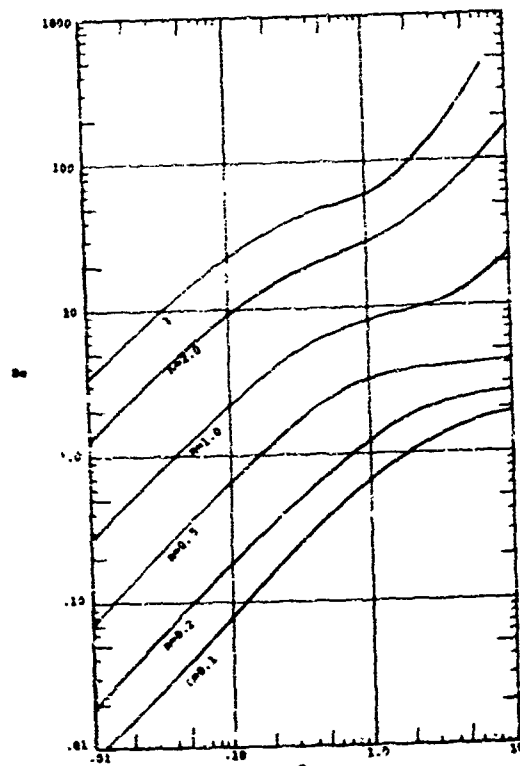
Figure 6.   Graphs of Be
versus e and n
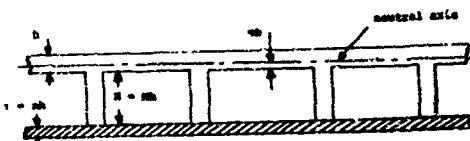
Figure 7.   Free layer treatment
configurations

of the first two resonances were noted
and graphs of measured loss factor η_s
and $(1+\rho_D h_D/\rho h)(f_s/f_r)^2$ versus tempera-
ture are shown in Figure 9. From equa-
tions (1) and (2), the values of E_D and
η_D, the modulus and loss factor of the
sample of LD-400* used, were calculated
and are plotted in Figure 10.
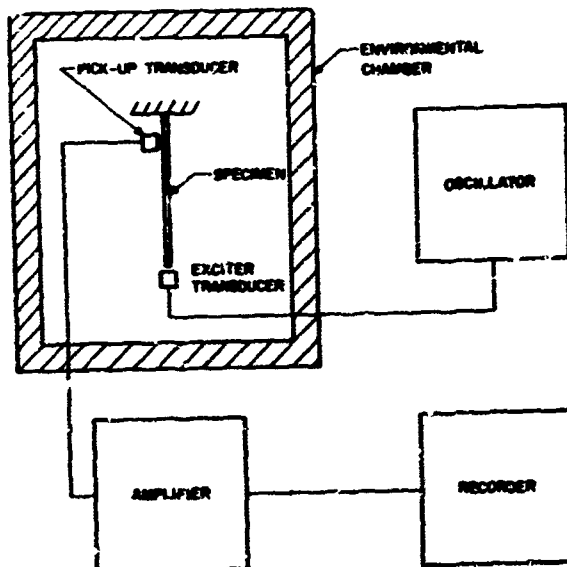
Figure 8.   Specimen in
Complex Modulus
Apparatus

*Lord Mfg. Co., Erie, Pa.

110

Figure 9. Graphs of η_s and
$(1+\rho_D h_D/\rho h)(f_r/f_n)^2$
versus temperature

Figure 10. Complex modulus data

In order to verify the analysis for stiffened structures, a one-span structure was built in such a way as to retain as great a degree of simplicity as possible. The geometry of the structure is shown in Figure 11. The skin was attached to the frames by means of bolts and the frames in turn were attached to a shaker table through two pairs of three-quarter inch deep blocks

Figure 11. Geometry of one-span stiffened structure

The first tests were carried out to determine mode shapes, resonant frequencies and initial damping, using a sub-miniature accelerometer to measure response. The first two modes are illustrated in Figures 12 and 13, and were obtained by moving the accelerometer over the structure and measuring the response at constant input. It is seen that the longitudinal modal functions are very close to sinusoidal in shape, whereas those in the transverse direction are practically those of a clamped-clamped beam with an effective length between clamping points of 7.0 inches. The fundamental mode of a clamped-clamped beam [8] is superimposed. Figure 14 shows the variation of resonant

111

frequencies with skin thickness. From
these figures, estimated values of ζ^4_{11}
and $\zeta^{''}_{11}$ are plotted in Figure 15.
Using these values of ζ and ζ_{11}, and
the assumed mode shapes and deriva-
tives [8], it was readily shown that
$\beta_{11} = 3.2$ and $\beta_{31} = 2.7$ for $h_p = 0.050$
inches and α_{11} and α_{31} were approximate-
ly unity. The initial damping was
small, being of the order 0.007.
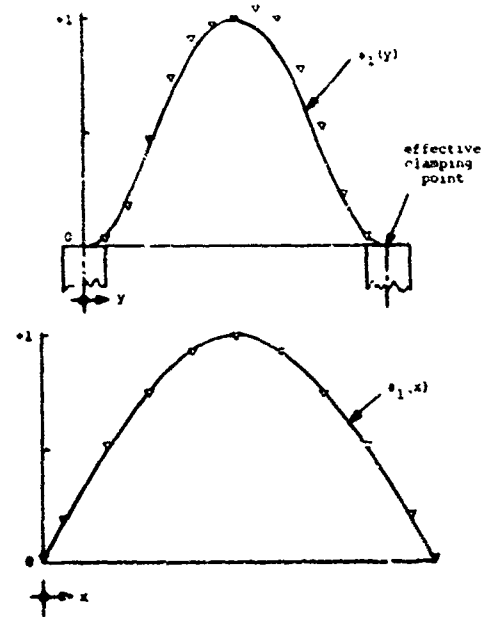
Figure 12. Observed mode 1,1 shapes
for h = 0.050"

The next tests were carried out
for a 0.05 inch panel thickness, with a
layer of damping material [LD-400] 0.04
inches thick attached to the surfac. by
means of a very thin layer of the self-
adhesive tape as in the beam tests. The
structure was then placed in an environ-
mental chamber as in Figure 16 and ex-
cited by means of a small magnetic
transducer at the center. The response
amplitude was picked up by means of a
sub-miniature accelerometer at the cen-
ter and the damping η measured in the
1,1 and 3,1 modes by means of the "half-
power bandwidth" method. Measured val-
ues of η and $(1+\rho_D h_D/\rho h)(f_x/f_{nm})^2$ are
plotted against temperature in Figures
17 and 18. Analytical results based on
$\beta_{11} = 3.2$ and $\beta_{31} = 2.7$ in equations
(23) and (24), are superimposed and
agree well with the measured results.

The good agreement between theory
and experiment indicates that the modal
coupling is indeed low for nearly full
coverage and that the estimates of β_{11}
and β_{31} are reasonably accurate. In the
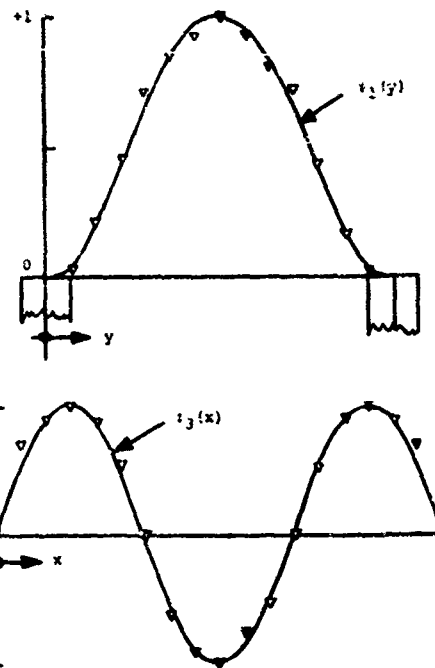
Figure 13. Observed mode 3,1 shapes
for h = 0.050"
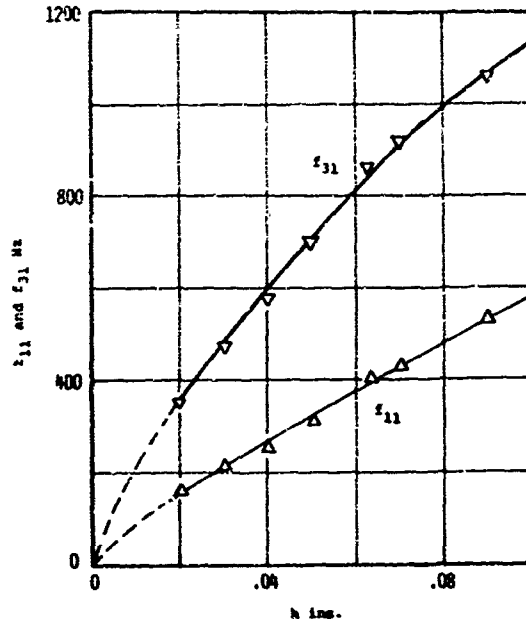
Figure 14. Frequencies of
stiffened plate

case of more general structures, the
estimation of β_{pq} is a very difficult
matter since the modes and their deriva-
tives are rarely known to the requisite
degree of accuracy. In that event, one
may often invert the procedure and esti-
mate β_{pq} by applying a known treatment

112
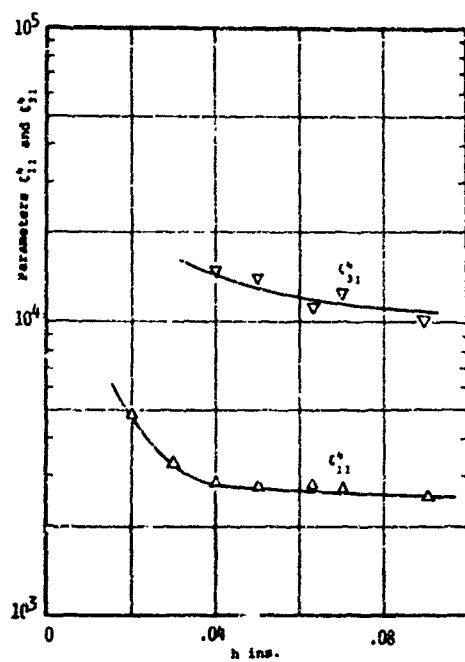
Figure 15. ξ_{11}^4 and ξ_{31}^4 versus h
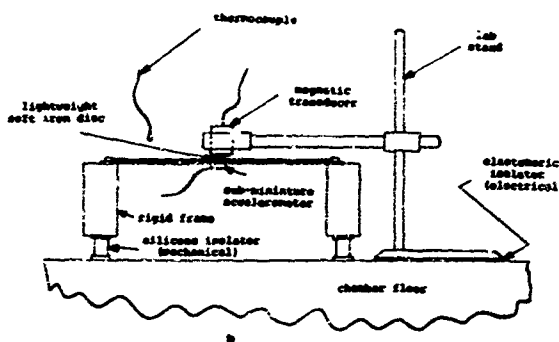
Figure 16. One-span structure in environmental chamber

Figure 17. η_s and $(1+\rho_D h_D/\rho h)f_r^2/f_{11}^2$ versus temperature for 1 1 mode
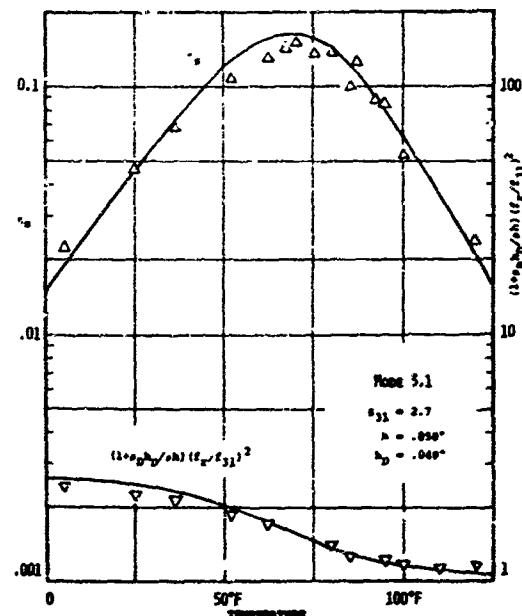
Figure 18. η_s and $(1+\rho_D h_D/\rho h)f_r^2/f_{31}^2$ versus temperature for 3,1 mode

in such a way as to eliminate, or nearly eliminate, coupling and then vary β_{pq} in equations (23) and (24) until the analy is and the measured data agree. This may seem a trivial point, but the then known values of β_{pq} can thereafter be used along with these equations to estimate the effect of other treatments. This procedure will be followed in the case of the three-span skin-stringer structure.

c. Tests on a Three-Span Stiffened Structure

In order to verify, at least qualitatively, the usefulness of the analysis for more complex structures, a three-span skin-stringer structure was built, as illustrated in Figures 19-21.

The structure was first excited in the undamped state in the manner illustrated in Figure 22. Using the magnetic transducer and sweeping frequency, it

Figure 19. Overall geometry of three-span structure

FRAME SECTION

STRINGER SECTION

TYPICAL STRINGER / FRAME JOINT
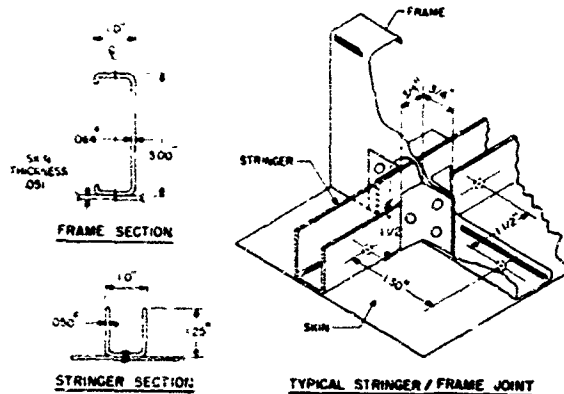
Figure 20. Details of stiffener geometry
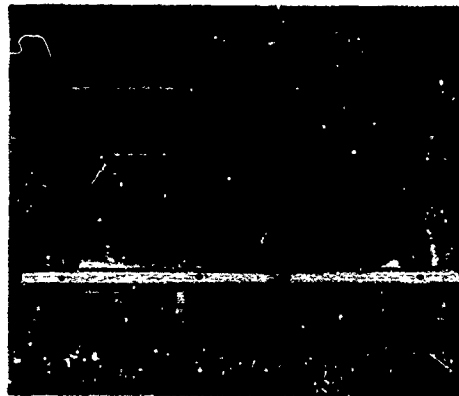
Figure 21. Photograph of three-span structure

was readily established that the first "stringer torsion" mode and the first "stringer bending" mode could readily be excited. The intermediate mode, being unsymmetrical about the center of the plate, was not excited. Higher

modes could also be excited but only with great difficulty because of very close spacing of the modes in the frequency domain. Typical response spectra in the three bays, as measured by miniature accelerometers, are illustrated in Figure 23. The significant resonant frequencies were observed to change very slightly over the temperature range 0°F to 125°F.
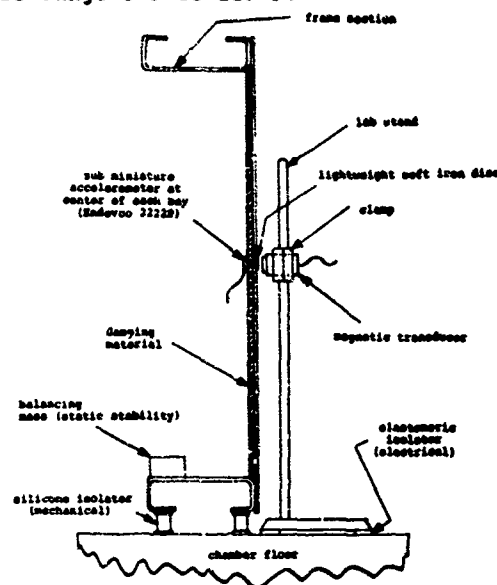
Figure 22. Three-span structure in environmental chamber
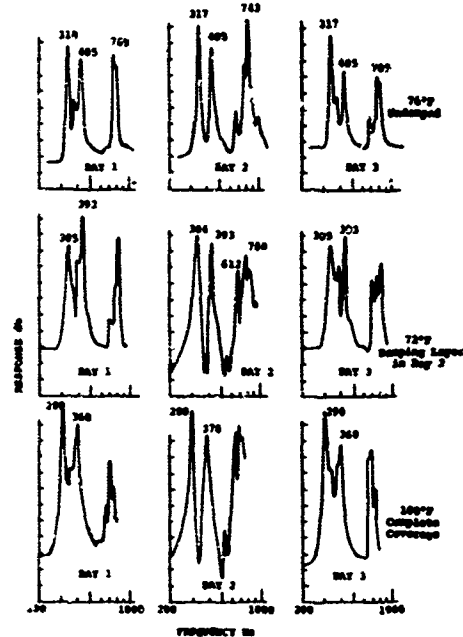
Figure 23. Response Spectra

114

The next tests were carried out with a single layer of LD-400, attached by means of the double-back tape as before, on the center bay only. Coupling between modes was quite strong, apparently, because the observed values of η_s for the two first band modes behaved as shown in Figure 24 with temperature. This variation bore little resemblance to that anticipated if no coupling were present.
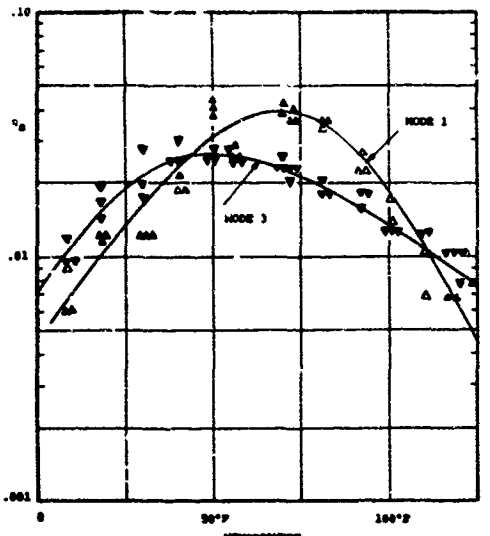
Figure 24.   Graphs of η_s versus temperature

When LD-400 sheets were attached to all three bays and the tests repeated, the variation of η_s with temperature was as shown in Figure 25. The data is plotted for both modes and for all three bays. If β_{pq} is taken to be equal to 8 and if the same LD-400 properties are used, the analysis predicts the results shown in Figure 25. The consistency of the agreement is quite satisfactory and indicates that a single parameter β_{pq} for both modes, equal to 8.0, is sufficient to account for the observed damping and resonant frequencies.

RESPONSE TO UNIFORM RANDOM LOADING

Response of Skin-Stringer Structure

So far, we have calculated the loss factor and frequency of a damped stiffened structure. These quantities in turn affect the behavior of the structure under random excitation, as by a jet engine, and the effect of the damping treatment on rms stresses is of considerable importance. The problem of predicting the stress response levels in
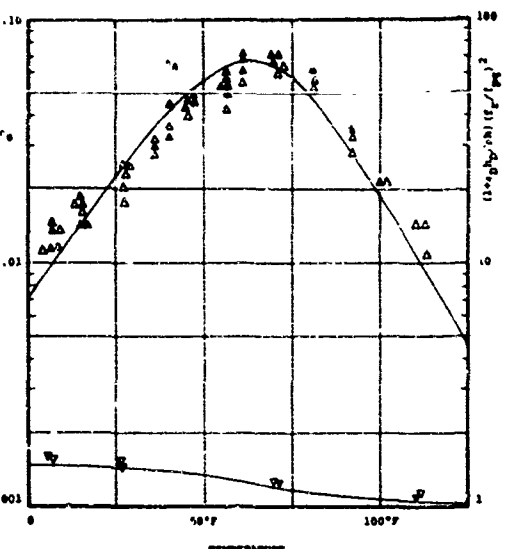
Figure 25.   Graphs of η_s and $(1+\rho_D h_D/\rho h)^s (f_r/f_{pq})^2$ versus temperature

skin-stringer structure under acoustic excitation has been examined by many investigators in recent years, the work of Ballantine et al [9], Clarkson [10], and Wang [11] being indicative of the current state of the art. These investigations have shown the role of detail design and structure geometry and have led in some cases to design charts, based on testing of specific types of structure. Limitations have included the need to assume only one significant mode of vibration, a certain lack of conservatism in the agreement between the analyses and the available experimental data and lack of information concerning the magnitude of the damping.

It is assumed in the present analysis that the random pressure loading on the skin-stringer structure is uniform over the entire surface, that the power spectral density of the excitation is uniform over the frequency range of significant response and the damping material is applied uniform   so that modal coupling can be negl

Consider first any flat skin-stringer structural element under uniform harmonic loading $P \exp(i\omega t)$ as in Figure 21. Then from equation (20), the response at any point (x,y) is:

$$\left[\frac{E_0}{L^4 P}\right] W(x,y) =$$

$$\sum_p \sum_q \frac{\gamma_{pq}\phi_{pq}(x,y)\exp(i\omega t)}{\xi_{pq}^4 - \xi^4\left[1+\frac{\alpha_{pq}\rho_D h_D}{\rho h}\right] + (A-2+Be+i\eta_D Be)\dfrac{\xi_{pq}^4}{\beta_{pq}}} \qquad (28)$$

115

where

$$\gamma_{pq} = \int_S \phi_{pq}\, dxdy \bigg/ \int_S \phi_{pq}^2\, dxdy \qquad (29)$$

The stress response in the x-direction, parallel to the frames for the skin-stringer structure, is given by:

$$\sigma_x = E(1-m)h[(d^2W/dx^2)+\nu(d^2W/dy^2)]; \qquad (30)$$

and, if the frames are very much stiffer than the stringers, $\phi_{pq}(x,y)$ can usually be written in the separable form $\phi_p(x)\phi_q(y)$ where $\phi_q(y) \sim \mathrm{Sin}(q\pi y/\ell)$. Therefore, upon simplification:

$$\sigma_x = \frac{EhL_p^4}{2D_0 L^2}\left[\frac{1+ne(2+n)}{1+ne}\right] \quad \times$$

$$\sum_{pq}\frac{\gamma_{pq}[\phi_p'' + (\nu q^2 L^2 \pi^2/\ell^2)\phi_p]\phi_q}{\xi_{pq}^4\left[1+\frac{A-2+Be}{\beta_{pq}}\right]\left[\left(1-\frac{\xi^4}{\xi_{pq}^4}\right)+i\eta_{spq}\right]} \qquad (31)$$

where $\phi_p'' = L^2 d^2\phi_p/dx^2$, η_{spq} is the value of η_s for the p,q mode and

$$x_{pq}^4 = \frac{\xi_{pq}^4[1 + (A-2+Be)/\beta_{pq}]}{1 + \alpha_{pq}\rho_D h_D/\rho h} \qquad (32)$$

If we now replace the harmonic excitation P by a random loading of spectral density $G_p(\omega)$, the mean square stress response $\overline{\sigma_x^2}$ is given by:

$$2\pi\left[\frac{2D_0(1+ne)}{EhL^2(1+2ne+an^2)}\right]^2 \frac{\overline{\sigma_x^2}}{G_p^2(\omega)}\left(\frac{\rho hL^4}{D_0}\right)^{\frac{1}{2}} =$$

$$\int_0^\infty \sum_{pq}\frac{\gamma_{pq}[\phi_p'' + (\nu q^2 \pi^2 L^2/\ell^2)\phi_p]\phi_q}{\left[1-\frac{\xi^4}{x_{pq}^4} + i\eta_{spq}\right]\left[1+\frac{A-2+Be}{\beta_{pq}}\right]\xi_{pq}^4} \times$$

$$\sum_{nm}\frac{\alpha_{nm}[\phi_n'' + (\nu m^2 \pi^2 L^2/\ell)\phi_n]\phi_m\, d\xi^2}{\left[1-\frac{\xi^4}{x_{pq}^4} - i\eta_{snm}\right]\left[1+\frac{A-2+Be}{\beta_{nm}}\right]\xi_{nm}^4} \qquad (33)$$

where $d\xi^2 = d\omega(\rho hL^4/D_0)^{1/2}$. The integral in equation (33) can be evaluated numerically if the maximum values of p and q are not too great within the range of significant response and if γ_{pq}, ϕ_p, ϕ_q and ξ_{pq} are known. For the present, however, we shall utilize Mercer's observation [12] that the errors involved in neglecting cross terms in the expansion of the double series in equation (33) is small, so that to a reasonable degree of approximation:

$$2\pi\left[\frac{2D_0(1+ne)}{EhL^2(1+2ne+en^2)}\right]^2 \frac{\overline{\sigma_x^2}}{G_p^2}\left(\frac{\rho hL^4}{D_0}\right)^{\frac{1}{2}} =$$

$$\sum_{pq}\frac{\gamma_{pq}^2[\phi_p'' + (\nu q^2 \pi^2 L^2/\ell^2)\phi_p]^2\phi_q^2}{x_{pq}^6(1+\alpha_{pq}\rho_D h_D/\rho h)} \times$$

$$\int_0^\infty\frac{d(\xi/x_{pq})^2}{(1-\xi^4/x_{pq}^4)^2 + \eta_{spq}^2} \qquad (34)$$

The integral in equation (34) has been evaluated by Mead [13]:

$$\int_0^\infty\frac{d\theta}{(1-\theta^2)^2+\eta^2} = F^2(\eta) =$$

$$\left\{\frac{\pi}{2\sqrt{2\eta}}\sqrt{\frac{1+\sqrt{1+\eta^2}}{1+\eta^2}}\right\}^2 \qquad (35)$$

so that, finally:

$$\frac{2D_0(1+ne)}{EhL^2(1+2ne+en^2)}\left(\frac{\rho hL^4}{D_0}\right)^{\frac{1}{4}}\overline{\sigma_x^2} =$$

$$\frac{G_p\beta F(\eta_{spq})(1+\alpha_{pq}\rho_D h_D/\rho h)^{1/2}}{N[1+(A-2+Be)/\beta_{pq}]^{3/2}} \qquad (36)$$

where

$$\beta = \sum_{pq}\frac{N^2\gamma_{pq}^2\phi_q^2[\phi_p'' + (\nu q^2 \pi^2 L^2/\ell^2)\phi_p]^2}{\xi_{pq}^6} \qquad (37)$$

if we assume that α_{pq}, β_{pq} and η_{spq} are approximately independent of mode number, as is often the case for uniform coverage of damping treatment.

The advantage of equation (36) is that it does allow, in some degree, for multi-modal response and the damping and

stiffening effects of the treatment in a simple equation. Furthermore, it most fortunately turns out that the maximum value of $\beta(x,y)$ does not vary greatly from structure to structure even though the point at which this maximum occurs may vary widely. The value of β_{max} may be determined readily in specific idealized cases from a knowledge of the modes, their derivatives and the eigenvalues. For example, it can be shown that (i) $\beta_{max} = 0.52$ for a pinned-pinned plate at the center in the fundamental mode (ii) $\beta_{max} = 0.45$ for the first mode of a clamped-clamped-pinned-pinned plate at the clamped edges (iii) $\beta_{max} = 0.52$ at the two center support locations for a five span pinned plate [14] vibrating in the first band of modes only (iv) $\beta_{max} = 0.57$ for the two center support locations of a nine-span pinned plate vibrating in the first band of modes only and (v) $\beta_{max} = 0.55$ for a typical skin-stringer structure [15]. It may therefore be taken that $\beta_{max} = 0.51$. Now $\nu = 1/3$ and $F(\eta_s) \doteq \sqrt{\pi/2\eta_s}$ for small η_s, so that equation (36) becomes, for a typical stiffened plate structure:

$$\overline{\sigma^2}_{max} \doteq 0.75 G_c (L/N) E^{1/4} h^{-3/2}$$

$$\times \rho^{-1/4} \eta_s^{-1/2} f(n,e) \qquad (38)$$

where

$$f(n,e) = \left[1 + \sigma_{pq} \frac{\rho_D h_D}{\rho h}\right]^{\frac{1}{4}} \left[\frac{1+2ne+en^2}{1+ne}\right]$$

$$\times \left[1 + \frac{A \cdot 2 + Be}{\beta_{pq}}\right]^{-\frac{3}{4}} \qquad (39)$$

If $n = 0$, $f(0,e) = 1$ and we recover the rms stress levels for a nominally undamped structure. In order to ensure that the structure can withstand a given spectral density G_D without exceeding a specified rms stress, therefore, one may vary the geometrical parameters L/N and h, the physical parameters E and ρ and the damping treatment parameters, η_s and $f(n,e)$. Clearly, L/N and h are the most influential variables and should be chosen properly at the design stage. Once fixed, however, changes are difficult and expensive to make and the only other parameters capable of being varied without major structural alterations are the damping parameters. The quantity $\eta_s^{-1/2} f(n,e)$ is therefore a direct measure of the effectiveness

of a given damping treatment in reducing the rms stress levels in a given structure.

In order to illustrate the application of equation (39), consider the structures tested earlier, for which h = 0.05 inches and ℓ_{ne} varies from 2.0 to 8.0. If LD-400 is applied uniformly, using the adhesive tape as before, in a 0.036 inch uniform thickness, then $\sigma_{pq} \doteq 1.0$ and n = 0.72. The properties of the LD-400 sample are taken from Figure 10. The resulting graphs of $\eta_s^{-1/2} f(n,e)$ are plotted versus temperature in Figure 26. It is seen that for $\beta_{pq} = 8$, $[\eta_s^{-1/2} f(n,e)]_{min}$ is equal to about 4.2 whereas for a nominally undamped structure, for which $f(n,e) = 1$ having $\eta_s = 0.005$, $\eta_s^{-1/2} f(n,e) \doteq 14.1$. This amounts to a significant reduction in random stress level. The temperature range of useful stress level reduction can be observed in Figure 26 also.
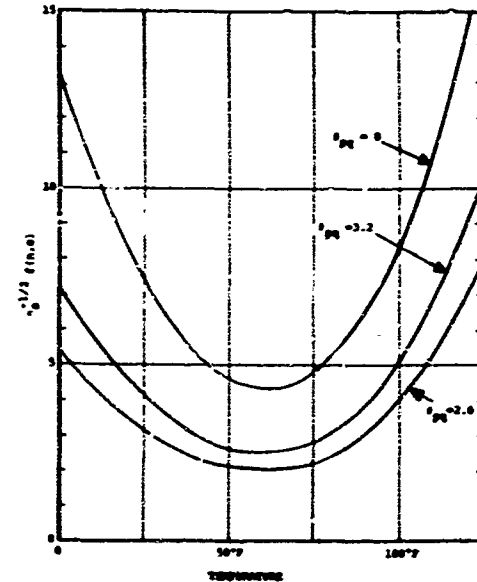
Figure 26. Graphs of $\eta_s^{-1/2} f(n,e)$ versus temperature

Experimental Investigations

No directly applicable data relating to measured rms stress levels in structures damped by a free layer appear to be available. However, for nominally undamped structures, a considerable body of information has been published. In order to compare equation (38) with this experimental data, it is advantageous to recall that $\sqrt{\sigma^2}_{max}$, η_s and G_D are quantities associated with each particular test condition, whereas E, h, L, N and ρ are associated with the structure geometry and materials. It is therefore more

117

convenient to rearrange this equation into the dimensional group form:

$$\overline{\sigma_{max}}/G_p = 0.75 (L/N) E^{1/4} h^{-3/2} \rho^{-1/4} \tag{40}$$

Two separate major sources of test data are cited, one associated with an Air Force Flight Dynamics Laboratory contractual investigation reported in reference [9] and the other with an Air Force Materials Laboratory sponsored investigation reported in references [10,16].

a. Test Series No. 1[9]

In this test series, a number of skin-stringer structures of various thicknesses h and loss factors η were excited by various random acoustic loadings G_p. For these structures, L=20 ins., N = 3 or 4, $E = 10^7$ Lb/in², $\rho = 0.101$ Lb/in³. Some of the test results, reduced according to equation (49), are shown in Table 1.

b. Test Series No. 2[16]

In this test series, a wide variety of skin-stiffener structures were tested under random acoustic excitation. Test results for those configurations applicable to the present analysis, namely equation (40), are shown in Table 1.

Figure 27 shows the graph of $\sqrt{\sigma_{max}^2}\,\eta/G_p$ versus $0.75(L/N) E^{1/4} L^{-3/2} \rho^{-1/4}$. It is seen that the analysis does indeed come close to being an upper bound to the observed stress levels.
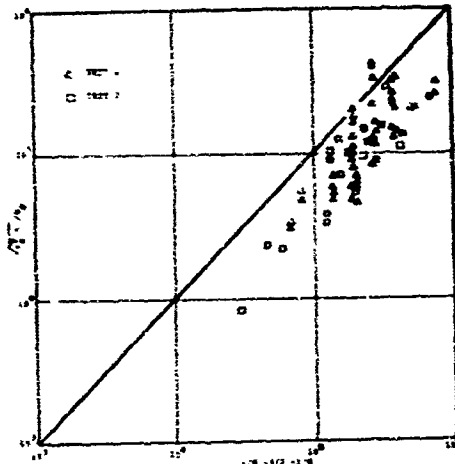
Figure 27. Comparison of theory and experiment for acoustically induced stresses.

CONCLUSIONS

It has been shown that extremely simple algebraic expressions can be used to estimate the response and damping characteristics of stiffened skin-stringer structures uniformly covered with a free layer damping treatment. These equations are simple generalizations of the classical equations of Oberst for uniform coverage of unstiffened structures.

REFERENCES

1. Oberst, H. and Frankenfeld, "Über die Dämpfung der Biegeschwingungen dünner Bleche durch festhaltende Belage", Acustica, Vol. 2, Leaflet 4, AB 181-194, part 1, 1952, Vol. 4, part 2, p. 433, 1954.

2. Mead, D. J., "The Optimum Use of Unconstrained Layer Damping Treatments", Air Force Materials Laboratory Report ML-TDR-64-51, August 1964.

3. Henderson, J. P. and McDaniel, T. J., "The Analysis of Curved Multi-Span Structures", Proc. Symp. on Structural Dynamics, Paper No. C6, Loughborough University, England, March 1970.

4. Plunkett, R. and Lee, C. T., "Length Optimization for Constrained Viscoelastic Layer Damping". Air Force Materials Laboratory Report, APML-TR-68-376, July 1969.

5. Nashif, A. D., "New Method for Determining Damping Properties of Viscoelastic Materials", Shock and Vibration Bulletin 36, Part 4, pp. 37-47, January 1967.

6. Jones, D. I. G., "Some Aspects of the Analysis of Damping and Vibrations in Simple Structures", Air Force Materials Laboratory Report AFML-TR-65-151, December 1965.

7. Clarkson, B. L. and Cicci, F., "Methods of Reducing the Response of Integrally Stiffened Structures to Random Pressures", Paper No. 69-Vibr-26, Trans. ASME, J. Eng. for Industry, 1969.

8. Bishop, R. E. D. and Johnson, D. C., The Mechanics of Vibration, (Cambridge Univ. Press, London, England, 1960, ed. 1).

9. Ballentine, J. R., Plumblee, H. E. and Schneider, C. W., "Sonic Fatigue in Combined Environment", Air Force Flight Dynamics Laboratory Report AFFDL-TR-61-7, 1966.

10. Clarkson, B. L., "Stresses in Skin Panels Subjected to Random Acoustic Loading", The Aeronautical Journal, Vol. 72, No. 695, pp. 1000-1010, 1968.

11. Wang, P., "Modeling Techniques for Sonic Fatigue", Air Force Flight Dynamics Laboratory Report, AFFDL-TR-65-171, 1966.

12. Mercer, C. A., "Response of a Multi-Supported Beam to a Random Pressure Field", J. Sound and Vibration, Vol. 2, p. 293, 1965.

13. Mead, D. J., "The Effect of Certain Damping Treatments on the Response of Idealized Aeroplane Structures Excited by Noise", Air Force Materials Laboratory Report AFML-TR-65-284, p. 103, 1965.

14. Jones, D. I. G., "Effect of Isolated Tuned Dampers on Response of Multi-Span Structures", J. Aircraft, Vol. 4, No. 4, pp. 343-346, 1967.

15. McDaniel, T. J., "Vibrations of a Stringer-Panel Structure with Mass Loading", Air Force Materials Laboratory Report AFML-TR-68-294, Part I. March 1969.

16. Clarkson, B. L., "Stresses in Skin Panels Subjected to Random Acoustic Loading", Air Force Materials Laboratory Report AFML-TR-67-199. 1967.

TABLE 1. EXPERIMENTAL STRESS AND EXCITATION LEVELS

Test No.	Orig. Des.	L ins	N	ℓ ins	h ins	Spect Level db	G_p psi $(Hz)^{-\frac{1}{2}}$	$\sqrt{\sigma^2}_{max}$ ksi	η	$\frac{\sqrt{\sigma^2}\eta}{G_p}$	$.75\left(\frac{E}{\rho}\right)^{\frac{1}{2}}\frac{L}{N} \times h^{-\frac{3}{2}}$
1	STR-1A	20	3	12	.032	123	.00415	5.22	.030	218,000	386,000
	STR-2A	20	3	12	.032	123	.00415	4.53	.036	205,000	386,000
	STR-3A	20	3	12	.032	119	.00258	5.05	.028	328,000	386,000
	STR-5B	20	3	12	.050	129	.00830	4.71	.026	91,500	197,000
	STR-6A	20	3	12	.071	130	.00930	6.40	.020	97,400	200,000
	STR-8A	20	3	12	.100	140	.0292	5.11	.034	32,800	70,000
	STR-9A	20	3	12	.040	120	.00294	6.20	.034	38,800	274,000
	STR-20A	20	3	12	.090	137	.0209	6.85	.026	53,000	82,000
	STR-23A	20	4	12	.032	121	.0033	3.41	.024	160,000	280,000
2	3-C	7.35	1	7.35	.040	116	.0018	1.50	.034	154,000	306,000
	4-E	8.20	1	–	.040	119	.00255	4.00	.034	289,000	341,000
	5R-E	4.13	1	–	.050	121	.00325	1.78	.034	101,000	123,000
	6-C	4.1	1	–	.032	125	.0051	4.04	.034	146,000	238,000
	8-E	5.75	1	–	.040	112	.00112	0.70	.034	115,000	238,000
	9-C	6.50	1	–	.048	118	.00228	1.25	.034	101,000	205,000

A,B	non-dimensional parameters	α_{nm}	non-dimensional parameters
D	flexural rigidity of plate allowing for shift of neutral axis caused by damping layer; also symbol representing area covered by damping material	β, β_{nm}	non-dimensional parameters
		γ_{nm}	non-dimensional parameter
		Δ	x/L
		δ	y/ℓ
D_D	flexural rigidity of damping layer allowing for shift of neutral axis	$\delta(x)$	Dirac Delta Function of argument x
e	E_D/E - modulus ratio	η_s	loss factor of structure in a specific mode
E	Young's modulus of structure material	η_D	loss factor of free layer material
E_D	Young's modulus of free layer material	ν	Poisson's ratio, assumed same for plate and free layer material
$f(n,e)$	non-dimensional parameter	ξ	$(\rho h \omega^2 L^4/D_0)^{1/4}$ - frequency parameter
f_r	resonant frequency of damped plate	ξ_{nm}	nmth eigenvalue - $(\rho h \omega_{nm}^2 L^4/D_0)^{1/4}$
f_{nm}	nmth resonant frequency of undamped plate	ξ_r	$(\rho h \omega_r^2 L^4/D_0)^{1/4}$
$G_p(\omega)$	spectral density	ρ	density of plate material
h	thickness of plate	ρ_D	density of free layer material
h_D	thickness of free layer	σ_x	stress amplitudes at surface of structure
i	$\sqrt{-1}$	$\overline{\sigma_x^2}$	mean square stress
$I(x_1,x_2)$	step function ($I = 1, x_1 \leq x \leq x_2$; $I = 0$ otherwise)	ϕ_{nm}	nmth normal mode of undamped plate
I_{pq}	integral - see Equation (19)	$\phi_n(x)$	mode shape variation in x-direction for separable mode
L	length of structure	$\psi_m(y)$	mode shape variation in y-direction for separable mode
ℓ	breadth of structure	χ_{nm}	non-dimensional parameter - equation (32)
M_x, M_y	moments	ω	frequency
n,m	integers	ω_1	fundamental frequency of undamped beam
n	h_D/h		
N	number of spans	ω_r	resonant frequency
p,q	integers	ω_{nm}	nmth natural frequency
$P(x,y)$	pressure loading		
S	symbol representing area of plate		
W	transverse displacement of plate		
x,y	orthogonal coordinates in surface of plate		

120

"VIBRATION CONTROL BY A MULTIPLE-LAYERED

DAMPING TREATMENT"

A. D. Nashif*
and
T. Nicholas**

The multiple constrained layer damping treatment is represented
conceptually in terms of an equivalent free layer damping treat-
ment. The analysis for this representation is accomplished by
considering the treatment to be an anisotropic beam with differ-
ent stiffnesses and damping in shear and extension. Optimization
for this treatment is shown to be a function of wave length, tem-
perature and geometry for a given damping material. Experimental
results are presented to verify the analysis.

INTRODUCTION

Reduction of excessive vibrational
amplitudes in structures is frequently
obtained through the application of
single or multiple-layered damping
treatments. Recent applications of
multiple constrained damping layers in
aerospace structures [1] have indicated
that such treatments can be very effec-
tive in controlling vibrations. The
optimization and practical development
of such a treatment has been hampered,
however, by a lack of adequate analysis
techniques and by a scarcity of good
experimental data and has been confined
for the most to specialized cases and
geometries. It would be desirable to
be able to represent such a treatment
in terms of an equivalent free layer
homogeneous treatment [2,3]. However,
such a representation could result in
an oversimplification because of the
complex behavior of such a material
configuration. In the present investi-
gation, the multiple-layered damping
treatment is treated as an equivalent
homogeneous but anisotropic material.
The properties of the equivalent treat-
ment are derived maintaining compati-
bility of resultant forces in shear and
extension and approximating the dis-
placement field across each layer by a
linear distribution across the thick-
ness. The treatment is then considered
to be an anisotropic beam with differ-
ent stiffnesses and damping in shear
and extension and is analyzed using a

theory of higher order than Timoshenko
beam theory [4]. In the present analy-
sis, a displacement field is considered
which allows for up to quadratic terms
in the thickness direction, which is an
extension of previous work where only
linear variations were considered [5].
The equations of motion of the result-
ing two layered beam are solved for
waves travelling in the direction of
the axis of the beam and the damping of
the composite beam is determined as a
function of wave length or frequency.
The analysis is used to predict the re-
sults of damping measurements from num-
erous experiments on cantilever beams
vibrated in their first, second, and
third modes. Analytical predictions
are made for a wide variety of combina-
tions of moduli, thicknesses, and damp-
ing properties. From the analytical
and experimental results it is shown
that (a) the multiple constrained layer
damping treatment can indeed be thought
of in terms of an equivalent free layer
damping treatment and (b) that the
damping properties of such an equiva-
lent homogeneous treatment, which de-
pend on wave length, temperature, geom-
etry, etc. can be optimized.

ANALYSIS

The damping treatment consists of
a number of alternate elastic and vis-
coelastic layers sandwiched to the base
beam. If the number of layers is large,

*University of Dayton Research Institute, Dayton, Ohio

**Air Force Materials Laboratory, WPAFB, Ohio

it may be treated as an equivalent homogeneous but anisotropic material. Consider a typical element consisting of a segment of one viscoelastic layer and two halves of the adjacent elastic layers as depicted by the dashed lines in Figure 1.
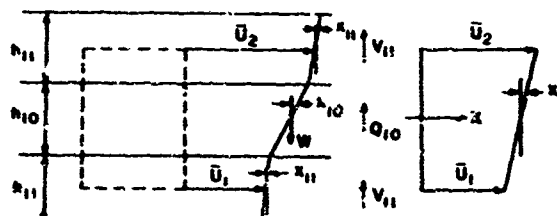
Figure 1. Geometry of layered treatment and equivalent homogeneous material

If each layer is assumed to be very thin in comparison with the overall thickness it may then be assumed that the displacement field across each layer is linear as shown. The rotation of an originally plane section of the viscoelastic layer is denoted by ψ_{10} while that of the elastic layers is denoted by ψ_{11}. The thicknesses of the viscoelastic and elastic layers are denoted by h_{10} and h_{11} respectively while the transverse shear forces are denoted by Q_{10} and V_{11}. The centerline axial displacements of two consecutive elastic layers are denoted by $\bar{u}_2$ and $\bar{u}_1$. The transverse shear forces are given by

$$Q_{10} = G_{10} h_{10} \left(\psi_{10} - \frac{\partial w}{\partial x} \right) \tag{1a}$$

$$V_{11} = \frac{h_{11}}{h_{10}} Q_{10} \tag{1b}$$

where w is the transverse displacement component and G_{10} the shear modulus of the viscoelastic layer. Equation (1b) is based on the assumption that the shear stresses are uniform across the thickness of each layer. Assuming that shear deformation may be neglected in the elastic layers, then $\psi_{11} = \partial w/\partial x$, and the expressions for the total shear force in the typical element and the displacements are

$$Q_{tot} = G_{10} \left(\psi_{10} - \frac{\partial w}{\partial x} \right) (h_{10} + h_{11}) \tag{2a}$$

$$\bar{u}_2 - \bar{u}_1 = h_{11} \frac{\partial w}{\partial x} + \psi_{10} h_{10} \tag{2b}$$

If the typical element is thought of as an equivalent homogeneous material as

shown on the right in Figure 1 with rotation ψ_1, and identical displacement components $\bar{u}_2$ and $\bar{u}_1$, as in the layered media, the shear force is

$$Q_1 = G_1 (h_{10} + h_{11}) \left(\psi_1 - \frac{\partial w}{\partial x} \right) \tag{3}$$

and the continuity of displacements requires

$$\bar{u}_2 - \bar{u}_1 = (h_{10} + h_{11}) \psi_1 \tag{4}$$

Here, G_1 is an equivalent shear modulus. Equating the real and imaginary parts of the total shear force in the layered media and the equivalent homogeneous material results in

$$G_1 = G_{10} (1 + \gamma) \tag{5a}$$

$$\eta_G = \eta_{10} \frac{1}{(1 + \gamma)} \tag{5b}$$

where

$$\gamma = \frac{h_{11}}{h_{10}} \tag{5c}$$

and where η_{10} is the loss factor of the viscoelastic layer in shear. The complex shear modulus of the equivalent material is given as

$$G_1^* = G_1 (1 + i \eta_G) \tag{6}$$

In a similar manner, the axial force in the layered media is equated to the axial force in the equivalent material, leading to expressions for an equivalent extensional stiffness in the form

$$E_1 = \frac{E_{11} h_{11} + E_{10} h_{10}}{h_{11} + h_{10}} \tag{7a}$$

$$\eta_E = \eta_{10} \frac{E_{10} h_{10}}{E_{11} h_{11} + E_{10} h_{10}} \tag{7b}$$

where the complex Young's modulus of the equivalent material is

$$E_1^* = E_1 (1 + i \eta_E) \tag{8}$$

and E_{11} and E_{10} represent the Young's moduli of the elastic and viscoelastic layers respectively and η_{10} is the loss factor of the viscoelastic layer, assumed to be the same in extension as in shear. Equations (5) to (8) consti-

122

lute expressions for an equivalent homogeneous material which will have the same overall displacement field and shear and normal forces as the typical element of the layered media.

Consider the layered damping treatment now as a homogeneous, anisotropic beam having the properties given by Equations (5) to (8) sandwiched to an elastic beam as shown in Figure 2 with τ and σ the interface shear and normal forces, u_1 and u_0 the centerline axial displacement components, h_1 and h_0 the thicknesses of the two beams and w the transverse displacement component. The bending moments, shear, and axial forces on the two beams are as shown in Figure 2.
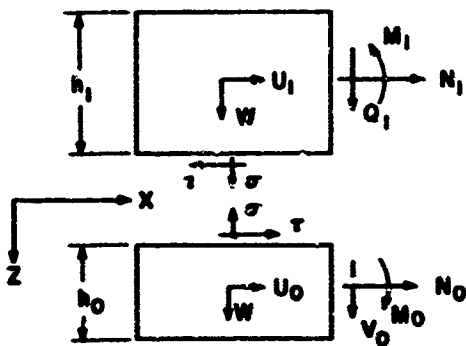
Figure 2. Nomenclature for sandwich beam

Conservation of linear and angular momentum of the two beams and analyzing the lower or base beam in accordance with simple beam, or Bernoulli-Euler beam, theory leads to the equations of motion:

$$\frac{\partial N_1}{\partial x} - \tau = 0 \tag{9a}$$

$$-\frac{\partial M_1}{\partial x} + Q_1 + \tau \frac{h_1}{2} = 0 \tag{9b}$$

$$\frac{\partial Q_1}{\partial x} + \sigma = \rho_1 h_1 \frac{\partial^2 w}{\partial t^2} \tag{9c}$$

$$\frac{\partial N_0}{\partial x} + \tau = 0 \tag{10a}$$

$$\frac{\partial M_0}{\partial x} + V_0 + \tau \frac{h_0}{2} = 0 \tag{10b}$$

$$\frac{\partial V_0}{\partial x} + \sigma = \rho_0 h_0 \frac{\partial^2 w}{\partial t^2} \tag{10c}$$

where

$$N_0 = E_0 h_0 \frac{\partial u_0}{\partial x} \tag{11a}$$

$$M_0 = E_0 I_0 \frac{\partial^2 w}{\partial x^2} \tag{11b}$$

Here, only the transverse inertia of the two beams is considered, the rotatory and extensional inertia being neglected, and ρ represents the mass density and I the moment of inertia about the beam's centerline. A preliminary analysis was carried out considering the top beam (the damping treatment) as an anisotropic Timoshenko beam, i.e., a beam where plane sections remain plane but shear deformation is allowed. The analysis did not agree too well with the experimental results and it was therefore decided to include non-linear deformation terms for the damping treatment in order to reduce the constraints on the system. The axial displacement field of the top beam was thus taken to include terms up to quadratic order in the form

$$u = u_1 + \psi z + \xi z^2 \tag{12}$$

The resultant axial force, bending moment, and transverse shear force are then

$$N_1 = \int \sigma_x dz = E_1 h_1 \frac{\partial u_1}{\partial x} + E_1 I_1 \frac{\partial \xi}{\partial x} \tag{13a}$$

$$M_1 = \int \sigma_x dz = E_1 I_1 \frac{\partial \psi}{\partial x} \tag{13b}$$

$$Q_1 = \int \tau_{zx} dz = G_1 h_1 (\psi + \frac{\partial w}{\partial x}) \tag{13c}$$

Continuity of displacements at the interface of the two beams is assured by taking

$$u_1 + \frac{h_1}{2} \psi + \frac{h_1^2}{4} \xi = u_0 + \frac{h_0}{2} \frac{\partial w}{\partial x} \tag{14}$$

where the lower or base beam is treated according to elementary beam theory where plane sections remain plane and perpendicular to the deformed centerline. The number of unknowns now exceeds the number of equations by one. An additional condition is obtained by prescribing the interface shear stress in terms of the displacement components from the stress-strain and strain-displacement equations of elasticity in

the term

$$= -G_1 \left(\psi + \frac{\partial w}{\partial x} + h_1 \psi \right) \qquad (15)$$

It is to be noted that the shear stress is not necessarily zero at the top face of the upper beam. This is a condition similar to that obtained in Timoshenko beam theory where shear stresses are assumed uniform across the thickness. The actual nonuniformity can be partially taken into account through the introduction of a shear correction factor in equation (13c); however, no attempt to do so was made in the present analysis. Successive elimination of variables from equations (9) through (15) results in a set of three simultaneous partial differential equations in the three displacement components w, v, and ψ in the form

$$-E_1 I_1 \psi'' + G_1 \cdot (\psi + w') - G_1 \frac{h_1^2}{2} \psi = 0 \quad (16a)$$

$$-E_0 I_0 w^{IV} + G_1 (h_1 + \frac{h_0}{2})(\psi' + w'') + G_1 \frac{h_1 h_0}{2} \psi' -$$

$$(\rho_1 h_1 + \rho_0 h_0)\ddot{w} = 0 \qquad (16b)$$

$$-G_1 (1 + \frac{E_0 h_0}{E_1 h_1})(\psi + w' + h_1 \psi) + E_0 \frac{h_0 h_1^2}{6} \psi'' +$$

$$E_0 \frac{h_0 h_1}{2} v'' - E_0 \frac{h_0^2}{2} w''' = 0 \quad (16c)$$

where primes and dots denote differentiation with respect to x and t respectively. Equations (16) are solved for waves travelling in an infinite beam in the x direction of the form

$$w = \bar{w} \exp[i(\xi x - \omega t)] \qquad (17a)$$

$$\psi = \bar{v} \exp[i(\xi x - \omega t)] \qquad (17b)$$

$$\psi = \bar{\phi} \exp[i(\xi x - \omega t)] \qquad (17c)$$

where ω is the circular frequency and ξ the wave number related to the wave length λ through

$$\xi = \frac{2\pi}{\lambda} \qquad (18)$$

The following non-dimensional quantities are introduced:

$$h^* = \frac{h_1}{h_0}$$

$$E^* = \frac{E_1}{E_0}$$

$$G^* = \frac{G_1}{E_1}$$

$$\bar{x} = \frac{h_1 + h_0}{\lambda} = \frac{h}{\lambda}$$

$$\omega^* = \frac{\omega}{\Omega_1} \qquad (19)$$

where Ω_1 is an arbitrarily chosen reference frequency which is that of the first thickness shear mode of a beam having the geometrical average properties of the two-layered beam and is given by

$$\Omega_1^2 = \frac{\pi^2}{h_0(1+h^*)^2} \frac{E_0(1+E^* h^*)}{3(\rho_1 h_1 + \rho_0 h_0)} \qquad (20)$$

Non-zero solutions to equations (16) and (17) give rise to the frequency equation

$$\omega^{*2} = \frac{\beta^2}{1+E^* h^*} \frac{C_1 + C_2 \alpha^2 + \frac{2}{9}\alpha^4}{C_3 + C_4 \alpha^2 + \frac{2}{9}\alpha^4} \qquad (21)$$

where the following abbreviations have been introduced

$$\beta = \frac{2\pi \bar{x}^2}{1+h^*}$$

$$\alpha = \frac{\pi h^* \bar{x}}{1+h^*}$$

$$C_1 = G^{*2}(1+4E^* h^* + 6E^* h^{*2} + 4E^* h^{*3} + E^{*2} h^{*4})$$

$$C_2 = (G^*/3)(5 + 4E^* h^* + E^* h^{*2} + 2E^* h^{*3})$$

$$C_3 = G^{*2}(1 + E^* h^*)$$

$$C_4 = (G^*/3)(5 + E^* h^*) \qquad (22)$$

When damping terms are included in the frequency equation through the introduction of the complex moduli G_1^* and E_1^* as given by equations (6) and (8), the resulting frequency is complex

$$\omega \rightarrow \omega(1 + i\frac{\delta}{2\pi}) \qquad (23)$$

where δ is the logarithmic decrement for free damped oscillations. The loss factor η_1 of the composite beam is related to δ through

$$\eta = \frac{\zeta}{\pi} \tag{24}$$

Solutions to the complex frequency equation (21) are obtained numerically by setting the real and imaginary portions equal to zero individually.

EXPERIMENTAL INVESTIGATION

This investigation was carried out on the standard complex modulus apparatus and its associated electronic equipment which is described in Ref.[6]. Two different geometries of the multiple-layered damping treatment were used to investigate the damping of cantilever beams as a function of temperature over a wide range of wave lengths. Each configuration consisted of 7 alternate layers, each of a constrained viscoelastic band and a constraining metal band sandwiched on to the base beam. The viscoelastic material designated as 3M-466 is a damping adhesive manufactured by the 3M-Company, St. Paul, Minnesota. The properties of this material as a function of temperature and frequency are shown in Figure 3.
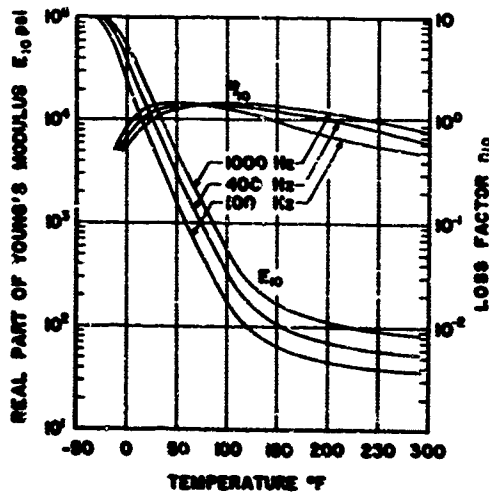
Figure 3. Damping properties of 3M-466 (Manufacturer's data)

The first configuration utilized an adhesive thickness $h_{10} = 0.0023$ in. and an aluminum constraining band thickness $h_{11} = 0.0052$ in. which gave a $\gamma = 2.25$. For the second configuration h_{10} was 0.0046 in. and h_{11} was 0.0023 in. and the resulting γ was 0.5.

Each configuration was assembled on an aluminum cantilever beam which had a length of 8 in., a width of 0.45 in. and a thickness of 0.062 in.

Each beam was placed inside an environmental chamber and excited at the free end by means of a magnetic transducer. The response was obtained by means of another transducer near the root. The damping and the frequency for each observed mode was then measured by the half-power bandwidth method. Data were obtained for the first, second, and third mode of the cantilever beam in most cases. Tests were carried out between 0°F and 200°F. The experimental results for the damping of the composite beam are plotted in Figures 4 through 9 as a function of temperature for the several mode numbers.

DISCUSSION

Effects of temperature on the performance of the constrained layer damping treatment are shown in Figures 4 through 6 for $\gamma = 2.25$ and $h^* = 0.85$ and in Figures 7 through 9 for $\gamma = 0.5$ and $h^* = 0.75$. The theoretical predictions in these figures were computed at temperatures corresponding to those of the experiment. This was accomplished by observing the frequency for which each mode occurred and then using the appropriate damping properties from Figure 3 for each temperature.
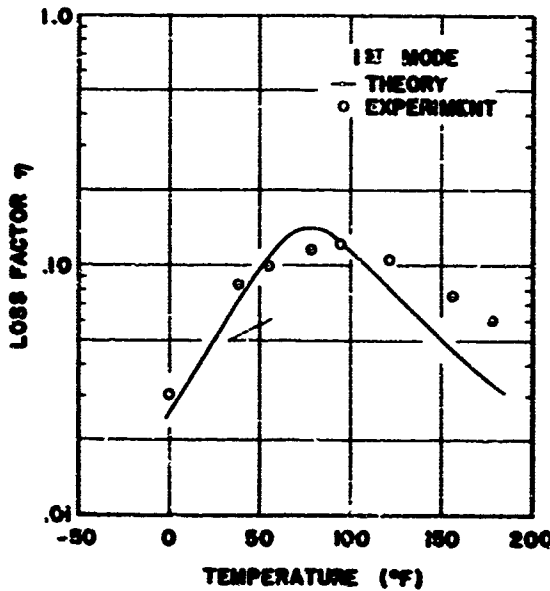
Figure 4. Effect of temperature on the system damping for $\gamma=2.25$ and $h^*=0.85$

125
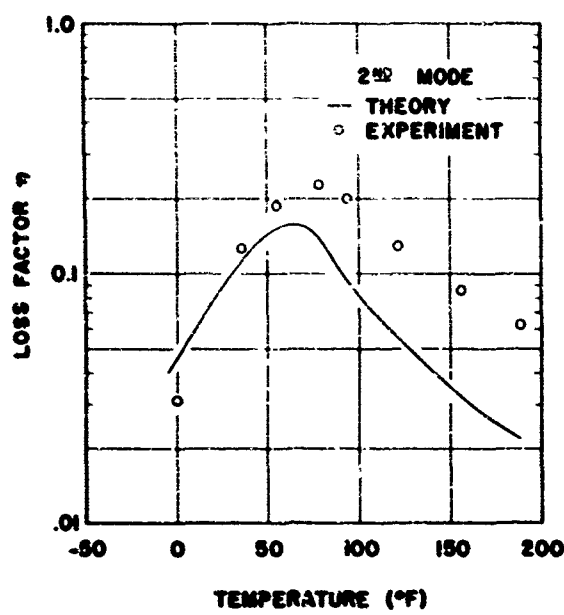
Figure 5.   Effect of temperature
           on the system damping
           for γ=2.25 and h*=0.85
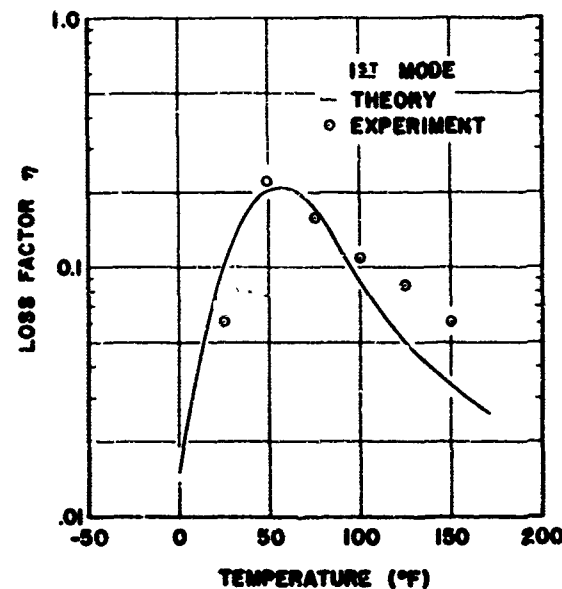
Figure 7.   Effect of temperature
           on the system damping
           for γ = 0.5 and h*=0.75

Figure 6.   Effect of temperature
           on the system damping
           for γ=2.25 and h*=0.85
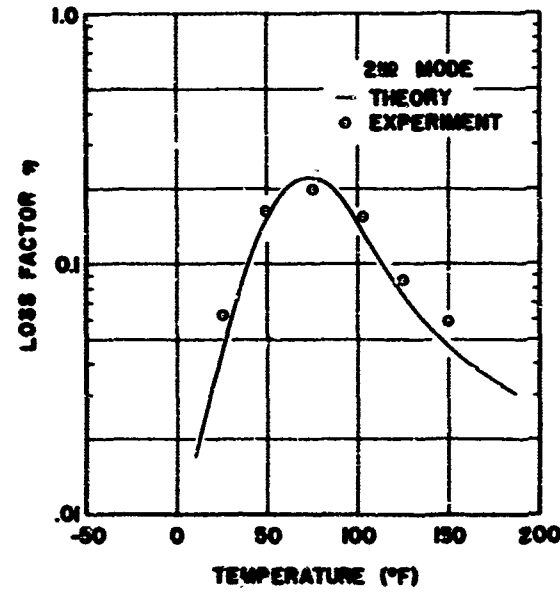
Figure 8.   Effect of temperature
           on the system damping
           for γ = 0.5 and h*=0.75

126

Figure 9. Effect of temperature on the system damping for $\gamma = 0.5$ and $h^* = 0.75$

Good agreement between theory and experiment was found in most cases. The measured values for $\gamma = 2.25$ were somewhat higher than the predicted values, especially for higher modes. A possible explanation for this difference is the fact that the properties shown in Figure 3 do not accurately describe the particular batch of material used for the experimental investigation. This may have been due to an ageing effect in the material or prolonged exposure to a humid environment. Therefore, a new batch of the same material was used for the case of $\gamma = 0.5$. In this second case, the agreement improved considerably which tends to indicate that the properties of Figure 3 are more representative of the second batch than the first. In both cases, the best agreement was for the first mode with decreasing correlation for the second and third modes. It should be noted that boundary conditions for cantilever beams are difficult to control for higher modes of vibration and hence variations between theory and experiment are possible. Also, at higher modes, the wave lengths are much smaller, hence the assumptions of negligible rotatory inertia and the use of beam theory as opposed to plate theory become less accurate.

A numerical analysis was carried out to determine the effects of the various material and geometric parameters on the damping of the composite beam. Equations (21)-(24) were programmed on a computer and solved for various combinations of parameters which might be used in actual damping treatments. In all calculations, the base beam on which the layers are placed is considered to be aluminum with $E_0 = 10^7 psi$ and n_{10} is taken equal to unity. The numerical results for n/n_{10} were found to be relatively independent of the actual value of n_{10}. The various results are summarized in Figures 10 through 13. Figure 10 shows the typical variation of damping with wave number for two values of G_{10} and three thickness ratios h^*. In all cases, the maximum or peak damping was independent of the shear modulus G_{10} of the damping layer, the only difference being the wave number at which it occurred. Increasing the thickness ratio had the obvious effect of increasing the damping. In general, the peak damping depended upon the thickness of the damping treatment in a nearly linear way for thickness ratios h^* less than unity. Doubling the thickness of the treatment is thus equivalent to doubling the damping, but also results in double the weight added to the base beam. The wave number or wave length at which the peak damping occurs depends on the shear modulus G_{10} as is shown in Figure 11. If the wave length of an undesirable vibration is known, the appropriate value of G_{10} can be found which will give maximum damping for that wave length. Figure 12 presents damping curves as a function of wave length for various values of γ, the ratio of the thickness of the elastic layer to the viscoelastic layer. For the values of the other parameters shown it can be seen that the maximum damping available is approximately the same for values of γ of .25, .5, and 1. The peak damping was then plotted as a function of γ for two values of h^* and two values of E_{11} as shown in Figure 13. It can be seen that an optimum value of γ can be found in each case although the peak is not very sharp. Two curves in Figure 13 represent aluminum constraining layers on an aluminum beam for which $E = 10^7 psi$. The other two for $E_{11} = 5 \times 10^7 psi$ represent a ficticious material but show the trend for a very high modulus material such as boron. The curves show a definite increase in damping, especially for the thinner damping treatment where $h^* = .25$. These curves are drawn for $G_{10} = 100 psi$ but are identical for all values of G_{10} between 10 and 10^5 psi, the range investigated here.
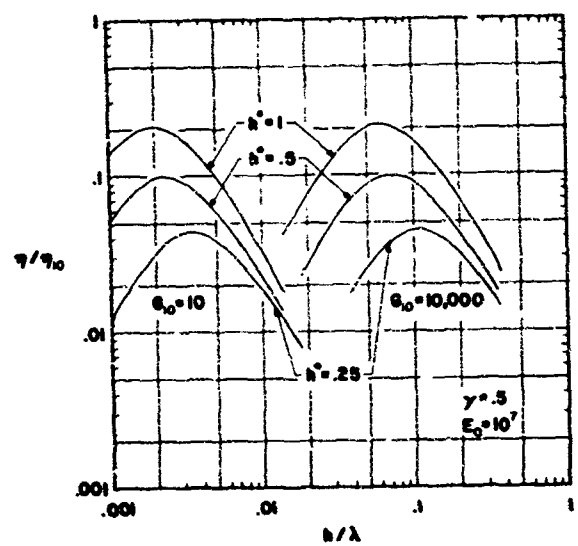
Figure 10. Effects of thickness of damping treatment and wave length on damping of composite beam
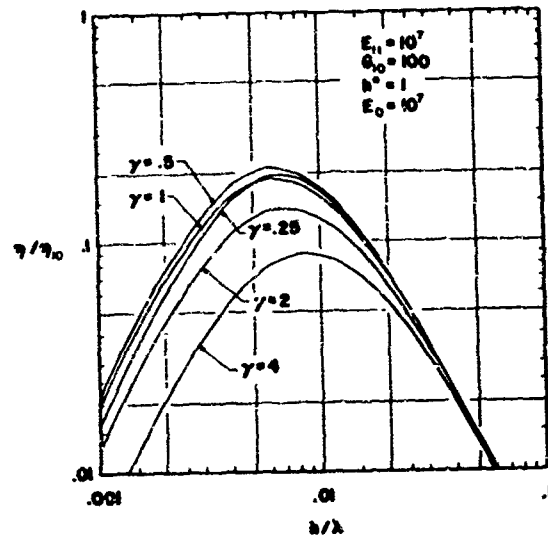
Figure 12. Composite beam damping for several thickness ratios of elastic to viscoelastic layers
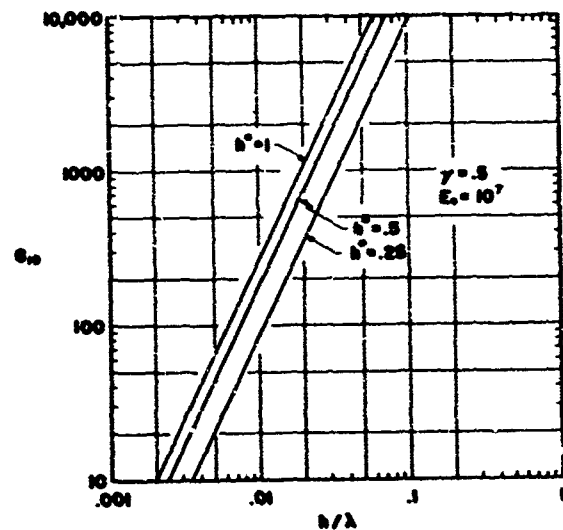
Figure 11. Wave length for maximum damping as a function of shear modulus of damping layer
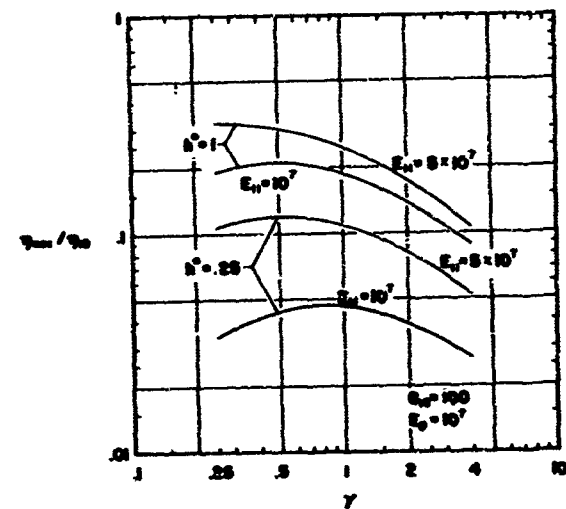
Figure 13. Maximum damping as function of thickness ratio γ

128

CONCLUSIONS

The analysis presented herein allows for a displacement field in the equivalent homogeneous damping layer which includes terms up to parabolic order, and gave good agreement with experimental results. The damping predictions of this theory were approximately twenty percent higher than those using anisotropic Timoshenko beam theory where displacements vary linearly across the thickness. The theory could be improved by considering higher order terms in the displacement field, at the expense of increased mathematical complexity. The relatively good agreement between theory and experiment seems to indicate the adequacy of the existing theory.

The results of this investigation illustrate a number of features about multiple-layer damping treatments and their application:

1. The damping for a given set of material and geometric parameters is strongly dependent on wave length. The composite beam (or structure in general) cannot be thought of in terms of a single equivalent "EI" or flexural rigidity because of this variation.

2. Changing the modulus of the damping layers changes the wave length at which peak damping may be obtained but does not change the magnitude of the damping.

3. An optimum value of γ, the thickness ratio of the elastic to the viscoelastic layers, may be found for specific materials. In the present investigation, values close to one-half provided the most efficient damping.

4. Calculations indicate that higher stiffnesses of the constraining layers serve to increase the damping of the entire system. It would appear then that further improvements are possible in multiple-layer damping treatments through the introduction of higher modulus materials as constraining layers [7].

5. Optimum damping for the treatment occurs when the loss factor of the damping material takes on its maximum value.

It is interesting to note that this condition is satisfied only in the transition region of the damping material and hence a simple criterion for optimizing the multiple-layer treatment can be stated as follows: in order to achieve maximum damping by the multiple-layer treatment for a specific application, it is necessary to use a viscoelastic damping material whose transition region coincides with the temperature region over which the treatment is utilized. This was found to hold for a number of cases discussed in Reference [8].

REFERENCES

1. Jones, D. I. G., Henderson, J. P., and Nashif, A. D., "Reduction of Vibrations in Aerospace Structures by Additive Damping", Shock and Vibration Bulletin No. 40, Part 5, December 1969.

2. Lazan, B. J., Metherell, A. F. and Sokol, G., "Multiple-Band Surface Treatments for High Damping", Air Force Material. Laboratory Report AFML-TR-65-269, September 1965.

3. Plunkett, R. and Lee, C. T., "Length Optimization for Constrained Viscoelastic Layer Damping", Air Force Materials Laboratory Report AFML-TR-68-276, July 1969.

4. Timoshenko, S., "Vibration Problems in Engineering", 3rd ed. (D. Van Nostrand Co., New York), 1955, p. 330.

5. Nicholas, T., "The Effects of Rotatory Inertia and Shear Deformation on the Flexural Vibrations of a Two-Layered Viscoelastic-Elastic Beam", Shock and Vibration Bulletin, No. 38, Part 3, November 1968.

6. Nashif, A. D. and Nicholas, T., "An Analytical and Experimental Investigation of a Two-Layer Damping Treatment", Shock and Vibration Bulletin, No. 39, Part 4, April 1969.

7. Simmons, D. R., Henderson, J. P., Jones, D. I. G., and Cannon, C. M., "Multi-Layer Alternately Anchored Treatment for Damping of Skin-Stringer Structures", Shock and Vibration Bulletin, No. 39, Part 4, April 1969.

8. Nashif, A. D., "Influence of Temperature on Damping of Plates by Constrained Viscoelastic Layers", presented at the Symposium on Structural Dynamics, Loughborough, England, March 1970.

λ	Wave length
ψ	Rotation of cross section
ϑ	Displacement component
ρ	Mass density
σ	Normal stress
τ	Shear stress
ω	Circular frequency
Ω	Reference frequency
ξ	Wave number
$*$	Superscript denoting dimensionless quantity
0	Subscript denoting base beam
1	Subscript denoting multiple-layer treatment
10	Subscript denoting viscoelastic layer
11	Subscript denoting elastic layer

(No subscript denoting the composite system)

SYMBOLS

E   Young's modulus

G   Shear modulus

h   Thickness

I   Moment of inertia

M   Bending moment

N   Axial force

Q   Transverse shear force

t   Time

u   Axial displacement

V   Transverse shear force

w   Transverse displacement

$x = \dfrac{h}{\lambda}$ also Cartesian coordinate along beam axis

γ Thickness ratio (equation 5c)

δ Logarithmic decrement

η Loss factor

130

Mr. Ripperger (University of Texas): I would like to ask two questions. I assume that in these models the shear transfer to the elastic layers is entirely through the viscoelastic layers. If that is the case I am puzzled as to what the physical explanation is of the effectiveness of these elastic layers in increasing the damping. Can you explain this?

Mr. Nicholas (AFML): Everyone else working in the field seems to have a very good physical understanding for this. I can only repeat what they all say. Basically the stiff elastic layer induces shear deformation into the viscoelastic layers which are sandwiched between them. It acts as a constraining layer, but physically it is a very difficult thing to see. Mathematically it introduces all of the shear deformation into the viscoelastic layer, the soft layer, and the shear stresses throughout the entire treatment are about equal. Because of the low modulus there is a lot of shear deformation in the viscoelastic layer and hardly any in the elastic layers.

Mr. Henderson (AFML): I wonder if I could interject one comment here. The result of increasing the modulus of the constraining layer is consistent with several other previous investigations. One physical explanation that has been offered by such people as Lazan and Plunkett at the University of Minnesota is that the stretching of the constraining layer decreases the total volume of viscoelastic material that experiences high shear strain. Most

of our constrained layer damping treatments could be improved by increasing this stiffness of the constraining layer because it actually shears more viscoelastic material before the stretching catches up and wipes out the shear strain. I do not know if that makes any sense or not but there are some sketches of displacement fields in both Lazan's and Plunkett's previous papers and I think you might be able to look at those and get a little better physical understanding.

Mr. Prouse (Battelle Memorial Institute): I was interested in the experimental approach you used to obtain the damping in the third mode. Are coupling effects from other modes eliminated? Did you really obtain a pure third mode?

Mr. Nashif: I do not think you have to worry about coupling if your modes are fairly well separated and the damping is fairly low in the composite system, and that was the case. The total damping was on the order of 0.1 and 0.2, and the modes were fairly well separated for the cantilever beam.

Mr. Prouse: I guess as these damping approaches get better and better the experimental part will get harder and harder.

Mr. Nashif: That is right. As you go higher with mode number the agreement between the theory and experiment gets worse.

DETERMINATION OF DAMPING PROPERTIES OF

SOFT VISCOELASTIC MATERIALS

Fakhruddin Abdulhadi
IBM General Systems Division
Rochester, Minnesota

The frequency and composite loss factor equations for a beam with a constrained damping layer are uncoupled to yield equations for the loss factor and the shear storage modulus of the constrained viscoelastic layer. Each of the loss factor and storage modulus equations is expressed in terms of the resonant frequency, the composite loss factor, the mode number, and the geometry of the cross-section of the beam. Error analysis is performed using these two new equations to determine the magnification of the relative errors in the calculated material loss factor and the storage modulus due to errors in the measured resonant frequency and composite loss factor.

INTRODUCTION

Analysis of laminated plates and beams, including a viscoelastic layer, has been performed by several investigators [1,2,3,4,5,6]. This analysis provided equations to determine the relationship between the composite loss factor and the resonant frequency of the composite laminate. References [6,7,8] describe methods to determine the resonant frequencies and corresponding composite loss factors for beams and plates of known dimensions, material properties, and boundary conditions.

The properties of the viscoelastic damping layer are frequency- and temperature-dependent for small strains. Thus, it is necessary to know each of the curves of G (shear storage modulus) and β (material loss factor) versus frequency at each temperature, in order to employ the existing theory to provide data usable by the designer of such laminates.

The damping layer used in the unconstrained layer configuration, shown in Fig. 1, is usually stiff. The storage modulus E and the material loss factor β of such stiff damping materials can be successfully obtained [9,10] from a vibration test of a beam of the configuration shown in Fig. 2. Error analysis performed by Nashif [9] for such beams shows that this configuration produces unreliable results when the damping layer is relatively soft.
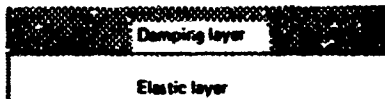
Fig. 1 - Nonconstrained damping layer composite

G* = G(1 + iβ)
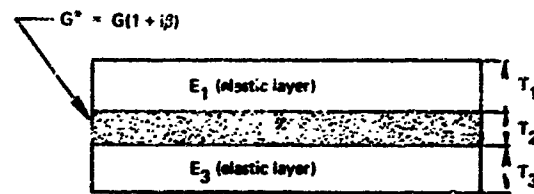
Fig. 2 - Constrained damping layer composite

Relatively soft viscoelastic materials are used in the constrained layer configuration. Properties of such materials have been determined by Nicholas and Heller [11] by using a beam with a thick core sandwiched between two thin membrane type facings. The use of such beams is limited to low frequencies (usually Hz < 300). The exact identification of the resonant frequencies becomes difficult due to increased damping. A tuned damper resonant technique has been successfully used by Canon, Nashif and Jones [12]. The present investigation considers the use of a constrained damping layer beam for the evaluation of the complex modulus for soft viscoelastic materials. Such a sample with identical elastic layers has been used by Roscoe, Thomas, and Blasingame [13]. However, the required computations are lengthy and the expressions relating the measured quantities to the computed properties do not readily yield themselves to error analysis. This investigation presents two new equations relating the shear storage modulus and the material loss factor to the measured resonant frequency and the corresponding composite loss factor for the beam tested.

ANALYSIS

The complex frequency of the constrained damping layer laminate is written as [6,2]:

$$\omega^2 = \Omega^2(1 + i\eta) \qquad (1)$$

where

$$\Omega^2 = \frac{D\alpha^2}{\rho}\left[1 + \left(\frac{K_e \delta^2}{D}\frac{\psi}{\varsigma}\right)\right] \qquad (2)$$

$$\eta = \frac{\beta\left(\frac{T_2 K_e \alpha}{G}\right)\left(\frac{K_e \delta^2}{D}\right)}{\left(\varsigma + \frac{K_e \delta^2}{D}\psi\right)} \qquad (3)$$

$$\psi = 1 + \beta^2 + \frac{T_2 K_e \alpha}{G}$$

$$\varsigma = \beta^2 + \left(1 + \frac{T_2 K_e \alpha}{G}\right)^2$$

$$K_e = \frac{E_1 T_1 E_3 T_3}{E_1 T_1 + E_3 T_3}$$

$$\delta = \frac{T_1}{2} + \frac{T_3}{2} + T_2$$

$$D = \frac{E_1 T_1^3}{12} + \frac{E_3 T_3^3}{12}$$

$$\rho = \rho_1 T_1 + \rho_2 T_2 + \rho_3 T_3.$$

The subscripts indicate the layer number as shown in Fig. 2. Constants E_1, E_3 are elastic moduli; T_1, T_2, and T_3 are thicknesses; Ω is the real part of the complex frequency and η is the composite loss factor. The mode parameter α is defined for each mode for the given length and the boundary conditions of the beam. The mass density per unit length of the composite beam is ρ and the densities of the three layers are ρ_1, ρ_2, and ρ_3.

Eqs. (2) and (3), which are two polynomials in β and G, are written as follows:

$$(\lambda^2 - 1 - Y)\beta^2 + (\lambda^2 - 1)\phi^2 - Y\phi = 0 \qquad (4)$$

$$\eta(1 + Y)\beta^2 + Y(1 - \phi)\beta + \eta\phi(Y + \phi) = 0 \qquad (5)$$

where

$$\lambda^2 = \frac{\rho\Omega^2}{D\alpha^2}$$

$$Y = \frac{K_e \delta^2}{D}$$

$$\phi = \frac{T_2 K_e \alpha}{G} + 1.$$

Eq. (4) is multiplied by η and added to Eq. (5) to yield

$$\eta\lambda^2\beta^2 + Y(1 - \phi)\beta + \eta\lambda^2\phi^2 = 0. \qquad (6)$$

Solving for β^2 in Eq. (4), substituting the result only in the first term of Eq. (6), and solving for the remaining β gives

$$\beta = \frac{\eta\lambda^2\phi}{1 + Y - \lambda^2}. \qquad (7)$$

Eq. (7) is now used in Eq. (4) to eliminate β and yield

$$\phi = \frac{Y(\lambda^2 - 1 - Y)}{\eta^2\lambda^4 + (\lambda^2 - 1)(\lambda^2 - 1 - Y)}. \qquad (8)$$

The quantity ϕ can be eliminated from Eq. (7) by using Eq. (8) to give the material loss factor equations as

$$\beta = \frac{\eta\lambda^2 Y}{(1 - \lambda^2)(\lambda^2 - 1 - Y) - \eta^2\lambda^4}. \qquad (9)$$

Using the definition of the quantity ϕ in terms of shear storage modulus gives

$$G = T_2 K_e \alpha\left[\frac{(1 - \lambda^2)(\lambda^2 - 1 - Y) - \eta^2\lambda^4}{(\lambda^2 - 1 - Y)^2 + \eta^2\lambda^4}\right]. \qquad (10)$$

Thus, Eqs. (9) and (10) can easily be used to compute β and G. The constants Y, T_2, and K_e are known for the beam tested. The mode parameter α assumes different values for different modes. If the beam is tested as a cantilever beam, the values of α for the first four modes are

$$\alpha_1 = \left(\frac{1.875}{L}\right)^2 , \quad \alpha_2 = \left(\frac{4.694}{L}\right)^2$$

$$\alpha_3 = \left(\frac{7.855}{L}\right)^2 , \quad \alpha_4 = \left(\frac{10.996}{L}\right)^2 ,$$

where L is the vibrating length of the beam. The symbol λ is directly related to the measured resonant frequency. Thus, if Ω_0 is designated as the uncoupled frequency defined by

$$\Omega_0^2 = \frac{\alpha^2 D}{\rho_1 T_1 + \rho_3 T_3},$$

then λ^2 becomes

$$\lambda^2 = \left(\frac{\rho_1 T_1 + \rho_3 T_3 + \rho_2 T_2}{\rho_1 T_1 + \rho_3 T_3}\right)\frac{\Omega^2}{\Omega_0^2}$$

$$\lambda = (1 + \epsilon)^{1/2}\frac{f}{f_0}, \qquad (11)$$

where

$$\Omega = 2\pi f; \Omega_0 = 2\pi f_0; \epsilon = \frac{\rho_2 T_2}{\rho_1 T_1 + \rho_3 T_3}.$$

The frequency f (in Hz) is measured for the given mode, and f_0 (in Hz) is calculated for the same mode. The only dynamically measured quantities on the right side of Eqs. (9) and (10) are η and f. The rest of the quantities are known for the beam tested at the given mode.

A slightly more exact expression for λ can be obtained by considering the effect of damping on the resonant frequency. Using Eq. (1) for small values of η, the actually measured damped frequency f_d is related to the undamped frequency f through [13]

$$f = \frac{f_d}{1 + \frac{3}{8}\eta^2} \qquad (12)$$

Using Eq. (12) in Eq. (11) gives a slightly more accurate expression for λ:

$$\lambda = \frac{(1+\epsilon)^{1/2}}{1 + \frac{3}{8}\eta^2} \frac{f_d}{f_o} \qquad (13)$$

Eqs. (9) and (4) can yield expressions for η and $G_2/T_2 K_e \alpha$ in terms of β and λ^2 as

$$\eta = -\frac{Y}{2\beta\lambda^2} + \left| \left(\frac{Y}{2\beta\lambda^2}\right)^2 \right.$$

$$\left. + \frac{(\lambda^2 - 1)(Y + 1 - \lambda^2)}{\lambda^4} \right|^{1/2} \qquad (14)$$

$$\frac{G}{T_2 K_e \alpha} = \left\{ \theta/2 - 1 + \left| \frac{\theta^2}{4} + \beta^2(\theta - 1) \right|^{1/2} \right\}^{-1} \qquad (15)$$

$$\theta = \frac{Y}{(\lambda^2 - 1)}$$

ERROR ANALYSIS

The effect of small relative errors in the measured λ and η on the relative errors of the computed quantities G and β are evaluated by using Eqs. (9) and (10). Analysis was performed by using the expression for λ given by Eq. (11), and for λ given by Eq. (13). The expressions obtained for the magnification factor, using the latter λ, are far more complicated than those obtained by the use of the former λ. Numerical results have shown little difference between these two sets. Therefore, the simple equations obtained by using λ of Eq. (11) are given. Thus,

$$-\frac{\Delta\beta}{\beta} = \frac{\Delta f}{f} M_1 \qquad (16)$$

$$\frac{\Delta\beta}{\beta} = \frac{\Delta\eta}{\eta} M_2 \qquad (17)$$

$$\frac{\Delta G}{G} = \frac{\Delta f}{f} M_3 \qquad (18)$$

$$\frac{\Delta G}{G} = \frac{\Delta\eta}{\eta} M_4 \qquad (19)$$

where

$$M_1 = \frac{[2(1 + Y) - 2(1 + \eta^2\lambda^4)]}{\mathcal{L}} \qquad (20)$$

$$M_2 = \frac{[(\lambda^2 - 1)(\lambda^2 - 1 - Y) - \eta^2\lambda^4]}{\mathcal{L}} \qquad (21)$$

$$M_3 = \frac{2Y\lambda^2[2\eta^2\lambda^2(1 + Y) - \mathcal{R}]}{(\mathcal{L}\mathcal{R})} \qquad (22)$$

$$M_4 = \frac{[2\eta^2\lambda^4 Y(Y + 1 - \lambda^2)]}{(\mathcal{L}\mathcal{R})} \qquad (23)$$

$$\mathcal{L} = (\lambda^2 - 1)(\lambda^2 - 1 - Y) + \eta^2\lambda^4$$

$$\mathcal{R} = (\lambda^2 - 1 - Y)^2 + \eta^2\lambda^4$$

The quantities M_1, M_2, M_3, and M_4 are the magnification factors. The factors M_2 and M_4 have been evaluated for various values of η, λ, and Y. It was found that M_2 was close to one and M_4 was less than one. Thus, the relative error in the calculated β is the same as that of the measured η. The computed value of M_4 indicates that errors in the measured η produce very small errors in the computed G.

The magnification factors M_1 and M_3 vary greatly in magnitude, depending on λ, Y, and to a lesser degree on η. Since it is more convenient to present the results in terms of β, λ, and Y, the values of η in Eqs. (20) and (22) are computed for the given β from Eq. (14).

The parameter λ^2 can be considered as a measure for the degree of coupling between the elastic layers. In the absence of damping, Eq. (2) reduces to

$$\lambda^2 = 1 + \frac{Y}{\frac{T_2 K_e \alpha}{G} + 1}. \qquad (24)$$

This equation shows that, without coupling, $G = 0$ and $\lambda = 1$. When coupling is perfect, $G = \infty$ and $\lambda^2 = 1 + Y$. The actual values of λ^2 for a finite G will be in the range $1 < \lambda^2 < 1 + Y$. Since α increases for the higher modes, λ decreases as the frequency increases. The composite loss factor η becomes zero at $\lambda^2 = 1$ or at $\lambda^2 = 1 + Y$. This is evident from Eq. (14). Thus, Eqs. (20) and (23) indicate that M_1 and M_3 are infinite at $\lambda^2 = 1$ and $\lambda^2 = 1 + Y$ for any value of β.

Fig. 3 shows that the minimum values of M_3 increase as Y decreases. Increasing values of β for the given Y change the right portion of the curve resulting in lower values of M_3, as shown in Fig. 4.

The magnification factor M_1 becomes zero at one point for each Y, regardless of the value of β. Fig. 5 shows the effect of Y on the values of M_1 for $\beta = 0.1$. Increased values of β shift the right portion of each curve slightly to the left.

The geometric parameter Y can be expressed as a function of thickness ratios when the material of the elastic layers is the same, i.e., $E_1 = E_3$. Thus,

$$Y = \frac{3n(1 + n + 2mn)^2}{(1 + n)(1 + n^3)}, \qquad (25)$$

where

$$m = \frac{T_2}{T_3}, \qquad n = \frac{T_2}{T_1}.$$

For a given total thickness of the elastic layers, the value of Y is the largest when the elastic layers are equal in thickness, as shown in Fig. 6.
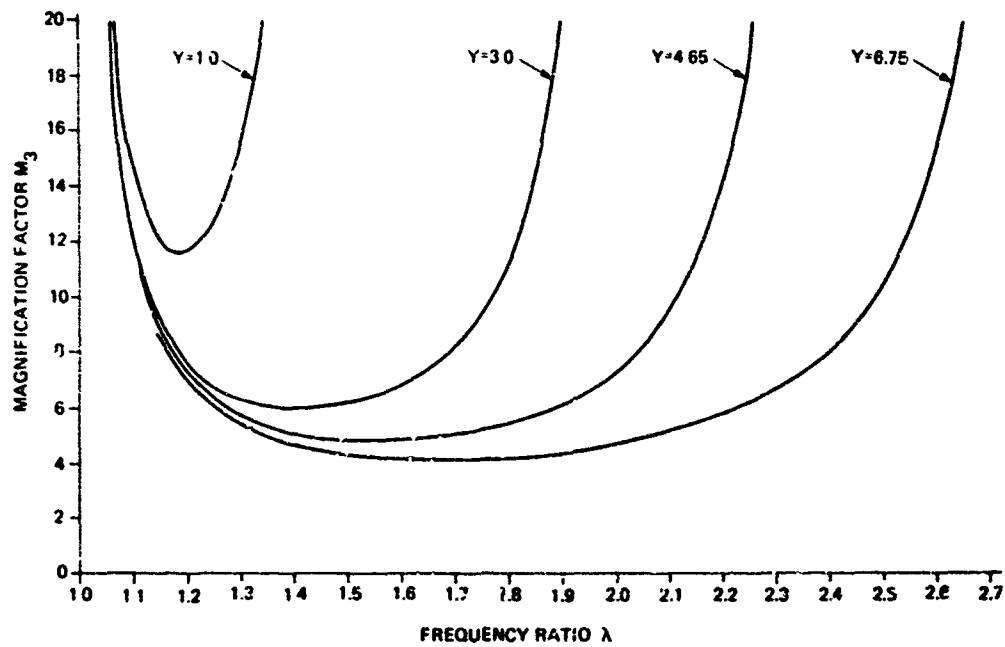
Fig. 3 - Effect of Y on M₃ for β = 0.1

Fig. 4 - Effect of β on M₃ for Y = 4.65

136
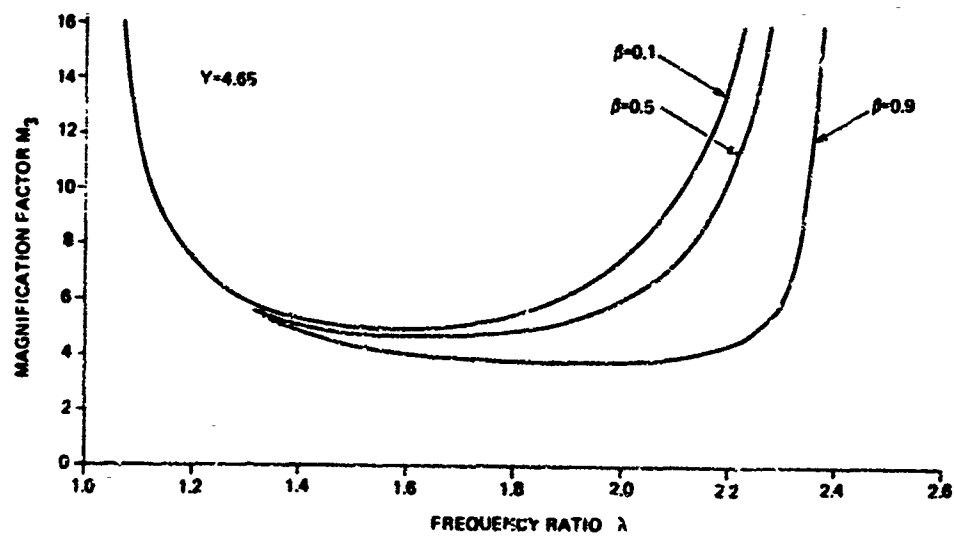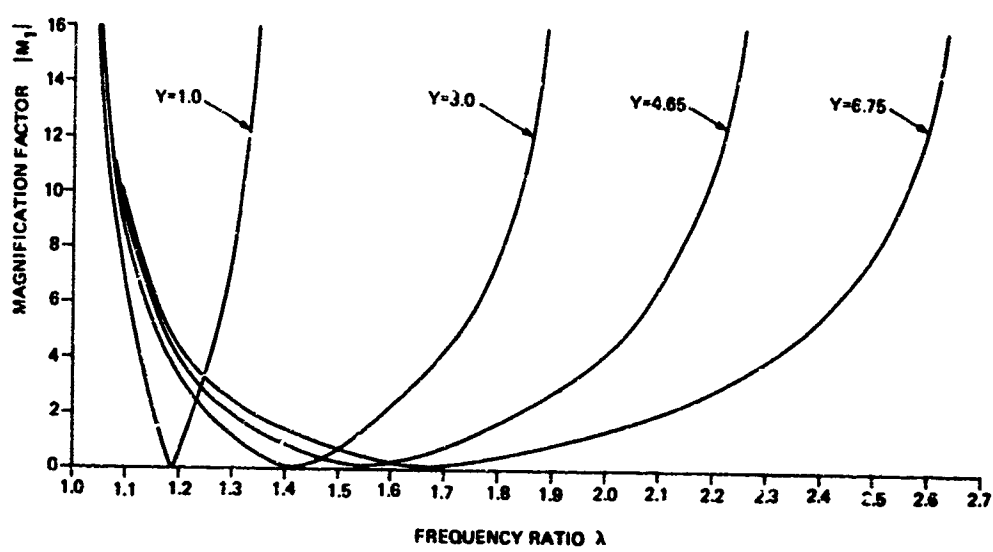
Fig. 5 - Effect of Y on M_1 for $\beta = 0.1$
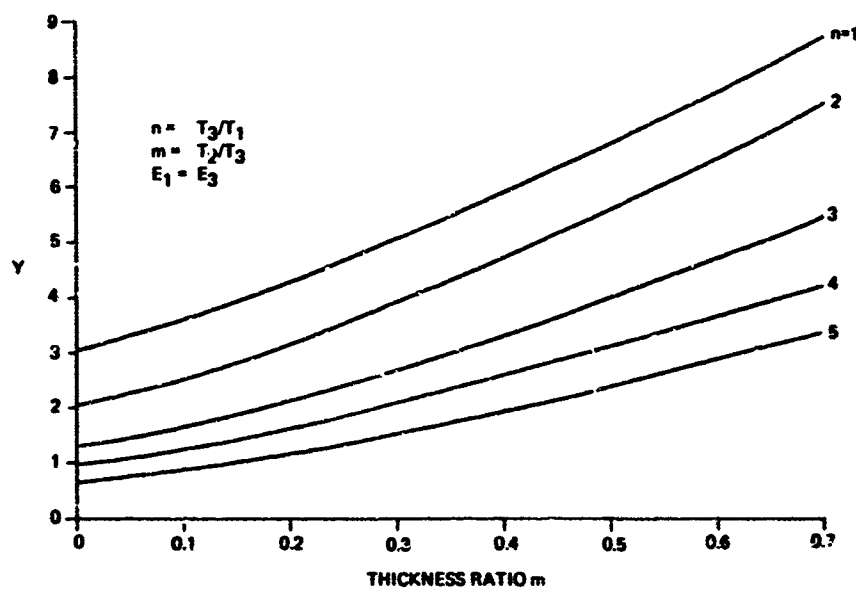
Fig. 6 - Effect of thickness ratios on Y

137

CONCLUSIONS

The equations derived for J and G, in terms of the measured quantities, provide a simple means of calculation. The magnification factors M_2 and M_4 are small. However, the magnification factors M_1 and M_3 vary greatly, depending on the geometry of the cross section and the degree of coupling of the layers. Several specimen of various core thicknesses and facing materials may be necessary to obtain the values for J and G for a wide frequency range at the given temperature.

NOMENCLATURE

D	= the sum of the flexural stiffnesses of layers one and three
E_1, E_3	= elastic moduli of layers one and three, respectively
f	= natural frequency (Hz) of the composite for small composite loss factor
f_d	= measured natural frequency (Hz) of the composite beam
G	= storage shear modulus of the viscoelastic damping layer
i	= $\sqrt{-1}$
K_e	= equivalent extensional stiffness
L	= beam length
M_1, M_2, M_3, M_4	= magnification factors
T_1, T_2, T_3	= thicknesses of layers one, two, and three, respectively
Y	= geometric parameter
α	= mode parameter
β	= material loss factor
η	= composite loss factor
ρ	= density of composite per unit length
ρ_1, ρ_2, ρ_3	= densities of layer one, two, and three, respectively
δ	= distance between the centroidal planes of layers one and three
λ	= frequency ratio
ϵ	= density per unit length ratio
Ω^2	= real part of complex frequency
ω^2	= complex frequency

REFERENCES

1. H Oberst, "Uber die Dampfung der Biegeschwingungen dunner Bleche, durch fest haftende Belage", Acoustica, Vol. 2, Akustische Beihefte, No. 4, pp. 181-194, 1952 (translated by H. L. Blachford, Inc., Newark, N. J.).

2. R. A. DiTaranto, "Theory of Vibratory Bending for Elastic and Viscoelastic Layered Finite Length Beams", J. of Applied Mechanics, Vol. 32, Trans, ASME, Vol. 87, Series E, pp. 881-886, 1965.

3. E. E. Ungar, "Loss Factors of Viscoelastically Damped Beam Structures", J. Acous. Soc. Am., Vol. 34, No. 8, pp. 1082-1089, August, 1962.

4. D. Ross, E. E. Ungar, and E. M. Kerwin, Jr., "Damping of Plate Flexural Vibrations by Means of Viscoelastic Laminate", Structural Damping. J. E. Ruzicka, Ed., ASME, New York, 1959.

5. R. A. DiTaranto and J. R. McGraw, "The Free Vibratory Bending of Damped Laminated Plates", ASME Paper No. 69-Vibr-68.

6. F. Abdulhadi, "Transverse Vibrations of Laminated Plates with Viscoelastic Layer Damping", The Shock and Vibration Bulletin No. 40, Part 5, pp. 93-04, December, 1969.

7. J. E. Ruzicka, T. F. Derby, D. W. Schubert, and J. S. Pepi, "Damping of Structural Composites with Viscoelastic Shear-Damping Mechanisms", NASA, CR-742, March, 1967.

8. T. F. Derby and J. E. Ruzicka, "Loss Factor and Resonant Frequency of Viscoelastic Shear-Damped Structural Composites", NASA, CR-1269, February, 1969.

9. A. D. Nashif, "New Method for Determining Damping Properties of Viscoelastic Materials", The Shock and Vibration Bulletin No. 36, Part 4, pp. 37-47, January, 1967.

10. T. J. Dudek, "Determination of the Complex Modulus of Viscoelastic Two-Layer Composite Beams," J. Composite Materials, Vol. 4, pp. 74-88, January, 1970.

11. T. Nicholas and R. A. Heller, "Determination of the Complex Shear Modulus of a Filled Elastomer from a Vibrating Sandwich Beam", Experimental Mechanics, pp. 110-116, March, 1967.

12. C. M. Canon, A. D. Nashif, and D. I. G. Jones, "Damping Measurements on Soft Viscoelastic Materials Using a Tuned Damper Technique", The Shock and Vibration Bulletin No. 38, Part 3, pp. 151-163, November, 1968.

13. A. J. Roscoe III, E. V. Thomas, and W. Blasingame, "Measurement of Complex Shear Modulus of Viscoelastic Materials by Mechanical Impedance Methods," The Shock and Vibration Bulletin No. 35, Part 7, pp. 267-274, April, 1966.

Mr. Fox (Barry Controls): In your analysis, was it assumed that there was no damping in the elastic layer?

Mr. Abdulhadi: Yes, we assumed that the damping in the elastic layers was very small compared to that of the viscoelastic layers.

Mr. Fox: Would it be easy to modify that to include damping if one knew the loss factor and the shear modulus of the elastic layer itself?

Mr. Abdulhadi: If you introduce the loss factor of the elastic layers into the original frequency equation you will end up with two new polynomials which have to be recoupled again. The equations that I have shown resulted from assuming that the damping is in the middle layer. If the damping of the elastic layers is included we have to inspect the equations that result from such an assumption and see if we can couple them.

Mr. Henderson: I would like to interject one comment and that is that the case of the two viscoelastic layers or damping in two outside layers, was covered by Nicholas and Nashif in the 39th Shock and Vibration Symposium. It is a different treatment of the problem, but the problem was discussed.

IMPROVING RELIABILITY AND ELIMINATING MAINTENANCE

WITH ELASTOMERIC DAMPERS FOR ROTOR SYSTEMS

J. L. Potter
Lord Manufacturing Company
Erie, Pennsylvania

Elastomeric dampers are a new generation of dampers designed to prevent helicopter and/or VTOL rotor system instability. The damper employs a highly damped visco-elastic polymer, vulcanized and bonded to metallic members which in turn are connected to the rotor system. Deformation of the viscoelastic material produces a total resisting force composed of a damping and an elastic component operating 90° out of phase due to the hysteresis inherent in the polymer. The damper service life (T.B.O.) can be in the range of 1500 to 2000 flight hours with no maintenance or lubrication required. Elimination of maintenance and lubrication are accomplished through use of the viscoelastic material, design simplicity, and no sliding surfaces. Operation is possible throughout a temperature range of -65° to +200°F. Adverse environmental effects such as weathering, oil, and sand and dust are virtually non-existent. Laboratory and flight testing have provided evidence that the elastomeric damper can prevent rotor instability.

INTRODUCTION

The term elastomeric damper describes a new concept of devices to dissipate energy through the use of visco-elastic materials. The elastomeric damper has some new characteristics which may make it attractive for use in preventing instability of helicopter and/or VTOL rotor systems and perhaps other applications where auxiliary damping devices are required. Its most important assets are improved reliability and elimination of costly maintenance usually associated with conventional energy dissipative devices such as friction or viscous dampers. As a result, use of the elastomeric damper can lead to reduced operating cost and aircraft downtime.

RESUME OF A TYPICAL ELASTOMERIC DAMPER

Figure I and II are photographs of a typical viscoelastic damper designed, manufactured, and tested for service in a fully articulated helicopter rotor system.
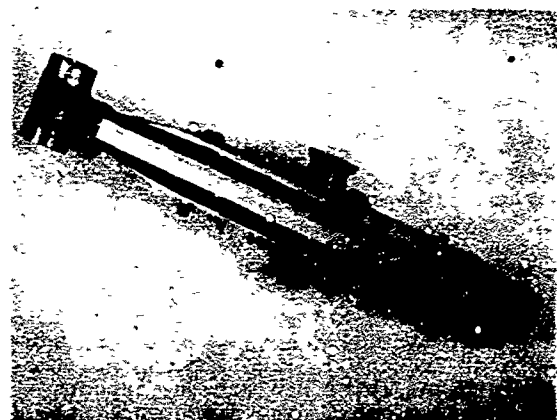

FIGURE I.   TYPICAL VISCOELASTIC DAMPER

The damper shown weighs less than five pounds and will fit within a two by three by fifteen inch space envelope. The construction is primarily of aluminum and a custom compounded silicone type elastomer, while the hardware is alloy or stainless steel. The elastomer is vulcanized and bonded to the aluminum members. The center and end connections, containing teflon bushings to eliminate lubrication, attach to clevises of the rotor head and blade cuff. No maintenance is required for this damper throughout its overhaul period except for occasional visual inspection while installed in the rotor system. Cost is comparable or less than conventional viscous or friction type dampers.
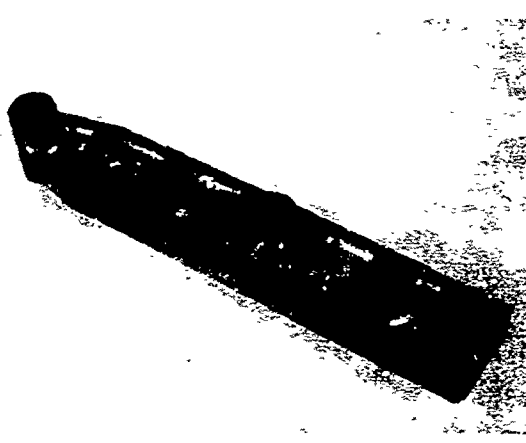
FIGURE II. TYPICAL ELASTOMERIC PROTOTYPE DAMPER.

WHY ROTOR SYSTEM DAMPERS?

Helicopters and/or VTOL rotor systems most generally require a certain amount of damping in the rotor system to prevent an instability phenomena known as ground or air resonance from occurring while the rotor is operating on the ground or during flight. The instability is called resonance due to the fact that it occurs when a fuselage natural frequency, involving horizontal or in-plane rotor hub motion, is coincident or close to the difference between the rotor speed and the rotating blade in-plane natural frequencies.[1] Failure to adequately control this phenomena can lead to total destruction of the aircraft.

Rotor systems which utilize in-plane or drag hinges usually employ some type of damping device to prevent instability, while hingeless rotors, especially those of low stiffness (a rotor system with blade in-plane natural frequencies below the normal rotor operating speed) may require some auxiliary damping to prevent rotor instability, particularly during flight.

PROBLEMS WITH VISCOUS OR FRICTION DAMPERS

The most common types of auxiliary dampers in widespread use today for helicopter or VTOL rotor systems are of the viscous (ex. hydraulic) or friction variety. While these types perform satisfactorily, they may require frequent inspection and maintenance due to their characteristic mode of operation -- that is, employment of sliding surfaces which tend to promote wear or leakage -- reliability can, therefore, be a problem. Environmental effects common to aircraft operation, such as sand & dust, oil, humidity, fungus, and weathering may further reduce the time between overhauls (T.B.O.), leading to costly aircraft downtime.

THE ELASTOMERIC DAMPER CONFIGURATION

As the name implies, the elastomeric damper employs a highly damped (low resilience) viscoelastic material, vulcanized and bonded to metallic components, which in turn are attached to the rotor head and blade cuff as shown schematically in Figure III. Normal lead-lag (in-plane) motion of the blade causes an oscillatory angular (one cycle per revolution) motion of the blade cuff about the drag hinge as shown for the fully articulated system of Figure III. By geometry, this angular motion is transformed into oscillatory axial linear motion of the damper which in turn causes deformation (shearing) of the viscoelastic material between the outer and inner metallic attachment plates as shown in view A-A of Figure III. The deformation of the elastomeric material produces the dynamic forces necessary to prevent air or ground resonance of the rotor system.
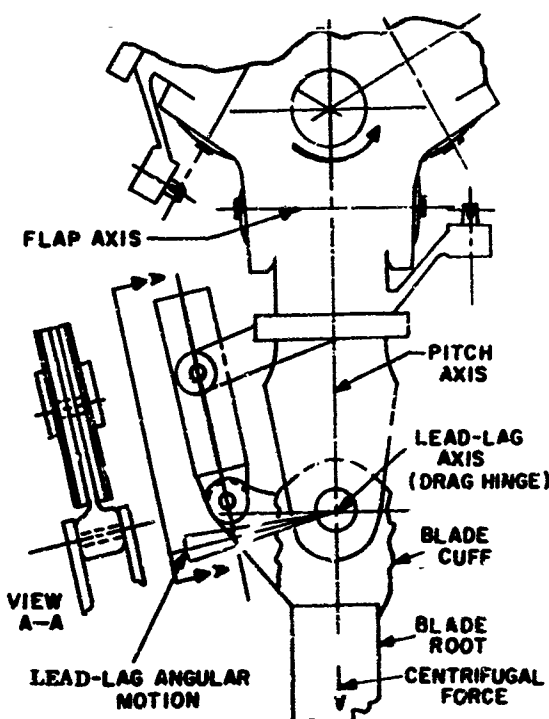
FIGURE III. INSTALLATION OF VISCO-ELASTIC DAMPER IN ARTICULATED ROTOR SYSTEM.

Figure IV is a partially detailed view of an elastomeric damper to explain the construction. The damper inner member is attached at one end to the rotor blade cuff while the two outer members are connected to the rotor head. The viscoelastic material is vulcanized and bonded between the outer plates and the inner member. The two bolts and spacers at each end of the damper body provide for proper alignment of the outer plates and improved load distribution. In this particular damper, elastomeric bearings are provided at the attachment points. The elastomeric bearings completely eliminate any sliding surfaces by accommodating all relative motion between the inner sleeve and the damper body through a shearing deformation of the rubber. In the installation, similar type elastomeric bearings are locked as shown, into the rotor head and blade cuff attachment clevises. Tightening torque on the bolts provides sufficient clamping force on the

three bearing inner sleeves to insure that all relative motion (due to slight rotation) occurs in the elastomer and not metal to metal, to prevent wear or fretting. This eliminates all lubrication and reduces maintenance. The elastomeric bearings have soft and extremely stiff spring rates in the torsional and radial modes, respectively. Other dampers have been manufactured using self-lubricating teflon type bearings at the attachment points.

VISCOELASTICITY [2]

The molecular structure of all elastomeric (viscoelastic) materials is such that internal friction (hysteresis) is produced when the material is deformed. Sinusoidal deformation of a viscoelastic material results in a resisting force which, if the force-deflection relation is linear, is sinusoidal. The internal friction produces a phase difference between the force and the deflection. The total force can be represented as a vector composed of two components, one in phase with the deformation and the other 90° out of phase. The two forces are referred to as the elastic and damping components as shown in Figure V.
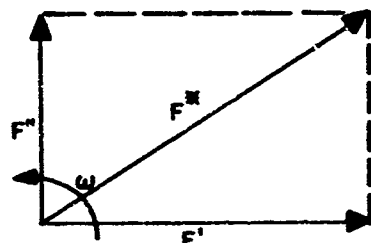
FIGURE V. VECTORIAL REPRESENTATION OF ELASTIC AND DAMPING COMPONENTS FOR ELASTOMERIC MATERIALS.

where:

F'' = Damping force

F' = Elastic force

F^* = Total resisting or complex force.

The magnitude of F'' and F' depend upon the amplitude of deflection, the shape and size of the elastomeric material and the complex dynamic modulus of the viscoelastic material. If G^* represents the complex dynamic modulus and its damping and elastic

143

modulii by G" and G', respectively, then:

$$G^* = G' + iG^* \quad \text{eq. (1)}$$

$$|G^*| = \sqrt{(G')^2 + (G^*)^2} \quad \text{eq. (2)}$$

Where

$$G' = F'(q)/X \quad \text{eq. (3)}$$

$$G^* = F''(q)/X \quad \text{eq. (4)}$$

X = Amplitude of deflection-inches

q = Factor dependent on size and shape

Since FORCE/DEFLECTION = STIFFNESS, it can be shown using equations (3) and (4) that:

$$F'/X = G'/q = K' \quad \text{eq. (5)}$$

$$F''/X = G''/q = K^* \quad \text{eq. (6)}$$

Where

K' = Dynamic elastic stiffness of an elastomeric damper or mounting.

K" = Damping stiffness of an elastomeric damper or mounting.

The preceding reviews the operating principle of the elastomeric (viscoelastic) damper. The total resisting force (F*) produced by the damper elastomer deformation is composed of the damping (F") and the dynamic elastic (F') forces acting 90° out of phase. Since the elastomeric damper has an elastic and damping stiffness, the total force produced when the damper is deflected would be consequently higher (than that of a viscous or friction type device) in order to obtain the same damping force (F").
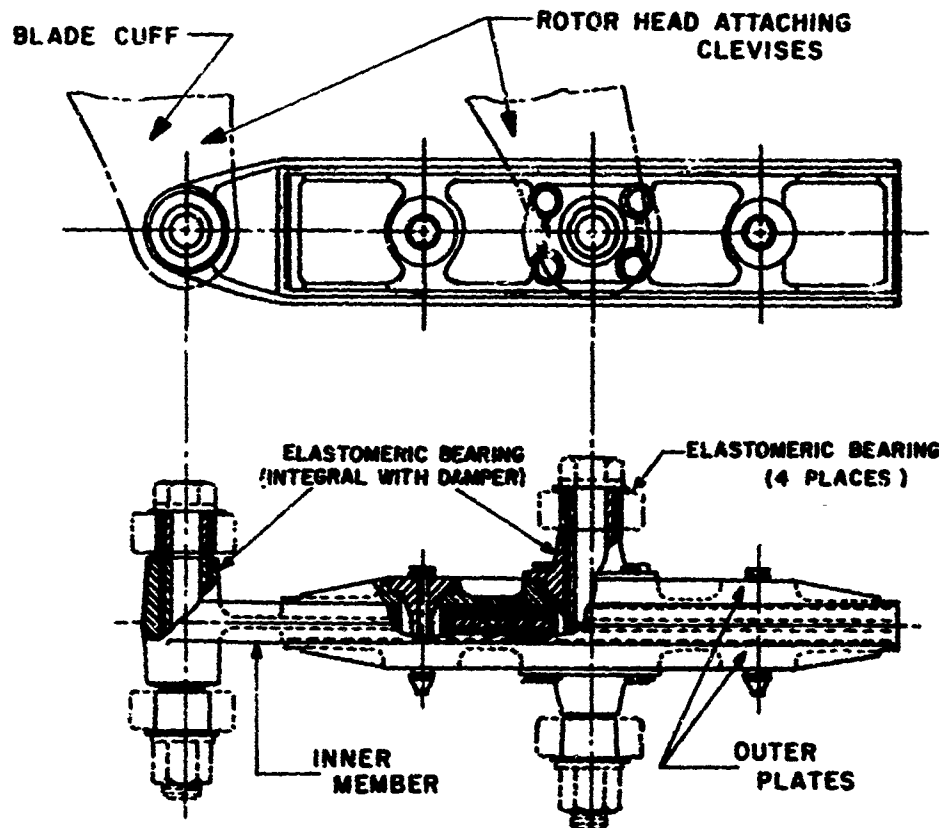
FIGURE IV. CUTAWAY OF ELASTOMERIC DAMPER WITH ELASTOMERIC BEARINGS AT ATTACHMENT POINTS.

DAMPING CHARACTERISTICS

In order to further understand the elastomeric damper it is convenient from an engineering dynamics standpoint to determine an equivalent viscous damping ratio (ζe).

$$\zeta e = C/C_c \qquad \text{eq. (7)}$$

Where

C = Viscous damping constant

C_c = Critical damping constant

It is known [3] that the ratio of the elastic (K') to damping (K") stiffness can be utilized to determine the transmissibility of a vibratory system operating at resonance.

$$T' = \sqrt{1 + \left(\frac{1}{K''/K'}\right)^2} \qquad \text{eq. (8)}$$

Where

T' = Transmissibility at resonance.

From the well known equation for transmissibility of a viscous damped vibratory system:

$$T = \sqrt{\frac{1 + (2\ C/C_c \cdot f/f_n)^2}{\left((f/f_n)^2 - 1\right)^2 + (2\ C/C_c \cdot f/f_n)^2}} \qquad \text{eq. (9)}$$

Where:

T = Transmissibility of system

C/C_c = damping ratio

f/f_n = ratio of excitation to system natural frequency.

If $f/f_n = 1$, the system is at resonance and the corresponding transmissibility (T') can be calculated:

$$T' = \sqrt{\frac{1 + (2\ C/C_c)^2}{(2\ C/C_c)^2}} \qquad \text{eq. (10)}$$

Since equations 8 and 10 are the transmissibilities for resonant systems, the T's can be set equal to each other and the equivalent damping ratio (ζe) for the elastomeric damper may be found:

$$1 + \left(\frac{1}{K''/K'}\right)^2 = \frac{\left(1 + (2\ C/C_c)^2\right)}{4\ (C/C_c)^2} \qquad \text{eq. (11)}$$

If:

$$Q = K'/K'', \text{ then} \qquad \text{eq. (11a)}$$

$$1 + Q^2 = \frac{\left(1 + (2\ C/C_c)^2\right)}{4\ (C/C_c)^2} \qquad \text{eq. (11b)}$$

finally, the equivalent viscous damping ratio (equation 5) can be found:

$$\zeta e = \frac{1}{2Q} \qquad \text{eq. (12)}$$

The value of ζe for elastomeric dampers lies in the range of .12 to .19, depending on the design, and the strain-frequency relationship imposed on the elastomeric section. It should be noted that ζe is true for systems operating at resonance only.

MOTION - FREQUENCY EFFECTS

The damper dynamic characteristics of K', K" and ζe are affected by the motion (strain) and operational frequency that results from the rotor speed and blade in-plane (lead-lag) motions.

As a general rule, as the axial motion (strain) imposed on the damper increases, the elastic (K') and damping (K") stiffnesses decrease. The equivalent damping ratio also decreases with increasing motion, but at a slower rate -- what this all means is that the damping force available to prevent rotor instability is decreasing as the in-plane blade motion increases. Design of the elastomeric portion of the damper must be such that sufficient damping is available during ground start-up and shut-down, flight, and autorotation. Variation of damper dynamic characteristics versus axial motion (blade in-plane motion) for a typical damper are demonstrated in Figure VI.

The effect of rotor frequency on the dynamic elastic and damping ratio for a damper is shown in Figure VII. This test was performed with a constant axial motion imposed on the damper at room temperature. As can be noted, the change in characteristics over the broad frequency range shown is slight. For normal helicopter rotor speeds (3 to 7 Hz), the effect is negligible.

TEMPERATURE EFFECTS

The specially compounded silicone type polymer used in the damper exhibits relatively minor changes in dynamic characteristics over a wide

temperature range. Operation of the
damper from -65° to +200°F. is there-
fore possible, providing the changes
in dynamic characteristics are within
acceptable performance requirements.
Laboratory tests show a moderate change
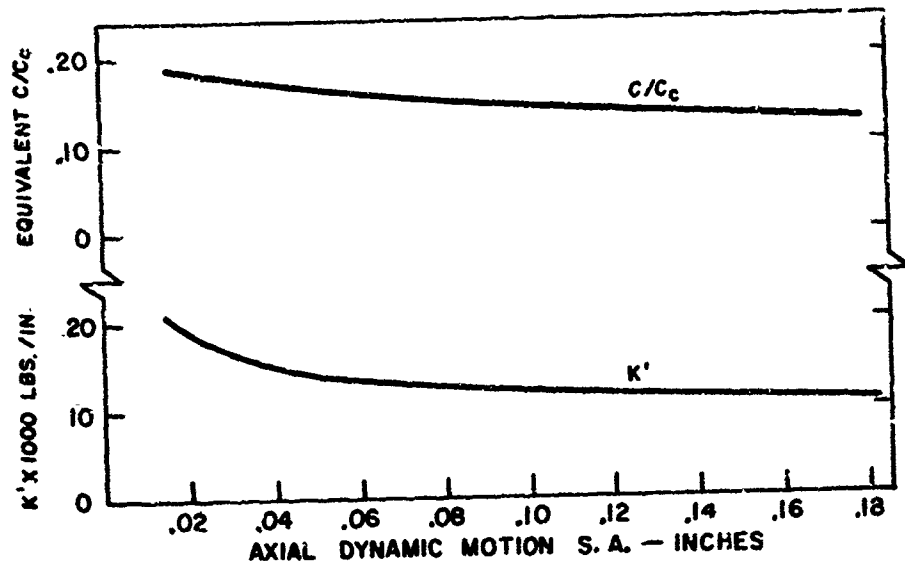
FIGURE VI.   ELASTIC AND EQUIVALENT DAMPING RATIO VERSUS MOTION AT ROOM
TEMPERATURE FOR A TYPICAL ELASTOMERIC DAMPER.
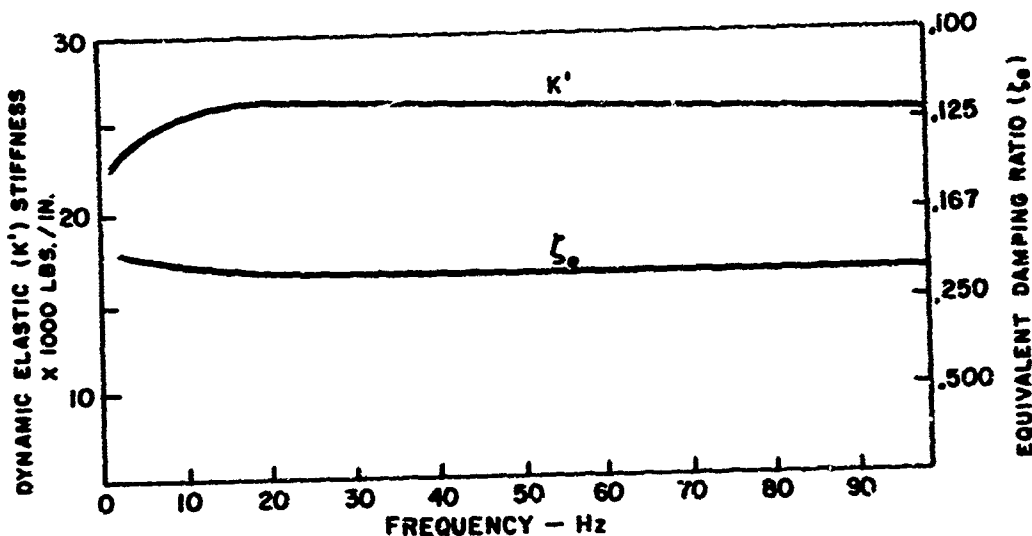
FIGURE VII.   FREQUENCY EFFECT ON DAMPING RATIO AND ELASTIC STIFFNESS FOR AN
ELASTOMERIC DAMPER.

146

in the equivalent damping ratio (ζ_e) throughout the -65° to +200°F. spectrum even though a relatively large change in the elastic stiffness is noted as demonstrated in Figure VIII.

time between overhaul (T.B.O.) of the elastomeric damper can be in the range of 1500 to 2000 or more flight hours. Laboratory and flight tests have verified this predicted life. The
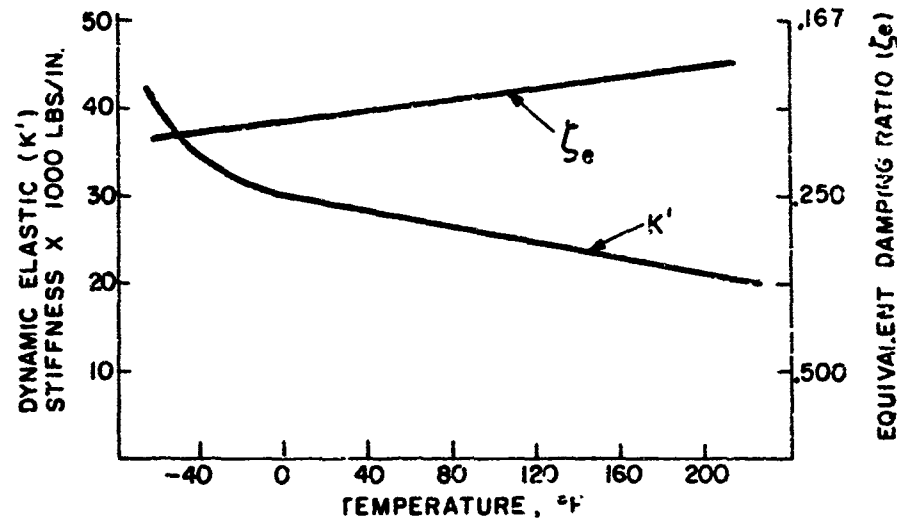
FIGURE VIII. TEMPERATURE EFFECT ON DAMPING RATIO AND ELASTIC STIFFNESS FOR A TYPICAL VISCOELASTIC DAMPER.

ENVIRONMENTAL EFFECTS

The adverse effects of environments such as sand and dust, ozone, humidity, oil, fungus, and sunlight are practically nonexistent because of the following basic factors:

1. Use of a specially compounded silicone polymer minimizes chemical deterioration.

2. Metallic components are protected against corrosion by suitable chemical treatment.

3. Potentially troublesome boots or seals are eliminated.

4. There are no sliding surfaces which may tend to trap contaminants.

5. Lubricants or fluids cannot leak and effect performance degradation.

ENDURANCE LIFE

The endurance life or predicted

fatigue life characteristic of the elastomer is similar to nonferrous metals (ex. aluminum), that is, there is a finite life depending on the stress-strain relationship. A modified form of Miner's Theory of Accumulative Damage may be used to predict the endurance life of the elastomer. Tests to date, indicate a fifth power function to describe the S-N curve:

$$N = \left[\frac{C}{E}\right]^5 \qquad \text{eq. (13)}$$

where:

N = Number of cycles at E.

E = Dynamic strain, single amplitude.

C = Constant dependent upon size, shape, and frequency of operation.

Tests are continuing, to verify the S-N curve. Failure of the elastomeric damper is very gradual and not

147

tastrophic. Figure IX demonstrates the rate of stiffness loss of a typical elastomeric damper throughout a 1200 hour laboratory test under a simulated flight-motion spectrum. No physical deterioration of the damper was evident after testing was halted at 1200 hours. Low cycle fatigue tests (increased axial motion at reduced frequencies) show that long time deterioration is characterized by a gradual loss of elastic and damping stiffnesses while the damping ratio remains relatively constant. Some "checking" or cracking of the elastomer was also experienced during the low cycle fatigue tests.

Since the elastomeric material is highly damped, the hysteresis effect develops an internal heating. Premature deterioration of the elastomer can occur if the frequency and/or motion are too high. The energy dissipated per volume of elastomer is proportional to the internal heating (thus temperature) according to the following:

$$P/V = h \ (f) \ (E)^2 \ K'' \ \varpi \ T \quad \text{eq. (14)}$$

where

P/V = Power or energy in watts per unit volume.

f = Operating frequency

E = Strain in shear, single amplitude due to axial motion.

K" = Damping spring rate (stiffness) of damper.

h = Constant depending on shape, size.

T = Internal temperature due to hysteresis heating.

Excessive internal heating can lead to premature deterioration. The type deterioration of the elastomer due to accelerated testing is not representative of the type of degradation expected under normal simulated flight conditions of rotor speed and motion -- for this reason accelerated tests are not valid. Design of the damper must be such
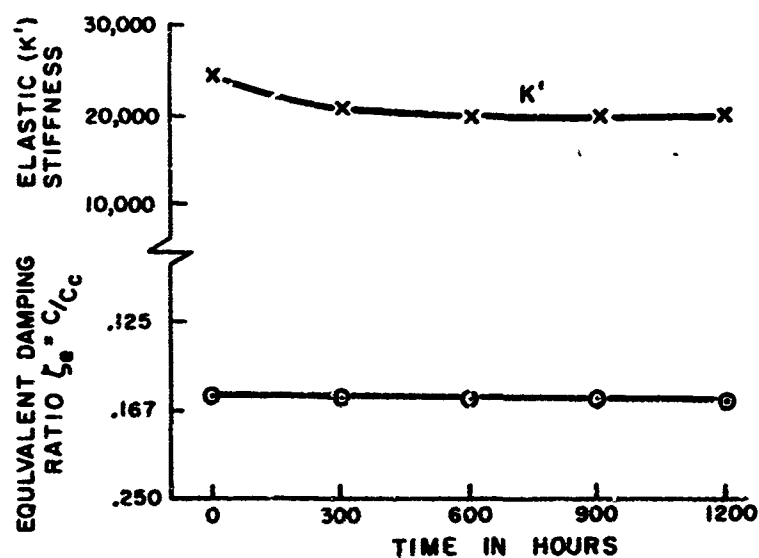
FIGURE IX. RATE OF STIFFNESS LOSS OF A TYPICAL ELASTOMERIC DAMPER THROUGHOUT A 1200 HOUR ENDURANCE TEST.

148

that the energy dissipated per unit volume of elastomer during normal operation does not lead to early degradation.

FLIGHT TEST RESULTS

In cooperation with a helicopter manufacturer, prototype elastomeric dampers were designed and manufactured. These were, in accordance with specifications, to be whirl tower and flight tested as a potential replacement for a viscous damper. Initial testing of the dampers verified the concept that viscoelastic dampers could replace the conventional hydraulic dampers. The dampers were matched in sets (for a rotor system) to a ± 5% tolerance on the dynamic elastic (K') stiffness for the normal flight condition. The matching was performed to minimize the variation in the dynamic damper forces between blades. As of this writing, flight testing is continuing and the results appear very encouraging.

SUMMARY

The elastomeric damper concept and its advantages have been described and its characteristics identified. The most attractive feature of the damper is the elimination of maintenance and its improved reliability through simplicity of design principles. Reduced operating cost and aircraft downtime can be foreseen.

REFERENCES

(1) R. T. Hytwyn and W. Mias, "Airborne and Ground Resonance of Hingeless Rotors", Preprint No. 414 of American Helicopter Society Forum, June, 1970, p. 1.

(2) G. W. Painter, "Dynamic Characteristics of Silicone Rubber", Lord Library No. 12, Reprinted from transactions of ASME, October 1954, p. 1131.

(3) G. W. Painter, "Dynamic Properties of BTR Elastomer", Lord Library No. 14, Reprinted from SAE National Aeronautic Meeting, 1958.

EFFECT OF HIGH POLYMER ADDITIVES ON DIFFUSER FLOW NOISE

B. M. Ishino
California State College
Fullerton, California

and

R. C. Binder
University of Southern California
Los Angeles, California

An exploratory investigation was conducted to determine the effects of dilute concentrations of high molecular weight polymers in water on liquid flow noise. Experimental measurements were made in a two-dimensional variable-angle diffuser with water and aqueous solutions of the polymers, Polyethylene Oxide and Guar Gum for different flow conditions. In the region of marginal separation, reductions in overall sound pressure level up to 10 decibels were obtained.

The investigation required the design and development of a bench-type blow-down water tunnel system and the instrumentation necessary for acquiring flow data. Test results show noise and energy level comparisons between polymer solutions and water for various flow rates and diffuser wall angles.

INTRODUCTION

Considerable effort, particularly by the Navy, has been directed toward the study of the remarkable drag reducing effects of certain high molecular weight polymer additives in the flow of water over surfaces. The question of what effects such polymers would have on flow noise evolved as a result of the above observation. The value of being able to reduce or control flow noise is quite apparent.

Very small concentrations of many natural and synthetic high-polymer substances have the property of reducing the turbulent friction drag of the liqu ' in which they are suspended or dissolved. Toms [1, apparently was the first to report this remarkable phenomenon. Hoyt and Fabula [2] showed a drag reduction in turbulent pipe flow by as much as 70 percent. Other investigators [3] have reported similar results. To date, the theory or mechanism of this anomalous behavior has not been fully established.

This investigation, which is of an exploratory nature, was undertaken with the main objective of obtaining experimental values on the effect of high-polymer additives on flow noise. Measurements were made of water flow, with and without polymer additives, in a two-dimensional variable-angle diffuser. This approach provides means for obtaining different flow regimes and a method

of determining the effect, if any, of additives on flow noise. Such measurements might furnish information which would establish the mechanism or theory for the effect of high-polymers on fluid friction.

EXPERIMENTAL APPARATUS AND INSTRUMENTATION

A bench-type blow-down water tunnel system was designed and developed for this investigation. This system provides a suitable method for testing with polymer additives which degrade under shear flow conditions.

The system includes a storage tank in which the polymer additive is mixed with water, a plenum chamber at inlet to water tunnel with honeycomb and screens for the purpose of reducing inlet flow noise and turbulence, a variable-angle, two-dimensional diffuser test section and an exit flow region with straightening vanes. A float tank control acts on a compressed air supply to maintain a constant pressure head at inlet to the plenum chamber. This control provides a constant flow rate through the test channel during a test run and could be used for different flow rates by a vertical adjustment of the float tank position.

Details of the variable-angle diffuser test section are shown schematically in Fig. 1. As

Illustrated in View A-A of Fig. 1, the upper and lower walls which were made of clear acrylic were used to hold the adjustable side walls in place and to allow visualization of the flow; provision was made for dye injection. Hard rubber, stiffened by an aluminum block, was used for each adjustable side wall; rubber provided flexibility in adjusting the side walls and helped seal the enclosed channel. For static pressure tap measurements an aluminum island strip was arranged flush with the inner rubber wall surface. As shown in View A-A of Fig. 1, the distance between the upper and lower walls was 2 inches and the straight length of each diffuser wall was 8 inches. For all tests run in this investigation, the throat width was set at 0.50 inch.

A hydrophone was mounted on the left wall midway between the upper and lower surfaces of the diffuser test section at a distance of 4 5/6 inches from the throat section. A Massa M-213 microphone with a 1/8 inch diameter face was converted to a hydrophone by placing a latex boot over its casing. Vaseline was used to couple the microphone boot with the microphone face. This coupling provided a very low acoustic transmission loss since the specific impedance of the latex boot and vaseline used in the tests were approximately equal to that of water. A latex sleeve was placed on the microphone to isolate it from possible wall vibration. In order to maintain a constant check on wall vibration, a dummy microphone was mounted to the wall of the aluminum stiffener and the signals were observed on an oscilloscope.

Figure 2 is a schematic of some of the instruments used in measuring diffuser flow noise. The hydrophone signals at the diffuser side wall were used to measure the overall sound pressure level. The signals were first recorded on tape and then analyzed by means of the sonic analyzer. The entire flow noise measuring system shown in Fig. 2, with the exception of the tape recorder and sonic analyzer, was calibrated with a small electrodynamic shaker using the method "Vibrating Column of Liquid" described by Schloss and Strasberg [4]. The tape recorder and sonic analyzer were calibrated in accordance with the manufacturers instructions.

POLYMER ADDITIVES

Tests were made with the high-molecular weight polymers, Polyox (Polyethylene Oxide, WSR-301 by Union Carbide) and Guar Gum (J-2FP by Westco-Research). The primary consideration in mixing polymers is to obtain a homogenous medium with a minimum of shear degradation. There are several methods of mixing polymers. The method used in this investigation was to pre-disperse first the powder form of polymer in ethanol; then this mixture was mixed with 4 percent of the total volume of tap water used in the test runs by means of a slowly revolving cylinder. After mixing, the concentrated solution was stored for a period from one to two days to allow for complete hydration. The concentrated solution was subsequently mixed with tap water in the storage tank; in the storage tank the mixture was stirred slowly by hand until a uniform solution was obtained.

Tests with a capillary tube viscometer showed no significant difference in viscosity for solutions stored for one day and for solutions stored for two days. Also, flow noise runs were not significantly affected by storage periods up to two days. The pH readings which were taken periodically of samples from actual tap water runs, were found to remain reasonably constant. The pH readings ranged from 7.2 to 8.9.

EXPERIMENTAL PROCEDURES AND RESULTS

All test runs made in this investigation were under steady flow conditions and at the temperature of tap water (68 ± 2 degrees Fahrenheit). Diffuser flow instability was found when the side walls were arranged symmetrically, whereas the flow was observed to be stable when one side wall was fixed parallel to the stream line at the diffuser throat. As illustrated in Fig. 1, all test runs were made in the stable configuration with the left side wall fixed and the right side wall adjusted for different angles of diffusion. In addition to tap water, tests were made with Polyox in concentrations ranging from 1/2 to 8 ppm and Guar Gum in concentrations ranging from 25 to 400 ppm.

Diffuser wall angles $\underline{D}$, varying from 0 to 25 degrees were employed in the experiments. The wall angles were set within a tolerance of 5 minutes. Average throat velocities $\underline{U}$, ranged from 7 to 15 feet per second.

To demonstrate the consistency of the water tunnel results with other works, the ratio of the rms pressure fluctuations to the dynamic pressure (based on the average throat velocity) was determined for the parallel wall configuration. This ratio was found to be .006 which is in fair agreement with the results of other investigators who have used both water and air flow media. [5], [6], and [7].

Figure 3 shows dimensionless plots of the power spectral density as a function of the Strouhal number by various investigators. The plots of Harrison and Franz were obtained from a review report by Richards, Bull and Willis [8]. Harrison made his arrangements in a subsonic wind tunnel and Franz made his measurements on the submarine U.S.S. Albacore. In Fig. 9 d/δ^* is the ratio of the microphone face diameter to the boundary layer displacement thickness and l/L is the ratio of the distance of the hydrophone from the bow of the submarine to its total length (200 feet).

Data obtained from the parallel wall configuration with water as the flow medium were used to compute the dimensionless power spectrum shown in Fig. 9 which shows that the results of the present investigation are in good agreement with the measurements obtained by Franz at a location 3 feet from the bow of the submarine where $l/L = 0.015$ and $\delta^* = 0.079$ inch. Measurements obtained at a location of 45.6 feet from the bow where $l/L = 0.228$ and $\delta^* = 0.55$ inch compares favorably with the results of Harrison. In the present investigation the boundary layer displacement thickness was approximately 0.01 inch.

152

Diffuser flow noise was measured in terms of the overall sound pressure level SPL defined by the relation

$$SPL = 20 \log_{10} P/P_o \qquad (1)$$

where P is root mean square sound pressure, and P_o is a reference sound pressure of 1 dyne per square centimeter.

For all noise measurements obtained in this investigation the SPL at zero throat velocity was 19 decibels.

Figure 4 shows a plot of the overall sound pressure level SPL as a function of the average throat velocity U for different concentrations of Guar Gum in water and diffuser wall angle D of 10 degrees. Figure 4 shows that tap water, over a range of velocities, had the highest SPL. A concentration of 200 ppm Guar Gum had the lowest SPL over a range of velocities.

Figure 5 shows a plot of SPL versus velocity for Polyox for a diffuser wall D of 10 degrees. The SPL for concentrations of 1/2 and 1 ppm show that water, over a range of velocities, had a higher SPL than the Polyox mixture. The curves for concentrations of 2 ppm and 4 ppm Polyox show values above that for water at the lower velocities and below that for water at the higher velocities.

A review of all data showed that, for the diffuser wall angle of 10 degrees, the lower concentrations of 1 ppm Polyox and 200 ppm Guar Gum gave the greatest reduction of flow noise below that of tap water; this is illustrated in Figs. 4 and 5.

A survey of all the significant data (plotted on semilog paper) showed that, within the limits of data scatter, the functional relation between SPL and U could be described by a logarithmic function of the form given by the equation

$$SPL = S \log U/U_o \qquad (2)$$

where S is a parameter which is dependent upon the diffuser and the solution used for the flow medium, but independent of the velocity. U_o is a reference velocity corresponding to the reference pressure of 1 dyne per square centimeter used in obtaining the overall sound pressure levels.

For specific cases, Eq. (2) may be written as follows:

$$SPL_o = S_o \log U/U_o \qquad (3)$$

and

$$SPL_D = S_D \log U/U_o \qquad (4)$$

Figure 6 illustrates two curves: curve AB representing Eq. (3) and curve AC representing Eq. (4). Consider the curve AB with the factor S_o corresponding to the flow of tap water only between parallel side walls. Consider the curve AC with the

factor S_D for fluid and wall conditions different from that for S_o. Let SPL_o represent the SPL for curve AB corresponding to S_o and let SPL_D represent the SPL for the curve AC corresponding to S_D. A relationship which is independent of velocity is obtained by dividing Eq. (4) by Eq. (3).

$$N = SPL_D/SPL_o = S_D/S_o \qquad (5)$$

Let N represent this ratio of sound pressure levels. This parameter N is a dimensionless ratio which can be used to organize data; in this case the SPL for diffuser flow using various concentrations of polymer additives is compared with the SPL for tap water flow noise with parallel walls.

Figure 7 shows a plot of N versus wall angle for tap water, Polyox and Guar Gum. The SPL for tap water with parallel walls was taken as a reference SPL_o. For parallel walls, Fig. 7 shows that both Guar Gum and Polyox had noise levels somewhat higher than that of tap water. Observations (using dye injection at different pressure tap locations) over a range of throat velocities and diffuser wall angles indicated three general flow regimes. Table 1 lists the results. The flow is defined as separated when it no longer adheres to the surface adjacent to the flow field. In one regime, for wall angles D, from 0 to 6 degrees, there was no evidence of separation. In another regime, for wall angles at 14 degrees and higher, the regime was definitely separated flow. In a third regime, for wall angles between 6 and 14 degrees, separation was considered "marginal" in this regime the fluid hovered between incipient and definite separation.

As illustrated in Fig. 7 in the region of no separation, the SPL for Polyox and Guar Gum was slightly above that for tap water. In the region of definite separation, the curves show that Polyox and Guar Gum give SPL values essentially the same as that of tap water. Polyox and Guar Gum give significant reductions in SPL below that of tap water in the region of marginal separation.

FREQUENCY CHARACTERISTICS

Traces from the sonic analyzer were reduced to give power spectral density PSD as a function of frequency. Figure 8 shows plots of PSD for tap water, Polyox and Guar Gum with a wall angle of 10 degrees and throat velocity of 15.6 feet per second. The polymer additives reduced the PSD significantly below that of tap water. Significant values of PSD are in the low frequency range below 200 cycles per second. Figure 8 shows a trend in which the greatest reduction in PSD is in the lower frequencies.

CONCLUDING REMARKS

In this exploratory investigation various measurements and observations were made. The salient points are listed below.

1. The SPL of the flow noise through the diffuser channel was found to be approximately related to the throat

velocity by a logarithmic relation of the form

$$SPL = S \log_{10} U/U_o$$

where $\underline{S}$ is a function of the diffuser wall angle and solution type; $\underline{U}_o$ is a reference velocity.

2. The SPL for a constant throat velocity decreased as the diffuser wall angle increased from 0 degrees, to approximately 6 degrees. This is the region in which flow was not separated. As the wall angle increased from 6 to 14 degrees (marginally separated region) separation increased from an incipent to a fully separated condition. Beyond an angle of 14 degrees the flow was fully separated.

3. In the region of marginal separation the dilute solutions of polyox and Guar Gum reduced flow noise below that of tap water; reductions of up to 100 decibels were obtained. The results showed that the effectiveness of the polymer additives in reducing the SPL increased with velocity. In the fully separated region there was essentially no difference between the SPL using water and the SPL using polymer solutions. The acoustic energy was primarily in the low frequency range below 200 cycles per second.

4. The characteristic "knee" found on the curves of dimensionless power spectral density plots occurring at a Strouhal number of approximately unity does not appear to develop when the boundary layer thickness is small.

It would be desirable to obtain measurements of the velocity distribution of water and polymer solution in the marginally separated region where the greatest noise reduction is obtained. This information would be helpful in interpreting the results. The region of marginal separation, however, is very sensitive to disturbances and is unstable. In this region probes or projections in the stream had a marked effect on the flow. Thus it was considered wise to avoid inserting any probe in the diffuser flow.

ACKNOWLEDGEMENT

REFERENCES

1. B. A. Toms, "Some Observations on the Flow of Linear Solutions Through Straight Tubes at Large Reynolds Numbers," First International Congress on Rheology, 2, 1948.

2. J. W. Hoyt and A. G. Fabula, "The Effect of Additives on Fluid Friction," Fifth Symposium on Naval Hydrodynamics, Bergen, Norway, 1964

3. A. G. Fabula, "Bibliography on the Flow Properties of Dilute Polymer Solutions," U. S. Naval Ordnance Test Station, Pasadena, California, Part 1, Tech. Note P5006-33, May 1965.

4. F. Schloss and M. Strasberg, "Hydrophone Calibration in a Vibrating Column of Liquid," JASA, 34, 7, 1962.

5. C. R. Nisewanger and F. B. Sperling, "Flow Noise Inside Boundary Layers of Buoyancy-Propelled Test Vehicles," Underwater Ordnance Dept., U. S. Naval Ordnance Test Station, China Lake, California, Navy Report 8519, NOTS TP 3511, April 1965.

6. W. W. Willmarth, "Space-Time Correlations and Spectra of Wall Pressure in a Turbulent Boundary Layer," NASA Memorandum 3-17-59W, March 1959.

7. M. Harrison, "Pressure Fluctuations on the Wall Adjacent to a Turbulent Boundary Layer," David Taylor Model Basin, Report 1260, December 1958.

8. E. J. Richards, M. K. Bull and J. L. Willis, "Boundary Layer Noise Research in the U. S. A. and Canada; Critical Review," University of Southampton, Dept. of Aeronautics and Astronautics, Report No. U. S. S. A. 131, April 1960.

9. B. Ishino, "Effect of High Polymer Additives on Diffuser Separation Flow Noise," Ph. D. Thesis, University of Southern California, Los Angeles, California, 1967.

NOMENCLATURE

Symbol

d	microphone face diameter
D	wall angle, degrees
f	frequency
k	spring constant
ℓ	distance

L	total length of the submarine U.S.S. Albacore
LW	left side wall
N	overall sound pressure level ratio, SPL_D/SPL_O
P	root mean square pressure fluctuation
P_O	reference pressure
Polyox	Polyethylene Oxide
ppm	weight parts per million
PSD	power spectral density
rms	root mean square
RW	right side wall
S	parameter associated with SPL
S_D	parameter associated with SPL_D
S_O	parameter associated with SPL_O
SPL	overall sound pressure level
SPL_D	overall sound pressure level corresponding to fluid and wall configuration other than SPL_O
SPL_O	overall sound pressure level corresponding to water and parallel wall configuration
U	average throat velocity
U_o	reference velocity
U_∞	free stream velocity
w	throat width
δ^*	boundary layer displacement thickness
ρ	density
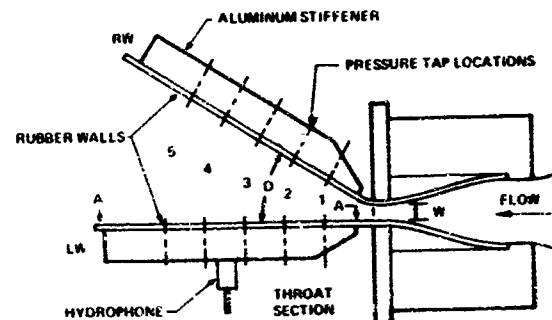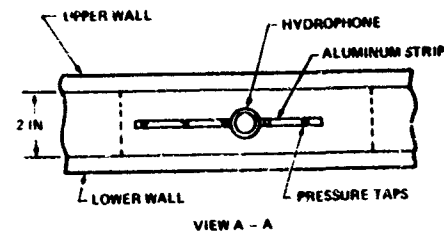
Fig. 1. Diffuser Test Channel
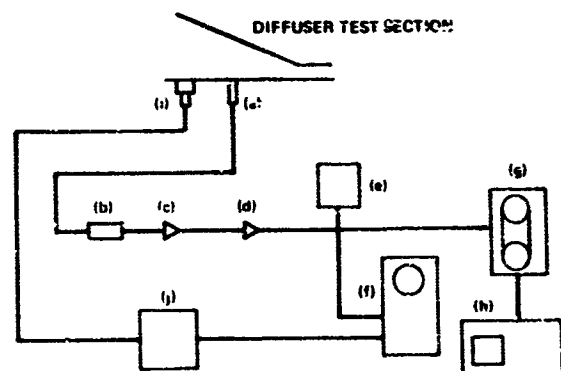
(a) Massa M 213 Microphone
(b) Massa M 114B Preamplifier
(c) Massa M 185 Amplifier
(d) Hewlett Packard 465A Amplifier
(e) Hewlett Packard 3400A True RMS Voltmeter
(f) Tektronix 502A Dual Beam Oscilloscope
(g) Honeywell 8100 Tape Recorder
(h) Panoramic Sonic Analyzer LP-1a
(i) Massa M 141B Microphone
(j) General Radio 1561A Sound Level Meter

Fig. 2. Flow Noise Measuring Equipment Schematic

155
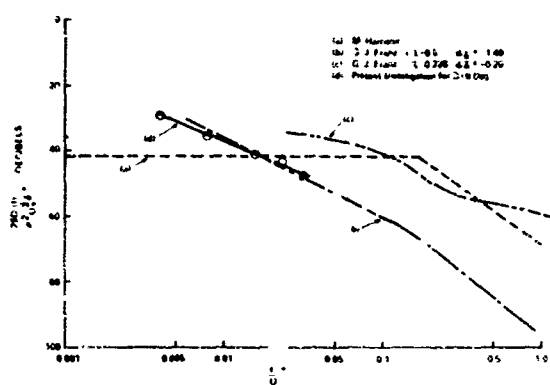
Fig. 3. Power Spectral Density
vs Strouhal Number
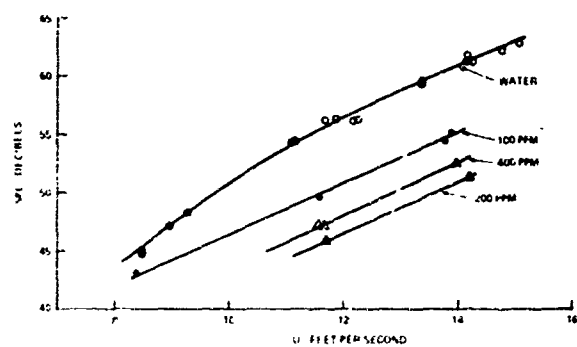
Fig. 4. Overall Sound Pressure Level
vs Velocity, Guar Gum, D=10 Deg.
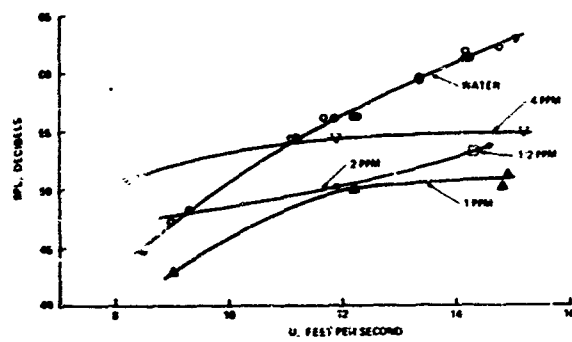
Fig. 5. Overall Sound Pressure Level
vs Velocity, Polyox, D=10 Deg.
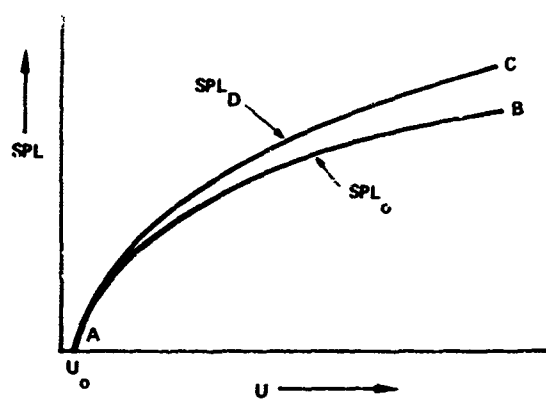
Fig. 6. Overall Sound Pressure Level
vs Velocity
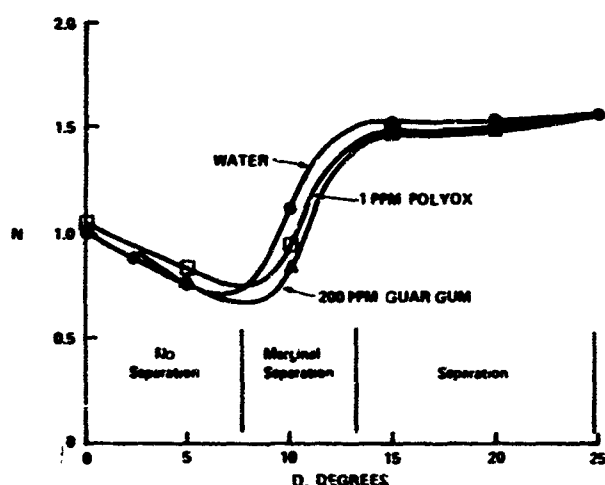
Figure 7. Ratio, N vs Included Wall Angle
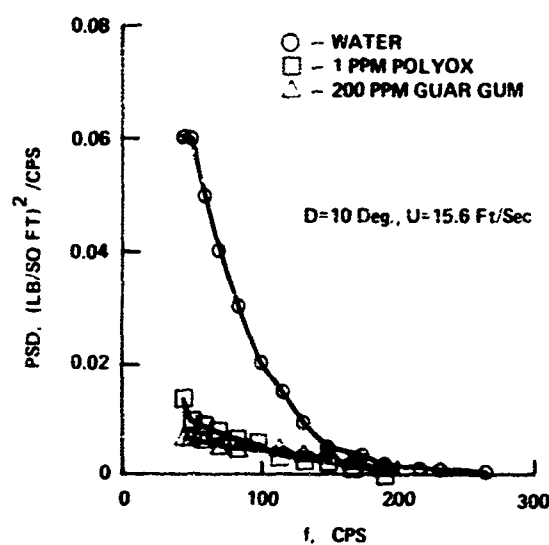
Fig. 8. Power Spectral Density
D=10 Deg., U=15.6 Ft/Sec

156

TABLE 1
Observations of Water Flow Separation

D Deg.	U Ft/Sec	Left Side Wall					Right Side Wall				
		1	2	3	4	5	1	2	3	4	5
0	12.8	N	N	N	N	N	N	N	N	N	N
2.5	13.0	N	N	N	N	N	N	N	N	N	N
5.0	13.1	N	N	N	N	N	N	N	N	N	N
8.0	13.4	N	N	N	N	N	N	N	N	M	M
10.0	12.8	N	N	N	M	M	M	M	M	S	S
12.5	12.5	N	N	M	M	M	M	M	S	S	S
15.0	11.9	N	N	M	M	M	M	S	S	S	S
20.0	11.5	N	N	M	S	S	S	S	S	S	S

M   Marginal Separation

N   No Separation

S   Separation

Column numbers refer to dye injection tap locations.
(same as pressure tap locations shown in Fig. 1)

157

HAWK SUSPENSION SYSTEM PERFORMANCE
ON M754 TRACKED VEHICLE

Paul V. Roberts

Raytheon Company

Missile Systems Division

Bedford, Massachusetts

The rubber isolator, hydraulic damper, HAWK launcher suspension, protects existing HAWK missiles from severe tracked vehicle vibration and shock over rough terrain. The isolators are canted 25 degrees in the pitch-vertical plane to decouple vertical, longitudinal, pitch modes and reduce longitudinal and pitch motion.

The suspension system was particularly effective in attenuating a broad band of severe tracked vehicle vibration to within ±1g on the missiles. Short period shock of 5 ms to 10 ms duration on the vehicle front sprocket and read idler were attenuated from peaks up to 30g on the vehicle to 7g on the missiles. Equivalent static combined load criteria of 7.5g down, 1.5g up ±4.5g fore and aft and ±3g transverse were substantiated by statistical studies of shock data obtained over the Perryman 3 Cross Country Course at Aberdeen Proving Grounds.

INTRODUCTION

The M754 tracked vehicle, which is a modification of the Food Machinery Corp. M113 class vehicle, was specially adapted by the Raytheon Company, Missile Systems Division, to carry the HAWK launcher and three missiles. The system is known as Self-Propelled HAWK, SPH.

The launcher with missiles was initially designed for slewing and tracking as compared to transportation loads and the missiles were principally designed for flight loads. A suspension system which provided adequate protection from severe tracked vehicle vibration and ground shock over rough terrain was considered essential.

The tracked vehicle vibration and shock environment, initially established from background reports and early tests, has been well substantiated by acceleration measurements, between 2 and 2000 Hz, on at least eight vehicles. Natural frequency, mode shape and response analyses to optimize isolation of the vibration and shock environments are described under Suspension System Analyses.

Instrumented engineering and qualification tests were conducted over special concrete bump courses and paved roads at Raytheon Bedford, tank trails and hilly cross country terrain at Fort Devens, Massachusetts, rough desert terrain at White Sands New Mexico and appropriate courses at Aberdeen Proving Ground such as Munson shock and vibration, Perryman 3 cross country and Churchville hills.

Launcher missile simultaneous shock response in principal directions over specific large bumps was studied in detail to establish combined and unidirectional static limit load criteria for hardware design. Statistical studies were made of shock data over the 3.3 mile Perryman 3 qualification course at Aberdeen Proving Ground (APG) to determine probability and number of times various load levels may be reached.

VIBRATION SHOCK AND LOADS ENVIRONMENT

Input vibration and shock from the M754 vehicle to the suspended launcher missile assembly, as well as launcher missile design loads, have been established from measurements on at least eight SPH vehicle systems over a wide variety of terrain.

Vibration

Vehicle vibration is due primarily to track laying impulses which are most severe when travelling at higher speeds on hard pavement. Fundamental track laying impulses for the M754 vehicle occur at a frequency F_v given by:

$$F_V = \frac{S}{0.5}$$

where S is the vehicle velocity in feet per second and 0.5 is the pitch length of the M754 track links. The fundamental frequency F_V at various speeds is therefore:

Speed (fps)	Freq. F_V (Hz)
5	10
10	20
15	30
20	40
30	60
40	80

Since vehicle speeds on hard pavement are generally above 10 fps, corresponding to 6.8 mph, the suspension system should be designed to isolate vibration above 20 Hz and be very effective in attenuating most severe inputs between 40 and 80 Hz.

Significant vehicle vibration is also due to the second, third and fourth harmonics of the track laying frequency; motor, drive system and accessory forcing functions and drumming of cab and body sheet metal panels.

Environmental vibration conditions used for separately mounted vehicle equipments are as follows:

> 0.06 inch DA from 10 to 36 Hz
> ±4g from 36 to 500 Hz
> ±7g from 500 to 2000 Hz

The launcher missile suspension system isolates the above vibration above about 14 Hz. Without the suspension system resonances in the distributed launcher missile structure would result in missile vibration substantially above these levels.

Shock

Most severe vehicle shock which must be attenuated by the launcher missile suspension, is due to rigid elements above the vehicle suspension such as the front drive sprocket and rear idler, striking hard ground while traversing rough terrain, see Figure 1.

Shock levels up to 30g have been measured above the front sprocket with typical durations of about 5 milliseconds. Shocks up to 25g have been measured above the rear idler with typical durations of 10 milliseconds.

Long period shock from about 0.1 to 1 seconds duration also occurs due to basic motion over terrain and excitation of vehicle vertical and pitch frequencies of about 1.7 and 1 Hz, respectively. The following are representative maximum levels.

Vertical 5g down - 2g up
Longitudinal ±4g
Transverse ±2g
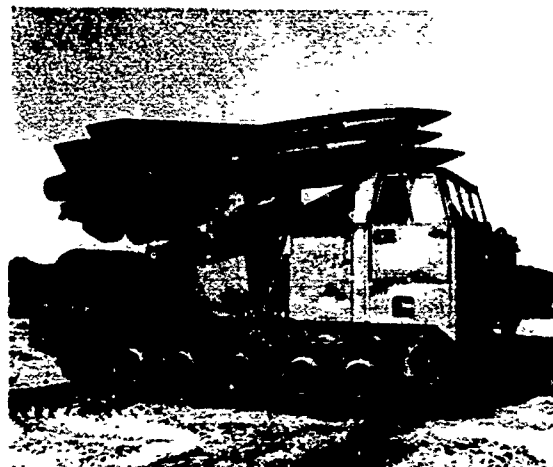
CN-1-600

Fig. 1 - Photograph of SPH

Design Loads

Equivalent static limit loads which were used for newly designed SPH launcher missile attachments as well as upgrading of existing launcher hardware are as follows:

	Combined	Unidirectional
Vertical down	7.5g	8g
Vertical up	1.5g	2g
Longitudinal	±4.5g	±6g
Transverse	±3.0g	±4.5g

These loads are based on combined and unidirectional launcher missile shock response at sufficiently long durations, generally between 40 and 200 ms, to approach static conditions. The response levels are due to a combination of short and longer duration vehicle inputs described in preceeding paragraphs.

SUSPENSION DESIGN CRITERIA

A vertical natural frequency between 6 and 8 Hz is desired to attenuate the peak 25g, 10 ms half sine shock, due to hard bottomming of the rear idler, to 7g at the missiles.

The fore and aft frequency should be between 3 and 5 Hz to limit longitudinal accelerations to about 4.5g. The longitudinal pitch mode should be decoupled as much as possible to minimize pitch motion and the possibility of the outboard missile radomes hitting the top of the cab.

160

The transverse frequency should be between 3 and 4 Hz to limit transverse missile accelerations to about 3.5g.

Frequencies in six degrees-of-freedom, along and about the X, Y, Z axes, with the vehicle considered rigid, should exceed 3 Hz in order to avoid coupling with vehicle suspension frequencies below about 1.7 Hz.

Natural frequencies below 8 Hz would provide about 4 to 1 attenuation of vehicle vibratory inputs above 20 Hz and between 13 and 30 to 1 attenuation of most severe track inputs between 40 and 80 Hz.

Damping must be provided in the suspension system to prevent continuous resonant motion of the launcher and missiles at mount natural frequencies. A high damping ratio of approximately $C/C_c = 0.25$ proved satisfactory during initial tests of the prototype system.

The rubber isolators must have sufficient elastic travel at principal natural frequencies to prevent bottomming due to peak shock inputs.

In summary, the suspension system should control the six principal natural frequencies of the launcher missile assembly on the rigid vehicle between 3 and 8 Hz, provide a damping factor of about $C/C_c = 0.25$ and have sufficient elastic travel to prevent bottomming.

DESCRIPTION OF SUSPENSION SYSTEM

A sketch of the suspension system is shown in Figure 2. Four Lord J5130 sandwich rubber mounting units were specially developed for use in the overall Raytheon engineered suspension system along with seven Delco hydraulic shock absorbers for additional energy absorption and damping.

The two forward and two rear mounts are tilted 25 degrees to the horizontal in the longitudinal, vertical X - Z plane to decouple and limit motion in the longitudinal and pitch modes. In addition to analyses, tests were conducted over the Bedford concrete bump course with the mounts at 12 degrees, 25 degrees and 38 degrees which confirmed better all round performance at the 25-degree angle.

Consideration was also given to tilting the mounts in the lateral as well as longitudinal planes but was not implemented due to high outboard structural loads on the tracked vehicle fenders.

The cg dimensions on Figure 2 are with a three missile total load of approximately 6400 lbs. The cg moves down about 7 inches toward the mounting plane and aft about 1 inch per missile as the load is decreased from the full three missiles.

The J5130 mounting units are 3-inch thick overall, which leaves 2.5-inch rubber thickness, after subtracting 0.5-inch for the top and bottom 0.25-inch steel plates. The mounting unit base is 5 1/8 inch square and the upper load face is 4.74 inch square giving a face area of 22 in.^{2}.

Shear stiffnesses of the front and rear mounts are approximately 1500 lbs/in. and 1200 lbs/in., respectively. The L ratio, or ratio of compression to shear stiffness, is approximately 6.5 to 1 for all mounts.

The mounting unit elastometric material is natural rubber at the rear and more highly damped Lord Co. BTR IV at the front. The more highly damped elastomer was used for the front mounts since space was not available to install vertical and longitudinal hydraulic dampers at the front of the launcher.

Seven Delco standard automotive size shock absorbers are used in the suspension system which furnish additional energy absorption as well as damping capacity. These shock absorbers are described as follows with respect to location, direction and damping force versus velocity.

> Four 1-inch diameter piston, lateral shock absorbers at the four mounts each furnish about 50 lbs/in./s damping force at velocities up to 30 in./s

> Two 1 3/8 inch piston, vertical longitudinal shock absorbers at the rear mounts each furnish about 70 lbs/in./s damping force up to about 30 in./s velocities

> One 1 3/4 inch piston, vertical longitudinal shock absorber at the rear of the launcher furnishes a damping force of 200 lbs/in./s up to 4000 lbs and 80 lbs/in./s up to 6100 lbs
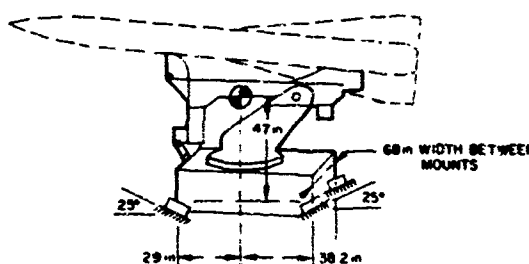
Fig. 2 - Sketch of Suspension Geomtery

SUSPENSION SYSTEM ANALYSES

Analyses were made to determine the natural frequencies and mode shapes of the launcher missile assembly, in six degrees-of-freedom along and about the X, Y, Z axes, considered as a rigid body on the suspension system.

These analyses were conducted by means of a UNIVAC 1108 computer using a special program devised at Raytheon which solves any lumped parameter or distributed system for transient, sinusoidal or matrix form inputs. For dynamics purposes, the program determines undamped natural frequencies and mode shapes as well as transient accelerations, velocities and displacements at the cg and mounts, with time.

The form of the equations used is:

$$M\ddot{x} + C\dot{x} + Kx = F$$

which written out in matrix form and neglecting damping becomes:

$$\begin{bmatrix} Mx & 0 & 0 & 0 & 0 & 0 \\ 0 & My & 0 & 0 & 0 & 0 \\ 0 & 0 & Mx & 0 & 0 & 0 \\ 0 & 0 & 0 & Iy & 0 & 0 \\ 0 & 0 & 0 & 0 & Iz & 0 \\ 0 & 0 & 0 & 0 & 0 & Ix \end{bmatrix} \begin{bmatrix} \ddot{X} \\ \ddot{Y} \\ \ddot{Z} \\ \ddot{\theta} \\ \ddot{\beta} \\ \ddot{\gamma} \end{bmatrix}$$

$$\begin{bmatrix} K_1 & K_2 & K_3 & K_4 & K_5 & K_6 \\ K_2 & K_7 & K_8 & K_9 & K_{10} & K_{11} \\ K_3 & K_8 & K_{12} & K_{13} & K_{14} & K_{15} \\ K_4 & K_9 & K_{13} & K_{16} & K_{17} & K_{18} \\ K_5 & K_{10} & K_{14} & K_{17} & K_{19} & K_{20} \\ K_6 & K_{11} & K_{15} & K_{18} & K_{20} & K_{21} \end{bmatrix} \begin{bmatrix} X \\ Y \\ Z \\ \theta \\ \beta \\ \gamma \end{bmatrix}$$

$$\begin{bmatrix} F\ u(t) \\ 0 \\ 0 \\ 0 \\ 0 \\ 0 \end{bmatrix}$$

The masses $Mx = My = Mz = \dfrac{W}{g}$ where W is the launcher missile weight.

The inertias Iy, Iz and Ix are the pitch, yaw and roll mass moments of inertia about the cg. respectively.

The stiffnesses K_1, K_2, etc., are determined from Lagranges equations of motion in the six coordinate directions wherein:

$$\epsilon = T + U = \frac{M}{2}(X^2 + Y^2 + Z^2) + \frac{1}{2}(I_y\ \partial^2$$

$$+ I_z\beta^2 + I_x\gamma^2) + \frac{k1}{2}\gamma_1^2 + \frac{k2}{2}\gamma_2^2 \cdots + \frac{kn}{2}\gamma_n^2$$

where k_1 ---- k_n are individual mount stiffnesses and γ_1 ---- γ_n are deflections at each mount.

K_1 becomes the overall stiffness due to motion of M_x in the X coordinate in terms of k1 ---- k_n and system geometry. Only 21 of the 36 stiffnesses K need be calculated since the [K] matrix is symmetrical. The units of K are lbs/in., lbs/rad. in.-lbs/in. and in.-lbs/rad.

The inputs F u(t) for these calculations were half sine shock pulses as described under vehicle environment in terms of force at specific time intervals through the pulse.

Natural frequencies and mode shapes obtained from these analyses are listed below.

Mode	Frequency (Hz)	Mode Location (cg)
Vertical	6.9	493" Forward
Lateral	2.5	179" Below
Long-Pitch	3.7	54" Below
Pitch Long	4.6	34" Above
Yaw	4.14	3" Forward
Roll	8.33	6" Above

Results of analyses to determine response at the launcher missile cg to half sine shock inputs are as follows:

Input	Direction	Response
30g - 5 ms	Vertical	4.2g
25g - 10 ms	Vertical	6.9g
30g - 5 ms	Longitudinal	2.3g
25g - 10 ms	Longitudinal	4.1g

A twelve degree-of-freedom system, including the six principal modes of the launcher missile assembly, plus the corresponding six modes of the vehicle considered as a rigid body, was also analyzed for natural frequencies and shock response using the UNIVAC 1108 computer program.

A dynamic model of this system showing the twelve degrees-of-freedom, along and about X, Y, Z axes through the launcher missile cg and the vehicle cg, is shown in Figure 3.

Vehicle suspension stiffnesses are considered in these analyses as well as the launcher suspension and can be varied from actual road arm stiffnesses to infinity for a rigid vehicle case.

The larger twelve mode analytical approach yields lower more accurate launcher missile shock response, especially for inputs at the

162
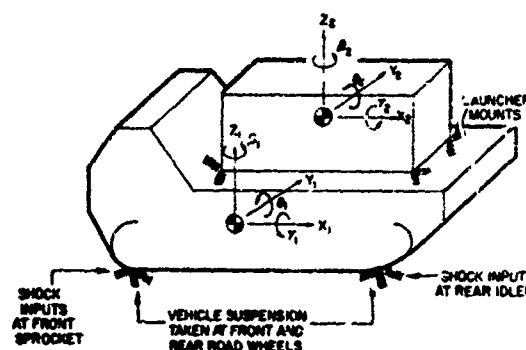
Fig. 3 - Dynamic Model Twelve Degrees-of-
Freedom System

front of the vehicle which are attenuated considerably at the launcher suspension system due to vehicle pitch.

Launcher missile assembly natural frequencies and mode shapes on the suspension system, obtained from the twelve degree-of-freedom analyses, are listed as follows. The six predominantly vehicle frequencies are below 2 Hz.

Mode	Frequency (Hz)	Mode Location (cg)
Vertical	9.2	360" Forward
Lateral	4.1	244" Above
Long-Pitch	5.6	91" Above
Pitch-Long.	4.5	8.5" Below
Yaw	4.4	0.9" Forward
Roll	9.5	5.8" Above

Results of analyses to determine response at the launcher missile cg to half sine inputs at the front and rear of the vehicle are as follows:

Input	Input Direction	Response (g)
30g - 5 ms	Vertical Front	1.1
25g - 10 ms	Vertical Rear	4.9
20g - 10 ms	Vertical Rear	5.8
30g - 5 ms	Longitudinal	2.3
25g - 10 ms	Longitudinal	3.9
20g - 15 ms	Longitudinal	4.6

The above vertical shock response with the twelve degree-of-freedom system is, as anticipated, much lower than with the six, especially due to inputs at the front of the vehicle. Longitudinal response is about the same.

A further extension of these analyses is to consider the vehicle as a distributed mass spring system as compared to a rigid body.

Flexing of the vehicle occurs primarily in the fundamental vertical bending and torsion modes. Although vehicle flexing occurs well above suspension frequencies and is generally relieving from a launcher shock standpoint, vehicle vibratory motions could be treated more accurately using the distributed approach. A further refinement is considering the launcher missile assembly as a distributed system. Launcher missile structural resonances are sufficiently above suspension frequencies, however, not to significantly effect suspension system performance.

Test Correlation

Experimental natural frequency tests were conducted with the vehicle blocked to provide a rigid platform for the suspension system. Results indicated principal natural frequencies of the launcher missile assembly approaching the frequencies calculated for the twelve degree-of-freedom vehicle launcher system.

Natural frequencies closer to the twelve than the six degree-of-freedom system were primarily due to the vehicle not being completely blocked. An increase in dynamic rubber stiffness also occurs at the small ±0.05 inch test response amplitudes as compared to actual deflections up to about 1 inch in compression and 3 inch in shear due to peak shock inputs.

The hydraulic shock absorbers had little effect on natural frequency values. Magnifications at resonance with and without the dampers are listed below from tests in principal directions.

	No Dampers	With Dampers
Vertical	4.7	3.3
Lateral	6.8	2.7
Longitudinal	6.0	4.2

Typical resonance curves measured at the rear of the center missile at the longitudinal rocking frequency, both with and without dampers are shown in Figure 4.

Deflections of the standard automotive type rubber end fittings used on the shock absorbers have the desirable feature of decreasing transmission of most severe higher frequency vehicle vibration through the dampers. The shock absorbers are very effective for their primary design purpose of damping shock induced high velocity large displacement motion of the launcher missile assembly.

Rough Terrain Tests

One of the principal problems in designing a suspension system and launcher missile support hardware for a tracked vehicle application is clearly establishing the severity of the mobility conditions which the system should withstand.

Fig. 4 - Typical Resonance Curves-Long
Pitch Mode

An almost infinite variety of rough terrain
and different size and shape bumps can conceiv-
ably be encountered up to maximum vehicle
speeds. It is evident that judgements must be
exercised in establishing mobility conditions
which are realistic for design purposes as
compared to accidents.

In consideration of the above, certain
natural limitations become predominant. The
first of these is driver safety and degree of
discomfort. In general, the comfort and safety
of the driver are directly related to the speeds
and driving techniques used in negotiating rough
terrain. Tracked vehicle drivers learn from
experience given adequate checkout, permissible
speeds and best driving techniques such as
braking, turning and accelerating to use in
negotiating rough terrain and obstacles without
risking back or head injuries. Accidents must
be separately identified and minimized by
military vehicle procedure and personnel train-
ing.

A second principal consideration from the
standpoint of launcher missile attachment design
conditions is the basic capability of the tracked
vehicle. The suspension system and mounted
equipment can generally be considered struc-
turally satisfactory if they can withstand as
severe mobility conditions as the tracked vehicle
which has undergone considerable testing and
operational military experience.

The above discussion relates principally
to design loads to prevent operational structural
failures. The important overall consideration
is that the missiles fire reliably from the
launcher after being subjected to the total
vehicle mobile environment including vibration,
shock, etc., as well as structural loads.

A special concrete bump course was
constructed at the Raytheon Bedford Laborator-
ies during prototype engineering and develop-
ment to evaluate the SPH mobility environment
over severe terrain.

The course, described below, was more
severe than Munson courses at Aberdeen Prov-
ing Grounds used for vibration and shock tests
of Army vehicles and represented engineering
judgement of the type conditions necessary to
provide a rugged and trouble free SPH system
for the rough country mobility usage intended.

The course consisted of:

1) Two 6-inch bumps, with peaks
   13 feet apart and roughly sinusoidal
   in shape to simulate mild undulat-
   ing terrain.
2) Two 14-inch sinusoidal bumps with
   peaks 17 feet apart to simulate
   severe undulating terrain. The
   peak of the first 14-inch bump was
   21 feet from the second 6-inch
   peak. These bumps were found
   very severe from a vertical and
   longitudinal shock standpoint due
   to sprocket bottomming on the up
   slope of the second 14-inch bump.
3) Four 8-inch racking bumps 7 feet
   apart and staggered to give racking
   motion. The peak of the first
   racking bump was 21 feet from the
   last 14-inch bump.
4) Four 8-inch bumps with peaks 7
   feet apart to simulate washboard
   type terrain. The peak of the first
   washboard bump was 21 feet from
   the last 8-inch racking bump.
   These bumps are also roughly
   sinusoidal in shape.
5) One 3-foot sinusoidal bump to
   simulate a ridge type condition.
   The peak of the 3-foot ridge was
   about 29 feet from the peak of the
   last 8-inch washboard bump.
6) One 8-inch by 6-inch timber
   imbedded in hard surface with
   approximately 200-foot high speed
   approach.
7) Sudden 9-inch dropoff from hard
   surface into hole found to produce
   high rear vehicle shock due to the
   rear idler dropping back on the
   step.
8) Paved roads for most severe
   vehicle vibration.

Fort Devens Course

Engineering and development tests of pro-
totype systems were conducted over rough
roads, tank trails and hilly rocky open terrain
at Fort Devens, Massachusetts. A short 16-mm
movie of tests at Fort Devens and the following

164

Donna Anna course are included in the verbal presentation to illustrate the severe conditions used for SPH mobility tests.

Donna Anna Course

Qualification tests were conducted by the Army Test and Evaluation command, TECOM, over rough desert roads and open terrain on the Donna Anna test range near White Sands Proving Ground, New Mexico. One of the most severe bumps used for repeated testing was a 30-inch deep washout in the hard desert road at the bottom of a small ravine.

Aberdeen Proving Ground

Army TECOM qualification tests were conducted over Munson hard surface courses used for shock and vibration, Churchville Hills and Perryman cross country courses, at Aberdeen Proving Ground, Maryland.

The most severe of these courses from a shock load standpoint was the Perryman 3 cross country course. Approximately 600 miles of continuous 24 hours per day testing was required over this course using drivers in relays at typical to severe driving conditions. Speeds over larger bumps in this course, located about every 100 feet, are generally less than 10 mph increasing up to about 15 mph over smoother sections.

The Perryman 3 course (see Reference 1) varies somewhat with the season, weather and usage. Typical profiles of larger bumps surveyed during SPH tests are shown in Figure 5.
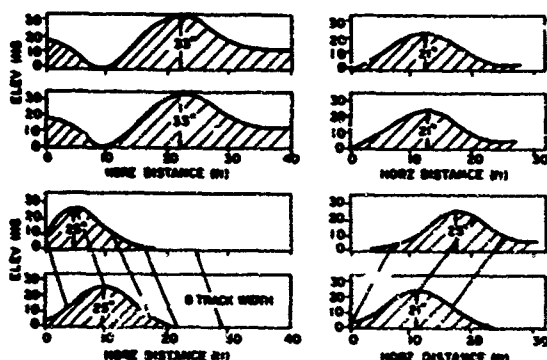
Fig. 5 - Typical Profiles of Larger Bumps on APG Perryman 3 Course

VIBRATION ISOLATION RESULTS

Vibration measurements over the various courses previously described, at frequencies up to 2 kHz, show extremely effective isolation of vehicle vibration from the missiles and launcher.

Results were compatible with design analyses based on the predicted vehicle vibration environment and suspension system design criteria. Missile peak vibration was below ±1g at all frequencies up to 2 kHz whereas vehicle steady vibration frequently reached ±7g with peaks over ±20g.

Peak vibration measured on the launcher missile assembly and vehicle are shown in Figure 6. Peak vibration plotted is defined as the average of about five consecutive peak cycles which occurred repeatedly throughout test runs.
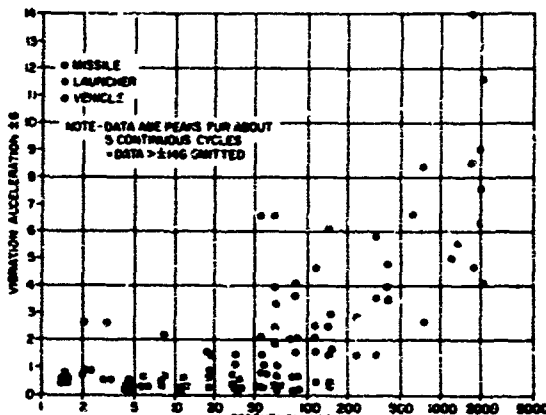
Fig. 6 - SPH Vibration Summary

The high degree of attenuation accomplished by the SPL suspension system is shown graphically in Figure 7, which is a reproduction of steady vibration oscillograph data over a gravel road at 30 mph. The contrast is self-evident between the upper nine quiet traces on the launcher and missiles and the lower six high g broad frequency band traces on the vehicle.

Electronic vibration data reduction conducted by Aberdeen Proving Ground Development and Proof Services, see Reference 2, agree favorably with the results reported above. The maximum vibratory acceleration measured at the center of gravity of the missiles during paved road operation was less than 1g crest and 0.2g rms. Attenuation of g rms levels by as much as 19 to 1 were reported from the cg of the vehicle to the cg of the missiles.

165
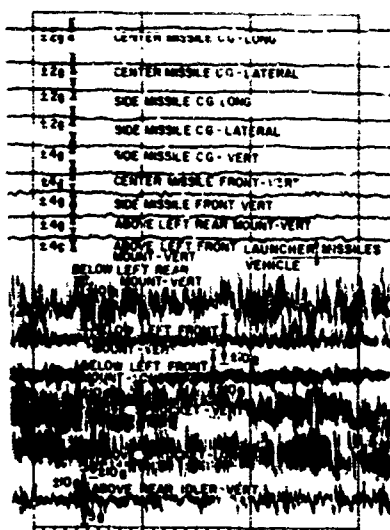
Fig. 7 - Typical SPH Vibration Data at
30 mph

SHOCK RESPONSE

Acceleration data measured at frequencies
up to 2 kHz, over prepared and rough terrain
courses previously described, show very effec-
tive isolation of short period shock inputs from
the launcher and missiles.

Peak shock results on the vehicle and
launcher missile assembly measured on all
courses are plotted in Figure 8. The shock data
plotted are single highest peaks at various half
sine durations reflected back to the zero accel-
eration baseline.
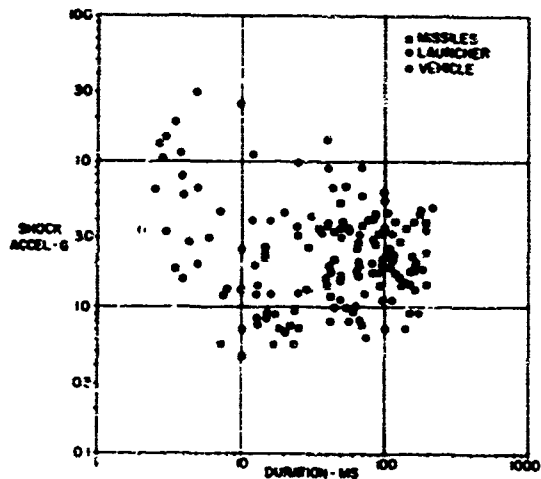
Fig. 8 - SPH Shock Data

As predicted by design analyzes, the data
of Figure 8 shows that the suspension system
attenuated short period shock such as 30g-5 ms
and 25g-10 ms, to less than 7g on the launcher
and missiles.

The decreasing shock isolation effectiveness
as vehicle shock input durations increase can be
clearly seen on Figure 8. Since vehicle shock
levels decrease as durations increase, launcher
missile shock levels are in all cases below
limit load conditions used for design of launcher
and missile attachment hardware.

STRUCTURAL DESIGN LOADS

Simultaneous shock in various directions on
the launcher missile assembly were analyzed
over most severe bumps at Bedford, Fort
Devens, Donna Anna and the Perryman 3 course
at APG for use in establishing structural design
loads.

The Perryman 3 profiles shown in Figure 5
are typical of bumps used for detailed shock load
analyses. Durations of the launcher missile
shock considered applicable for structural loads
were generally between 40 and 200 ms.

The oscillograms of Figures 9 and 10 show
simultaneous shock resulting from traversing
two of the most severe bumps in the Perryman
3 course at so-called maximum safe driving
speeds.

The oscillogram of Figure 9 is used as
follows to illustrate the engineering approach
used in analyzing detailed shock signatures for
simultaneous loads. A peak down vertical
inertia load of 6.8g occurred on the right rear
launcher shaft above the mount. Lower down
loads occurred however, above the other launcher
shafts and at the B missile aft support boom,
such that the maximum simultaneous down load
on the launcher missile assembly averaged 5g.
Simultaneous loads in other directions were
2.5g aft at the B missile aft boom, 0.5g trans-
verse at the launcher shafts and only 0.2g
transverse.

The above simultaneous shock loads are
well below combined limit loads used for struc-
tural design. A combination of the peak shock
levels in various directions, which occur at
slightly different times than the simultaneous
shock values, were also well below the limit
load criteria.

A summary of simultaneous loads deter-
mined over the sixteen most severe bumps
encountered in the Perryman 3 course is con-
tained in Table 1. The bumps were most severe
from the standpoint of resulting accelerations
due to a combination of bump size, higher speeds
and driving technique. It is seen that although
local shock in single directions approaches
limit load levels, combined loads are in all
cases less severe than the structural design
criteria.

Simultaneous shock signature analyses plus the following statistical studies confirmed the SPH design limit load criteria listed below as adequate for structural design purposes

	Combined	Unidirectional
Vertical down	7.5g	8g
Vertical up	1.5g	2g
Longitudinal	±4.5g	±6g
Transverse	±3g	±4.5g

The above vertical down factors include the 1g static load and the up factors represent actual dynamic up inertia loads of 2.5g and 3g.


Fig. 9 - Simultaneous Loads Analysis Bump 8
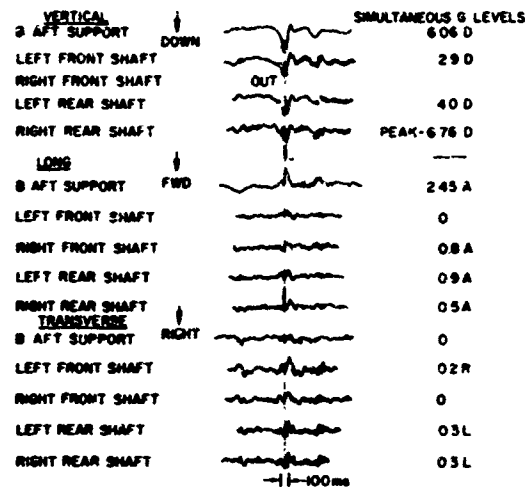
Fig. 10 - Simultaneous Loads Analysis Bump 3

TABLE 1

Simultaneous Loads on Perryman 3 Course Over 16 Most Severe Bumps

	Combined Loads				
	Vertical		Longitudinal		
Bump	Down	Up	Aft	Forward	Transverse
1	3.34M		1.11M 0.31		0.39M 0.31L
2	3.33M		1.25M 0.18L		0.22M 0.24L
3		0.42M	0.04M 0.58L		1.26M 1.5L
4	5.4AS 3.4L		2.0AS 0.42		0.2
5	4.0AS 2.4L		1.4AS 0.4L	0.5L	0.2
6	0.3AS 1.41	1.42		1.4AD 0.6L	1.6AS 1.2L
7	1.4AS 4.4L		2.4AC 1.0L	1.7L	0.3AS 0.5L
8	1.4AS 4.4L		2.4AS 0.51		0.2
9	5.1M 1.8L	1.7AS	3.2M 1.41		1.4M 0.1L
10	2.3M 2.0L		1.3M 0.4L		0.8M 0.1L
11	1.0M 0.4L	1.6M 1.0AS		1.6M 1.3L	3.0M 1.5L
12	3.8M 2.7L		1.6M 0.2L		0.2
13	0.2M			2.1M	3.4M 2.0FS
14	0.3M			1.3M	3.1M 1.1FS
15	2.1M				2.3M
16	1.2M 2.1L	1.7M 1.9AS	0.5L	2.2M	3.7M 0.6FS and AS

M - Missiles
L - Launcher
AS - Aft Missile Support
FS - Forward Missile Support

STATISTICAL SHOCK ANALYSES

Shock data measured over the Perryman 3 course at maximum safe driving speeds was statistically analyzed by means of the UNIVAC 1108 computer.

The shock data used for statistical analyses consisted of peak longer period shock measured over specific bumps, such as the shock data of about 40 to 200 ms duration used for simultaneous loads, see Figures 9 and 10.

Statistical analyses of the large amount of shock data obtained over the Perryman 3 course, at severe driving conditions, was considered of primary significance in confirming structural design loads.

Shock peaks on major elements such as the missiles, launcher and vehicles, in principal directions, were first treated using a standard statistical program to find the arithmetic mean, standard deviation and probability distribution of the data collection. The most convenient form,

however, since most shock data can be consid-
ered symmetrical about zero, used a mean
value of 0G and the Grms or 1σ value as the root
mean square of the shock peaks.

Examples of the later approach are shown
in Figures 11, 12 and 13 for the vehicle spons-
ons below the mounts, the launcher shafts above
the mounts, and the missiles, all in the vertical
down direction.
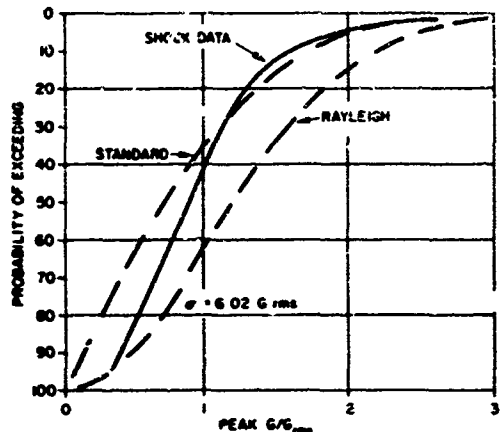
Fig. 11 - Statistical Shock Loads Analyses
Sponsons Vertical Down
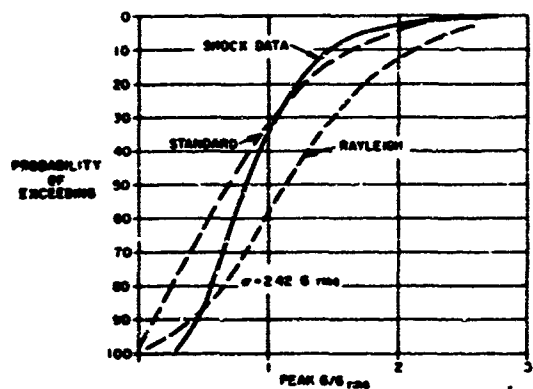
Fig. 12 - Statistical Shock Loads Analyses -
Shafts Vertical Down

The statistical probability curves on Fig-
ures 11, 12 and 13 are typical of all shock data
treated in this manner. The shape of the curves
at higher shock levels is more similar to a
standard than a Rayleigh type distribution,
which are shown on the figures for comparison.
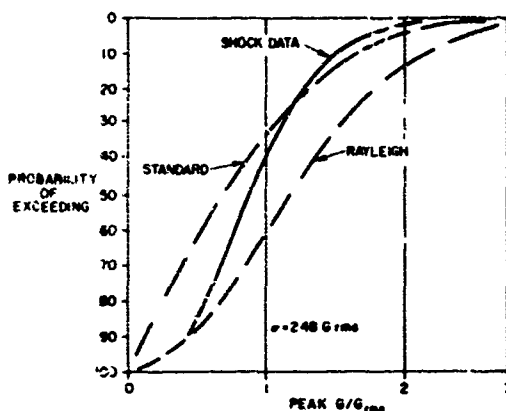
Fig. 13 - Statistical Shock Loads Analyses
Missiles Vertical Down

The probability of reaching high values such as
3σ appear somewhat less than in a standard dis-
tribution.

The following table indicates Grms (1σ)
levels, the peak shock measured and its corre-
sponding nσ value for elements of greatest
interest.

	1σ Grms	Peak G	nσ
All missiles vertical down	2.48	6.0	2.12
All missiles vertical up	1.13	1.9	1.51
All missiles trans-verse	2.14	4.6	2.17
All missiles long-itudinal	1.86	3.7	1.97
Vehicle sponsons below mounts	6.02	13.8	2.30
Launcher shafts above mounts	2.42	6.7	2.79

The above tabulation shows that peak shock
measured was below structural design criteria
levels. The peak nσ values are also below the
3σ level indicating that 3σ loads should generally
represent a conservative approach in designing
for severe rough terrain mobility. Care must
be taken in using this approach for load criteria,
however, to convert data measured locally at
all locations on a major element, such as plot-
ted in Figures 11, 12 and 13, to overall loads
on the element acting in the manner used for
structural analyses.

Further more detailed statistical studies
of the SPL shock data obtained at Aberdeen Prov-
ing Ground are planned in connection with an
improved version of the system currently under
development.

CONCLUSIONS

The SPL secondary suspension system satisfactorily protected the launcher and missiles from excessive vehicle vibration and shock during most severe engineering and qualification test mobility conditions.

Early mobility tests of actual hardware are of primary value during development of tracked vehicle secondary suspension systems to positively establish payload response characteristics. Design analyses should be thoroughly conducted, in consideration of the known environment, to insure a properly engineered system for test evaluation. Computer simulations are valuable in insuring adequate knowledge of significant dynamic behavior.

Design limit loads at 3σ values over longer period Grms shock levels, measured over a variety of representative rough terrain such as the Perryman 3 course at APG appear reasonable for structural design. An adequate statistical sampling must be obtained, however, using typical driving speeds and techniques approaching the limit of driver capability. Overall as well as local loads, should be treated statistically along paths used for structural analyses.

REFERENCES

1) Aberdeen Proving Ground, DPS Report "Automative Test Facilities", May 1966 Fourth Edition.

2) Sobczyk, J., "Final Report on Engineering Test of Self-Propelled HAWK", Aberdeen Proving Ground Report DPS-2548, October 1967.

3) Suhr, E., "Vibration and Shock Environments in Vehicles of the Airborne Multipurpose Family", Food Machinery and Chemical Corporation Report ORD619, December 27, 1960.

4) Clive, H., "Road Shock and Vibration Environment for a Series of Wheeled and Tracked Laying Vehicles", Aberdeen Proving Ground Report DPS-999, June 1963.

5) Smith, R., "Computer Applications in the Dynamic Response Analysis of a Vehicle Traversing a Random Terrain", Food Machinery Corporation Report ORD-ENG-694, September 1963.